ENERGY HARVESTING FROM LIFEJACKETS: MODELLING, DESIGN AND ANALYSIS

A TECHNICAL REPORT SUBMITTED TO AUCKLAND UNIVERSITY OF TECHNOLOGY
IN PARTIAL FULFILMENT OF THE REQUIREMENTS FOR THE DEGREE OF
DOCTOR OF PHILOSOPHY

Jeffrey To

30 July 2024

School of Engineering, Computer and Mathematical Sciences
Auckland University of Technology

Abstract

"If there is something we can do to save lives through technology, there is no reason not to do it"

This thesis presents the development and experimental validation of an energy harvesting system integrated into an IoT lifejacket to assist the sustainable power source for the IoT modules, such as real-time location tracking, health monitoring, and emergency communication. The research aims to address the challenge of limited energy storage in IoT lifejackets by capturing kinetic energy from the wearer's body movements during a drowning event.

In the energy harvesting system developed, a brushed DC motor is attached to the lifejacket's waist strap, with a telescopic linkage connecting it to the thigh strap. The kinetic energy from the vertical rotation of the thigh movements during the active stage of drowning, known as the "ladder climbing" motion, is captured by the motor and converted into electrical power.

The research involves modelling, simulation, and experimental testing to evaluate the system's performance. The results show that the energy harvester can generate a maximum power output of 754 mW and an average power output of 450 mW, which is sufficient to meet the power requirements of basic IoT sensors (210.6915 mW). With an overall power generation efficiency of 89.7%, the power output is adequate for supporting essential IoT functionalities in water safety applications.

The study identifies several limitations, including power losses in the telescopic linkage affecting the wearer's movements. Recommendations for future research include optimizing the motor type and refining the mechanical linkage. Additionally, incorporating a mechanical rectifier and flywheel system could help maintain consistent rotational speed, eliminating the "dead zone" observed during experimental testing.

Overall, the research successfully demonstrates the feasibility of integrating an energy harvesting system into a lifejacket to provide a reliable and sustainable power source for IoT lifejackets, making them more effective for search and rescue operations and improving overall water safety. This innovative solution also has the potential to be applied to other types of wearable devices.

Contents

List of Tables

List of Figures

Attestation of Authorship

I hereby declare that this submission is my own work and that, to the best of my knowledge and belief, it contains no material previously published or written by another person nor material which to a substantial extent has been accepted for the qualification of any other degree or diploma of a university or other institution of higher learning.

Signature of candidate

Publications

To, J., & Huang, L. (2022, December). Life jacket based energy harvesting to assist search and rescue-a review. In *2022 17th International Conference on Control, Automation, Robotics and Vision (ICARCV)* (pp. 925-930). IEEE.

To, J., & Huang, L. (2023, December). An Approach to Model Human Kinetic Energy Harvesting with Wearable Lifejackets to Assist Search and Rescue. In 2023 *5th International Conference on Electrical Engineering and Control Technologies (CEECT)* (pp. 370-374). IEEE.

To, J., & Huang, L. (2024). Experimental Study on Human Kinetic Energy Harvesting with Wearable Lifejackets to Assist Search and Rescue. *Electronics*, *13*(20), 4059.

To, J., & Huang, L. (2024). Energy harvesting from wearable life jackets to assist search and rescue: modeling and design. *Journal of Mechanical Science and Technology*, 38(11), 5817-5828.

Acknowledgements

First and foremost, I would like to express my deepest gratitude to my wife, Chloe, for her unwavering patience, love, and support throughout the entire journey of my PhD. Her encouragement and understanding have been invaluable, and I could not have completed this work without her.
I also want to express my gratitude to the following persons at Auckland University of Technology that have provided essential support to this project:

- **Professor Loulin Huang**
  my primary supervisor, for his expert guidance, insightful feedback, and continuous support. His vast knowledge and relentless encouragement have been critical to the success of this research.
- **Professor Sarat Singamneni**
  my second supervisor for his valuable advice, constructive feedback, and support during the challenging stages of this work.
- **Mr Thomas Boudinot**
  A French student who assisted me in 2023. His help with post-processing the data and performing calculations was essential to advancing this research, and I am deeply grateful for his contributions during his time with the project.
- **Mr Simon Hartley**
  AUT senior technician, for his invaluable support with the experimental setup and troubleshooting. His expertise and assistance were crucial to the success of this research.

  To all of you, I am truly thankful for your belief in my abilities and for pushing me to strive for excellence. Your support has been invaluable in helping me achieve this goal.

Chapter 1

Introduction

1.1 Background

New Zealand is well-known for its large water resources and the popularity of water activities among locals and tourists. However, this also leads to many water-related accidents, making water safety a serious concern. Even though various organisations put efforts into improving water safety skills and education for the public, the number of accidents, including drownings, remains worryingly high [19].

Water Safety New Zealand identifies drowning as the fourth leading cause of accidental death in the country, with 74 deaths in 2020 and 82 in 2019 [20]. Between 2010 and 2017, drownings made up 82% of the total 320 water-related deaths, while hypothermia contributed to only 1% [21]. New Zealand ranks eighth highest for drowning rates per 100,000 people among OECD (Organisation for Economic Co-operation and Development) countries [19]. In health science, drowning is defined as breathing problems caused by being submerged or immersed in liquid [22]. When someone struggles in the water and is at risk of drowning, the term drowning is used, even if the person only experiences minor breathing difficulties.

In recent years, the number of drownings has continued to rise. Water Safety New Zealand reported 91 preventable drowning deaths in 2021, a 7% rise from 2020 and a 13% increase from the five-year average [23]. This marked the highest number of preventable drownings recorded since 2011. The figure rose to 94 in 2022, the highest annual total in a decade. Although 2023

saw a small decrease to 90 preventable drownings, this remains well above the 10-year average.

The data also reveal some concerning trends. In 2023, 83% of drowning victims were male, and 58% were people over the age of 45. There was an increase in incidents involving children under the age of five, with eight deaths recorded—three more than the 10-year average [23]. Auckland saw a sharp rise in preventable drownings, with 26 deaths in 2023, higher than the 2022 figure of 17 and the 10-year average of 16. Waikato also saw a major increase, with 16 drownings, far above its 10-year average of nine.

These statistics underscore the seriousness of the water safety problem in New Zealand. Despite ongoing efforts by organisations like Water Safety New Zealand, the high number of drowning incidents indicates the need for better strategies. These strategies may involve enhanced educational programmes, stricter rules, and increased resources for rescue services.

One of the most effective ways to prevent drowning is through the use of lifejackets. Lifejackets, also known as personal flotation devices (PFDs), are essential safety gear [24]. They work based on the principle of buoyancy, where the weight of water displaced by an object is equal to the object's weight. Lifejackets are constructed from lightweight materials with densities much lower than the average human body. This ensures that when worn, the combined weight of the person and the lifejacket is less than the buoyant force, enabling the person to float. According to Drowning Prevention Auckland [25], of the 220 drowning deaths recorded between 2011 and 2020, 172 deaths were due to people not wearing lifejackets.

Lifejackets are designed for various recreational activities, distances from shore, weather conditions, and sea states. In New Zealand, Maritime Rule Part 91 requires lifejackets to meet New Zealand Standard 5823:2005 – Specification for Buoyancy Aids and Marine Safety Harnesses and Lines – or other standards recognised by Maritime New Zealand, including those from the United States, Australia, Europe, and the International Organization for Standardisation (ISO) [26]. Advisory Circular Issue No. 91-2, released in September 2012, classifies lifejackets meeting or nearly meeting NZ Standard 5823 into several types: Type 401 (open water lifejackets), Type 402 (inshore waters PFDs), Type 403 (buoyancy garments), Type 406 (specialist PFDs for kayaking, white-water rafting, and jet and power boat racing), and Type 408 (specialist PFDs for white-water rafting and jet and power boat racing). For example, Type

401 lifejackets are specifically designed to keep the wearer upright and ensure their mouth and nose remain above water if they become unconscious [27].

Traditional lifejackets are indispensable in drowning situations, but the wearer remains at risk until help arrives. To improve survival chances, finding ways to accelerate the rescue process by accurately sharing the wearer's location with rescuers is essential. The Internet of Things (IoT) offers a promising solution for real-time communication of this critical information. IoT involves connecting devices via wireless or wired networks, allowing them to operate autonomously without human intervention.

Recent research has introduced intelligent IoT lifejacket systems that address the limitations of traditional lifejackets by incorporating modern technology to enhance safety and rescue efficiency [28]. A prototype IoT-enabled lifejacket is developed using components like an Arduino, pulse sensor, Raspberry Pi, Global Positioning System (GPS) module, and a smartphone [29, 30]. These systems typically consist of three main parts: the intelligent IoT lifejacket, a cloud service platform, and a mobile app. The lifejacket is equipped with multiple sensors and actuators, such as water sensors, GPS, general packet radio service (GPRS), LED lights, and a buzzer. The sensors detect when the wearer falls into the water and activate the actuators to send alerts and location details to rescuers [31]. The cloud service platform displays the location information on a map, and the mobile app synchronises with the platform to send real-time updates and alerts to rescuers.

Tests demonstrate that these intelligent IoT lifejacket systems reliably detect falls, provide accurate location information, and send alerts within seconds. GPS accuracy is generally within 10 metres, ensuring that rescuers can quickly locate the person in danger. These systems store historical data on the cloud platform, offering valuable insights for identifying dangerous water areas [31].

1.2 Problem Statement

1.2.1 Limitations of IoT Lifejackets

Energy storage is one of the main challenges for IoT devices. While a more powerful transmission module can support a wider range of communication, it also requires more energy. This trade-off is also true for any extra electronic features that can improve the lifejacket's function, such as shark-shielding technology, which uses two submerged electrodes to create a three-dimensional electrical field that causes nearby sharks to have muscle spasms [32]. While this feature can be lifesaving, it needs more electrical energy to operate.

To add more functions without reducing the time that the device can operate, the energy storage capacity must be increased. However, this usually means a larger and more powerful energy storage device, like a battery, which is too bulky for the lifejacket. Furthermore, batteries used in most IoT devices need regular recharging or replacement. This can be an issue, especially in emergencies when the lifejacket may have been stored for a long time without care. The risk of battery running out at a critical moment can reduce the IoT lifejacket's effectiveness.

1.2.2 The Importance of Energy Harvesting for IoT Lifejackets

One possible solution is to add an energy harvester to the lifejacket. Different types of harvesters can capture various forms of energy, which ideally, can power an IoT lifejacket to continuously send strong signals for a long time, increasing the chances of a successful rescue in an emergency. With the development and integration of energy harvesters into lifejackets, a new generation of IoT lifejackets can be created, offering better solutions for search and rescue missions.

The overall effort and costs of maintaining IoT lifejackets will also be reduced to make them more affordable for general users.

Energy harvesting enables the addition of advanced IoT features as well, like real-time location tracking, health monitoring, and emergency signalling, which enhances the overall effectiveness of the lifejackets. With a reliable power source, these IoT lifejackets can support additional sensors and communication devices, improving rescue coordination and efficiency. The convenience of energy harvesting also enhances the reliability and ease of use of IoT

lifejackets specifically in life-saving situations.

1.3 Thesis Overview

The primary aim of this thesis is to develop and validate an energy harvesting system for IoT-lifejackets, enhancing their functionality and reliability in water safety and rescue operations.

1.3.1 Research Objectives

The primary objective of this research is to develop an energy harvesting system that can be integrated into wearable lifejackets for search and rescue applications. This system aims to provide a reliable and sustainable power source to enable basic IoT functionalities, such as real-time GPS tracking, health monitoring, and communication capabilities, during emergency situations. The research objectives are detailed as follows:

1. **Develop an Energy Harvesting Solution for IoT-Enabled Lifejackets**

   The research focuses on designing an energy harvesting system capable of generating sufficient power from the kinetic energy of human motions during a drowning event. The solution is seamlessly integrated into existing lifejacket designs, making it compact and lightweight without compromising the safety and, comfort of the wearer.

2. **Evaluate Different Energy Harvesting Methods**

   The study investigates various energy harvesting techniques, such as triboelectric, piezoelectric, and electromagnetic methods. Each method is evaluated based on its power output, efficiency, durability, and suitability for water environments. A comparative analysis is done to determine the most effective method for integration with lifejackets, considering factors such as power density, mechanical stability, and ease of integration.

3. **Design the Integration of the Energy Harvester with the Lifejacket**

   One of the objectives is to develop a design for integrating the energy harvester into the structure of the lifejacket. This includes determining the best placement of the harvester to maximise energy capture from a drowning person's limb motions in the water. The

factors such as material properties, waterproofing, and mechanical resilience ensure the energy harvester can function effectively in harsh conditions are to be considered.

4. **Model and Simulate Human Motion During Drowning Events**

   To design the energy harvesting system, the human motion with a pattern of "ladder climbing" during a drowning event [33] is modelled and simulated. The objective is to identify the most energy-rich motions and use this information to refine the design of the energy harvester.

5. **Validate and Test the Performance of the Integrated System**

   The final objective is to validate the performance of the integrated energy harvesting system through a series of simulations and experiments. The experiments will include both ground and water tests to evaluate the system's power output and operational efficiency, demonstrating the feasibility and effectiveness of the system in real-world scenarios.

1.3.2 Scope of the Study

The scope of the study includes the design, development, and testing of an energy harvesting system integrated into wearable lifejackets. The research will address the following aspects:

1. **Energy Harvesting Technologies**

   Different energy harvesting methods suitable for wearable devices, including triboelectric, piezoelectric, and electromagnetic technologies are reviewed and evaluated. Each technology's principles, materials, efficiency, and potential challenges are considered. The scope also includes the development of custom energy harvesting prototypes tailored to capture energy from human motion in a drowning scenario.

2. **Human Motion Analysis in Water Environments**

   Human motions during drowning incidents are modelled, simulated and analysed to understand how energy can be harvested effectively. This will involve biomechanical modelling of the body's motion patterns, such as the "ladder climbing" motion, to identify energy-rich motions that can be targeted for energy capture. The impact of water resistance and buoyancy forces on these motions are considered.

3. **Design of the Lifejacket Integration**

   The physical integration of the energy harvester with the lifejacket is another key part of the research. It includes designing the mechanical structure to accommodate the harvester, ensuring that it does not interfere with the lifejacket's primary function of providing buoyancy and safety. It also involves identifying the suitable position and orientation of the energy harvester to maximise energy capture without affecting the comfort or mobility of the wearer.

4. **Experimental Testing and Validation**

   Experimental tests in both controlled laboratory settings (on the ground) and real-world water environments are conducted to evaluate the energy harvester's performance in generating power from human motions.

5. **Consideration of Environmental and Safety Factors**

   The study addresses environmental factors, such as water resistance, saltwater effects, and physical impact during motion, that could impact the performance and longevity of the energy harvesting system. It also includes safety considerations to ensure that the integrated energy harvester does not compromise the lifejacket's buoyancy, stability, or emergency flotation mechanisms.

6. **Recommendations for Future Development**

   Based on the findings, recommendations for the further development of IoT-enabled lifejackets are provided. They include suggestions for improving the efficiency of the energy harvesting system, potential upgrades to IoT functionalities, and strategies for commercial implementation.

1.3.3 Research Questions

The following research questions are addressed in the study:

1. **Which energy harvesting method is most suitable for integration with wearable lifejackets in water environments?**

This question focuses on evaluating various energy harvesting technologies, such as triboelectric, piezoelectric, and electromagnetic methods, to determine their feasibility, efficiency, and power output. The research assesses the capability of each method to capture energy from human motion and water interactions without compromising the lifejacket's primary safety features.

2. **What are the design and performance trade-offs when integrating an energy harvester with a lifejacket?**

   This question is about the impact of integrating an energy harvester on the lifejacket's buoyancy, stability, and user comfort. The research will identify and evaluate the mechanical and design constraints, ensuring that the addition of the energy harvester does not hinder the lifejacket's ability to perform its primary function of keeping the wearer afloat.

3. **What are the design parameters for the energy harvesting system in terms of placement, size, and material properties?**

   This question is on the design parameters for the energy harvester to maximise energy capture from the wearer's motions. It includes determining the placement within the lifejacket, selecting suitable materials, and determining the ideal size and configuration of the energy harvester.

4. **How can the proposed system be tested and validated in real-world scenarios to ensure it meets safety and operational requirements?**

   This question focuses on the experimental testing and validation of the integrated system. It involves testing the energy harvester in both controlled laboratory settings and real-world water environments to evaluate performance, reliability, and safety under various conditions.

1.3.4 Significance of the Study

This study makes contributions to the field of wearable technologies and water safety by providing a solution to enhance the functionality and reliability of IoT lifejackets. The research is significant for several reasons:

1. **Improved Safety and Rescue Efficiency**

   By developing an energy harvesting system for IoT lifejackets, the research enhances the ability of these devices to operate continuously without solely relying on batteries which risk being flat in the worst cases. This extends the duration of IoT functionalities, such as real-time location tracking and distress signal transmission, thereby improving the chances of successful search and rescue operations.

2. **Contributions to Energy Harvesting Research**

   This research contributes to the knowledge of energy harvesting by exploring applications of existing technologies in the context of wearable lifejackets. It includes the evaluation of various energy harvesting methods, identification of the most suitable techniques for water environments, and a design for integrating these systems into wearable devices.

3. **Enhanced Functionality for Search and Rescue Equipment**

   The developed system allows lifejackets to power additional functionalities, such as environmental monitoring, health status tracking, and emergency signalling, without requiring larger battery capacity or frequent battery replacements. This enhances the utility of IoT lifejackets as comprehensive search and rescue tools that can provide critical information in real-time.

4. **Direction of Future Development**

   The research offers a framework for the development of next-generation IoT lifejackets, providing recommendations for future research and potential pathways for commercial implementation. The findings can lead to the development of commercially viable products that enhance water safety and save lives in emergency situations.

1.3.5 Methodology Overview

The research methodology is designed to develop, test, and validate an energy harvesting system integrated with wearable lifejackets. The following steps outline the approach used in this study:

1. **Literature Review**

A literature review is conducted to identify existing research on energy harvesting technologies, IoT integration, and lifejacket designs. It provides the foundation for selecting the appropriate energy harvesting method and developing the system architecture for the integrated lifejacket.

2. **Human Motion Modelling, Simulation and Analysis**

   Human motion during drowning events is modelled and simulated to identify the most energy-rich motions. Motion capture data are used to simulate the model in typical drowning motion, and the simulation results are analysed to provide a guidance on the placement and configuration of the energy harvester within the lifejacket.

3. **Energy Harvester Design and Modelling**

   The design phase involves developing a prototype energy harvester. This includes selecting materials, mechanical designing, and simulating the system using software tools such as MATLAB. The modelling focuses on predicting the power output and identifying potential design challenges.

4. **Experimental Setup and Testing**

   The integrated system is tested in both the laboratory and the real-world water environments. Tests in the laboratory ("ground tests") are conducted to evaluate energy generation from human motions, while tests in water ("water tests") assess the system's performance under simulated drowning scenarios. Power output and operational efficiency are measured in the experiments.

5. **Data Analysis and Performance Evaluation**

   Data collected from the experiments are analysed to evaluate the performance of the energy harvesting system and its ability to power IoT modules. The analysis results are compared with the initial design objectives to identify the areas for improvement.

1.3.6 Structure of the Thesis

The thesis consists of the following chapters:

- **Chapter 2: Literature Review** - In this chapter, existing research on energy harvesting systems in wearable lifejackets is reviewed, providing an understanding of the current knowledge, key studies, methods, and technological advancements in this field. It covers various energy harvesting technologies, their principles, efficiency, and suitability for integration into lifejackets. The challenges and solutions related to waterproofing, durability, and the impact of environmental factors on energy harvesting systems are discussed.

- **Chapter 3: Human Motion Modelling for Energy Harvesting** - This chapter covers the process of modelling typical human ladder climbing motion a drowning person in the water, with an emphasis on assessing the potential for energy harvesting from the motion. It includes the segmentation of the human body into rigid components, the application of multi-body dynamics, and the calculation of forces and torques acting on the limbs during the motion.

- **Chapter 4: Motion Capture** - This chapter is on motion capture techniques used to collect data on human motions in simulated drowning scenarios, providing the necessary data for analysis. It covers the setup and calibration of motion capture systems, the process of capturing and processing motion data, and the actions taken to tackle the challenges associated with capturing human motion in water environments.

- **Chapter 5: Analysis of Motion Capture Results** - This chapter presents the analysis of the motion capture data, focusing on the angular displacement, velocity, and acceleration of the limbs, and their effects on energy harvesting based on the model established. It includes the calculation of joint angles, the identification of motion patterns, and the estimation of the energy harvested from the recorded motions.

- **Chapter 6: Energy Harvesting Mechanism Design - Overview** - This chapter details the design considerations for the energy harvesting mechanism, including the selection of components, integration with the lifejacket, and waterproofing techniques. It covers the design of the telescopic linkage, the selection of a brushless DC motor as an energy harvesting component and, the design and fabrication of the electrical circuit.

- **Chapter 7: Energy Harvesting Mechanism Design - Modelling, Calculations, and Simulations** - This chapter focuses on the detailed modelling and calculations of the harvested energy. It includes the derivation of the equations for power generation and their simulations under different conditions, and the comparison of simulation results with theoretical predictions from the equations.

- **Chapter 8: Experimental Validation of Energy Harvesting System** - This chapter presents the experimental validation of the energy harvesting system, including laboratory tests and field tests in water, and compares the results with those predicted from the models. It covers the setup and execution of experiments, the collection and analysis of experimental data, and the evaluation of the system's performance in real-world conditions.

- **Chapter 9: Discussions** - This chapter summarises the key findings of the research, discusses the implications for water safety and rescue operations, and outlines potential areas for future research. It includes recommendations for improving the energy harvesting system, suggestions for further studies, and the potential impact of the research on the development of advanced life-saving technologies.

In conclusion, the development of an energy harvesting system for IoT lifejackets represents a contribution to water safety technology. By addressing the limitations of battery-powered lifejackets and providing a continuous power supply through energy harvesting from a drowning person's own motions, this research aims to enhance the functionality and reliability of lifejackets in emergency situations. The following chapters will detail the design, modelling, and testing of the energy harvesting system.

Chapter 2

Literature Review

In this chapter, the water safety issues in New Zealand are described first with the statistics of drowning incidents and the efforts made by various organisations to reduce these risks, stressing the importance of effective strategies like using lifejackets.

Next, the review covers the design and effectiveness of lifejackets and the recent applications of Internet of Things (IoT) technologies to enhance its functionality including sensors and communication tools used to provide real-time data and improve rescue chances. The necessity of equipping the lifejacket with energy harvesting capabilities for reliable power needed for IoT modules is highlighted.

The review then looks at different energy harvesting methods, such as triboelectric, piezoelectric, and electromagnetic systems, and their potential use in lifejackets. The principles behind these technologies, their efficiency, and how suitable they are for wearable devices are explained. Examples of existing applications and research developments are provided to show how these methods can be adapted for lifejackets.

As a potential source for energy harvesting, the motions of people in water, especially during drowning incidents, and how these motions can be used to generate energy are examined. The challenges of energy harvesting in water, such as waterproofing and the impact of saltwater, and suggested solutions to these problems are also discussed.

2.1 Water Safety Issue in New Zealand

New Zealand is widely known for its vast water resources and the popularity of water-related activities among its residents and visitors. However, this high level of water activities also correlates with a high incidence of water-related accidents, making water safety a significant concern in the country. Despite the efforts of various organisations focused on improving water safety skills and education, the number of accidents, including drownings, remains concerningly high [19].

Water Safety New Zealand reports that drowning is the fourth leading cause of accidental death in the country, with 74 fatalities recorded in 2020 and 82 in 2019 [20]. The term "drowning" is used in health sciences to describe respiratory impairment resulting from submersion or immersion in liquid, and it applies even when an individual is at risk of drowning, struggling, or in distress, regardless of whether respiratory impairment has occurred [22]. Between 2010 and 2017, drownings accounted for 82% of the total 320 water-related fatalities, while hypothermia contributed to just 1% [21]. Despite the seemingly small percentage, New Zealand ranks as the eighth highest in drowning rates per 100,000 people among OECD (Organisation for Economic Co-operation and Development) countries [19].

Recent years have seen an increase in drowning incidents. According to Water Safety New Zealand's report, there were 91 preventable drowning fatalities in 2021, marking a 7% increase from 2020 and a 13% rise from the five-year average [23]. This was the highest number of preventable drowning deaths recorded since 2011. In 2022, the number rose further to 94, representing the highest annual loss of life due to drowning in a decade. Although 2023 saw a slight decrease to 90 preventable drownings, this figure still remains significantly above the 10-year average.

The data also reveals some concerning trends. In 2023, 83% of drowning fatalities were male, and 58% were individuals over the age of 45. A worrying increase was observed in incidents involving children under the age of five, with eight deaths recorded—three more than the 10-year average [23]. Auckland experienced a spike in preventable drownings, with 26 fatalities in 2023, surpassing both the 2022 figure of 17 and the 10-year average of 16. Waikato

also saw a dramatic increase, recording 16 drownings, well above its 10-year average of nine.

These statistics underscore the severity of the water safety issue in New Zealand. Despite the ongoing efforts of organisations like Water Safety New Zealand, the high number of drowning incidents highlights the need for more effective strategies to improve water safety. This may involve enhanced educational programmes, stricter regulations, and increased resources for rescue services. The primary goal of this research is to contribute to these efforts by enhancing the effectiveness of lifejackets, thereby improving the chances of survival in search and rescue during a drowning incident.

2.2 Lifejacket and IoT Lifejacket Development

One of the most recognised methods for preventing drowning is the use of lifejackets, also known as personal flotation devices (PFDs)[24]. According to Drowning Prevention Auckland [25], 172 out of 220 drowning fatalities recorded between 2011 and 2020 were due to individuals not wearing lifejackets.

Lifejackets operate on the principle of buoyancy: the weight of the water displaced by an object is equal to the object's weight. They are made from lightweight materials with density much lower than that of the average human body. Consequently, when worn, the combined weight of the individual and the lifejacket is significantly less than the buoyancy from the lifejacket, enabling them to float. In New Zealand, under Maritime Rule Part 91, lifejackets must adhere to New Zealand Standard 5823:2005 – Specification for Buoyancy Aids and Marine Safety Harnesses and Lines – or other national or international standards recognised by Maritime New Zealand, including those from the United States, Australia, Europe, and the International Organization for Standardisation (ISO) [26]. Advisory Circular Issue No. 91-2, issued in September 2012, categorises lifejackets and PFDs that comply or substantially comply with NZ Standard 5823 into several types: Type 401 (open water lifejackets), Type 402 (inshore waters PFDs), Type 403 (buoyancy garments), Type 406 (specialist PFDs for kayaking, white-water rafting, and jet and power boat racing), and Type 408 (specialist PFDs for white-water rafting and jet and powered boat racing). For instance, Type 401 lifejackets are specifically engineered

to keep the wearer upright and ensure their mouth and nose remain above water in the event of unconsciousness [27].

As an example, The Hutchwilco Easy-Fit Inflatable Lifejacket, shown in Figure 2.1, is a popular lifejacket in New Zealand, certified under ISO 12402 and AS4758.1 [27]. The International Organisation of Standardisation (ISO) standard outlines the requirements for buoyancy, performance, materials, and accessories, as well as the protocols for testing. This lifejacket has a buoyancy rate of 170N which is higher than the common inflatable lifejacket on the market, making it suitable for a wider demographic. Inflatable or semi-rigid lifejackets are preferred due to the superior comfort they offer the wearer and their ability to stay inflated for extended periods. This longer inflation duration also allows for more extended potential energy harvesting, making it the chosen subject for this research.

Figure 2.1: *Hutchwilco Easy-Fit Inflatable Lifejacket. [3].*

Although lifejackets are invaluable in drowning incidents, they still leave the wearer at risk until a rescuer arrives. Given the importance of survival, any measures that increase the chances of rescue should be pursued. One potential improvement is to reduce search and rescue times by accurately transmitting the wearer's location to rescuers. The Internet of Things (IoT) offers great promise as an effective method for real-time communication of this critical information,

among other functions. IoT refers to the interconnection of devices via wireless or wired networks, enabling them to perform tasks autonomously without direct human intervention.

Recent studies have introduced intelligent IoT lifejacket systems to enhance safety and rescue efficiency [28]. A prototype IoT-enabled lifejacket was developed using components such as an Arduino, pulse sensor, Raspberry Pi, GPS module, and a smartphone [29, 30]. These systems typically consist of several key components: the intelligent IoT lifejacket, a cloud service platform, and a mobile app. The intelligent IoT lifejacket is equipped with multiple sensors, including water sensors, GPS and GPRS. These sensors detect when the wearer falls into the water, triggering the system to send alerts and location information to rescuers [31]. The cloud service platform displays the location information on a map, and the mobile app synchronises with the platform, allowing rescuers to receive real-time updates and alerts.

Testing has demonstrated that these intelligent IoT lifejacket systems can reliably detect falls, provide accurate location information, and send alerts within seconds. These systems store historical data on the cloud platform, offering valuable information for analysing dangerous water areas [31].

However, energy storage remains one of the primary constraints of IoT devices. While a more powerful transmission module can support a broader range of communication, it also demands more energy. This trade-off applies equally to any additional electronic features that might enhance the lifejacket's functionality, such as shark-shielding technology in which two submerged electrodes emit a three-dimensional electrical field, causing nearby sharks to experience muscle spasms [32]. This function could be life saving but it requires more energy to perform.

To include additional functionalities without compromising operational duration, the energy storage capacity must be increased. However, this typically requires a larger and more powerful energy storage device, such as a battery, which may be too bulky for the lifejacket to accommodate. The limitations of energy storage devices also restrict the operational time of IoT systems. One potential solution is to integrate an energy harvester. Various types of harvesters are available to capture different forms of energy. Ideally, an IoT lifejacket could continuously transmit a strong signal for an extended period by harvesting sufficient energy

from the wearer and their environment, and so it improves the chances of survival. With the development and integration of energy harvesters into lifejackets, a new generation of IoT lifejackets could emerge, providing more effective solutions for search and rescue missions.

In conclusion, lifejackets are essential safety equipment that significantly reduces the risk of drowning. Integrating IoT technologies into lifejackets enhances their functionality by providing real-time location information and alerts, thereby improving the chances of timely rescue. The integration of energy harvesting devices will allow more advanced functionalities to be incorporated into these systems, further improving their effectiveness and duration of operation.

2.3 Devices in an IoT Lifejacket and Their Energy Consumptions

2.3.1 Beacons and VHF (Very High Frequency) Marine Radio

Beacons are effective devices used for locating individuals in distress, particularly in water environments. In search and rescue operations, their effectiveness lies in their ability to transmit precise location signals, allowing rescue teams to respond swiftly. Maritime New Zealand advises the use of three primary types of beacons for search and rescue: Emergency Position-Indicating Radio Beacons (EPIRBs), Personal Locator Beacons (PLBs), and Emergency Locator Transmitters (ELTs) [34]. Among these, PLBs with waterproofing and floating capabilities are the most suitable option for lifejackets [35].

When a PLB is activated, it transmits a distress signal to a network of satellites [36]. This signal is relayed to ground stations and passed on to the Rescue Coordination Centre New Zealand (RCCNZ). Operating at a frequency of 406 MHz with a power output of 5 watts, the signal includes GPS coordinates to pinpoint the user's location. Each PLB has a unique identifier, which is registered with the RCCNZ. Upon receiving a distress signal, RCCNZ coordinates the search and rescue effort to locate the individual in distress. In addition to the main signal, PLBs transmit a secondary signal at 121.5 MHz, which is used by aircraft to conduct more precise searches. With this two-tiered communication system, rescue teams typically arrive within one to three hours after activation, depending on environmental factors and proximity to rescue resources. This dual-frequency transmission system plays a crucial role in reducing the search

Line of sight range	10km
Transceiver power source	Internal battery
CB outpower	3W
IP rating	IP67
Li-ion battery	7.4V 950mAh

Table 2.1: *Specifications of a marine VHF [1]*

time and increasing the chances of survival for individuals in distress.

VHF (Very High Frequency) radio is another key communication tool in emergency situations. In New Zealand, Channel 16 on VHF radios is reserved for distress calls, allowing users to contact the coastguard in emergencies [37]. VHF/UHF radios are also commonly used for monitoring atmospheric conditions, such as tropospheric radio propagation, which is essential in certain rescue operations. Having dual communication systems, such as both VHF radios and beacons, ensures redundancy and reliability in search and rescue efforts, enhancing the chances of a successful mission.

The power consumption of beacons varies depending on their design and functionality. For example, CubeSAT VHF radio beacons can adjust their transmit power output between 27 and 33 decibel-milliwatts (dBm), depending on the requirements of the situation. The XMB-11K, a fully submersible VHF beacon that can operate at depths of up to 11,000 metres, is an example of a self-powered, durable solution for deep-sea applications. In terms of power management, modern beacons are designed to optimise power consumption to extend operational life, which is crucial during extended rescue operations. The specifications of a marine VHF radio from Digitech are listed in Table 2.1, demonstrating the range of power output capabilities for such devices.

In summary, beacons and VHF radios remain critical components in search and rescue operations, providing reliable communication and precise location tracking. Their robust design ensures functionality under extreme conditions, contributing to their efficiency in life-saving missions. These devices, particularly PLBs equipped with GPS and VHF radios, enable rapid localisation of individuals in distress, enhancing the chances of a successful rescue. The combination of these technologies ensures comprehensive coverage, allowing rescue teams to track and locate individuals both from the ground and by air. However, the relatively cost

and high power consumption of VHF radios and beacons presents a challenge, particularly for extended operations in remote areas. This issue is compounded by the fact that these devices often rely heavily on battery power. Prolonged operations can drain the battery quickly, potentially compromising the device's effectiveness when it is needed most. As a result, future developments in search and rescue communication systems may benefit from the integration of alternative communication technologies. Emerging technologies such as Bluetooth, 4G/5G networks, and LoRa (Long Range) communication present promising alternatives to traditional VHF radios. Bluetooth and LoRa are known for their low power consumption, making them suitable for applications where battery longevity is critical. While these technologies may not provide the same range and reliability as VHF radios in all circumstances, their lower energy demands make them attractive options for integration into IoT lifejackets for emergency situations. In combination with energy harvesting techniques, these communication methods could provide continuous functionality without over-reliance on batteries.

2.3.2 Basic IoT Sensor and Supporting Modules

In the study of IoT-based search and rescue devices, a wide range of sensors and supporting modules work together to ensure precise data collection, processing, and communication. These devices typically rely on various components including sensors, a microcontroller unit (MCU), an analog-to-digital converter (ADC), a DC-DC converter, a power management unit, a wireless communication module, and a human-computer interaction interface [38]. Each component plays a vital role in the overall functionality, contributing to the effectiveness and reliability of these devices in critical rescue scenarios. Below are some examples.

Thermistor

A thermistor is a resistor whose resistance varies significantly with temperature, making it a commonly used sensor in IoT devices for monitoring environmental and the wearer's conditions. It operates based on its sensitivity to temperature changes [39]. In a Negative Temperature Coefficient (NTC) thermistor, resistance decreases as the temperature increases, while in a Positive Temperature Coefficient (PTC) thermistor, the resistance increases with temperature [40]. This variation in resistance is converted into an electrical signal, allowing the MCU to

read temperature changes.

Pressure Sensor

A pressure sensor is another common component in IoT devices, especially in rescue situations involving physical contact. It detects falls or entrapment, triggering alerts for immediate assistance The sensor measures the force exerted on a surface, which can provide data about the wearer's motions and interactions with their environment [41]. The sensor typically consists of a diaphragm that deforms under pressure, altering the material's resistance. The corresponding electrical signal is processed by the sensor electronics to calculate the pressure.

MCU

The MCU is the central component of any IoT device, handling data processing, control functions, and communication. An MCU integrates the processor, memory, and input/output peripherals into a single compact unit [42]. For search and rescue IoT devices, the MCU manages data from sensors, processes it, and controls communication protocols such as Bluetooth Low Energy (BLE) and Long Range (LoRa) [43]. The MCU needs to be energy-efficient while maintaining sufficient computational power to perform real-time data analysis, which is essential in life-saving situations.

ADC

An ADC is needed for converting the analog signals generated by sensors, like thermistors and pressure sensors, into digital data that can be processed by the MCU [44]. The ADC samples the continuous analog signal at specific intervals and translates it into digital values. The resolution of the ADC, measured in bits, determines the accuracy of the data conversion.

DC-DC Converter and Energy Storage Module

Energy management is an important module in IoT devices used in rescue missions. DC-DC converters and energy storage modules are essential to maintain a stable power supply, especially in prolonged operations where battery replacement may not be feasible. DC-DC converters efficiently step down or step up voltage levels, ensuring that each device component operates at its required power level [45]. Energy storage components, such as rechargeable batteries or supercapacitors, store energy for later use, allowing the device to function even if the primary power source is unavailable.

Bluetooth Low Energy (BLE) Processing

Bluetooth Low Energy (BLE) is a wireless communication protocol designed specifically for low-power IoT devices, making it ideal for use in search and rescue operations [46] [47]. BLE modules enable the device to communicate with other devices or networks while consuming minimal power. This is needed in rescue operations where the device may need to transmit data over long periods without frequent battery recharges. BLE can be used to connect the rescue IoT device to smartphones or other wearable devices, allowing rescuers to monitor data such as location or vital signs in real time.

Long Range (LoRa) Communication

LoRa technology offers long-range, low-power communication, which is particularly useful in remote or challenging environments encountered in search and rescue operations [48]. LoRa allows communication over several kilometres. It operates on a low-frequency band, making it highly effective at penetrating obstacles such as buildings or dense vegetation. The LoRa module modulates data into radio waves for long-distance transmission [49], ensuring that rescue teams remain connected to individuals in need, even in remote or hard-to-reach areas.

Display Interface

A display interface is essential for providing visual feedback to users, displaying information such as sensor readings, battery levels, and communication signals. In search and rescue missions, the display must be durable, energy-efficient, and clear, even in harsh environmental conditions. LCD or OLED screens are typically used, offering a user-friendly way to present data that can inform decisions during a rescue operation.

Global Positioning System (GPS) Module

A GPS module utilises signals from a network of satellites to calculate precise geographical coordinates, including latitude, longitude, and altitude [50]. It operates by analysing the time delay between signal transmission from satellites and reception by the GPS receiver. IoT-compatible GPS modules often integrate with microcontrollers via standard protocols like UART (Universal Asynchronous Receiver-Transmitter) or I2C (Inter-Integrated Circuit) and are equipped with low-power modes for energy efficiency. These modules are widely used in navigation, geofencing, and asset tracking. Advanced models also incorporate Differential GPS

(DGPS) for centimetre-level accuracy.

Accelerometer

An accelerometer measures acceleration along one or more axes, typically using MEMS (Micro-Electro-Mechanical Systems) technology [51]. These sensors rely on capacitive, piezoelectric, or piezoresistive principles to detect changes in motion. Accelerometers commonly output raw data in terms of g-forces, which can be processed further for applications such as motion tracking, vibration monitoring, and gesture recognition. IoT implementations often utilise digital accelerometers with I2C or SPI (Serial Peripheral Interface) interfaces for seamless integration with microcontrollers. Advances in low-power design have made them ideal for wearable devices, with power consumption as low as a few microamps in standby modes.

Heart Rate Sensor

A heart rate sensor measures the beats per minute (BPM) of a user by detecting blood volume changes using photoplethysmography (PPG) or electrical signals using electrocardiography (ECG) [52]. PPG-based sensors utilise light-emitting diodes (LEDs) and photodetectors to measure variations in light absorption caused by blood flow, while ECG-based sensors detect the electrical activity of the heart. Heart rate sensors are widely used in fitness trackers, medical devices, and IoT health monitoring systems. Advanced sensors integrate algorithms for motion artefact reduction and operate efficiently with microcontrollers via standard interfaces like I2C or UART. They often include low-power modes to optimise battery life in wearable IoT devices.

2.3.3 Energy Consumption

The energy consumption of an IoT lifejacket is mainly for the operations of the communication systems and sensor modules. The communication systems tend to require a substantial amount of energy, especially in environments where network coverage is limited, or where long-range communication is necessary to maintain contact over large distances. For instance, VHF radios, which are often used in maritime and land-based rescue operations, are known for their high power consumption, particularly when transmitting data over long distances. The need to maintain a strong and reliable signal often results in increased energy demands, which can significantly impact the device's battery life during extended rescue missions. Beacons, such

as PLBs or EPIRBs, are designed to send distress signals and precise location data. While these devices are generally designed to be energy-efficient, the transmission of signals over long distances, often in challenging conditions, requires a substantial amount of energy, especially when the device must operate for extended periods.

The sensor and supporting modules used in the IoT lifejacket are the other factors in the overall power consumption. These sensors are designed to monitor the wearer's condition and their surroundings, providing real-time data that can be crucial for making informed decisions during rescue missions. In addition to the sensors discussed above, other typical sensors include GPS, accelerometers, heart rate monitors, and environmental sensors for monitoring temperature and other vital parameters. GPS modules, for example, are often used to track the precise location of the wearer in real time, which is critical for coordinating rescue efforts. However, continuous GPS tracking requires substantial energy, as the device must constantly communicate with satellites to determine its position. Additionally, accelerometers, which are used to monitor motion and detect falls, also contribute to energy consumption due to the need for constant data acquisition and processing. Similarly, heart rate monitors and other biometric sensors require continuous data collection and transmission, which can quickly drain the device's battery, particularly when real-time monitoring is required. These sensors often require real-time data processing to ensure that the information gathered can be quickly and accurately relayed to rescuers. This data processing, coupled with the need for frequent data transmission, further contributes to the overall energy consumption of the device.

For this research, understanding the power consumption of each component is critical as it helps to understand what is the minimum requirement for the energy harvester. It is included the specification of the typical components in Table 2.2.

Part	Category	Size	Voltage (V)	Current (mA)	Power (mW)
Sensors	Thermistor	50mm x 10mm	10	0.00079 - 0.00134	0.0134
	Pressure sensor	65mm x 65mm x 0.5mm	1.5	0.55	0.825
	GPS Module	10mm x 10mm x 1mm	3.3	10	33
	Accelerometer	2mm x 2mm x 2mm	1.8	0.005	0.009
	Temperature sensor	2mm x 2mm x 2mm	2.7	0.001	0.0027
	Heart rate sensor	3mm x 3mm x 2mm	1.8	0.5	0.9
MCU	Active mode	3mm x 3mm x 0.8mm	3	1.28	3.84
	Sleep mode	3mm x 3mm x 0.8mm	3	0.001	0.003
ADC	Signal conversion	3mm x 3mm	3	0.3	0.9
DC-DC Energy storage	Power management	2mm x 2mm 0.74mm	4.2	0.008	0.0336
Data transmission	BLE processing	8mm x 8mm x 1mm	3.3	1	3.3
	BLE sleep	8mm x 8mm x 1mm	3.3	0.001	0.0033
	LoRa Rx/Tx	16mm x 16mm x 3.5mm	3.3	33	108.99
	LoRa Sense	16mm x 16mm x 3.5mm	3.3	4.2	13.86
	LoRa Sleep	16mm x 16mm x 3.5mm	3.3	0.0247	0.0815
Display interface	LED	$10cm^2$	3	15	45
	Electronic ink		0.02	1	0.02
				Total	210.6915

Table 2.2: *Typical IoT sensors specification*

2.4 Energy Harvesting from Natural Energy Sources and Drowning Persons

2.4.1 Energy Harvesting from Natural Energy Sources

There is a considerable amount of research focused on harvesting energy from natural sources such as wave and solar energy. In the context of wave energy, a linear generator is often employed within a wave energy converter. It is commonly referred to as a heaving system [53]. In this system, the buoy moves up and down in response to the wave motion, causing the translator within the generator to slide vertically. This motion leads to a change in the magnetic flux, thereby inducing voltages. Other wave energy systems include oscillating water columns, overtopping devices, and oscillating body systems [29]. These systems all harness the motion of waves to generate rotational or linear motions, which are then converted into electrical energy.

Solar energy has gained attention in recent years as a clean, cost-effective, and renewable energy source [32]. Extensive research has been conducted on solar photovoltaic technology, leading to the development of various solar films designed to enhance energy conversion efficiency. The efficiency of solar energy harvesters is subject to several influencing factors such as temperature, dust accumulation, wind conditions, humidity, and shading. These variables can significantly impact the performance of solar panels, making it challenging to achieve consistent

energy output.

Most studies on solar energy harvesting are focused on large-scale industrial applications, where environmental conditions can be monitored and managed more effectively. The unpredictable nature of weather conditions, particularly during emergency situations like drowning events, complicates the direct application of solar technologies in lifejackets.

Given these limitations, the focus of energy harvesting in lifejackets shifts towards alternative methods that can reliably function under the dynamic conditions of a drowning event. This includes exploring energy harvesting directly from the motions of the drowning person, which offers a more consistent and practical source of energy.

2.4.2 Energy Harvesting from Human Motions

The drowning event can be divided into two stages which are the active and passive stages. During the active stage of drowning, the individual is typically conscious and capable of moving their limbs. During the active stage, the motions of a drowning victim can generate substantial kinetic energy. For example, it has been reported that a 68 kg person's heel strike can produce up to 67 W of power when hitting the ground [54]. Bicep curls and arm lifts can generate approximately 24 W and 60 W, respectively. Additionally, an 80 kg person walking at 4 km/h can generate about 2 W of energy from heel strikes [55]. In comparison, a two-degree-of-freedom (DOF) floating board carried by a lifejacket has been found to harvest around 4 W from waves during both bench and lake tests [56]. This is significantly less than the 6.47 W harvested from a knee joint when a person walks at 4.5 km/h using an electromagnetic harvester [57].

It is important to recognise that human motions during a drowning event are more vigorous and intense than during typical walking. A common response during drowning is the "ladder climbing motion," a behaviour associated with the "Instinctive Drowning Response" (IDR), which is widely acknowledged as a visible sign of drowning [33]. During this motion, the victim typically extends their arms laterally in an attempt to breathe while underwater. The victim's arms may spin backward violently in an effort to keep their head above water. In such situations, it is rare for the victim to scream or wave for help.

This instinctive behaviour typically lasts between 20 and 60 seconds at the water's surface

if the victim is not wearing a lifejacket [33]. With a lifejacket, the active stage is likely to last longer as the lifejacket prevents the victim from sinking. It is evident that the amount of energy that can be harvested from human motions during the active stage of drowning is significantly higher than that generated from walking or wave energy.

This research primarily aims to harness energy from the kinetic motions generated by the person during this stage. To effectively capture this kinetic energy, one of the initial tasks is to observe and understand the specific body and limb motions that occur when a person is in the water. These motions vary significantly with the individual's swimming ability. For instance, a person who can swim exhibits controlled and coordinated motions, which can be advantageous for energy harvesting. In contrast, an individual who is a poor swimmer displays erratic and less predictable motions, making it more challenging to efficiently harness kinetic energy.

In contrast, in the passive stage of drowning, the individual is likely unconscious and unable to voluntarily move his/her limbs. This stage is not the main focus of this research because the lack of significant motion makes harvesting kinetic energy from human motion less viable. Instead, during this stage, environmental energy sources such as wave, solar, and wind energy could be considered for energy harvesting in future research.

Typically, in a drowning incident, there is a transitional period from the active stage to the passive stage. The duration of the active stage varies depending on the situation, but wearing a lifejacket generally prolongs this stage by preventing suffocation, provided the victim is not severely injured. Regardless of the method of energy harvesting used, the source of energy remains a major factor.

The motion of a drowning person is influenced by the structure his/her body. A dynamic model can be developed for such motion analysis. A human dynamic model can be used to determine the optimal integration of an energy harvester with a lifejacket, maximising energy output. During the active stage, a drowning person can control their limbs similar to how they might inflate a lifejacket using a mouthpiece. This research focuses on harvesting as much energy as possible during the active stage. When extracting kinetic energy from human motion, it is important to assess the amount of energy that can be generated and its relationship with the motions of different body parts, as governed by the dynamic model [58].

While research on harvesting human kinetic energy from lifejackets is limited, studies have been conducted on other wearable equipment. For example, energy harvesting from human daily motion to power a wristwatch-like fitness gadget is discussed in [59]. The gadget includes a heart rate monitor, accelerometer, temperature sensor, GPS, and ANT transceiver. The energy harvester employed is a Velocity Damped Resonant Generator (VDRG), which is based on electromagnetic or piezoelectric principles where the damping force is proportional to the relative velocity between the proof mass and the generator frame [60]. Research has been conducted on harvesting energy from the lower limb that alternately accelerates and decelerates during walking [57]. The human body model involves 15 segments, including the head, upper trunk, upper arms, forearms, hands, lower trunk, thighs, legs, and feet. Since the upper arms, forearms, and hands do not swing significantly during walking, they can be grouped into one segment with the head as the upper body. Using the Lagrangian method, a seven-link rigid dynamic model is established in the sagittal plane, incorporating the upper body, thighs, legs, and feet.

Energy harvesting from knee rotation using a spring-damping mechanism in a lower limb exoskeleton has also been studied [55]. In this system, knee motion is transmitted by cables to spiral springs, which then drive a generator through a gearbox to produce electricity. To effectively harvest mechanical energy, it is necessary to distinguish between positive and negative mechanical work within human motion. Positive mechanical work is performed by muscles initiating motion, while negative mechanical work involves muscles absorbing energy to stop motion. If the harvesting device is used during positive work, it increases the muscle's workload, thereby raising the metabolic cost. By harvesting energy from negative work, the workload on the muscles is reduced. This concept is analogous to regenerative braking in hybrid vehicles and, theoretically, should have minimal impact on natural motion.

When evaluating potential power harvesting, five factors are considered:

1. The muscle's negative work phases during each motion,

2. The method by which the device is attached to the body,

3. The convenience of using the device,

4. The effect of the device's additional weight on the effort expended by the wearer, and

5. The impact of the energy harvesting device on the body.

The development of a negative work harvesting module (NWHM) for energy harvesting in an active exoskeleton involves targeting specific joint motions [61]. The energy harvesting motor utilised is an efficient direct current brushless motor. However, due to the unsteady voltage produced, a voltage regulating circuit is required.

2.5 Energy Harvesting Devices with Wearable Devices

Energy harvesting integrated into lifejackets has not been explored, but there are studies on energy harvesting technologies that can be integrated with other types of wearable devices [38]. These studies provide valuable insights into the requirements, power consumption, system architecture, energy storage, sensors, application scenarios, and future perspectives of energy harvesting in wearables. A comprehensive survey is conducted to study and compare different wearable energy harvesting systems [62]. According to this survey, triboelectric and piezoelectric generators demonstrate high efficiency for motions ranging from 1 Hz to 10 Hz, making them suitable for harvesting kinetic energy from limb motions. On the other hand, electromagnetic generators are noted for their ability to produce a high output current with a robust and durable design.

Another review focusing on energy harvesting for wearable devices in telemedicine applications points out that most wearable devices do not have energy harvesting capabilities [63]. The operation of these devices relies only on battery power and their performances are compromised when the batteries are flat. Energy harvesters are essential to overcome this limitation, providing a sustainable power source for continuous operations. The subsequent sections will delve into the fundamentals, applications, and characteristics of each energy harvesting method, providing an overview of their potential integration into lifejackets.

2.5.1 Triboelectric Nanogenerators (TENGs)

Triboelectric nanogenerators (TENGs) function by converting mechanical energy into electrical energy through the combined effects of the triboelectric effect and electrostatic induction [29]. The triboelectric effect occurs when two materials with different electron affinities come into contact and are then separated, causing one material to gain electrons while the other loses them. This interaction generates opposite charges on the surfaces of the two materials. TENGs consist of two primary layers made from materials chosen based on their position in the triboelectric series, which ranks materials according to their propensity to gain or lose electrons. When an external mechanical force—such as pressing, sliding, or vibration—causes these layers to come into contact, electrons transfer from one material to the other, leading to a charge imbalance. As the layers are separated, an electric potential difference is established due to the separated charges. This potential difference drives electrons through an external circuit to balance the charges, producing an alternating current (AC) as the materials continue to make contact and then separate. TENGs can be configured in various operational modes, such as vertical contact-separation, lateral sliding, single-electrode, and freestanding triboelectric-layer modes, depending on the application and desired output characteristics. The efficiency of a TENG is influenced by several factors, including the choice of materials, surface roughness, contact area, and the frequency of the mechanical input. Advanced techniques such as surface microstructuring and material optimisation can enhance the charge density and improve overall performance. TENGs are particularly suitable for powering small, low-power devices in applications like wearable electronics, environmental monitoring, and self-powered sensors due to their ability to efficiently harvest ambient mechanical energy and their simple, scalable design.

Since the first report on TENGs in 2012 [64], numerous applications have been developed, particularly those related to human motion. These applications range from capturing energy from large scale (gross) motions such as walking and finger tapping to small scale (fine) motions like breathing, swallowing, and blinking [65] [66] [67] [68].

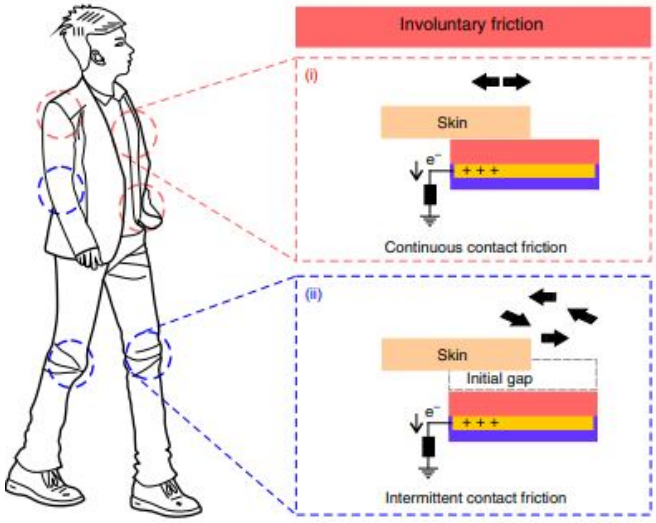

Figure 2.2: *Schematically illustration of the possible involuntary friction of textile-TENG on different regions of human body [4].*

A skin-touch-actuated wearable triboelectric nanogenerator, as illustrated in Figure 2.2, has been integrated into textiles to harvest kinetic energy from both voluntary and involuntary body motions [4]. This device demonstrates a maximum instantaneous output of 880V and 1.1μA cm^{-2} when subjected to voluntary touches with an applied force of approximately 5N at a frequency of 4Hz. It is capable of harvesting an output of 60V and 9nC cm^{-2} from involuntary friction with the skin. These results highlight the device's potential for converting various types of mechanical stimuli into electrical energy, which can be used to power small electronic devices.

Another significant development in this field is the bionic stretchable nanogenerator (BSNG), which is inspired from the electric eel's natural ability to generate electricity, as shown in Figure 2.3 [5]. The design of the BSNG mimics the ion channel structure found in electrocytes of electric eels, with a mechanical control channel created by the stress-mismatch effect between polydimethylsiloxane (PDMS) and silicone. The device utilises triboelectrification, caused by the flow of liquid, along with electrostatic induction to generate an open-circuit voltage exceeding 10V underwater and more than 170V in dry conditions. The versatility of this device allows it to be applied to various body positions underwater, enabling the harvesting of mechanical energy from human motion in water environments.

An undersea rescue system was developed by incorporating four wearable BSNGs into a commercial diving suit, specifically around the elbow and knee areas. Each BSNG was connected to a 100μF capacitor via four rectifier bridges. The stored energy in the capacitor was then used to power a wireless transmission module, demonstrating the practical application of this technology in real-world scenarios. The ability to harvest energy from human motion underwater presents significant advancements in the development of self-powered systems for underwater rescue operations and other water applications.

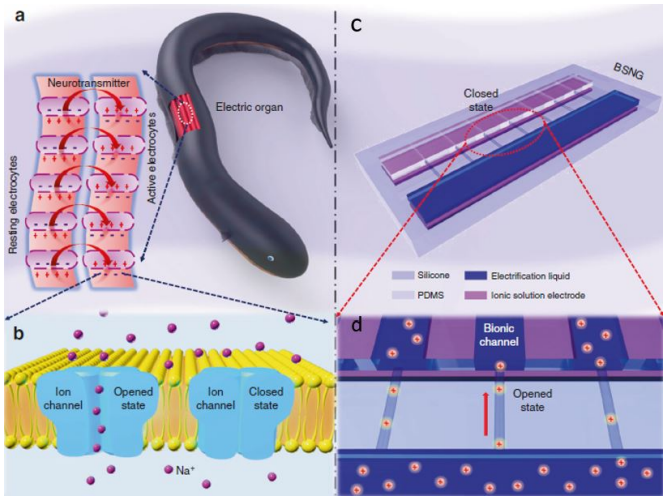

Figure 2.3: *Bionic principle and structure of bionic stretchable nanogenerator. (a) Schematic diagram of electric eel and electrocytes. (b) Schematic diagram of ion channels on cytomembrane. (c) Scheme diagram of bionic stretchable nanogenerator (BSNG) with double layer structure. (d) Output signal of BSNG in one working cycle. [5].*

A non-contact triboelectric nanogenerator (TENG) has been developed for the dual purpose of monitoring human motion and harvesting energy [6]. This TENG design incorporates the human body as an integral part of the system, with the remaining components consisting of a piece of printing paper coated with a metal electrode film. The basic structure and working principle of this TENG are illustrated in Figure 2.4a. Before operation, the paper is positively charged by tapping it with a Kapton film. As the participant walks, electronic signals are generated due to the variation in relative distance between the participant and the fixed paper-based TENG.

Figure 2.4b–i demonstrates that when the participant raises their left leg, bringing it closer to the TENG, negative charges flow from the electrode. Conversely, when the leg is lowered,

as shown in Figure 2.4b–ii, the increasing distance between the leg and the TENG results in negative charges flowing back into the electrode. A similar pattern is observed during the motion of the right leg, as depicted in Figure 2.4b–iii and iv.

It is important to note that the participant's clothing material may influence their charge, either positively or negatively, which in turn affects the signal amplitude and direction. This variation does not change the fundamental working principle of the TENG. The rectified output from the TENG system can charge a capacitor when the participant steps in place at a distance of approximately 30cm from four A4-sized paper-based TENGs connected in series. This demonstrates the practical application of the TENG for energy harvesting and motion monitoring in a non-contact setup.

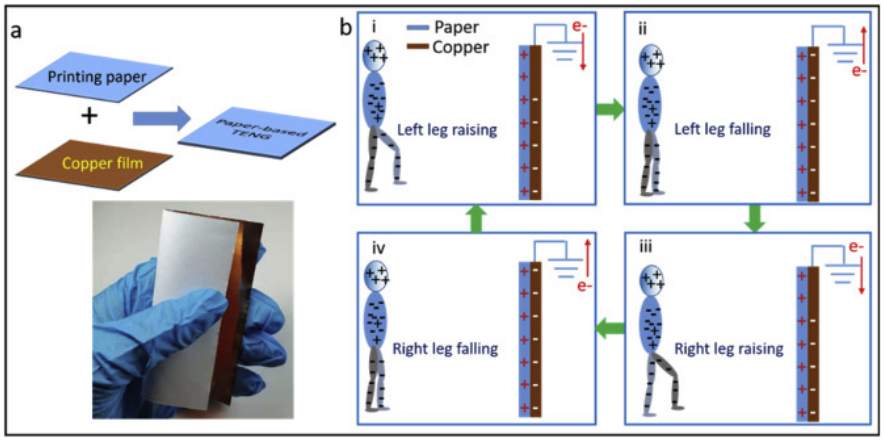

Figure 2.4: *Image and operational mechanism of the non-contact TENG. a) Schematic representation and photograph of the paper-based TENG with a surface area of 10 × 10 cm. b) Illustration of the working principle [6].*

To enhance the efficiency of energy harvesting using triboelectric nanogenerators (TENGs), a flexible arc-shaped TENG (F-TENG) has been developed. This innovative design aims to efficiently harvest biomechanical energy from all directions by utilising a 3D arc structure, as illustrated in Figure 2.5. The F-TENG is constructed by weaving core-shell yarns, which significantly reduces the angular dependence typically associated with energy harvesting in conventional TENGs. As a result, this design achieves a 35.5% improvement in energy harvesting efficiency compared to traditional sandwich-type TENGs, enabling the multi-angle capture of biomechanical energy.

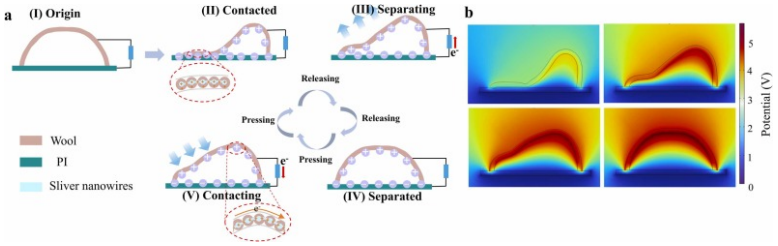

Figure 2.5: *Illustrates the operational principle of the 3D F-TENG. (a) Schematic diagram showing the operational principle; (b) Schematic of the COMSOL simulation.[7].*

The power generation mechanism of the F-TENG is detailed in Figure 2.5a. Initially, in State I, the two triboelectric layers remain apart, resulting in no charge generation or potential difference between the electrodes. When an external force brings the wool and polyimide layers into contact, positive and negative triboelectric charges are generated on their surfaces [69]. In this stage (State II), there is no potential difference between the electrodes, and hence no electron flow occurs in the external circuit. Upon the removal of the external force, the separation of the layers induces a dipole moment, creating a potential difference that drives electrons through the external circuit from the electrode of the electronegative material to that of the electropositive material (State III). Finally, in State IV, when the triboelectric layers are fully separated, dynamic equilibrium is established. If the layers are subjected to external force again, electrostatic induction causes charges to flow back through the external circuit until the two layers are in full contact once more (State V) [70] [71].

To further understand the working mechanism of the F-TENG, finite element simulations were performed to visualise the electrostatic potential distribution across the sample in different states, as shown in Figure 2.5b. By adjusting the projection ratio P, the relative motion distance and effective contact area are effectively coordinated. At an optimal projection ratio of P = 1.6, the voltage output of the F-TENG is three times greater than that of conventional 3D flexible-based TENGs, while the corresponding output current is 2.6 times higher. These results demonstrate the F-TENG's capability in managing irregular and complex human motions, making it more effective than traditional methods in harvesting energy from such activities.

2.5.2 Piezoelectric Energy Harvester

A piezoelectric energy harvester converts mechanical energy into electrical energy through the piezoelectric effect, a phenomenon in which certain materials generate an electric charge when subjected to mechanical stress. This technology is utilised in various applications, including pedestrian walkways, bridges, and machinery, where piezoelectric elements are strategically placed to capture energy from vibrations or motions. As these elements bend and flex under dynamic forces, they produce voltage that can be harnessed to power small devices or stored in batteries for later use. The piezoelectric effect offers a sustainable energy source by converting everyday mechanical activities into usable electricity, thereby reducing dependence on traditional power sources and promoting energy efficiency. Below are some examples of piezoelectric energy harvesting applications and research developments.

Various piezoelectric energy harvesting (PEH) methods have been investigated. One of the approaches involves capturing energy from road vibrations caused by moving vehicles. A specific harvester was designed to respond to typical road vibrations by tuning its natural frequency accordingly. Under high-frequency external vibrations (30Hz), this harvester can generate a maximum electrical power output of 300mW [72]. Another example involves a Polyvinylidene Fluoride (PVDF) bridge-type displacement amplification module, which has demonstrated the capability to produce up to 16.5 W/m² with a small vertical displacement of 2.5mm [8].

In marine environments, piezoelectric energy harvesters are also being studied. A commonly used piezoelectric ocean wave energy harvester (POEH) consists of a magnet and a metal ball mounted on a rail or tube designed to collect energy from waves coming from all directions, as shown in Figure 2.6 [73].

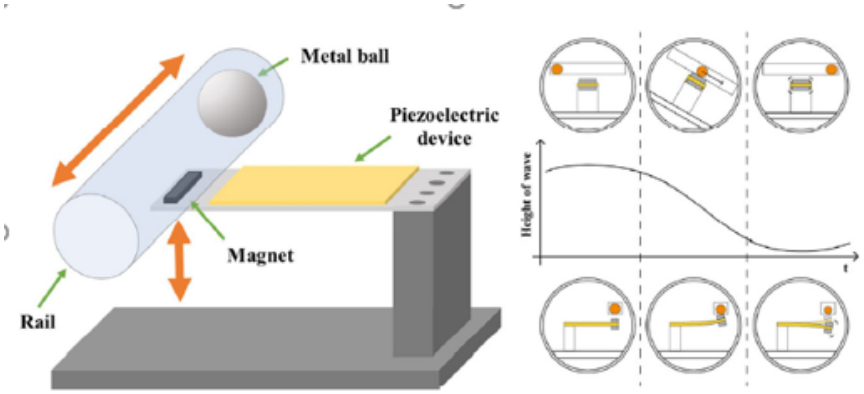

Figure 2.6: *Schematic of piezoelectric energy harvester (left) and its operation (right) [8].*

In a basic cantilever structure designed for energy harvesting, a magnet is attached to the free end of the piezoelectric module, while a metal ball is placed within a tube above the magnet. The motion of ocean waves causes the harvester to tilt, which makes the metal ball roll towards the lower end of the tube and attract the magnet. This interaction induces vibrations in the piezoelectric module, causing it to oscillate at its primary resonance frequency, which remains constant regardless of the speed of the metal ball. Experimental results indicate that the maximum open-circuit voltage achieved by this system is 21.1V, with a displacement of 13.2mm. Under the same conditions, the maximum power output recorded was 68.9μW at an impedance of 95kΩ.

Another study utilises organic piezoelectric polymer films which are know for their flexibility and ease of processing. These characteristics make them particularly well-suited for wearable sensors and energy harvesters. These films are useful for self-powered wearable systems used in IoT applications, owing to their ability to generate power independently [74]. For example, when applied to the chest surface, piezoelectric sensors can convert vibrations induced by respiratory and heartbeat activity into voltage signals. To enhance the flexibility and stretchability of these sensors, a serpentine structure is designed, using curved arcs instead of straight lines. This design allows the structure to be fully deformable in-plane and highly compliant with stretching, making it resilient enough to endure numerous cycles of deformation.

In the context of piezoelectric wearable-based energy harvesting (PWEH) and body motion energy harvesting (BMEH), experiments were conducted by placing the harvesters on various

body locations, including the neck, shoulder, elbow, wrist, hip, knee, and ankle [75]. Five types of locomotion—walking, stair climbing, jogging, and running—were selected to compare the energy harvested during these activities. The power output values varied from 6μW to 74μW. For direct skin contact, the piezoelectric harvesters were placed in the pockets of a tight elastic cotton suit. Two common types of piezoelectric materials were used: lead zirconate titanate (PZT), a ceramic piezoelectric, and polyvinylidene fluoride (PVDF), a polymeric piezoelectric. In terms of user comfort, PVDF technology fits better to body motions due to its higher flexibility, while PZT offers higher power output.

Beyond joint motions, the stretching of human body parts can also be studied for energy harvesting. A woven piezoelectric structure, as illustrated in Figure 2.7, was developed to harvest energy from the stretching of large body areas using a wearable platform [9]. This structure features polymer column threads and piezoelectric row threads that form a textile-like design. When stretched, identical strain polarities are generated on the top and bottom surfaces of the piezoelectric threads. The piezoelectric film undergoes tensile stress, leading to the generation of alternating potential during continuous stretching and contraction. With a load resistance of 120kΩ and a frequency of 8Hz, the maximum peak output power generated by a single piezoelectric thread (5 x 35mm²) was recorded at 1.1mW, 0.85mW, and 0.7mW for stretching lengths of 7mm, 5mm, and 3mm, respectively.

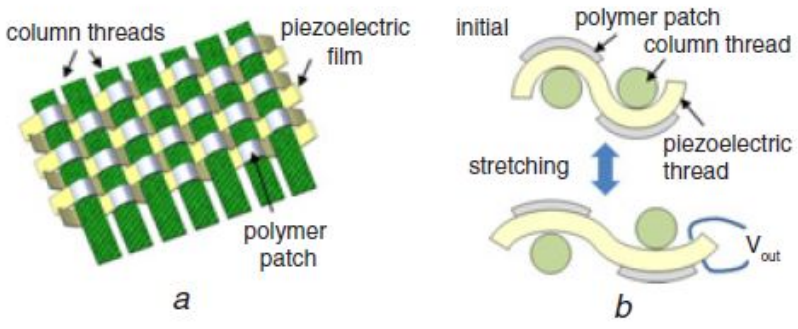

Figure 2.7: *Schematic representation of the proposed device. a. Conceptual illustration of the stretchable textile structure. b. Cross-sectional depiction of the device and its operational mechanism. [9].*

Given the relatively low frequency of human motion, researchers have developed an innovative design for a flexible piezoelectric energy harvester, which features an eccentric pendulum, as illustrated in Figure 2.8 (FPEH-P) [10]. This design is particularly effective at harvesting energy from irregular and low-frequency human motion. The FPEH-P possesses two critical attributes: frequency up-conversion and large deformation, both of which significantly enhance its energy output capabilities.

The frequency up-conversion characteristic generates multiple vibration signals within the signal clusters, effectively boosting the RMS (Root Mean Square) voltage during the effective time period. This results in a more efficient capture of the mechanical energy generated by low-frequency motions. The large deformation characteristic increases both the deformation and the tightening force exerted on the piezoelectric plate. This deformation is a major factor for enhancing the output power, as it maximises the strain experienced by the piezoelectric material. The combination of these two features—frequency up-conversion and large deformation—makes the FPEH-P a highly efficient energy harvester.

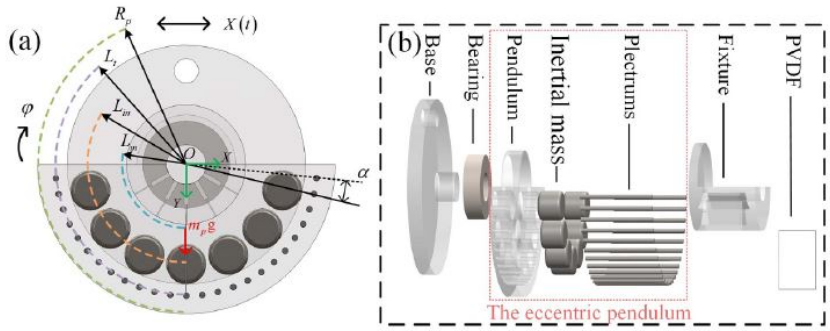

Figure 2.8: *(a) and (b) Schematic of the FPEH-P [10].*

The FPEH-P is capable of operating under low-frequency excitations of approximately 2 Hz, and the large deformation induced by plucking significantly enhances the maximum instantaneous voltage. This design achieves a peak open-circuit voltage of 6.82 V, which is advantageous for charging capacitors. At an excitation frequency of 1.9 Hz and an amplitude of 100 mm, the maximum average power output is recorded at 6.06 μW. The performance of the energy harvesting output is influenced by design parameters such as the eccentric mass m, eccentric distance L, and plectrum installation angle α. As the eccentric mass increases, the

output voltage initially rises and then decreases. Meanwhile, increasing the eccentric distance and plectrum installation angle gradually improves both the optimal output frequency and power. The proposed FPEH-P demonstrates good output performance in the context of low-frequency human motion energy harvesting. Treadmill experiments conducted on individuals of varying genders and body types indicate that the output generated by leg motions surpasses that of arm motions. It is also observed that signal variations between individuals can be attributed to factors such as exercise habits.

In water environments, energy harvesting presents unique challenges and opportunities. The development and analysis of an underwater piezoelectric energy harvester (MPEH) based on magnetic coupling provide valuable insights for low-speed water flow scenarios [11]. The MPEH is designed to address the energy needs of self-powered underwater wireless sensor nodes (WSNs) for fifth-generation mobile networks (5G) and the Internet of Things (IoT). By leveraging fluid-induced vibration (FIV) and magnetic coupling, the MPEH enhances energy harvesting efficiency in low-velocity water environments, as illustrated in Figure 2.9. The interaction between water flow and a vibrating column generates electrical energy, with magnetic repulsion and attraction optimising the energy harvesting process. At low flow rates, magnetic repulsion boosts the output voltage, while magnetic attraction is more effective at higher flow rates.

The performance of the MPEH is also depending on the diameter and mass of the vibrating column. Increasing the diameter improves energy conversion efficiency, while adjustments to the mass influence the resonant frequency and power output. At a flow rate of 0.5 m/s, the MPEH achieves a peak open-circuit voltage of 6.82 V, with the maximum average power output recorded at 6.06 μW at 1.9 Hz and 100 mm amplitude.

These findings underline the potential of integrating similar energy harvesting technologies into wearable lifejackets, thereby enhancing search and rescue operations. By optimising underwater FIV-based PEHs, this research lays the groundwork for self-powered sensors in water environments. Future research should explore adaptations of these technologies for wearable devices and their practical applications.

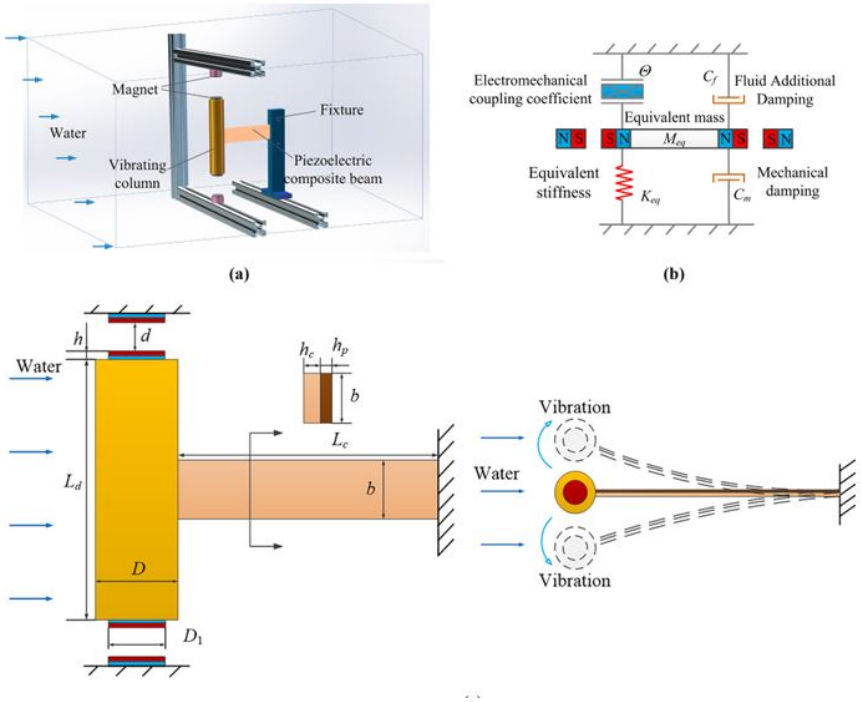

Figure 2.9: *Model of the magnetic nonlinear energy harvesting system: (a) Structural model, (b) Equivalent single-degree-of-freedom model, (c) Schematic diagram showing structural dimensions. [11].*

2.5.3 Electromagnetic Energy Harvester

Electromagnetic energy harvesters function based on the principles of Faraday's law of electromagnetic induction [76]. These devices primarily consist of two essential components: a coil (often referred to as a solenoid) and a permanent magnet. The core mechanism behind their operation involves the conversion of mechanical vibrational energy into electrical energy.

When the system experiences vibrations due to external forces or mechanical motions, the magnet moves relative to the coil, causing a fluctuation in the magnetic field within the coil. According to Faraday's law, a changing magnetic field induces an electromotive force (EMF) or voltage across the coil. As the magnet oscillates back and forth, the magnetic flux passing through the coil varies, generating an alternating current (AC) within the coil. The magnitude of the induced AC voltage depends on the amplitude and frequency of the vibrations. To make the generated electrical energy usable for electronic devices, a rectifier circuit is often employed. The rectifier converts the AC into direct current (DC), which ensures a steady, unidirectional

flow of electricity. The DC output can then be used to power electronic devices, charge batteries, or be stored in an energy storage system for later use.

Electromagnetic energy harvesters are versatile and find applications across various domains, including wireless sensor networks (WSNs), microelectromechanical systems (MEMS), and the Internet of Things (IoT). The ubiquity of vibrations—from sources such as machinery, infrastructure, or even human motion—makes these harvesters a reliable and sustainable energy source. Below are some application and research examples.

An example of electromagnetic energy harvesting is the development of a high-performance, cycloid-inspired wearable electromagnetic energy harvester (CEEH) designed to efficiently capture human motion energy at low frequencies (below 5 Hz) [12]. This device optimises the coil-magnet configuration to increase the rate of magnetic flux cutting, resulting in a 1.45-fold increase in energy generation compared to conventional geometric structures such as straight and circular designs. The schematic structure is shown in Figure 2.10. Under optimal load resistance of 104.7Ω, the device can deliver an average power output of 8.8 mW. Notably, with just 5 seconds of handshaking motion, the CEEH can power a commercial sports stopwatch for 16 minutes.

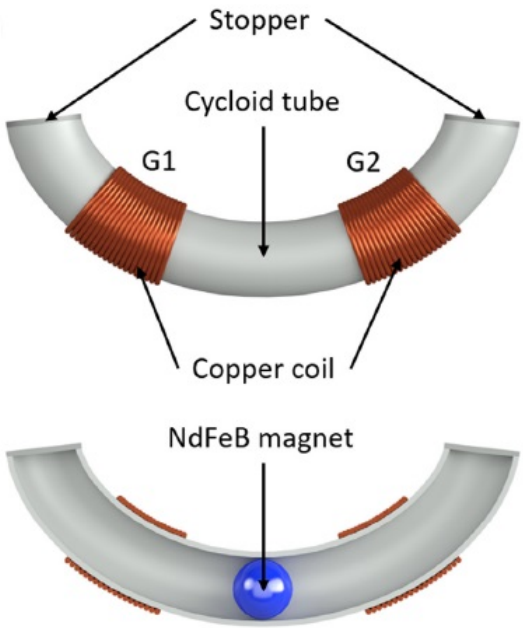

Figure 2.10: *Schematic structure of the cycloid-shaped electromagnetic energy harvester [12].*

Another research has been conducted to investigate the potential of energy harvesting from the lower limbs, which alternately accelerate and decelerate during walking [57]. The system under study consists of 15 segments, including the head, upper trunk, two upper arms, two forearms, two hands, lower trunk, two thighs, two legs, and two feet. Since the upper arms, forearms, and hands exhibit minimal motion during walking, they are grouped together into a single segment representing the upper body and head. A seven-link rigid dynamic model was developed in the sagittal plane, consisting of the upper body, two thighs, two legs, and two feet. This model allowed for a detailed dynamic analysis using the Lagrangian method. The system could generate approximately 5 W of electricity at a walking speed of 4.5 km/h.

Energy harvesting in this system is primarily focused on the knee joint, which provides mechanical energy through rotational motion. A spring-damping mechanism is used in conjunction with the knee's motion within an exoskeleton. The knee motion is transferred by cables to spiral springs, which in turn drive a generator through a gearbox to produce electricity. This setup has demonstrated the feasibility of harvesting energy from human locomotion in wearable systems designed for long-term use.

Further research into energy harvesting from limb motion explored the development of an AA-sized electromagnetic energy harvester, specifically designed to convert human motion into electrical energy [13]. This harvester features a cylindrical magnet housed in a tube, which is entirely wrapped in coils. The magnet moves freely inside the tube, driven by human motions such as leg swinging or handshaking, as depicted in Figure 2.11. As the magnet moves, it induces a changing magnetic flux through the coils, generating an electric current according to Faraday's law of electromagnetic induction. The AA-sized harvester's design enables the capture of mechanical energy from everyday human activities, making it suitable for portable and wearable electronics. The generated power can be used to charge small electronic devices or provide supplementary power to wearable systems.

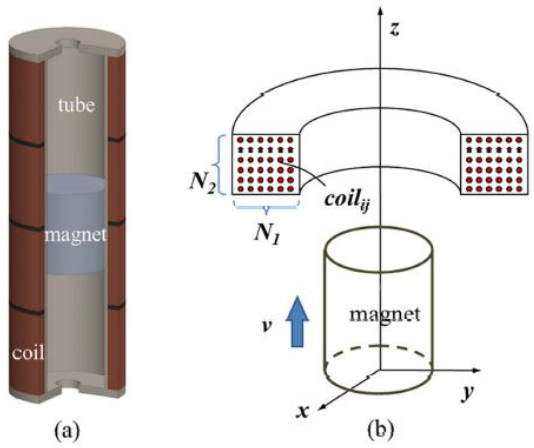

Figure 2.11: *(a) Structure of the human motion energy harvester, and (b) a simplified schematic of the derived model, where a magnet moves vertically across a coil. [13].*

The optimisation of the device was achieved through theoretical modelling and experimental validation, with particular attention given to the dimensions of the magnet and coil to maximise output power. The optimal configuration involved a magnet with a 5mm radius and a height of 10-12mm, paired with a coil of 10mm height. When the prototype was tested by hand-shaking at approximately 5Hz, it produced an average power output of 63.9mW, which is 51% higher than traditional tube-based electromagnetic energy harvesters. When worn on the ankle during normal walking at 1Hz, the harvester generated 4.2mW of power, demonstrating its capability for practical human energy harvesting applications. The research concludes that the proposed harvester shows potential for human energy harvesting, primarily due to its straightforward design, which eliminates the need for a restoring spring, and the simplicity of its fabrication. These features make the device suitable for low-power applications, such as wearable medical devices or consumer electronics like remote controls. Future research will aim to integrate a power management circuit into the AA-sized harvester and evaluate its feasibility in human healthcare applications.

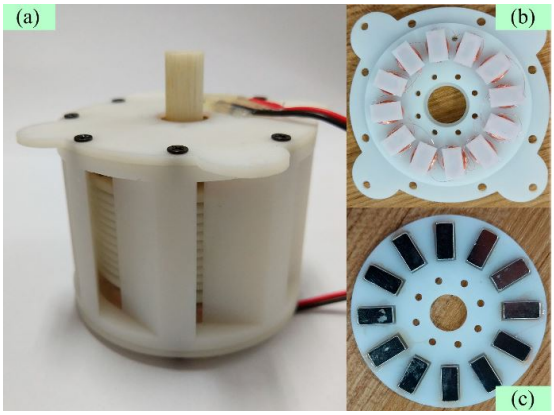

Figure 2.12: *Photographs of flow energy harvester prototypes: (a) Assembled prototype, (b) Coils fixed in the end cap, and (c) Permanent magnets mounted on the disk. [14].*

For energy harvesting with lifejackets in water environments, it is essential to assess how the harvester performs underwater, considering that water will be continuously flowing around the individual, whether from natural currents or their motions. In 2018, researchers introduced an integrated electromagnetic energy harvester designed for remote sensors [14]. This device combines a Tesla disk turbine with a miniature axial-flux permanent magnet generator in a compact structure, making it suitable for integration with autonomous oceanographic sampling networks. A prototype of this device is illustrated in Figure 2.12.

The energy harvester works by capturing kinetic energy from non-directional water flow. To ensure effectiveness in environments with erratic water currents, the device includes a ring cover with symmetrical grooves to rectify the flow direction. The permanent magnets are mounted on the end surfaces of the turbine disks, contributing to the compactness of the system. Both theoretical and experimental analyses confirmed the device's efficiency, with the harvester functioning at water flow velocities as low as 0.61 m/s, producing an electromotive force ranging from 2.64 to 11.92 V at flow velocities between 0.61 and 1.87 m/s. The study provides an analysis of the energy conversion process, from hydrokinetic energy to electrical output. The prototype achieved a peak electrical power output of 23.1 mW at a flow velocity of 1.87 m/s, with an efficiency of approximately 1.4%. These results are comparable to other electromagnetic harvesters in similar fluid environments, highlighting the device's potential for sustainable energy generation. In conclusion, this integrated electromagnetic harvester

is a notable development in the field of energy harvesting from water flow. Its compact and innovative design offers promising solutions for powering remote sensors in water environments like oceans or rivers, contributing to the development of efficient, sustainable energy harvesting technologies. Future studies could focus on further optimising the design and improving the device's performance, as well as its integration with various types of remote sensing systems and potentially onto lifejackets.

To integrate effectively with a lifejacket, the energy harvesting device must be compact and lightweight, ensuring it does not interfere with the primary functions of the lifejacket. A study focuses on the development of a tumbler-inspired electromagnetic energy harvester (T-EMH), designed specifically to harness energy from low-frequency human motion [15]. The T-EMH, based on the mechanics of a tumbler, efficiently captures low-frequency energy. The theoretical framework for the T-EMH was established using the Lagrange equation, while an analytical model was derived via the harmonic balanced method. This research also involved a numerical investigation into the effects of key geometric parameters, such as the radius ratio, the moment of inertia of the tumbler, the mass eccentricity, and the tumbler's total mass, on the overall energy harvesting performance.

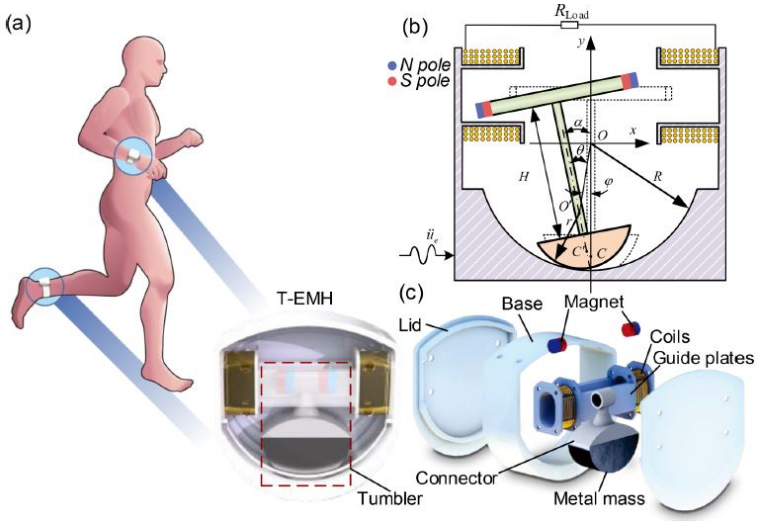

Figure 2.13: *(a) Scene graph of the T-EMH for human motion energy harvesting, (b) 3D model, and (c) schematic of the T-EMH. The T-EMH comprises two guide plates, two coils, a tumbler structure, two lids, and a base. The tumbler structure includes a semicircular metal mass, two cylindrical magnets, and their connectors. Designed to be worn on the limbs, the T-EMH captures energy generated by limb motion during body motion. [15].*

The prototype of the T-EMH, illustrated in Figure 2.13, was developed to capture energy from human motion, showcasing its potential in powering low-energy devices such as calculators, watches, electronic clocks, and LEDs. The device is specifically designed for wearable applications on the limbs, allowing it to harness the kinetic energy produced by activities like walking or running, which it subsequently converts into electrical energy. The experimental results are promising, with the T-EMH generating a maximum average power output of 0.86 mW at a running speed of 12 km/h. This performance highlights the potential of the T-EMH for applications in health monitoring and outdoor emergency rescue scenarios. The T-EMH represents a step forward in human motion energy harvesting technology. Future research could focus on further optimising the design and improving the overall performance of the T-EMH. Additionally, exploring its integration with other wearable technologies could expand its applications in fields such as healthcare, outdoor activities, and emergency rescue operations.

2.5.4 Comparison of Energy Harvesting Methods

Efficiency and Output Power

TENGs are efficient at harvesting ambient mechanical energy and are suitable for low-power applications. However, their output power is generally lower compared to PEHs and EMEHs. PEHs can generate higher power outputs, especially when using materials like PZT, but their efficiency depends on the consistency of mechanical stress. EMEHs offer the highest output power among the three methods, making them suitable for energy-demanding applications. A summary of the power densities is listed below in Table 2.3.

Table 2.3: *Energy harvesting technologies and their maximum power densities*

Energy Harvester Type	**Maximum Power Density [mW cm^{-2}]**
Electromagnetic Induction [77]	144.1
Piezoelectric [78]	16.4
Triboelectric Nanogenerators [79]	3.8

Material and Design Considerations

TENGs require materials with different electron affinities and can be designed in various configurations to optimise performance. PEHs rely on piezoelectric materials, with PZT providing higher power output and PVDF offering greater flexibility. EMEHs consist of a coil and a magnet, with design optimisations focusing on maximising magnetic flux changes.

Suitability for Lifejacket Integration

Given the space available in a lifejacket and the significant amount of kinetic energy generated by the wearer's motions, the EMEH method is more suitable for integration. The higher output power of EMEHs allows for the addition of more functionalities to the lifejacket, such as powering communication devices, sensors, and emergency lights. The consistent motion of the wearer ensures a reliable source of mechanical energy, making EMEHs a more suitable choice for this research.

2.6 Lifejacket as a Media for Energy Harvesting

From the reviews above, energy harvesters provide a sustainable solution for powering electronic devices without relying solely on batteries. Lifejackets, particularly Type 401 (open waters lifejackets), are highly recommended for New Zealand's water environments [27]. These lifejackets are available in two variants: semi-rigid and inflatable. Both types are designed to keep wearers afloat during unconsciousness. The inflatable type offers convenience for continuous wear, while the semi-rigid variant is best suited for emergency situations. The outer shell of lifejackets is typically made from durable materials such as nylon or vinyl. Inflatable lifejackets need to be filled with air, and this is achieved using carbon dioxide cartridges. These cartridges can be activated in various ways: some use a water-soluble stopper that dissolves to release the gas, while others require the user to pull a tab to puncture the canister and activate the lifejacket. The unique features of lifejackets make them an attractive platform for energy harvesting.

Lifejackets have direct contact with both the water and the wearer. Their buoyancy-driven motion, resulting from the wearer's motions and the surrounding water, contains kinetic energy that can be harnessed. As wearers bob up and down, the lifejacket experiences cyclical forces,

which are ideal for energy conversion. By integrating energy harvesters into the lifejacket's structure, this continuous motion can be utilised to power onboard electronics. Beyond buoyancy, lifejackets also interact with the wearer's limb motions. When a person treads water or swims, their arms and legs move in a pattern. These limb motions generate kinetic energy that can be captured. By strategically placing the energy-harvesting mechanisms near joints or areas of high motion, this energy can be harvested.

Lifejackets are worn securely, ensuring they remain in place during water-related emergencies. This firm wearability is essential for energy harvesting. Unlike other wearable devices that may shift or detach during motion, lifejackets stay firmly attached to the wearer. The energy harvester can consistently harvest energy from the limb-driven motion. The extended duration of lifejacket use provides sufficient time for energy harvesting.

While limited research directly addresses the integration of energy harvesters into lifejackets, existing studies on wearable energy-harvesting devices offer valuable insights that inform the current research. The analysis of these prior works, particularly those focusing on wearable electromagnetic energy harvesters, provides a foundation for understanding how similar principles can be applied to lifejackets for energy harvesting in water environments.

One notable example is the cycloid-inspired wearable electromagnetic energy harvester (CEEH), which has demonstrated the ability to generate energy from a wide range of human motions, including hand-shaking [12]. This technology's versatility suggests that it could also harness energy from the repetitive "ladder climbing" motion. Since the CEEH system is designed to capture energy from any form of body motion including limb motions in water, it can offer a promising solution for integrating energy harvesting into lifejackets.

Another relevant study focuses on an electromagnetic energy harvester designed to generate electricity from the motion of the lower limbs during walking [57]. The system utilises a seven-link rigid dynamic model to capture mechanical energy from the knee joint, which is then converted into electrical energy through cables and spiral springs that drive a generator. At a walking speed of 4.5 km/h, the system can produce approximately 5W of electricity, a significant amount for low-power devices. While walking differs from the "ladder climbing" motion in terms of biomechanics, the underlying principle of harnessing limb motion for energy is highly

relevant to this research. The similarities between walking and ladder climbing, particularly the rhythmic, repetitive motion of the legs, suggest that this harvester can be adapted to the motion dynamics of a drowning person, further informing the design of a lifejacket-based energy harvesting system.

In addition to land-based energy harvesters, research on water-based energy harvesting technologies offers valuable insights. For instance, an innovative energy harvester combines a Tesla disk turbine with a miniature axial-flux permanent magnet generator to capture energy from non-directional water flow [14]. This system is particularly relevant for environments like drowning scenarios, where water flow is continuously interacting with the limbs. The Tesla turbine harvester is able to generate voltages between 2.64V and 11.92V from flow velocities ranging from 0.62 m/s to 1.87m/s, with a peak power output of 23.1 mW at 1.87m/s. This research demonstrates the feasibility of harvesting energy from water flow around the body, a dynamic likely to occur during a drowning event where the victim's motions create irregular, multi-directional water flow patterns. Such findings could be directly applied to lifejacket designs that exploit both body motion and the surrounding water flow to maximise energy generation.

Overall, these existing studies not only highlight the potential of wearable energy harvesters to capture kinetic energy from human motion but also provide a foundation for designing an energy harvesting system specifically tailored for lifejackets in water environments. The ability to harvest energy from the combined effects of limb motion and water flow represents an opportunity to power life-saving devices in search and rescue operations.

In conclusion, lifejackets can serve a dual purpose by becoming media for wearable energy harvesters and a safety device. Their seamless integration into daily wear ensures continuous energy harvesting. By utilising the natural motion of lifejackets, the harvester can provide energy for additional functionalities while enhancing safety in open water scenarios.

2.7 Human Motion Modelling for Energy Harvesting

The existing literature reveals a lack of specific studies that directly address the modelling of human motion in a drowning scenario. This scarcity can be attributed to several factors, including the unpredictability of drowning incidents and the ethical concerns surrounding the deliberate recreation of life-threatening situations. Ethical guidelines strictly prohibit the exposure of individuals to dangerous environments, limiting the opportunity to gather real-world data on the biomechanics of a drowning person.

Although there is no direct reference for modelling a drowning person's motion, studies on human swimming and biomechanical motion in water environments offer valuable insights. The research on swimming dynamics and gait analysis can provide a useful framework for understanding how the human body moves in water. These studies focus on fluid-body interaction, which, although applied to swimming, can be adapted to model drowning scenarios [80].

One key research area is the development of human swimming simulation models like SWUM (Swimming Human Model) [81], which is used to analyse swimming dynamics. With this model, the whole-body motion in water, accounting for forces such as drag, buoyancy, and added mass, is simulated accurately. These forces are significant in swimming dynamics and are similarly relevant in the context of drowning. The principles governing the interaction between the body and water can be adapted from these studies to estimate the behaviour of a person in distress in water.

The MSC ADAMS software is another tool widely used in biomechanical simulations that can offer insights into human motion in water. This software is often employed to analyse joint moments and the dynamic forces involved in human motion. Although originally intended for gait analysis and other biomechanical applications, it can be adapted to simulate the joint mechanics of a drowning person [82]. By applying these models, researchers can estimate the forces exerted on the limbs and the energy required during drowning. In addition to general swimming dynamics, research examining the impact of external forces such as water currents on swimming provides further relevant insights [2]. Although swimming and drowning differ in terms of coordination and intent, the interaction between body motion and fluid forces remains

similar. The studies on freestyle and breaststroke swimmers offer useful information on how external forces, such as water flow, can affect human motion in a water environment. These principles can be adapted to model the forces acting on a drowning person, where chaotic water motions and the victim's own panic-induced motions can generate similar fluid dynamics to swimming in turbulent conditions.

In summary, while there is a lack of direct studies focused on the biomechanics of drowning, existing research on swimming and human motion in fluid environments provides a strong foundation for modelling these scenarios. By utilising simulation tools such as SWUM and MSC ADAMS, along with insights from swimming research, the dynamics of a drowning person's motion can be estimated with reasonable accuracy. These models provide a reliable alternative to collecting real-world data and allow researchers to simulate complex fluid-body interactions in a controlled, ethical manner. These insights are instrumental in designing energy-harvesting systems that can effectively utilise the kinetic energy generated during a drowning event.

2.8 Motion Capture Techniques

Motion capture (MoCap) techniques have become essential in studying biomechanics simulations. Various techniques exist, each with its strengths and limitations depending on the application and environment. This section reviews the primary motion capture techniques used in different fields, with a particular focus on optical, marker-based, and markerless methods.

In this research, two distinct methods of motion capture are utilised. In the first method, an underwater camera is used in combination with computer vision techniques to capture motion in a dynamic, water environment. The second method, called Optical Passive Motion Capture method, involves the use of infrared cameras available in the Auckland University of Technology (AUT) motion capture laboratory [83]. This system provides high-precision tracking of the participant's motions in a controlled environment. Each method has its own strengths and weaknesses, and the combination of these methods allows for a more comprehensive collection of data. By employing both techniques, it is possible to obtain a dataset that captures the

participant's simulated motion in both controlled and real-world conditions. It ensures that the data is accurate and comprehensive, providing a robust foundation for the subsequent dynamic and energy analysis.

Markerless Motion Capture - Computer Vision

Markerless motion capture does not require the use of physical markers on the subject's body. Instead, it relies on computer vision techniques to track the motion of the subject. This is achieved by using algorithms that can detect and analyse specific body parts in real-time, often using a two-dimensional camera view to infer three-dimensional motion.

Recent advances in machine learning, particularly convolutional neural networks (CNNs), have enhanced the accuracy of markerless systems. These algorithms can detect and track key points on the human body, allowing the system to estimate joint angles, limb positions, and overall posture without the need for markers [84].

Computer vision has become essential in the field of human motion data collection, driven by significant advancements in machine learning and artificial intelligence. It enables real-time capture, interpretation, and prediction of human motion, and finds applications in a wide range of fields, including virtual reality, healthcare, surveillance, and robotics [85]. One of the primary advantages of computer vision is its non-invasive nature, as it relies solely on video footage and advanced algorithms to track motion, eliminating the need for physical markers. This approach is especially beneficial in dynamic environments such as swimming pools, where traditional marker-based systems are impractical due to the interference caused by water and the need for freedom of movement [86].

Traditional motion capture systems, although highly accurate, are generally confined to controlled environments and involve attaching physical markers to the body. These markers can interfere with natural movement, making them unsuitable for water-based activities. In contrast, computer vision-based techniques, implemented in this research using powerful frameworks like OpenCV and Mediapipe, offer a more flexible and non-invasive alternative. These systems allow for the tracking of human motion in more realistic settings and from multiple angles, using an array of cameras to enable full-body tracking in three-dimensional space. For this study, an underwater camera was employed to capture motion data during drowning simulations, tracking

key body landmarks even when the participant was submerged. This method was essential for analysing naturalistic movement in water environments, where the limitations of traditional systems become particularly pronounced.

Recent advancements in deep learning, particularly convolutional neural networks (CNNs), have further enhanced the accuracy of computer vision systems. CNNs excel at detecting and tracking key points on the human body from images or video footage, thanks to extensive training on large-scale annotated datasets. This has allowed for improved generalisation and more reliable predictions of human motion across diverse environments [84]. The enhanced capability to process complex visual data makes computer vision systems well-suited for capturing motion in real-world settings, where the need to observe natural movement, especially in water, is critical to accurate analysis.

Despite these notable benefits, computer vision does have certain limitations. The accuracy of data collection is highly dependent on the quality of the video footage, with factors such as lighting conditions, camera positioning, and water clarity playing a significant role in the system's ability to track body landmarks. The absence of physical markers means the system must rely entirely on visual cues, which may not always be reliable, particularly when body parts are moving quickly or are obscured. Additionally, water reflections, splashes, and the movement of the participant through the water can introduce noise and distortions into the captured data. While recent advances in machine learning have reduced the margin of error, the potential for inaccuracies remains, especially when compared to more controlled, marker-based systems.

Marker based - Optical Motion Capture Systems

Optical motion capture is one of the most prevalent and accurate methods used in biomechanics and animation. These systems rely on cameras to track the motion of reflective markers attached to a subject's body. When infrared light from the cameras reflects off the markers, the system captures their positions, allowing for a precise reconstruction of motion in three-dimensional space.

The Motion Capture (MoCap) Lab at Auckland University of Technology (AUT) provides an advanced platform for the collection of precise human motion data, utilising a suite of high-speed cameras and sophisticated software that enables three-dimensional tracking from multiple

angles [83]. In contrast to computer vision techniques, marker-based motion capture systems, such as those used in the MoCap Lab, offer a higher level of precision. By attaching reflective markers to specific anatomical landmarks on the participant's body, such as the acromion process (shoulder), lateral epicondyle (elbow), and lateral malleolus (ankle), the system accurately tracks the three-dimensional motion of each marker. This results in highly detailed motion data that can be used to create precise kinematic models of the participant's motions. The controlled environment of the MoCap Lab further enhances data collection by allowing high-speed cameras to be strategically positioned around the participant, providing a comprehensive view of motion from multiple angles. This setup ensures that the system can reliably detect and track motion, even during rapid or complex movements, which is particularly advantageous when capturing the detailed biomechanics of the arms and thighs—key areas of interest in this study for energy harvesting purposes.

Before data collection can begin, the MoCap system must be calibrated to ensure accuracy, establishing a capture volume that defines the area in which the participant's motions will be recorded. This calibration process ensures that all cameras are synchronised and aligned, allowing for precise triangulation of the reflective markers in three-dimensional space [87]. During the data collection phase, the participant performs a simulated "ladder climbing" motion, which is carefully choreographed to replicate real-life drowning scenarios while prioritising safety. The MoCap system records these motions at high frame rates, typically between 100 and 1000 frames per second, depending on the analysis requirements [88]. High frame rates are necessary to capture rapid motions with precision, ensuring no loss of detail during recording.

After data collection, the raw motion data undergoes processing to create a digital representation of the participant's movements. This involves several important steps, including filtering to remove noise, labelling markers for accurate representation, and gap filling for frames where markers may be temporarily obscured [89]. The processed data is used to create a kinematic model of the subject, accurately reflecting the motion of each body segment relative to others. In this research, particular attention is given to the motion of the arms and thighs, identified as key areas for potential energy harvesting during simulated drowning events [90].

Moreover, the MoCap Lab has the capability to integrate additional data sources, such as

electromyography (EMG) and force plates, to enhance the analysis. EMG provides insights into muscle activation during motion, while force plates measure the ground reaction forces generated by the subject [91]. Although these additional sources are not utilised in this research, their combination with motion capture data could provide a more comprehensive understanding of biomechanics in future studies.

However, despite the many advantages of motion capture technology, it presents several challenges. Marker occlusion, where a marker is temporarily obscured from view by another body part or object, can lead to gaps in the data that must be addressed during post-processing. Additionally, the complexity of the data processing workflow requires specialised knowledge and software to ensure accurate results. The cost of MoCap systems and the necessity for a controlled laboratory environment limit accessibility outside research settings [92]. Nevertheless, the detailed and accurate data captured by the MoCap system proves invaluable for understanding human motion, particularly in simulated drowning scenarios, and for advancing research in areas such as energy harvesting [93].

Hybrid Motion Capture Systems

Hybrid systems, which combine marker-based and markerless approaches, aim to provide the best of both worlds [94]. These systems use both optical markers and computer vision algorithms to track motion. For instance, in scenarios where a subject moves between different environments (e.g., transitioning from land to water), a hybrid approach can offer both the precision of markers in a controlled environment and the flexibility of markerless tracking in a dynamic setting.

Data Collection and Accuracy

The accuracy of the data collected by each method varies depending on several factors. In computer vision-based motion capture, the resolution of the video footage, the quality of the algorithms used, and the conditions under which the data is captured all are major factors in determining the accuracy of the results. In this study, the combination of high-resolution underwater cameras and advanced machine learning algorithms ensured a reasonable level of accuracy in the captured data. However, it should be noted that computer vision systems are more prone to errors caused by visual obstructions, reflections, and lighting inconsistencies,

particularly in dynamic environments such as water.

On the other hand, marker-based systems offer a much higher level of accuracy, particularly in controlled laboratory settings. The reflective markers provide a reliable means of tracking motion, and the high-speed cameras used in the MoCap lab ensure that even rapid motions are captured in detail. The calibration of the system is essential to ensure the accuracy of the data, as any misalignment of the cameras or reflective markers can introduce errors into the motion tracking process. Despite these challenges, the marker-based system used in this research provided the most accurate and detailed motion data, which is essential for developing the kinematic model of "ladder climbing" motion. The downside is that the experiment has to be done on land which does not include the drag and buoyancy effects.

In conclusion, both computer vision and marker-based motion capture methods have their strengths and weaknesses when applied to the study of human motion in a drowning scenario. Computer vision offers flexibility and non-invasiveness, making it suitable for dynamic environments like swimming pools. However, its accuracy can be compromised by visual factors such as lighting and obstructions. On the other hand, marker-based systems, while more intrusive and reliant on controlled environments, provide superior accuracy and detail. By combining both techniques, this research is able to obtain a comprehensive dataset that captures the complexity of human motion during a drowning event, ultimately supporting the development of energy harvesting models for life-saving devices.

2.9 Research Gaps

1. Energy Harvesting in Water Environments:

Most existing studies on energy harvesting focus on land-based activities like walking and running, which are not applicable in water environments. There is a need for research on energy harvesting methods that are effective in water environments, particularly for lifejackets. This includes exploring the potential of harnessing energy from the wearer's motions in water. Additionally, the unique challenges posed by the water environment, such as waterproofing and the impact of saltwater on energy harvesting devices, need to be addressed.

2. Dynamics of Drowning Motions: The physical motions associated with drowning are different from those of swimming or other land-based activities. Research is needed to develop a dynamics model that accurately represents these motions and can inform the design of energy harvesting devices for lifejackets. This involves studying the specific limb motions and body dynamics during a drowning incident and how these can be leveraged to generate energy. Understanding these dynamics is essential for designing devices that can effectively harness energy without hindering the wearer's motions or compromising their safety.

3. Integration of Energy Harvesting Devices with Lifejackets: Research is needed to explore the integration of energy harvesting devices with lifejackets without compromising their primary function. This includes studying the optimal setup of these devices to maximise energy harvesting while minimising the user's effort. The integration process must ensure that the lifejacket remains comfortable and does not impede the wearer's motions. Additionally, the durability and reliability of the integrated devices in harsh water environments need to be considered.

Chapter 3

Human Motion Modelling for Energy Harvesting

Although there is a lack of direct motion data for drowning individuals, existing research on swimming dynamics and gait analysis provides valuable frameworks for modelling these complex scenarios. By applying principles for studies on swimming techniques and human motion patterns, it becomes possible to simulate the motion of a drowning person with a reasonable degree of accuracy for further analysis. This approach not only avoids the significant ethical challenges posed by real-world testing but also enables controlled, repeatable simulations, offering insights into the various forces and factors involved in a drowning event. Moreover, modern tools such as AI-driven technologies present potential alternatives for capturing necessary data, which can contribute to developing a more robust dynamic model. At the same time, it is equally important to understand the fundamental calculations that underpin these simulations.

This chapter outlines the modelling approach used to simulate the motion of a drowning person, with an emphasis on assessing the potential for energy harvesting from the body's motion in water. The model is constructed using multi-body rigid dynamics, incorporating established principles to effectively capture the complex interactions between the body and the surrounding water.

3.1 Human Body Segmentation and Geometric Model

The human body is segmented into 18 distinct rigid components in the simulation [2]. These segments include critical parts of the body, such as the head, limbs, trunk, and neck, ensuring full coverage of the body's structure. Each segment is geometrically represented as either a truncated elliptical cone or a cylindrical shape, providing an approximation of the body's mass distribution and moment of inertia. This approach is designed to closely mimic the dynamic behaviour of the human body during drowning scenarios. By using these geometrical representations, the model ensures that the complexities of body dynamics, such as balance, buoyancy, and rotational forces, are captured. The parameters of the individual body segments used in the simulation are listed in Table 3.1, detailing the sizes and shapes that are applied to create the model.

Table 3.1: *Example of geometric parameters and density of the model segments [2]*

Segment	Geometric Shape	Density (kg/m^3)	R1a (Semi-major axis length)(cm)	R2b (Semi-minor axis length)(cm)	T1c (Axial Length)(cm)	T2d (Axial Length)(cm)
Head	Ellipsoid	1042	19.65	17.38	26.55	26.55
Neck	Truncated elliptical cone	1042	12.59	14.01	12.78	11.59
Shoulder	Truncated elliptical cone	1042	19.44	38.26	12.59	14.01
Upper trunk	Truncated elliptical cone	700	22.52	29.84	19.44	38.26
Middle trunk	Truncated elliptical cone	1042	22.37	28.84	24.52	29.84
Lower trunk	Truncated elliptical cone	1042	22.37	28.84	23.41	36.70
Thigh	Truncated elliptical cone	1042	18.41	18.06	12.26	11.66
Shank	Truncated elliptical cone	1042	12.26	11.66	8.03	6.77
Upper arm	Truncated elliptical cone	1042	10.08	10.08	8.24	8.24
Forearm	Truncated elliptical cone	1042	8.24	8.24	4.73	5.41
			Side length	**Side length**	**Side length**	**Axial Length**
Hand	Frustum of a pyramid	1042	4.64	10.13	1.4	5.24
Foot	Frustum of a pyramid	1042	5.45	6.94	1.86	10.06

(a) "R1" means the sagittal axis of the section at the root of the segment;

(b) "R2" means the coronal axis of the section at the root of the segment;

(c) "T1" means the sagittal axis of the section at the tip of the segment;

(d) "T2" means the coronal axis of the section at the tip of the segment.

The sagittal plane is the anatomical plane that divides the body into left and right halves, with movement occurring in the anterior–posterior direction. The coronal (frontal) plane divides the body into anterior and posterior sections, with movement occurring in the medial–lateral direction. The sagittal axis runs perpendicular to the sagittal plane, while the coronal axis runs perpendicular to the coronal plane.

The geometric model simplifies the inherent asymmetry of the human body by treating it as symmetrical, a choice made to facilitate ease of computation. Despite this simplification, care has been taken to ensure that the mass, centre of gravity, and moment of inertia for each body segment are closely aligned with real physiological properties. The symmetrical assumption, while reducing computational complexity, does not compromise the ability of the model to simulate the dynamics of the human body in water effectively. The example of the model is shown in Figure 3.1.

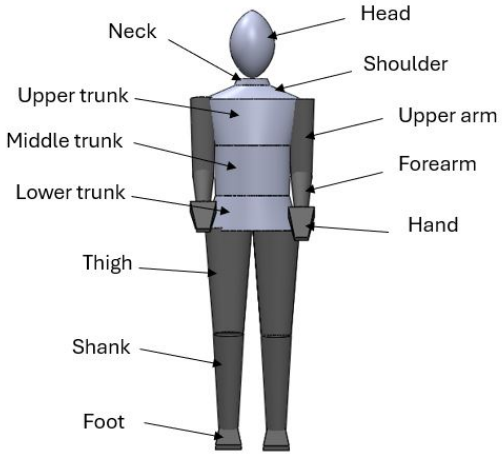

Figure 3.1: *Example of the human body model.*

3.1.1 Coordinate Systems and Frames of Reference

To accurately model the motion of the body segments during a drowning scenario, it is essential to define the coordinate systems used in this analysis. Two reference frames are established for this study:

1. **Global (World) Coordinate System:**

   This frame is fixed in space, representing the environment such as the swimming pool. It provides a reference for describing the overall position and movement of the body. The axes are defined as:

2. **Local (Body-Segment) Coordinate Systems:**

   These frames are attached to each individual segment, including the torso, thigh, and arm.

They are used to describe the relative motion of each segment with respect to the torso.

Joint Angles:

The hip joint angle (γ) is defined as the angle between the local coordinate system of the thigh segment and the torso coordinate system, projected in the sagittal plane. Similarly, the shoulder joint angle (β) is defined as the angle between the upper arm and torso coordinate systems. By defining these frames of reference, angular displacements, velocities, and torques can be consistently described and calculated.

3.2 Bio-Mechanics of Ladder Climbing Motion

3.2.1 Joint Motions and Muscle Activation

This motion pattern involves a series of coordinated motions aimed at trying to elevate the body and head above water. The primary focus is on the motions of the hip and ankle joints, with additional support from the shoulders and elbows.

- **Hip Joint**: The hip joint controls the motion of the thigh. During the drowning event, the thigh is lifted by the hip flexors (e.g. iliopsoas), creating a kicking motion as the body attempts to rise in the water. The hip extensors (e.g. gluteus maximus) help to stabilise and extend the leg, pushing the water downward.

- **Knee Joint**: The knee joint bends and straightens during the kicking motion. The knee flexes to lift the foot and leg, while the knee extension generates a downward thrust to keep the body buoyant.

- **Shoulder and Elbow Joints**: The arms play a key role in balancing the body and aiding in the upward motion. The shoulder flexes to lift the arms upward, and the elbows bend and extend as part of the instinctive swimming motion.

  - Shoulder Flexion: The shoulders lift the arms as part of the overall motion to keep the head above water.

  - Elbow Flexion and Extension: The elbows bend and straighten as the arms work in a paddling motion, contributing to both balance and propulsion.

The leg and arm motions in this drowning-related "ladder climbing" motion are important for maintaining buoyancy and stability. The thigh muscles in particular are responsible for generating significant upward thrust through repetitive kicking.

3.2.2 Phases of the Ladder Climbing Cycle During Drowning

The "ladder climbing" motion during a drowning event can be broken down into several phases, which involve coordinated motions between the legs and arms:

1. **Preparation Phase**:
   - The body prepares to lift the legs in a kicking motion to keep the head above water. The arms engage in a paddling motion for balance.
   - The hip flexes and the knee bends to lift the leg, while the shoulders and elbows move to stabilise the upper body.
2. **Ascent Phase**:
   - The thigh moves upward in a kicking motion to generate thrust. The hip flexors and knee flexors pull the leg upward.
   - The arms provide balance and support through shoulder flexion and elbow flexion.
3. **Support Phase**:
   - After the kick, the legs stabilise to maintain buoyancy, while the other leg prepares for the next motion. The arms help keep the body balanced.
   - The knee and hip extend to push water downward, while the arms maintain position for support.
4. **Descent Phase**:

- The body lowers slightly between kicks, and the legs prepare for the next cycle. The arms continue paddling to prevent sinking.
- The knees and hips flex slightly, and the arms move to keep the body afloat.

Each phase of the "ladder climbing" motion involves coordinated action between the legs and arms, with the focus on generating upward thrust to help keeping the head above water.

3.2.3 Rationale for Omitting Head and Trunk Motions

In this biomechanical analysis, the head and trunk are not included in the detailed modelling for several reasons:

1. **Insignificant motion**:

   The head and trunk remain relatively stable as the legs and arms work to keep the body afloat. Their motions are more for balance rather than generating motion or energy.

2. **Limited Role in Energy Harvesting**:

   The primary focus of energy harvesting is on the motions of the legs and arms, which involve significant muscle actions that can generate mechanical energy. The head and trunk are primarily involved in maintaining posture and balance, without contributing to significant mechanical work.

3. **Simplification of the motion model**:

   By excluding the head and trunk, the motion model remains focused on the joints directly producing the thrust needed to help the drowning person staying afloat. This will simplify the model more, making it more efficient and effective to analyse the motion related to energy generation.

3.2.4 Impact of Water Resistance

The resistance of water and the body's position while performing the ladder climbing motion during drowning affect how the legs and arms move. The dynamics of water create a greater

demand for forces generated by the legs and arms compared to what is needed for the motion in the air. As a result, more dynamic and sustained motions, especially from the legs, to keep the head above water are required. Even with the lifejacket worn, the legs can continuously generate upward thrust for a longer period of time, which creates opportunities for energy harvesting.

3.3 Inverse Kinematic Modelling of the Thigh and Arm Motion

Kinematic modelling of both the thigh and arm motions is essential to understanding the angular displacement and velocity involved in the "ladder climbing" motion during a drowning event. By analysing the motion of the thigh and arms, captured through motion capture techniques, the potential for mechanical energy harvesting can be quantified.

3.3.1 Motion Measurement

The following measurements are essential in capturing the kicking motion of the legs and the paddling motion of the arms:

- **Hip Joint Angle**: The angle between the thigh and the torso, measured as the hip flexes and extends during the kicking motion. This is an important factor in analysing the contribution of the thighs' motion to energy generation.
- **Shoulder Joint Angle**: The shoulder angle, represents the motion of the arms as they flex and extend during the "ladder climbing" motion to stabilise the human body in the water.

In addition to angular displacement, the angular velocity can be calculated for each joint. Data are collected over multiple trials to ensure consistency and reliability. The data are processed to remove noise and ensure smooth, accurate joint angle trajectories for both the thighs and arms. Key steps included:

- **Noise Filtering**: A median filter is applied to the raw data to reduce noise by replacing each data point with the median of surrounding points and creating a smooth representation of the joint motions.

- **Interpolation**: Missing or occluded data points are interpolated to provide a continuous dataset for both thigh and arm motions.
- **Smoothing**: Moving average smoothing is applied to the time-series data, allowing for a clear representation of angular displacement and velocity.

This processing ensured the accuracy and reliability of the data, which is then used to validate the kinematic model.

3.3.2 Kinematic Modelling

The angular displacement (γ) and angular velocity (ω) for both the thigh and arm can be simply as shown in Figure 3.2 described by

$$\gamma(t) = \gamma_0 + \omega_0 t + \frac{1}{2}\alpha t^2 \tag{3.1}$$

$$\omega(t) = \omega_0 + \alpha t \tag{3.2}$$

Where:

- $\gamma(t)$ is the angular displacement at time t,
- $\omega(t)$ is the angular velocity at time t,
- γ_0 and ω_0 are the initial angular displacement and velocity.
- α is the angular acceleration which is related to the force applied by the thigh and arm.

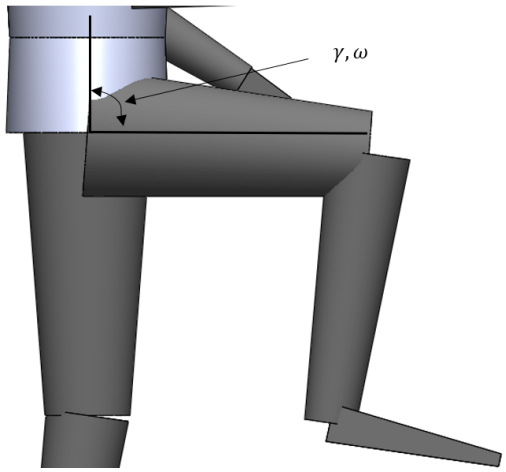

Figure 3.2: *Illustration of the kinematic modelling.*

Figure 3.3 presents a schematic kinematic diagram of the thigh and torso segments connected via the hip joint. This diagram clearly indicates the type of joint (revolute), its single rotational degree of freedom (DoF), the approximate length of the thigh segment (~406 mm), and the kinematic parameters used in modelling (joint angle γ and angular velocity ω). Such schematic representations are essential for formal biomechanical analysis of the linkage and for defining the motion input to the energy harvesting mechanism.

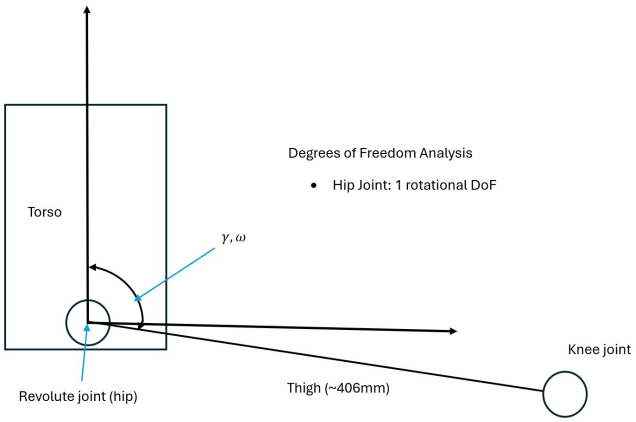

Figure 3.3: *Schematic kinematic diagram of the thigh–torso linkage*

By modelling the time-dependent motion of these joints, the kinematic behaviour of the thighs and arms during the "ladder climbing" motion can be studied in a simulated drowning event. It is also needed to evaluate the potential for mechanical energy harvesting, as the

combined motion of the thighs and arms offers valuable insights into how energy can be harvested from these instinctive motions.

3.4 Force and Torque Analysis of the Thigh and Arm Motion

Dynamic analysis focuses on understanding the forces, torques, and energy involved in the motion of both the thighs and arms during the "ladder climbing" motion in a drowning event. This analysis will involve key equations that describe the interaction of these forces and the energy produced during motion.

The forces acting on the thighs and arms include buoyancy, drag force, thrust, and gravitational force.

Two types of hydraulic resistance and buoyancy affect the person: passive drag and active drag. Passive drag generates hydrodynamic resistance when a person is towed through the water, while active drag occurs as the person moves independently, creating additional resistance. This composite quantity includes both passive drag, resistive forces, and the propulsive thrust generated by the person's motions. The combined drag forces, including both normal and tangential components, along with the added mass forces, are summed together. In this study, active drag is specifically evaluated to understand the interaction mechanisms between the human body and water during the process of "ladder climbing" motion. Passive drag F_{pd} is typically defined by

$$F_{pd} = F_t = -\frac{1}{2} C_{pd} \rho |\mathbf{v}| \mathbf{v} A \tag{3.3}$$

where C_{pd} is the equivalent passive drag coefficient, a dimensionless quantity that depends on the Reynolds number of the body. ρ is the density of the water, $\mathbf{v}$ is the absolute velocity of the body relative to the currents, and A is the orthogonal projection area of the human body in the motion direction in Equation (3.3) [2].

There is a close relationship between the active drag force F_{ad} and the relative motions of the person's joint. The active drag force consists of the tangential drag force F_t such as the passive drag force F_{pd}, the normal drag force F_n, and the added mass force F_a as shown in

Figure 3.4. All these forces are treated as vector quantities. The directionality of the forces is essential for accurately determining the resulting drag and its effect on torque and motion. Each component has both magnitude and direction, and their vector sum yields the total active drag force acting on the limb. Active drag F_{pd} is typically defined by

$$F_{ad} = F_{pd} + F_n + F_a \tag{3.4}$$

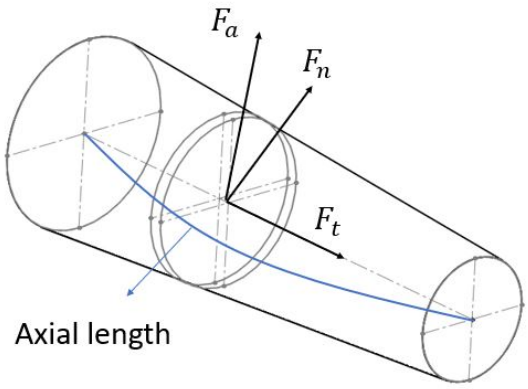

Figure 3.4: *Illustration of the fluid forces acting on the truncated elliptical cone-limb.*

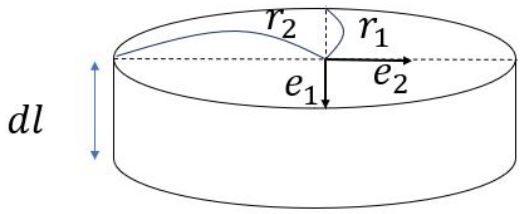

Figure 3.5: *Dimensions of a divided elliptical plate.*

To simplify calculations, the shape of the limbs is approximated as a truncated elliptical cone. A thin elliptical plate is taken along the longitudinal axis, with a circumference of c and a thickness of dl, $\mathbf{e}_1$ and $\mathbf{e}_2$ are unit vectors along the minor and major axis as shown in Figure 3.5. A longitudinal elliptical plate has a velocity component $\mathbf{v}_t$ along its longitudinal axis, and a current velocity component $\mathbf{v}_{ct}$ along its longitudinal axis. An elliptical plate's tangential drag force F_t is written as below:

$$F_t = -\frac{1}{2} C_{pd} \rho \epsilon_c \cdot dl \left[|\mathbf{v}_t - \mathbf{v}_{ct}| (\mathbf{v}_t - \mathbf{v}_{ct}) \right] \tag{3.5}$$

The normal drag force F_n is given by

$$F_n = -\frac{1}{2} C_n \rho \epsilon \cdot dl \left\{ r_2 \left(\frac{r_2}{r_1}\right)^e \left[|\mathbf{v}_n - \mathbf{v}_{cn}| \left((\mathbf{v}_n - \mathbf{v}_{cn}) \cdot \mathbf{e}_1 \right) \right] \mathbf{e}_1 + r_1 \left(\frac{r_1}{r_2}\right)^e \left[|\mathbf{v}_n - \mathbf{v}_{cn}| \left((\mathbf{v}_n - \mathbf{v}_{cn}) \cdot \mathbf{e}_2 \right) \right] \mathbf{e}_2 \right\} \tag{3.6}$$

where $\mathbf{v}_n$ represents the velocity component perpendicular to the longitudinal axis of an elliptical plate, $\mathbf{v}_{cn}$ denotes the current velocity component and C_n is the equivalent normal drag coefficient. The ellipse eccentricity is indicated by the superscript coefficient e, which is defined as $e = \frac{\sqrt{r_1^2 - r_2^2}}{r_1}$. The immersion ratio of an elliptical plate in equations (5) and (6) is denoted by ϵ, which is the ratio between the immersed lateral surface area and the overall lateral surface area of the plate.

As the limb moves in an unsteady motion, either accelerating or decelerating, a certain volume of water must be displaced as the limb moves through the surrounding fluid, thereby adding mass to the body. This additional resistance is described by the added mass force F_a.

$$F_a = -C_a \rho \epsilon \cdot dl \cdot \pi \left[r_2^2 (\mathbf{a}_n \cdot \mathbf{e}_1) \mathbf{e}_1 + r_1^2 (\mathbf{a}_n \cdot \mathbf{e}_2) \mathbf{e}_2 \right] \tag{3.7}$$

Here, $\mathbf{a}_n$ is the acceleration component of the elliptical plate's centre, perpendicular to its longitudinal axis, while C_a is the equivalent coefficient accounting for the added mass effect experienced by the body.

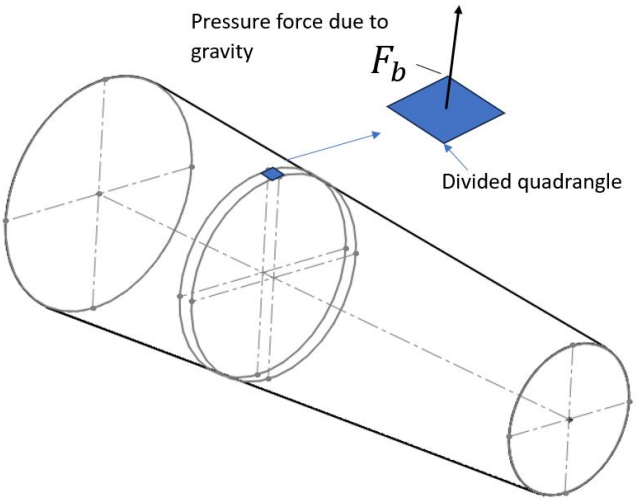

Figure 3.6: *Buoyancy is calculated by integrating the pressure force over divided quadrangles.*

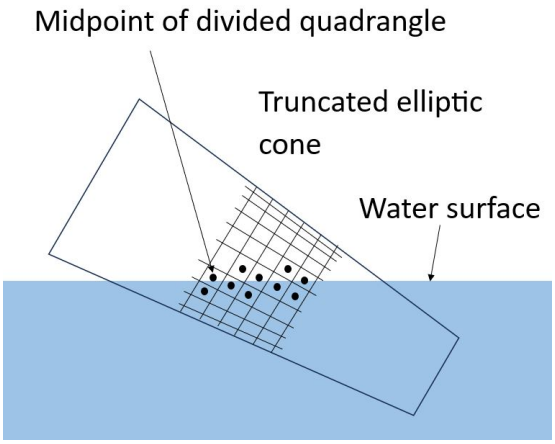

Figure 3.7: *Judgement whether quadrangles submerge or not.*

Buoyancy is calculated by integrating the pressure force F_b, which results from gravity acting on a small quadrangle, as illustrated in Figure 3.6. This pressure force F_b is determined by considering the area of the quadrangle, the vector normal to the surface, and the z-coordinate of the quadrangle's centre, denoted as ds, $\mathbf{e}_n$, and z_q, respectively. The pressure force F_b is expressed by the following equation:

$$F_b = -z_q \, ds \, g \, \mathbf{e}_n \tag{3.8}$$

where g represents the gravitational acceleration. Since the pressure force F_b does not

act above the water's surface, it is essential to verify the position of each small quadrangle to determine whether it lies below or above the water surface—specifically, whether $z_q < 0$ holds true, where $z = 0$ corresponds to the water surface level. It is assumed that F_b acts only on quadrangles located beneath the water's surface. The centres of these quadrangles are marked by black points, as depicted in Figure 3.7. By dividing an elliptical plate into small quadrangles along its circumference, a specific ratio can be determined for each elliptic plate:

$$\text{ratio} = \frac{\text{number of quadrangles where } z_q < 0}{\text{total number of quadrangles}}$$

In this study, both arms and thighs will be fully submerged in the water so the ratio will be 1. By combining the forces, the total force acting on the limb can be calculated.

Torques are generated at the hip and shoulder joints as the thighs and arms move. Torque (τ) as shown in Figure 3.8 is given by:

$$\tau = r \times F \tag{3.9}$$

where:

- r is the distance from the joint to the point of force application (lever arm),
- F is the force applied (e.g., muscle force or external water resistance).

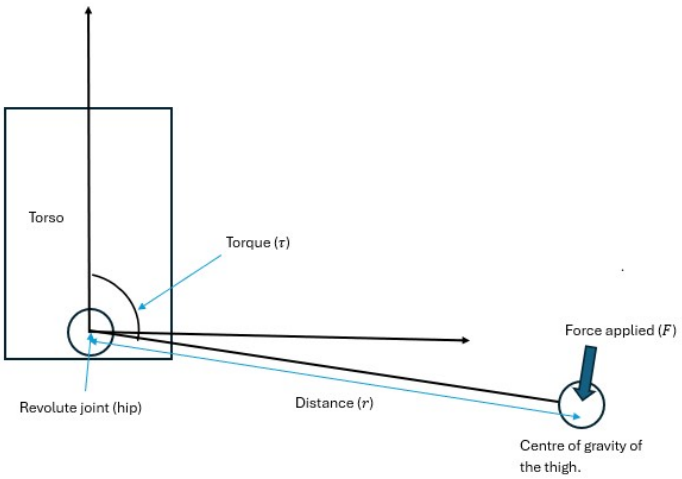

Figure 3.8: *Free body diagram of the thigh segment for force analysis*

For a distributed segment such as the thigh, the hydrodynamic force is spread along its length. An effective mass and its corresponding perpendicular distance r (moment arm) are determined to simplify this distributed load into an equivalent single force for torque calculation. The method for calculating this effective mass is described in the next section.

For the hip and shoulder joints, torques are calculated as follows:

- **Hip Joint Torque (τ_{hip})**:

$$\tau_{\text{hip}} = r_{\text{hip}} \times F_{\text{muscle,hip}}$$

- **Shoulder Joint Torque (τ_{shoulder})**:

$$\tau_{\text{shoulder}} = r_{\text{shoulder}} \times F_{\text{muscle,shoulder}}$$

3.5 Energy Calculations

The kinematic energy associated with the motion of both the thighs and arms during the "ladder climbing" motion in water can be analysed to estimate the corresponding electrical energy can be generated. The key forces acting on the limbs include drag, buoyancy, and thrust, which all contribute to the total energy generated. It also helps to determine the effort of the lifejacket wearer in his/her motion in the water as required by the harvester.

3.5.1 Mechanical Energy from the Thigh and Arm Motions

The mechanical energy generated by the thighs and arms during motion is primarily kinetic energy, which can be expressed as:

$$E_{\text{mech}} = \frac{1}{2}mv^2$$

where:

- E_{mech} is the mechanical energy produced by the limbs (thighs or arms),
- m is the effective mass of the limbs (including added mass from the displaced water),

- v is the velocity of the centre of gravity (COG) of the limbs moving through the water.

For both the thighs and arms, we must include the added mass effect, which accounts for the water displaced by the limbs during motion. As shown in Figure 3.9, the total effective mass of the limbs can be written as:

$$m_{\text{eff}} = m_{\text{limb}} + m_{\text{added}}$$

where:

- m_{limb} is the actual mass of the limb (thigh or arm),
- m_{added} is the added mass from the displaced water.

The added mass is calculated based on the volume of water displaced by each limb:

$$m_{\text{added}} = C_a \cdot \rho_{\text{water}} \cdot V_{\text{limb}}$$

where:

- C_a is the added mass coefficient (typically between 0.5 and 1 for human limbs),
- ρ_{water} is the density of water (approximately $1000\,\text{kg/m}^3$),
- V_{limb} is the volume of the limb moving through the water.

Thus, the mechanical energy generated by the thighs and arms is:

$$E_{\text{mech}} = \frac{1}{2} \left(m_{\text{limb}} + C_{\text{added}} \cdot \rho_{\text{water}} \cdot V_{\text{limb}} \right) v^2 \tag{3.10}$$

This equation represents the total mechanical energy generated by the limbs during the "ladder climbing" motion. Figure 3.9 shows the illustration of the energy calculation.

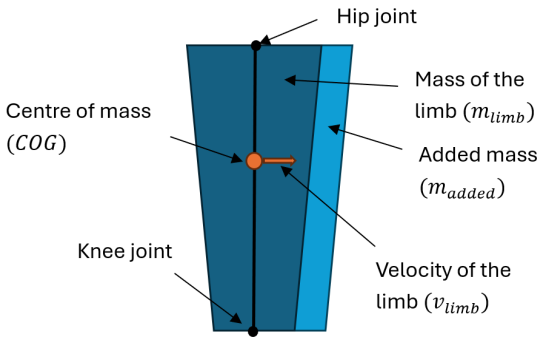

Figure 3.9: *Illustration of mechanical energy calculation*

3.5.2 Energy Harvesting Balance Ratio

The amount of electrical energy collected from the motion of the thighs and arms is only a small part of the mechanical energy generated. The ratio (η) shows how much of the mechanical energy is turned into electrical energy. It helps to understand how the energy to be collected imposes a demand on the thigh's (and limb's) motion, ensuring that the person wearing the device can still move freely without needing to use too much extra energy.

$$E_{\text{elec}} = \eta \cdot E_{\text{mech}} \tag{3.11}$$

where:

- E_{elec} is the electrical energy harvested,
- η is the energy harvester balance ratio
- E_{mech} is the mechanical energy generated by the limbs (thighs and arms).

The overall balance of energy harvested during a drowning event depends on several factors, particularly the design and optimisation of the electromagnetic energy harvester. The mechanism's design, including the linkage system and its positioning relative to the thighs and arms, directly affects energy conversion efficiency. The effective mass of the limbs, which includes the added mass from displaced water, influences the total energy captured. Additionally, water resistance and drag forces impact the available mechanical energy, particularly by resisting the motion of the thighs and arms, which reduces the energy that can be converted. The velocity

of limb movement plays a critical role, as energy generation is proportional to the square of the limb velocity, while the duration and frequency of the motion affect the total energy harvested. The approaches to optimise the harvester design, aiming to improve energy conversion efficiency and minimise losses, will be discussed in the next chapter.

3.6 Conclusion

This chapter has presented an analysis of human motion during ladder climbing, with a particular focus on its potential for energy harvesting. The model developed focuses on understanding the kinematics and forces/torques associated with human motion during drowning scenarios, with an emphasis on identifying motions that can potentially generate energy. The segmentation of the human body into rigid components allowed for an accurate simulation of the motion, incorporating key parameters such as mass distribution, moment of inertia, and fluid forces like drag and buoyancy.

A significant finding from this analysis is the important role of the thighs and legs in generating mechanical energy during the "ladder climbing" motion. The motion of the hip joint provides a substantial source of upward thrust during the repetitive climbing motion, which is helpful for maintaining buoyancy in water. This repetitive motion is crucial for energy harvesting applications, as it involves continuous and rhythmic force generation, creating opportunities for efficient mechanical-to-electrical energy conversion.

Furthermore, the forces acting on the limbs, such as buoyancy, drag, and added mass forces are discussed. These forces are needed in determining the energy potential of the motion, with the water's resistance increasing the demand for sustained leg and arm motions, thereby enhancing the potential for energy harvesting. The calculated torques at the hip and shoulder joints provided insight into the rotational dynamics of the motion, further supporting the conclusion that the thigh motion is the most suitable source for energy harvesting.

The energy calculations, which focused on the mechanical energy produced by the thighs and arms, showed that the limbs' effective mass, including added water mass, is a major factor in determining the total energy output. The conversion of mechanical energy into electrical

energy is discussed in terms of balance, which can vary based on the type of energy harvester used and the specific conditions of the motion. The purpose of this design is not to harvest as much kinetic energy as possible but to harvest efficiently without adding excessive extra effort from the wearer.

In conclusion, the analysis in this chapter has established the importance of thigh (limb) motion in generating mechanical energy during a drowning event. The "ladder-climbing" motion, characterised by repetitive and powerful leg motions, provides a promising basis for the development of energy-harvesting devices. The next chapter will involve motion capture to gather the necessary data to validate the model and analytical results presented in this chapter.

Chapter 4

Motion Capture

Based on the findings from the literature review, the active stage of a drowning event, where the person remains in motion, has been selected for further study in this research. At this stage, the individual tries to stay afloat with instinctive body motion which is often referred to as a "ladder climbing" motion [33]. It presents a unique source of kinetic energy to be harvested.

However, there is very limited data available on the specific motion patterns of a person in a drowning scenario. The lack of data highlights the need for a dynamic model to provide valuable insights into the body's motion during the active stage of drowning. By capturing and analysing this motion data, it is possible to gain a clearer understanding of the kinetic energy that can be harvested from these motions, specifically, it will allow

- Precise measurement of joint angles and velocities of the thighs and arms during the simulated drowning motion,
- Accurate modelling of the forces, including the effects of drag, buoyancy, and added mass from the water,

4.1 Challenges of Motion Capture in the Water

Capturing human motion in water presents unique challenges not typically encountered in land-based motion capture scenarios. These challenges come from the limitations of motion capture technology that is suitable for water environments. Specifically for this study, the key

challenges arise when capturing thigh and arm motions during the "ladder climbing" motion in a water-based drowning scenario.

In computer vision-based motion capture, visual obstruction is a common issue in water-based environments. Water surfaces, reflections, and splashing can obscure the cameras' view of the participant's limbs, leading to incomplete or inaccurate data. Reflections from the water surface can interfere with image processing algorithms, making it harder for the system to accurately detect and track key points on the body, particularly if the arms or thighs move in and out of the water.

To mitigate this issue, cameras must be positioned strategically to provide a clear and continuous view of the participant's limbs. In addition, advanced computer vision algorithms that can filter out reflections and detect submerged body parts are necessary to ensure the integrity of the captured data. In this case, an underwater camera is used to reduce the impact of water interference on the captured footage.

4.2 Motion Capture in the Water

4.2.1 System and Experiment Setup

To capture the motion data underwater, a controlled simulated experiment is carried out in a local swimming pool. In this experiment, the participant mimicked the actions of someone in a drowning situation. This approach is chosen to simulate a realistic scenario in a controlled setting, allowing for a detailed examination of the associated motions. Underwater video footage is recorded using a Kaiser Baas X350 ActionCam, a 4K camera designed specifically for underwater filming. Multiple recordings are made from both the sagittal and coronal planes to ensure a thorough view of the participant's motions. Each segment of the "ladder climbing" motion lasted around 30 seconds. Repeated recordings are necessary to ensure good video quality and consistent motion throughout the process. After recording, the next step is selecting suitable computer vision tools for analysing the video data.

For the video analysis, the software packages including OpenCV (Open Source Computer Vision) [95] [96] and Mediapipe [97] are used. OpenCV is a popular Python library for image

processing and computer vision. It provides a wide range of functions and algorithms for manipulating and analysing images and videos, enabling the extraction of key features from video footage, such as identifying and tracking body markers and recognising patterns that may indicate specific behaviours [98]. In this study, OpenCV is used to process the large volume of underwater video data, ensuring that key body motions are tracked efficiently.

In addition to OpenCV, Mediapipe, an open-source framework developed by Google, is also employed. Mediapipe facilitates the development of real-time, cross-platform applications in computer vision and machine learning [99]. It offers pre-built components, known as graphs, which can be combined to create complex pipelines for various tasks, such as pose estimation and object detection. The flexibility of Mediapipe makes it particularly useful for analysing multiple data streams simultaneously. In this study, Mediapipe's pose estimation and tracking features are used to monitor the participant's body motions during the simulated drowning scenario. Its ability to track key body landmarks provided data points for calculating angular velocity and body positioning during the motion.

The quality of the input data is crucial for achieving accurate results with Mediapipe. In this case, recordings are made in high-definition with adequate underwater lighting, allowing the software to detect and track key points on the participant's body accurately [100]. Notably, the participant did not wear a lifejacket during the motion capture to maintain simplicity and minimise variables, making the focus remain on the participant's natural motions. However, the absence of the lifejacket raises questions about how its presence might impact future analyses using Mediapipe. Specifically, it remains uncertain whether Mediapipe's tracking capabilities would be affected by the bulk or motion constraints of a lifejacket. Testing with a lifejacket will be conducted during the final field tests of this research.

Mediapipe has the capacity of identifying up to 33 pose landmarks [101], corresponding to key anatomical points of the human body, such as joints and facial features. For each landmark, coordinates are recorded in three dimensions (x, y, z) every second, enabling detailed tracking of the subject's motion over time. In this study, the x-axis represents the right side of the image, the y-axis represents downward motion, and the z-axis points out towards the viewer as shown in Figure 4.1. The origin of the coordinate system is located in the top-left corner of the image

or video frame, serving as a standard reference point for the data.

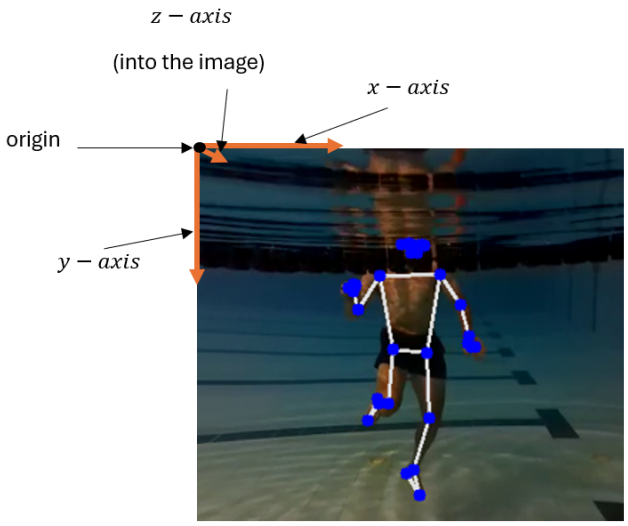

Figure 4.1: *The coordinate system of Mediapipe.*

The coordinates captured by Mediapipe are normalised relative to the size of the image or video frame [102] to ensure consistency and comparability of the data across frames of different sizes or resolutions, or from various recording devices.

Despite the high prevision of Mediapipe and OpenCV, errors may arise, such as when key points are blocked or if the participant's motions are too rapid to capture accurately. Those errors or anomalies are removed in a data cleansing process. After cleansing, the cleaned dataset is visualised in the form of graphs which illustrates the participant's motion patterns and provide a clear representation of the angular displacement, angular velocities, force and energy generated during the experiment.

4.2.2 Data Collection

After processing the underwater footage with OpenCV and Mediapipe, two main outputs are generated: a video file showing overlaid landmarks and linkages, as seen in Figure 4.2, and a corresponding CSV file containing the extracted motion data, presented in Table A.1 in Appendix A. Landmarks 12, 14, 24 and 26 are being used for further calculation, while the full list of the landmarks is in Table A.2 in Appendix A. These files serve as the primary sources of data for analysing the recorded motion.

The video file contains visual representations of the motion capture process, with landmarks being placed at specific joints and key points on the participant's body, and linkages indicating connections between these points. This visualisation aids in understanding the participant's motions, especially in relation to the simulated drowning motion. It provides an immediate reference for observing how different body parts interact, making it a valuable tool for both qualitative and quantitative analysis. It can also show how the body's posture and motion relate to energy harvesting opportunities, further guiding the design and optimisation of the energy harvesting system.

On the other hand, the CSV file offers a detailed and structured dataset for quantitative analysis. This file includes the coordinates (x, y, z) of each tracked landmark throughout the video, with values normalised to the dimensions of the input video frame. The normalisation process ensures that the data remains scalable and comparable across different frames, even with varying resolutions. The CSV also includes confidence scores for each landmark, providing a measure of the accuracy of each detection. Higher confidence scores indicate more reliable identification by the computer vision algorithms, making these scores essential for evaluating the quality of the extracted data.

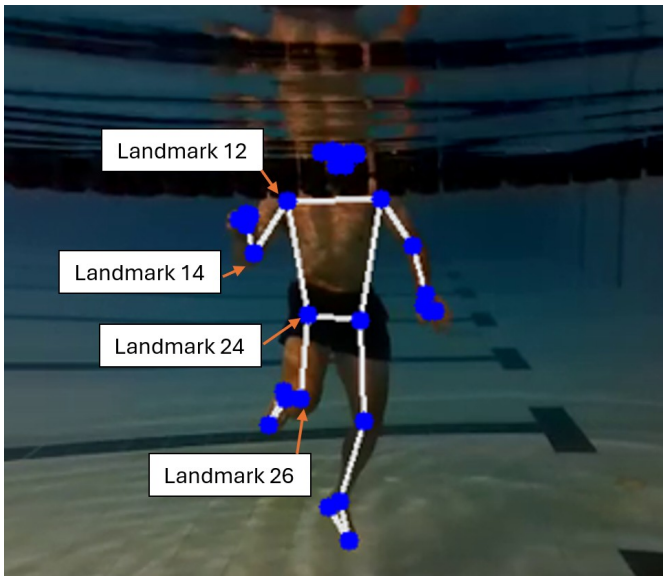

Figure 4.2: *Motion capture using Computer vision and Mediapipe.*

In Table A.1 in Appendix A, the first column lists the various landmarks identified by

Mediapipe, corresponding to key anatomical points on the participant's body, such as joints and limbs which are essential for calculating body motions and angles during the simulated drowning scenario. The full list of Mediapipe landmark codes and anatomical definitions is provided in Appendix A Table A.2 . The second, third, and fourth columns contain the normalised x, y, and z coordinates for each landmark. The fifth column presents the confidence scores for assessing the reliability of the tracked landmarks. Confidence scores are especially important for underwater motion capture, where factors such as lighting and water clarity can impact landmark detection accuracy. A higher confidence score suggests a greater likelihood that the detected landmark corresponds accurately to the participant's actual joint or limb position.

Key anatomical landmarks are identified and tracked during the computer vision analysis to clarify the limb motions. Points 12 and 14 represent the shoulder and elbow joints, with the linkage between them representing the arm. Points 24 and 26 correspond to the hip and knee joints, with the linkage between these points representing the thigh. By monitoring changes in these landmarks over time, the motion of the arms and thighs can be captured with high precision. The time interval between frames is set at 0.033 seconds, matching the frame rate of the footage.

4.3 Motion Capture on the Ground

4.3.1 Lab and Experiment Setup

The experimental setup for this study is carefully designed to capture and analyse the complex motions associated with simulated drowning scenarios with the highest possible accuracy. The Motion Capture Lab at Auckland University of Technology (AUT) provides the ideal environment for this purpose including 24 Raptor-4 digital cameras. These cameras are strategically positioned around the participant to ensure that every motion within the capture volume is recorded from multiple angles, providing comprehensive three-dimensional data.

To optimise the data collection process and reduce interference with the infrared cameras, the participant is required to wear a specially designed non-reflective suit. This suit is tailored to minimise the risk of introducing noise into the data by avoiding any shiny or reflective materials

that could interfere with the camera's ability to accurately track the reflective markers. The placement of these markers on the participant's body is also carefully considered. Markers are positioned at key anatomical points, such as the shoulders, elbows, hips, and knees, to capture relevant joint angles and body segment motions needed for this study.

The capture volume, measuring 5x5x3 metres, is clearly marked on the studio floor with tape lines, providing the participant with visual cues to stay within the field of view of the cameras. It is critical to ensure that all motions are performed within these boundaries to prevent any data loss or inaccuracies. The cameras are calibrated to cover this space, and any motions outside these boundaries would not be captured correctly, potentially compromising the integrity of the data.

One of the significant challenges of this experiment arises from the need to replicate drowning-related motions in a land environment. Drowning motions typically occur in water, where the buoyancy and resistance differ significantly from those in air. These differences in environmental conditions create difficulties when attempting to simulate the motions accurately. To address this challenge, a gym chin-up support frame is used to suspend the participant in the air, effectively simulating the body posture and motion patterns that would occur during a drowning incident in the water. The support frame is also essential for mimicking the weightlessness of motion that is characteristic of water environments.

The chin-up support frame is carefully covered with non-reflective material to prevent any interference with the infrared cameras, ensuring that the reflective markers on the participant's body are the only reflective surfaces within the capture volume. The participant is secured within the frame using a certified harness, which is illustrated in Figure 4.3, ensuring the participant's safety while performing the simulated drowning motions. The harness allows for controlled and stable motion, while also providing the flexibility needed to replicate the drowning-related motions.

Figure 4.3: *Setup at motion capture lab*

The motion capture software generates 54 distinct anatomical points on the participant's body.These virtual markers correspond to specific anatomical landmarks used to define the body's movement in 3D space. These points include, but are not limited to: Head_Asym, LFrontHead, LBackHead, RFrontHead, RBack- Head, TopSpine, TChest, LSternum, BChest, RSternum, RShoulder, RBicep, RElbow, RFore- arm, RWristInner, RWristOuter, R_Thumb_hand, R_Palm_hand, R_Pinky_hand, LShoulder, LBicep, LElbow, LForearm, LWristInner, LWristOuter, L_Thumb_hand, L_Palm_hand, L_Pinky_hand, MiddleBack, LowerBack, Root, Offset, LFront-Waist, LMiddleWaist, LBackWaist, RFrontWaist, RMiddleWaist, RBackWaist, RHip, RKnee, RTibia, RAnkle, RHeel, ROuterMeta, RTip, RToe, LHip, LKnee, LTibia, LAnkle, LHeel, LOuterMeta, LTip, LToe. The points provide a clear and structured means of tracking the participant's motion over time.

Before the actual data collection begins, the visibility of the markers is verified in real-time using a live display system. This system, as shown in Figure 4.4, ensures that all markers are clearly visible to the cameras throughout the motion sequence. Any markers that are not visible or are prone to occlusion are adjusted or repositioned to avoid data gaps. This step is needed for maintaining the integrity of the data, as missing markers can lead to incomplete or inaccurate motion tracking.

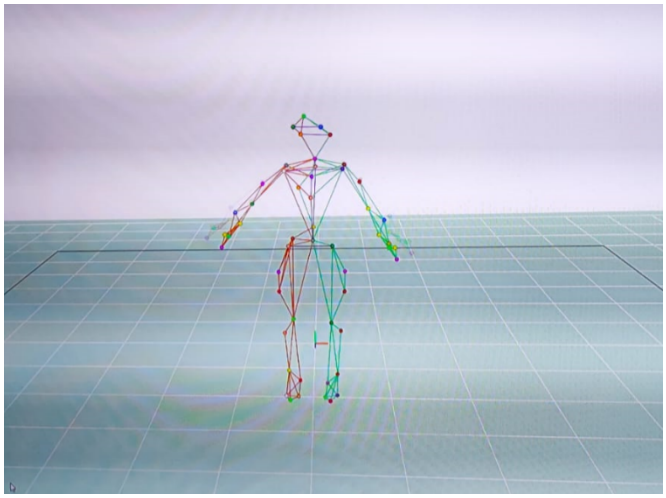

Figure 4.4: *Live view of markers during motion capture*

Once the data collection process begins, the participant performs the simulated drowning motions for approximately 30 seconds each time to capture a sufficient amount of data for analysis. The captured data set includes the three-dimensional positions of each reflective marker over time, which can be used to calculate not only the positions of various body segments but also their orientation and motion patterns. They can also be compiled into a datasheet, containing the linkage orientations and their corresponding timestamps are needed for further kinematic analysis.

The data produced by this experiment is highly accurate, with precision reaching the millimetre level. This level of precision is superior to that typically achieved with computer vision-based techniques, which often suffer from limitations such as lower resolution and occasional inaccuracies due to factors like lighting conditions. The advantage of using a marker-based motion capture system is that it provides clear, reliable data without the need for complex post-processing or correcting errors caused by imperfect image recognition. But the motion performed in air is free of the resistance and buoyancy effects that would normally be present in a water-based drowning scenario. In other words, the participant's motions, particularly those of limb angles, velocities, and overall motion patterns are different from those in the water.

Even though the experimental setup provides a valuable alternative for capturing motion data in a controlled environment. It enables the collection of high-quality data that can be subjected to detailed analysis and comparison with data collected from computer vision-based

methods. The use of a suspension system to simulate buoyancy allows for a more realistic approximation of the motions that would occur in water, even though the physical forces acting on the participant are not identical to those in a true water environment. Once the data are collected, they are processed and analysed to validate the kinematic model of the participant's motions which can be used for the comparison.

4.3.2 Data Collection

Once the footage captured by the digital cameras at AUT's Motion Capture Lab is processed by the lab technician, two primary output files are generated for analysis. The first output is a 3D animation of the full body of the participant in motion, as illustrated in Figure 4.5. It is useful for observing the general patterns of motion and identifying any irregularities or deviations from expected motion. The second output is a TRC (Tracking) file, which contains detailed numerical data including the coordinates of the markers placed on the participant's body. The data from the TRC file can be converted into an Excel file for further analysis, as shown in Table 4.1.

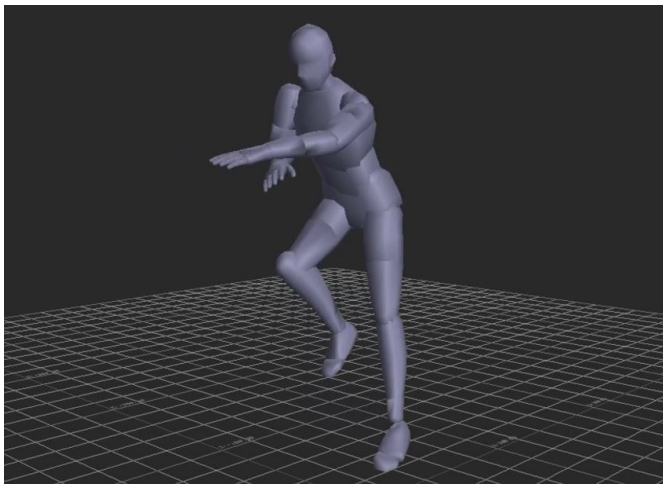

Figure 4.5: *3D Animation from motion capture lab*

The TRC file is a comprehensive data source, listing the x, y, and z coordinates for 54 distinct markers that correspond to specific anatomical landmarks on the participant's body. These markers include, but are not limited to: Head_Asym, LFrontHead, LBackHead, RFrontHead, RBackHead, TopSpine, TChest, LSternum, BChest, RSternum, RShoulder, RBicep, RElbow, RForearm, RWristInner, RWristOuter, R_Thumb_hand, R_Palm_hand, R_Pinky_hand, LShoulder,

LBicep, LElbow, LForearm, LWristInner, LWristOuter, L_Thumb_hand, L_Palm_hand, L_Pinky_hand, MiddleBack, LowerBack, Root, Offset, LFrontWaist, LMiddleWaist, LBackWaist, RFrontWaist, RMiddleWaist, RBackWaist, RHip, RKnee, RTibia, RAnkle, RHeel, ROuterMeta, RTip, RToe, LHip, LKnee, LTibia, LAnkle, LHeel, LOuterMeta, LTip, LToe. The markers provide a clear and structured means of tracking the participant's motion over time.

In Table 4.1, the metadata related to the motion capture process is outlined at the top of the table. This metadata includes essential information such as the data rate, camera rate, number of frames, number of markers, units of measurement, original data rate, and the original number of frames captured during the motion capture session. These details provide context to the captured data ensuring that analyses are based on accurate and reliable spatial measurements.

The main body of Table 4.1 is organised into multiple columns, each corresponding to specific parameters related to the motion capture data. The first column indicates the frame number which serves as a sequential identifier for each individual frame captured. The second column records the time interval between frames which is needed for determining time-dependent motion dynamics such as velocity and acceleration. The subsequent columns contain the x, y, and z coordinates for each marker, starting with Head_Asym. Each marker is associated with three separate columns providing detailed three-dimensional motion data for the participant's entire body. This detailed dataset forms the basis for further calculations, including kinematic analysis and the identification of potential energy-harvesting sites on the body.

The time interval between frames in the motion capture dataset is set at 0.01 seconds, a parameter determined by the frame rate of the original recording. Although it is possible to increase this interval to reduce the computational load, in this analysis, the interval is kept short to ensure maximum accuracy and resolution in the resulting data. The cameras used in this experiment are capable of capturing data at intervals as short as 0.001 seconds, providing even higher temporal resolution when necessary, although the 0.01-second interval is deemed sufficient for this study.

Using the coordinates of the markers placed on the arm and thigh, the angles, as well as the angular velocity of a body link (e.g. limb) in both the vertical and horizontal planes. This data can be further analysed to evaluate the potential for energy harvesting from the participant's

Frame#	Time	X1	Y1	Z1	X2	Y2	Z2	X3	Y3	Z3
1	0.00	2.50194	1751.98157	1070.60571	125.60585	1706.68005	1196.73108	154.18686	1644.91528	1072.20752
2	0.01	2.38840	1752.00952	1070.66772	125.53018	1706.68372	1196.72571	154.07556	1644.94849	1072.16919
3	0.02	2.44337	1751.97522	1070.77539	125.47853	1706.67090	1196.72253	153.97491	1644.96375	1072.12683
4	0.03	2.37489	1752.01221	1070.80896	125.45422	1706.66382	1196.71057	153.89886	1644.99255	1072.09119
5	0.04	2.31883	1752.05652	1070.82080	125.42106	1706.69287	1196.69287	153.82130	1645.03198	1072.07983
6	0.05	2.10905	1752.12671	1070.75305	125.39203	1706.60217	1196.77722	153.76660	1645.04138	1072.05444
7	0.06	2.06120	1752.14954	1070.74524	125.39438	1706.78833	1196.63672	153.70000	1645.04480	1072.04834
8	0.07	2.01551	1752.15845	1070.73694	125.37842	1706.83203	1196.61218	153.64137	1645.03333	1072.05200
9	0.08	2.00125	1752.16296	1070.73523	125.38229	1706.86768	1196.58105	153.61214	1645.00769	1072.04578
10	0.09	1.98818	1752.17004	1070.72449	125.38006	1706.77087	1196.66980	153.57010	1644.99817	1072.04089
11	0.10	1.96844	1752.19458	1070.71631	125.38849	1706.79919	1196.66187	153.53212	1644.99170	1072.02637
12	0.11	1.94563	1752.21179	1070.71436	125.39232	1706.84729	1196.63196	153.49596	1645.01660	1071.99622
13	0.12	1.90200	1752.26038	1070.71570	125.38486	1706.91174	1196.60413	153.45851	1645.02612	1071.98901
14	0.13	1.87646	1752.27295	1070.71545	125.38651	1706.97961	1196.57239	153.41959	1645.04395	1071.98022
15	0.14	1.83296	1752.28149	1070.72339	125.40881	1707.04480	1196.54346	153.37672	1645.04773	1071.96509
16	0.15	1.79456	1752.28210	1070.73035	125.42195	1707.10376	1196.50330	153.33644	1645.06396	1071.97717
17	0.16	1.75313	1752.28296	1070.73242	125.43757	1707.16016	1196.46753	153.28609	1645.04126	1071.95728
18	0.17	1.70492	1752.29541	1070.72729	125.46110	1707.20374	1196.44861	153.21327	1645.03540	1071.94226
19	0.18	1.64294	1752.29846	1070.73425	125.45817	1707.24829	1196.42383	153.14566	1645.02844	1071.91553
20	0.19	1.57752	1752.26270	1070.75928	125.45222	1707.30298	1196.40137	153.09149	1645.01892	1071.91687
21	0.20	1.64623	1752.20020	1070.87158	125.44071	1707.35083	1196.38367	152.98828	1645.02209	1071.87671
22	0.21	1.54359	1752.17151	1070.91589	125.42939	1707.41516	1196.36353	152.93770	1645.03271	1071.89478
23	0.22	1.45594	1752.13452	1070.97925	125.41734	1707.48218	1196.35535	152.87184	1645.05029	1071.92712

Table 4.1: *Sample data table from motion capture lab*

motions during the simulated drowning scenario.

4.3.3 Data Processing Techniques

Data processing is the key step in turning raw motion capture data into meaningful information that can be used to study limb motion. Both the computer vision-based and lab-based methods generate large amounts of data, which mainly include joint positions over time. To make sense of this data, several techniques are applied to clean, filter, and analyse the motion data.

Data Cleaning and Noise Reduction

The first step in processing motion capture data is data cleansing. Because of the challenges in capturing motion, especially in water, the raw data often contains noise. This noise can come from water splashes, reflections, or problems with the cameras.

To reduce noise, a filtering method such as the median filter is used. The moving average method smooths out the data, removing unwanted variations without changing the actual motions of the limbs. This helps ensure that the processed data accurately reflects the person's motions during the "ladder climbing" motion.

Calibration and Coordinate System Alignment

Calibration makes sure that the data from both methods is consistent and accurate. In

the motion capture lab at AUT, a 3D coordinate system is used, which is calibrated to the physical space where the person performed the drowning simulation. Similarly, in the computer vision method, the videos are calibrated to ensure that the captured motions match real-world dimensions.

A key part of the data processing is aligning the coordinate systems from both methods. This makes it possible to compare the results and ensures that any differences are due to the actual motion and not measurement errors.

Chapter 5

Analysis of the Motion Capture Results

The analysis of the motion capture data obtained from both the computer vision-based approach and the Motion Capture Lab at Auckland University of Technology (AUT) will concentrate on the angular displacement and velocity of the limbs, particularly the thighs and arms, which are crucial to derive meaningful insights on how energy can be harvested from these motions.

As mentioned in the last Chapter, processing the raw motion data entails several important steps, including noise reduction, calibration, and the conversion of joint position data into angular displacements and velocities. These are done before the preparation and analysis in this chapter.

5.1 Data Preparation before Analysis

From the data output of the two motion capture methods, it is clear that the participant's trunk and head display relatively limited motion. This restriction in motion suggests that the kinetic energy available for harvesting from these parts of the body is minimal due to their small range of motion. As a result, the analysis naturally shifts focus to the limbs, which exhibit more dynamic motion and therefore present a greater potential for energy harvesting applications.

The arms and thighs have been identified as the primary areas of interest for this study. Although there may be minor variations between the left and right limbs, possibly influenced by factors such as handedness or dominant-side usage, the data indicates that these differences

are not significant enough to impact the overall analysis. For the purposes of this research, the motion of both sides is assumed to be symmetrical, thereby simplifying the investigation of limb motion and its potential for kinetic energy harvesting.

Key anatomical landmarks are identified and tracked during the computer vision analysis to provide a clearer understanding of the limb motions. Landmark points 12 and 14 represent the shoulder and elbow joints, with the linkage between them corresponding to the arm. Points 24 and 26 correspond to the hip and knee joints, with the linkage between these points representing the thigh. By monitoring the changes in these landmarks over time, it is possible to capture the motion of the arms and thighs with a high degree of precision. The time interval between frames is set at 0.033 seconds, corresponding to the frame rate of the original video footage. While it is technically feasible to increase this interval to reduce computational load, this study prioritised accuracy over computational efficiency. Therefore, the interval is kept minimal to ensure the highest possible resolution and fidelity in the resulting data.

For the motion capture lab data, the markers of interest for the arm are the LShoulder and LElbow, which correspond to the shoulder and elbow joints, respectively. The motion of the arm is represented by that of the linkage between these two markers. Similarly, for the thigh, the relevant markers are LHip and LKnee, representing the hip and knee joints. The linkage between these markers provides data on the angular motion of the thigh.

The time interval between frames in the motion capture dataset is set at 0.01 seconds, based on the frame rate of the original recording. Similar to the computer vision method, while increasing this interval could reduce computational load, it is kept short in this analysis to ensure high accuracy and resolution in the data.

5.2 Angular Displacements of the Arms and the Thighs

5.2.1 Angular Displacement of the Arm

Computer Vision-Based Results

The horizontal motion of the arm, as shown in Figure 5.1, demonstrates a substantial range of motion, with the maximum angle reaching approximately 170 degrees. On average, the angle

of motion across cycles is around 100 degrees. The time duration for each cycle of motion averages about 1 second. But even the regularity in cycle duration, it is challenging to identify a clear and consistent cyclic pattern from the data. This irregularity is likely due to the balancing role of the arms during the motion. The arms help the participant maintain stability, preventing them from tilting forward or backward during the drowning simulation. This balancing function introduces variability in the motion, complicating the identification of a well-defined cycle.

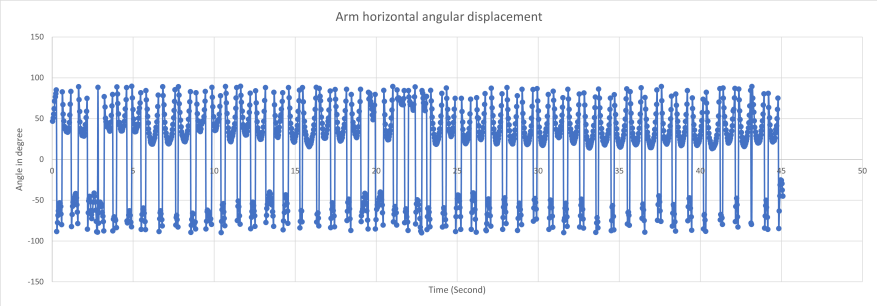

Figure 5.1: *Arm horizontal motion data from computer vision*

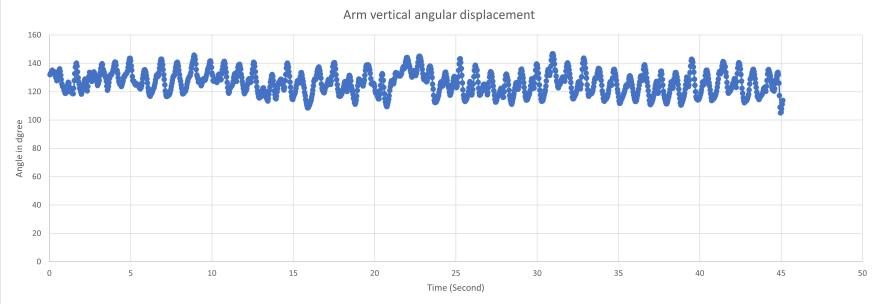

Figure 5.2: *Arm vertical motion data from computer vision*

In contrast, the vertical motion of the arm exhibits a more limited range. As shown in Figure 5.2, the maximum vertical angle of motion is around 32 degrees, with an average angle of approximately 20 degrees. The average time duration for each cycle remains close to 1 second. Similar to the horizontal motion, identifying a consistent motion cycle in the vertical plane proves challenging due to the arms' balancing function. The vertical motion of the arms seems to serve more of a stabilising role.

Motion Capture Lab Results

In the motion capture lab results, the arm's horizontal motion as shown in Figure 5.3,

reveals a significant range of motion, with the maximum angle reaching approximately 120 degrees. Across multiple cycles, the average angle for the horizontal arm motion is around 90 degrees. This broad range of motion reflects the participant's ability to consistently perform horizontal motions which could be used in energy-harvesting applications. The duration of each motion cycle averages about 1.4 seconds.

Figure 5.3: *Arm horizontal motion data from motion capture lab*

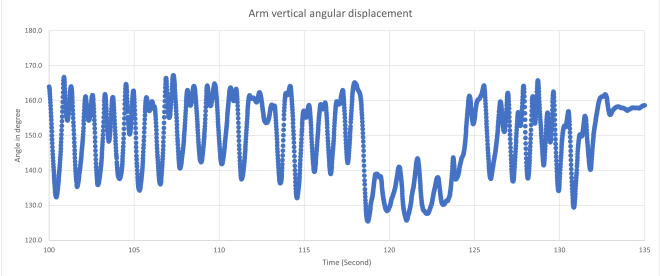

Figure 5.4: *Arm vertical motion data from motion capture lab*

The vertical arm motion is characterised by a more constrained range. As illustrated in Figure 5.4, the maximum vertical angle of motion is about 32 degrees, with the average angle settling at around 20 degrees. The range of vertical motion is more limited compared to the horizontal motion. The duration of each vertical motion cycle also averages 1.4 seconds, maintaining synchrony with the horizontal motions. This synchrony in timing is notable as it suggests a coordinated effort between horizontal and vertical motions. The cyclical pattern in vertical motion is less distinct compared to horizontal motion. This lack of clarity in the data may be attributed to the arm's involvement in maintaining balance and stability which adds a level of complexity to the motion.

5.2.2 Angular Displacement of the Thigh

Computer Vision-Based Results

The thigh motions display a more consistent and uniform pattern compared to the arm motions. As illustrated in Figure 5.5, the horizontal thigh motion shows a maximum angular range of approximately 17 degrees, with an average angle of motion of around 10 degrees. Unlike the arm motions, the thigh motion pattern is easily identified, with a consistent cycle duration of approximately 1 second. This regularity in motion suggests that the thighs play a more stabilised and rhythmic role in the overall body motion. Such consistency is particularly beneficial for energy harvesting applications, where steady and predictable motion is preferred for optimising the energy capture process. The rhythmic nature of thigh motion can ensure more reliable energy output compared to the less stable arm motions.

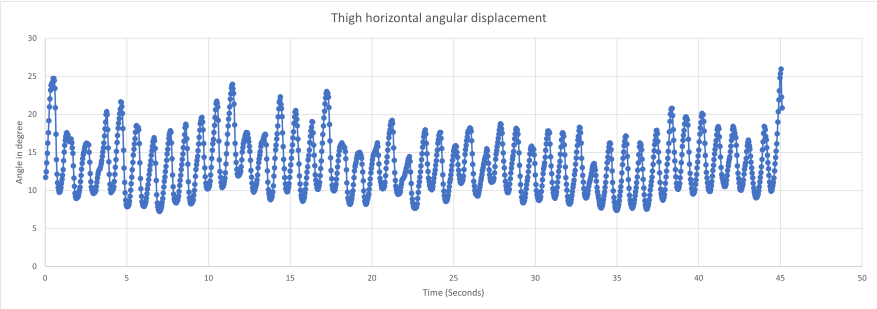

Figure 5.5: *Thigh horizontal motion data from computer vision*

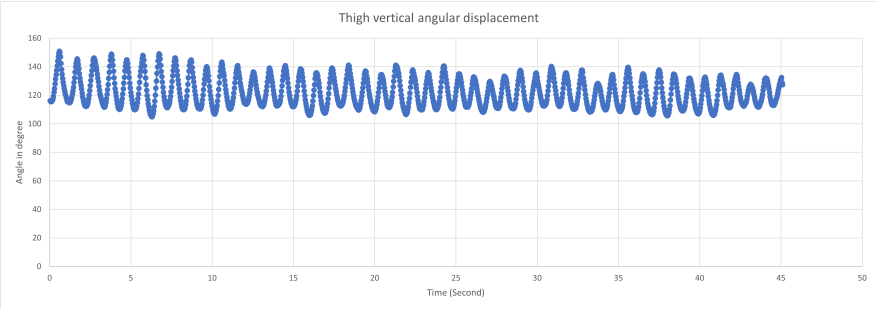

Figure 5.6: *Thigh vertical motion data from computer vision*

The vertical thigh motion exhibits an even more substantial range of motion compared to the horizontal plane. As shown in Figure 5.6, the maximum vertical angle of motion is around 55 degrees, with an average angle of approximately 50 degrees. This extensive range of motion

suggests that vertical thigh motion contributes significantly to the overall energy available for harvesting. The uniformity of this motion is emphasised by the consistent cycle duration, which remains at approximately 1 second throughout the 45-second recording.

Motion Capture Lab Results

Thigh motion data reveals a more consistent and patterned motion compared to the arms. The horizontal motion of the thigh as illustrated in Figure 5.7 shows a maximum angular range of approximately 23 degrees, with an average angle of 21 degrees.

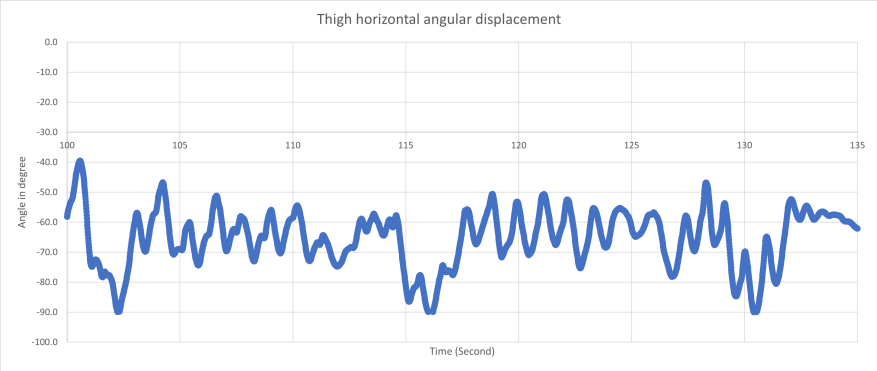

Figure 5.7: *Thigh horizontal motion data from motion capture lab*

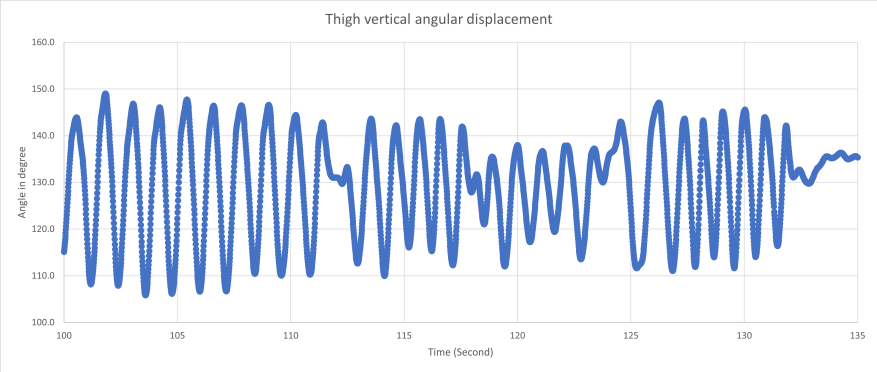

Figure 5.8: *Thigh vertical motion data from motion capture lab*

On the other hand, the vertical motion of the thigh exhibits a broader and more dynamic range of motion, with a maximum angular range of 60 degrees and an average angle of 55 degrees, as shown in Figure 5.8. This larger range of motion in the vertical plane, compared to the horizontal shows the thigh's role in generating significant kinetic energy. The uniformity of this vertical motion is further emphasised by the consistent cycle duration and the stable range

of motion observed throughout the recording. This cyclical, rhythmic pattern of vertical thigh motion indicates a potential for consistent energy capture.

5.3 Angular Velocities of the Arm and the Thigh

5.3.1 Angular Velocity of the Arm

Computer Vision-Based Results

In terms of angular velocity, the arm's horizontal motion reaches a peak of 640 degrees per second, with an average top velocity of approximately 290 degrees per second, as illustrated in Figure 5.9. This significant angular velocity suggests that the arm is involved in rapid and forceful motions. These findings suggest that horizontal arm motions may play a significant role in energy harvesting applications, given their dynamic range and velocity.

The angular velocity during the vertical arm motion is noticeably lower compared to the horizontal motion. The maximum angular velocity for vertical motion is about 170 degrees per second, with an average top velocity of roughly 100 degrees per second, as shown in Figure 5.10. The reduced range of motion and lower angular velocity suggest that the arm's vertical motion plays a lesser role in the overall drowning motion. This contrast between the arm's horizontal and vertical motions reinforces the idea that horizontal arm motion is a more critical component when considering energy harvesting potential.

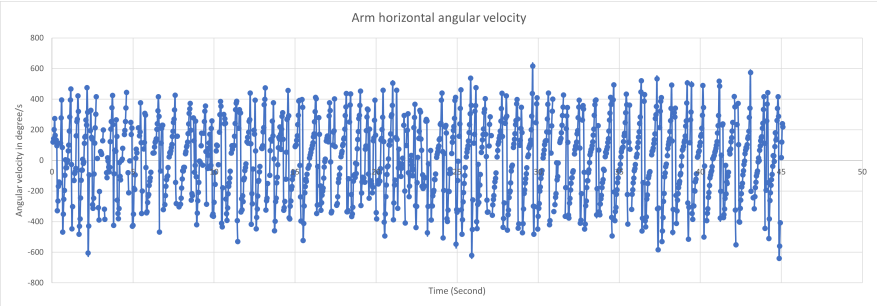

Figure 5.9: *Arm horizontal angular velocity from computer vision*

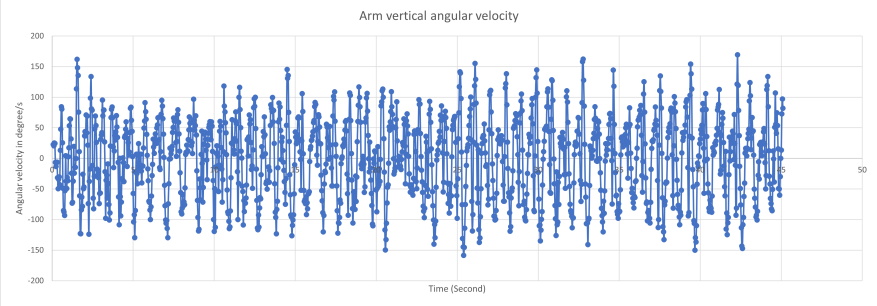

Figure 5.10: *Arm vertical angular velocity from computer vision*

Motion Capture Lab Results

The angular velocity during the horizontal arm motion reaches a peak of 854 degrees per second, with an average top velocity of around 140 degrees per second as shown in Figure 5.11. This high angular velocity underscores the arm's capacity for rapid and forceful motions. The high-speed motion also indicates the potential for energy harvesting. On the other hand, the vertical arm motion is characterised by a more constrained range.

The cyclical pattern in vertical motion is less distinct compared to horizontal motion. This lack of clarity in the data may be attributed to the arm's involvement in maintaining balance and stability which adds a level of complexity to the motion. The angular velocity in the vertical plane is also significantly lower, with a maximum of 166 degrees per second and an average top velocity of approximately 50 degrees per second, as shown in Figure 5.12. This difference suggests that the potential for kinetic energy harvesting from vertical arm motion may be less promising compared to horizontal motion. The vertical arm motion is necessary for certain functions such as balance but it contributes less to the overall kinetic energy potential when compared to the more dynamic horizontal motion.

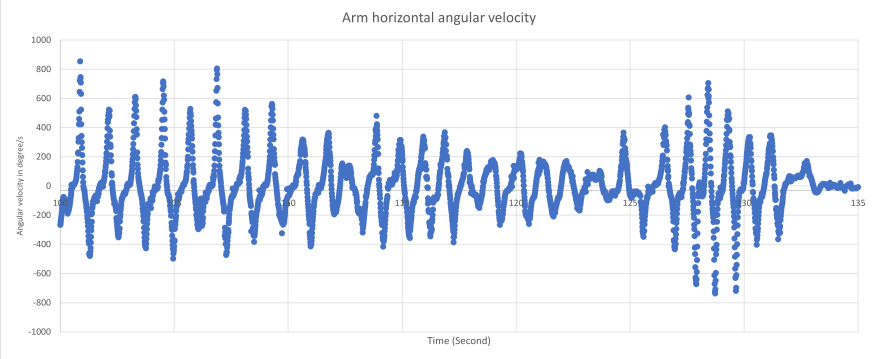

Figure 5.11: *Arm horizontal angular velocity from motion capture lab*

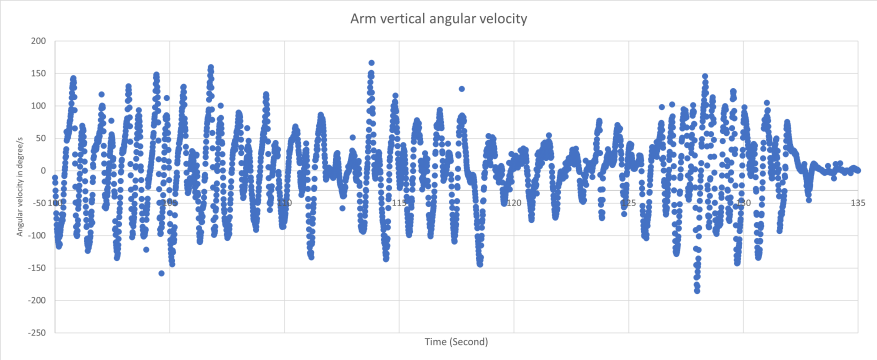

Figure 5.12: *Arm vertical angular velocity from motion capture lab*

5.3.2 Angular Velocity of the Thigh

Computer Vision-Based Results

The angular velocity of the thigh's horizontal motion reaches a peak of 110 degrees per second, with an average top velocity of about 65 degrees per second, as shown in Figure 5.13. Although the maximum angular velocity is lower than that observed in arm motions, the consistent and repetitive pattern in the thigh motion indicates a dependable source of kinetic energy which is desirable for energy harvesting. The angular velocity for the vertical thigh motion peaks at 200 degrees per second, with an average top velocity of about 125 degrees per second, as shown in Figure 5.14. The higher angular velocity observed in the vertical motion, compared to the horizontal plane, indicates that the thigh's vertical motion is a more significant source of kinetic energy. The combination of a substantial range of motion and relatively high angular velocity further enhances the potential for energy harvesting from vertical thigh motion.

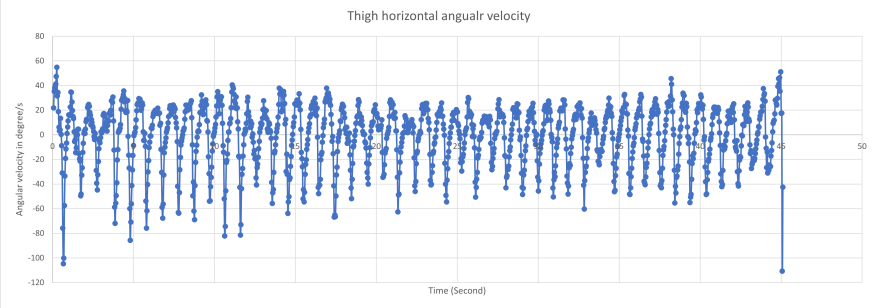

Figure 5.13: *Thigh horizontal angular velocity from computer vision*

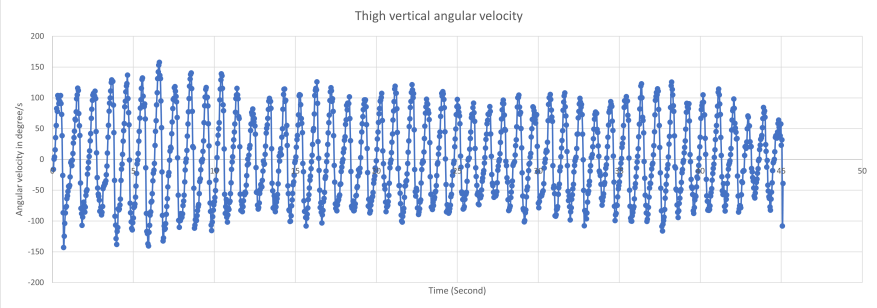

Figure 5.14: *Thigh vertical angular velocity from computer vision*

Motion Capture Lab Results

The angular velocity during the thigh's horizontal motion reaches a peak of 95 degrees per second, with an average top velocity of 40 degrees per second, as shown in Figure 5.15. Although this peak velocity is notably lower than that of the arm, the thigh's motion is marked by a higher degree of regularity which is beneficial for sustained and predictable energy harvesting. The lower angular velocity observed in the horizontal plane suggests that the kinetic energy harvested from this motion is lower compared to vertical motions.

The angular velocity for vertical thigh motion peaks at 130 degrees per second, with an average top velocity of approximately 100 degrees per second, as shown in Figure 5.16. These figures suggest that the vertical motion is faster and more powerful compared to that in the horizontal plane. The higher angular velocity in the vertical plane indicates a stronger potential for energy harvesting. The difference in angular velocity between the vertical and horizontal planes highlights the importance of directionality in motion analysis, as not all planes of motion contribute equally to energy-harvesting potential.

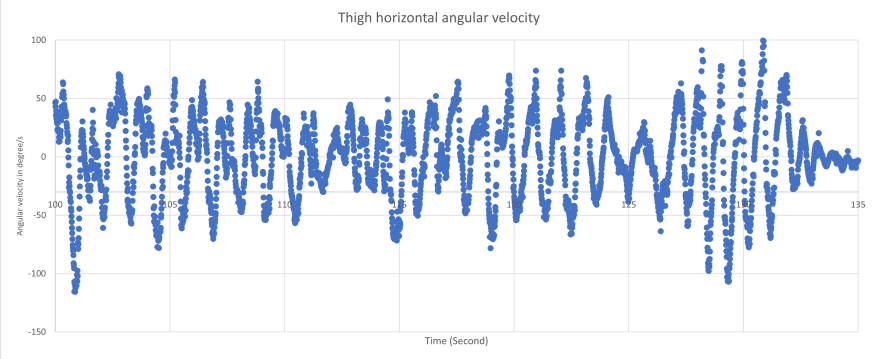

Figure 5.15: *Thigh horizontal angular velocity from motion capture lab*

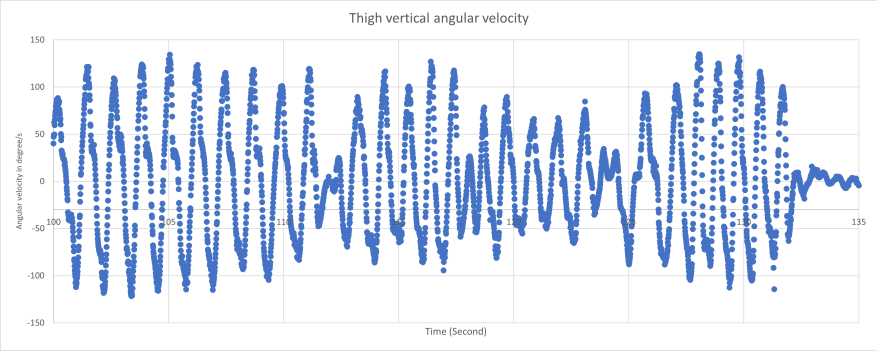

Figure 5.16: *Thigh vertical angular velocity from motion capture lab*

5.3.3 Findings from the Analysis of the Motion Capture Results

The data collected from both methods are mostly aligned, showing that the accuracy of these data collection techniques is reliable. Although there are some differences between the two methods, these differences can be attributed to factors such as water resistance and variations in how the motion is captured. The computer vision-based method may be more affected by external conditions, while the motion capture lab provides more controlled and consistent data.

Despite these variations, the differences are within a reasonable range and do not significantly affect the overall patterns observed in the motions. This suggests that both methods are suitable for measuring angular displacement during the "ladder climbing" motion in water. The consistent findings across the two methods also reinforce the reliability of using either approach for analysing motions.

The primary findings from the data collection and analysis are around the motion patterns

of the participant's limbs, particularly the arms and thighs, which are identified as the most promising sources of kinetic energy for harvesting from the human body. Both methods highlighted the importance of limb motion in the context of energy harvesting. The arms demonstrated significant horizontal motion where the average angular velocity reached 290 degrees per second. However, the vertical motion of the thighs is found to be more consistent and rhythmic, particularly in the aquatic environment, where the peak angular velocity reached 200 degrees per second. This suggests that the thighs may be a more reliable source of kinetic energy, particularly in environments where steady and regular motion is essential for efficient energy capture.

In Table 5.1, the comparison between the two methods clearly highlights that the vertical motion of the thigh is the most consistent and predictable, a major factor in the design of an energy harvester. This predictability is essential for applications that rely on regular, sustained motion for effective energy harvesting in search and rescue operations.

	Computer Vision		**Motion Capture Lab**	
	Peak value	**Average value**	**Peak value**	**Average top value**
Arm Horizontal Angular Displacement (degrees)	170	100	120	90
Arm Vertical Angular Displacement (degrees)	32	20	35	25
Thigh Horizontal Angular Displacement (degrees)	17	10	23	21
Thigh Vertical Angular Displacement (degrees)	55	50	60	55
Arm Horizontal Top Angular Velocity (degrees/s)	640	290	854	140
Arm Vertical Top Angular Velocity (degrees/s)	170	100	166	50
Thigh Horizontal Top Angular Velocity (degrees/s)	110	65	95	40
Thigh Vertical Top Angular Velocity (degrees/s)	200	125	130	100

Table 5.1: *Comparison of angular displacements and angular velocities*

The findings from the data collection also provided key insights into the dynamic analysis and design of the energy-harvesting device. Given the dynamic and sometimes inconsistent nature of arm motions, particularly in the horizontal plane, it may be more challenging to develop a device that can consistently capture energy from this motion. On the other hand, the consistent and rhythmic vertical motion of the thighs presents a more stable and reliable source of energy. This suggests that the energy-harvesting device should be designed to focus on the

thighs where the motion is more predictable and consistent. The potential for energy harvesting is also higher.

Force/Torque Calculations

Now that the vertical motion of the thigh has been identified as the primary source for energy harvesting, the equations 3.4 to 3.8 derived in Chapter 3 can now be applied for the force analysis.

Using the data obtained from the motion capture laboratory, the vertical force exerted by the thigh is calculated in a spreadsheet model, as shown in Figure 5.17. This calculation takes into account various forces acting on the thigh, including buoyancy force, drag force, and gravitational force. The analysis shows that the maximum vertical force reaches up to 110N, with the average peak value being around 60N.

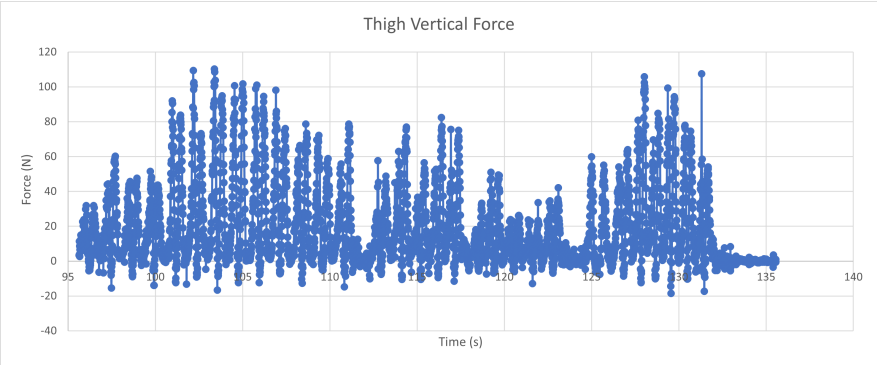

Figure 5.17: *Thigh vertical force calculated with motion capture data*

Further analysis of the thigh's motion confirms that the motion follows a cyclic pattern. This cyclic nature is important for consistent energy harvesting. With the velocity values derived from the captured data, it becomes possible to calculate the angular kinematics of the thigh. The cyclic motion suggests a repetitive pattern that is suitable for modelling energy harvesting.

With the forces acting on the thigh calculated, it is possible to determine the torque by applying Equation 3.9 in Chapter 3. Figure 5.18 shows the calculated torque values over time. The maximum torque reached is 45 Nm, while the average peak torque values fall between 20 Nm and 30 Nm. It is important to note that this calculation does not include the tibia, the actual torque at the hip joint will be higher.

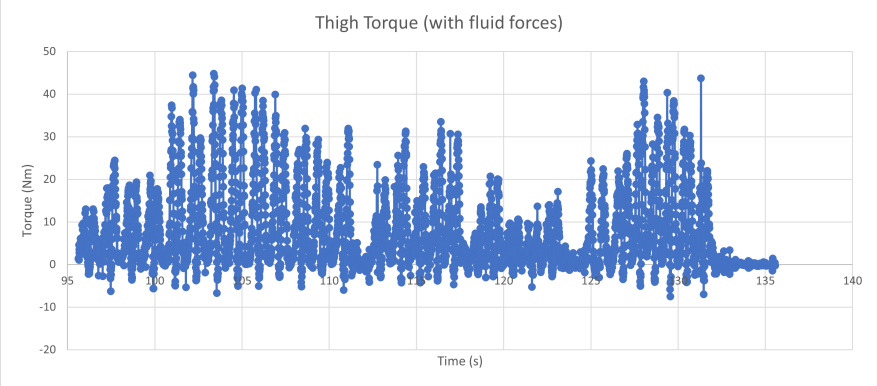

Figure 5.18: *Thigh torque with fluid forces calculated from motion capture lab data*

Energy Calculations

Once the velocity is calculated from the motion capture data, the mechanical energy associated with the thigh motion can be determined using Equation 3.10 in Chapter 3. The added mass coefficient used in this energy calculation is the same as the one applied in the fluid forces calculation. Figure 5.19 presents the results of the mechanical energy calculation. The maximum energy value is close to 9 Joules, with the average peak values ranging between 4 and 6 Joules. These findings help quantify the mechanical energy involved in the thigh's motion.

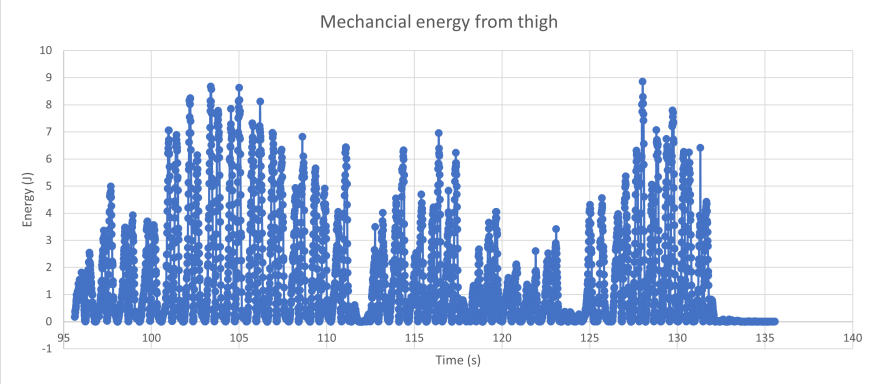

Figure 5.19: *Thigh mechanical energy calculated from motion capture lab data*

5.3.4 Potential for Energy Harvesting

The motion capture analysis, utilising both computer vision techniques and traditional motion capture lab methods, provides comprehensive insights into the potential for kinetic energy harvesting from limb motions. The findings from both methods align, reinforcing the accuracy

and reliability of the data when comparing the motions of the arm and thigh. While the arm demonstrates a wider range of motion and higher angular velocities, its irregular motion patterns, particularly in the horizontal plane, present challenges for consistent energy harvesting. On the other hand, the thigh's vertical motion, characterised by a regular and substantial angular velocity, emerges as a more viable candidate for efficient kinetic energy harvesting.

The energy potential of these motions can be quantified using the equation for rotational kinetic energy,

$$E = \frac{1}{2} I \omega^2$$

where I represents the moment of inertia and ω is the angular velocity. For the upper arm, the moment of inertia typically ranges from 0.02 to 0.03 kg·m^2, whereas for the thigh, it falls between 0.1 and 0.2 kg·m^2 [103]. Although the arm generally exhibits higher angular velocity, the thigh's significantly larger moment of inertia plays an important role in generating greater kinetic energy. Moreover, when additional segments such as the forearm for the arm or the tibia for the thigh are included in the analysis, the inertia difference becomes even more pronounced. This results in the thigh being able to generate more substantial energy output during motion.

In addition to its higher inertia, the thigh's consistent and uniform motion further enhances its suitability for energy harvesting. Regular, predictable motion is a key factor in the efficiency of energy conversion mechanisms, and the thigh's vertical motion provides a stable and reliable source of kinetic energy. This reliability is especially critical for wearable energy-harvesting devices designed for search and rescue operations, where sustained and dependable power generation is necessary.

In conclusion, although the arm demonstrates faster angular motion, the thigh's larger moment of inertia and consistent vertical motion make it a more promising focus for energy harvesting. The alignment of findings from both computer vision and motion capture lab methods strengthens the validity of this conclusion. These insights are crucial for the design of future wearable energy-harvesting systems, particularly in contexts requiring reliable power generation, such as search and rescue.

5.4 Conclusion

The data analysis presented in this chapter provides important insights into the motion patterns of the thighs and arms during the "ladder climbing" motion in a drowning simulation. This analysis, based on data captured from both the computer vision system and the Motion Capture Lab at Auckland University of Technology (AUT), highlights the importance of accurate motion tracking for understanding biomechanical motion and energy harvesting potential.

The two motion capture methods allow for a detailed comparison of the key parameters, including angular displacement and velocity of the limbs. While both methods produced consistent results, each had its strengths and weaknesses. The computer vision system offers flexibility in real-world settings, while the lab-based motion capture method provides higher precision due to the use of reflective markers and controlled conditions. By combining the strengths of both approaches, it allows for cross-validation of the results, ensuring that the findings are robust. While the lab-based method provided more detailed data, the computer vision system is better suited for real-world simulations. Together, they form a comprehensive approach to motion capture analysis of the "ladder climbing" motion in this study.

One of the major findings from this analysis is the clear difference in motion patterns between the thighs and arms. The angular displacement and velocity data revealed that the thigh motions are more consistent and predictable, especially in the vertical plane. The thigh's vertical motion exhibited a steady range of motion, with angular displacements of 50 to 60 degrees and angular velocities reaching 200 degrees per second. This regularity is particularly important for energy harvesting applications, as it indicates a stable and repeatable source of mechanical energy.

In contrast, the arm motions, while exhibiting a wider range of motion, are less consistent. The horizontal motion of the arms displays greater variability, with angular displacements ranging from 90 to 170 degrees and angular velocities peaking at 640 to 854 degrees per second. However, this high angular velocity is offset by the irregularity of the motion patterns, making it more difficult to harness consistent energy from the arms. The vertical motion of the arms is even more limited, with much lower angular velocities and less potential for energy harvesting.

The consistency of the thigh motion, combined with its significant range of motion and relatively high angular velocity, positions the thighs as the primary source of energy for harvesting in this drowning simulation scenario. The arms, though capable of generating higher velocities, contributed less to the overall energy harvesting potential due to their less predictable motion patterns.

The analysis clearly shows that the thighs, particularly in their vertical motion, offer the most promising potential for energy harvesting. The cyclical and repetitive nature of the thigh motion provides a reliable source of kinetic energy that can be captured and converted into electrical energy. The regular pattern of the thigh's vertical displacement, combined with its substantial angular velocity, makes it most suitable for designing energy harvesting devices that rely on predictable and consistent motion in this research.

In comparison, the arm motions, while more dynamic, are less suited for efficient energy harvesting due to their variability. The irregularities in the arm's horizontal motion make it challenging to capture energy consistently. Additionally, the lower angular velocity and a smaller range of vertical arm motion suggest that the energy potential from the arms is limited, particularly when compared to the thighs.

The findings from this analysis indicate that wearable energy harvesting systems for search and rescue operations should focus primarily on the thighs. The stable and rhythmic thigh motion offers a continuous source of power, which is essential for maintaining the reliability of devices such as emergency beacons or sensors that need to operate in life-threatening situations.

Chapter 6

Energy Harvesting Mechanism Design - Overview

In the field of energy harvesting, various mechanisms have been explored and implemented, each with its unique advantages and challenges, as highlighted in the literature review. The selection of an energy harvesting mechanism is often influenced by the specific requirements and constraints of the intended application. For lifejackets used in search and rescue operations, the energy harvesting mechanism must satisfy several criteria to ensure its effectiveness and feasibility. These criteria include size, energy harvesting potential, compatibility with the wearer's motions, minimal impact on the wearer's freedom of motion and lifejacket functionality, scalability, robustness, maintenance requirements, wearability, duration of use, and the ability to capture kinetic energy efficiently.

Through review and analysis, including data obtained from motion capture experiments, the electromagnetic energy harvester has emerged as the preferred solution. This chapter will delve into the design considerations for this harvester, integration with the lifejacket and the design of the mechanism. These are informed by the specific insights gained from the motion capture study.

6.1 Overview of the Energy Harvesting System

The energy harvesting system designed in this study aims to capture kinetic energy from the motion of the thigh during the "ladder climbing" motion and convert it into electrical energy. The system is built around a brushed DC motor that acts as the energy harvester and is integrated into a lifejacket worn by the user. As shown in Figure 6.1, the motor is attached to the waist strap of the lifejacket, and a telescopic linkage connects the motor to the thigh strap, ensuring that the thigh's vertical motion drives the motor.

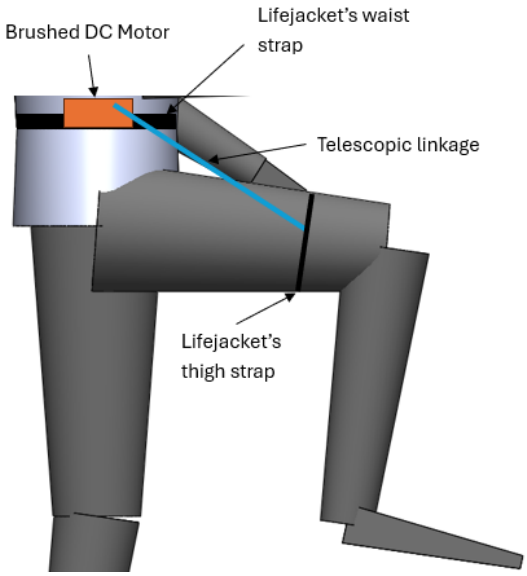

Figure 6.1: *High-level view of the energy harvesting system.*

The energy harvesting system consists of several key components:

- **Brushed DC Motor**: The motor is the central component of the system, responsible for converting the kinetic energy generated by the thigh into electrical energy. The selection of a brushed DC motor is based on its ability to generate power efficiently from relatively slow, repetitive motions, such as the thigh's vertical motion in the "ladder climbing" motion.

- **Telescopic Linkage**: The telescopic linkage connects the thigh strap to the motor and transmits the kinetic energy produced by the thigh's motion to the motor. The linkage

allows for smooth extension and retraction as the thigh moves, ensuring consistent energy transfer.

- **Lifejacket Integration**: The system is integrated into a standard lifejacket, with the motor mounted on the waist strap and the telescopic linkage connected to the thigh strap. This setup allows the user to generate energy without hindering their natural motion or compromising the functionality of the lifejacket.

- **Waterproofing and Durability**: Given that the system is designed for use in water, all components, including the motor, are waterproofed and designed to function reliably when submerged. The system must withstand the challenging conditions of water environments while maintaining its energy harvesting capabilities.

Principle of Operation

The energy harvesting system operates by capturing the kinetic energy generated from the repetitive flexion and extension of the thigh during the "ladder climbing" motion. As the user moves their thigh, the telescopic linkage extends and retracts, driving the motor. The brushed DC motor then converts this mechanical motion into electrical energy through electromagnetic induction.

The key steps in the operation of the system are as follows:

- **Thigh motion**: The "ladder climbing" motion, which is instinctively performed during a drowning event, involves the repeated lifting and lowering of the thigh. This motion generates kinetic energy that can be harnessed by the system.

- **Linkage Extension and Retraction**: The telescopic linkage retracts when the thigh is lifted and extends when the thigh is lowered. This motion drives the motor's gear-head, generating rotational motion.

- **Mechanical to Electrical Conversion**: The brushed DC motor converts the rotational motion into electrical energy through electromagnetic induction. As the rotor turns, it generates a voltage across the motor's terminals, which can be used to power small IoT devices or stored in a battery or capacitor.

- **Energy Storage or Direct Use**: The electrical energy generated by the motor can either be stored in a battery or capacitor for later use or be used directly to power devices such as IoT sensors and emergency communication tools.

Design Considerations

The design of the energy harvesting system takes into account several important factors to ensure that it is practical, efficient, and reliable in real-world applications. These considerations include:

- **Selection of the Thigh's Vertical Motion for Energy Harvesting:** This has been validated through the analysis of the motion data collected from both motion capture methods.

- **Size and Portability:** Electromagnetic energy harvesters, as referenced in the literature review, typically consist of two main components: a coil and a permanent magnet. The compactness of these components makes the harvester small enough to be integrated into a lifejacket without adding significant weight or bulk. This compact design, coupled with the simplicity of construction that allows it to be integrated easily, makes it suitable for applications where space and weight are critical, such as in lifejackets.

- **Energy Harvesting Potential:** When subjected to motions, the magnet within the harvester moves relative to the coil, inducing a changing magnetic field that generates electrical power. The amount of power generated is directly related to the amplitude and frequency of the motions are provided by the regular, low-frequency motions of the wearer during a drowning event. The thigh's vertical motion, as observed in the motion capture data, is a prominent example of such motion.

- **Freedom of Motion and Lifejacket Effectiveness:** The small size and lightweight nature of electromagnetic energy harvesters ensure that they do not significantly impact the wearer's freedom of motion or the overall effectiveness of the lifejacket. The harvester can be integrated into the lifejacket in a manner that allows it to capture energy from the

wearer's motions without hindering mobility or reducing the lifejacket's buoyancy and protective functions.

- **Scalability:** Electromagnetic energy harvesters are highly scalable. If more power is required, the design can be adjusted by increasing the number of coils or using larger magnets. The rotational speed can be adjusted by different gear-head ratios. This scalability, combined with the harvester's simple design and ease of fabrication, makes it a suitable solution for powering low-consumption devices within the lifejacket.

- **Robustness:** Electromagnetic energy harvesters are robust and capable of withstanding the harsh environments typically encountered during search and rescue operations in water. Their design is inherently durable, and able to function effectively in conditions involving saltwater, varying temperatures, and physical impacts. This robustness is important for ensuring the long-term reliability and functionality of the harvester in real-world scenarios.

- **Maintenance Requirements:** The maintenance requirements for electromagnetic energy harvesters are minimal. They do not require frequent servicing or replacement parts, which is an essential factor for their integration into lifejackets, as these devices are often stored for extended periods between uses. At present, lifejackets do not need regular testing. If a complicated maintenance process is needed, the owner might not keep the harvesting device in its best condition, which could make it unsafe to use.

- **Wearability and Duration of Use:** Lifejackets are designed to be worn securely, ensuring they remain in place during water-related emergencies. This secure wearability is vital for the consistent operation of the energy harvester, which relies on the predictable and repetitive motions of the wearer to generate power. Once the harvesting device is secured with the lifejacket, the lifejacket provides physical protection which improves its durability. Also, the secured position provides a stable fixed point for energy harvesting design.

6.2 Rationale for the Brushed DC Motor Selection

Direct Current (DC) motors are a common and versatile type of electromagnetic energy harvester. They are widely used in various applications due to their simplicity, reliability, and cost-effectiveness. They are readily accessible for purchase and replacement, significantly reducing both the cost and time involved in testing and production. The detailed specifications provided by the manufacturers also make it easier to perform manual calculations and simulations, eliminating the need to run extensive tests to identify each parameter.

DC motors come in two main types: brushed and brushless. Each type offers distinct advantages depending on the specific application.

Brushed DC Motors consist of a rotor (or armature), a commutator, brushes, an axle, and a field magnet. The brushes deliver current from the power supply to the commutator, which in turn transfers the current to the armature. The armature functions as an electromagnet, and when it is energised, it generates a magnetic field that interacts with the field magnet. This interaction produces a force that drives the rotor to spin. In energy harvesting applications, the rotation of the rotor can be used to generate electricity, effectively converting mechanical motion into electrical energy.

Brushless DC Motors As its name suggests, a brushless DC motor does not contain a brush which is subject to mechanical wear. In the motor, the rotor is a permanent magnet, and the motor housing contains multiple electromagnets. A controller, often referred to as an electronic speed control (ESC), supplies current to these electromagnets, generating a magnetic field that interacts with the permanent magnet of the rotor, causing it to spin. Like brushed motors, the rotational motion of the rotor in a brushless motor can be harnessed to produce electricity. Brushless motors are typically preferred in applications where higher efficiency and reduced maintenance are required.

6.2.1 Motor Characteristics

Key Parameters for Selection: When integrating a DC motor into a lifejacket for energy harvesting, several key parameters must be considered to ensure optimal performance. These

parameters include:

- **Size and Weight:** The motor should be compact and lightweight so as not to interfere with the wearability or buoyancy of the lifejacket.
- **Power Output:** The motor needs to generate sufficient power to meet the energy demands of the lifejacket's electronics.
- **Efficiency:** The motor's efficiency in converting mechanical motion into electrical energy is crucial for maximising power output from limited motions, especially in a rescue situation where the wearer's motions may be constrained.
- **Durability:** The motor must be robust enough to withstand the harsh conditions encountered during search and rescue operations, such as exposure to saltwater, physical impacts, and varying temperatures.

Specification of the Motor Selected:

The brushed DC motor YG2734 (12V) is selected as the energy harvester for this research due to its simplicity, practicality, and suitability for experimental purposes. A brushed DC motor is easier to integrate compared to a brushless motor, as it does not require an electronic speed controller (ESC) for operation. This reduces the complexity of the electronic system and minimises the components required, which is advantageous for experimental setups. Additionally, the YG2734 motor is chosen because the supplier provides a detailed specification sheet, including key parameters necessary for accurate calculations and modelling. While brushed motors can be bulkier and are more prone to electromagnetic interference (EMI) compared to brushless motors, these factors are manageable within the scope of this research. The simplicity of the brushed motor makes it a practical choice for focusing on the primary objective of validating the energy harvesting system. It is also acknowledged that brushless DC motors typically offer higher efficiency and longer lifespans. If a brushless motor is used in future iterations, the energy harvested could exceed the results obtained in this study. This trade-off highlights the brushed DC motor as a suitable choice for this research while allowing room for future improvements.

The specifications of YG22734 are shown in Figure 6.2. It is rated for operation up to 36 RPM (or 216 degrees per second) and is higher than the average top angular velocities recorded

from the two motion capture methods which are 125 degrees/second and 100 degrees/second respectively.

One of the defining features of the motor is its gear-head design, which incorporates a 244:1 gear ratio. This gear ratio allows the motor to generate electricity even at lower speeds of rotation, making it highly compatible with the relatively slow but consistent motions of a person during a drowning event. The motor operates at maximum efficiency at 29 RPM, producing up to 2.52 Watts of power, making it a robust model for testing in real-world conditions. While 2.52 Watts is higher than the power target of 210.6915 mW required to power basic IoT devices, an overestimation is necessary because the efficiency curve information from the supplier is not available. Without this information, it is difficult to predict exactly how efficient the system will be at different power levels. Also, since the rotation speed of the thigh is not constant during the motion, it is safer to choose a power harvester with a higher capacity at this stage. This allows for flexibility, as the performance can be verified during the experiment to ensure it meets the actual power requirements.

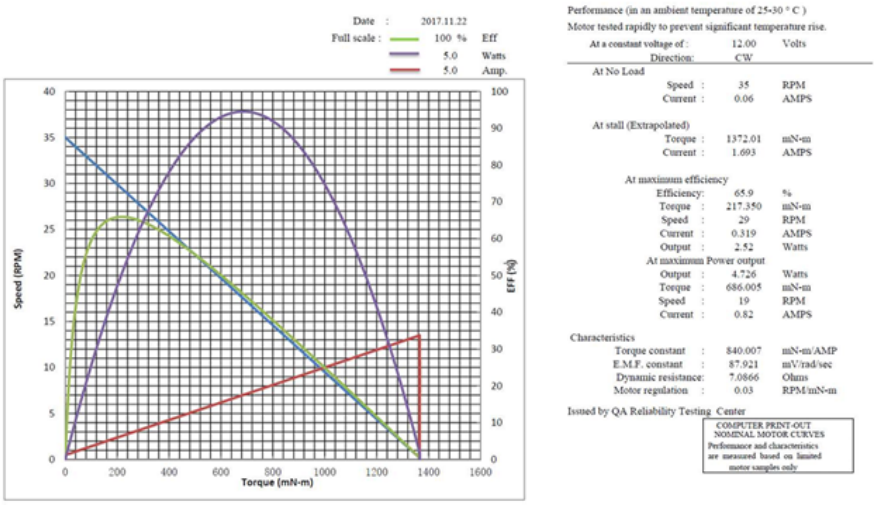

Figure 6.2: *Specification details of YG2734 12V motor [16].*

6.2.2 Circuit Design

With the selection of the YG2734 12V DC motor as the primary energy harvester for the system, the next step involves the design and implementation of a circuit capable of handling the fluctuating power generated by the motor during operation, which includes rectifying the

alternating current (AC) produced by the bi-directional motion of the motor, incorporating safety mechanisms to prevent damage from over-voltage, and providing energy storage for short to medium term use. If this design will lead to production in the future, the design must follow New Zealand standards for electrical safety and performance, especially in applications involving rescue operations. The circuit will also support the power requirements of standard sensors integrated into the system. Two different circuits will be discussed. The first circuit is for the prototype experiment and focuses on measuring the output from the energy harvester. The second circuit is a concept design intended for future integration with IoT devices in the lifejacket or energy storage systems.

Electrical Circuit for the Prototype

Figure 6.3 shows the electrical circuit for the prototype that is used in the experiment. Below is a breakdown of the circuit components and their functions:

1. **Bridge Rectifier**: Since the DC motor will rotate in both directions, producing alternating current (AC) voltage, a bridge rectifier is employed to convert this AC voltage into direct current (DC). The rectifier consists of four diodes arranged in a bridge configuration (D1, D2, D3, and D4), which ensures that the output polarity remains constant, regardless of the direction of rotation.

2. **INA219 current sensor Module**: The INA219 is a current-sense amplifier designed by Texas Instruments. It is used to monitor current by measuring the voltage across a low-side or high-side shunt resistor. The chip amplifies this small voltage differential, which is proportional to the current, and outputs a corresponding signal that can be read by microcontrollers or other systems for further processing.

3. **Microcontroller Unit (MCU)** : The Arduino UNO R3, a widely-used microcontroller board based on the ATmega328P microcontroller is used to receive the data from the sensor and process them to generate store and display the data on the electrical energy generated. The Arduino plays a critical role when using the INA219 sensor for current and power measurement. It communicates with the INA219 via the I2C protocol, acting as the master to configure the sensor's operating parameters, such as voltage range and

shunt resistance. The Arduino retrieves raw data from the INA219, including shunt voltage, bus voltage, and current. It processes this data to calculate meaningful values like current, voltage, and power. This functionality makes the Arduino essential for turning the INA219's raw data into actionable information.

4. **Electrical load:** The 12V 1.2W automotive globe is a small incandescent light bulb commonly used in vehicles for indicator or dashboard lights. In this circuit, it serves as an electrical load to consume the electrical power generated by the DC motor. The globe provides a simple way to measure the performance of the system because the current flowing through it can be monitored, and its brightness can be used as a visual indicator of the power output. Its low power rating makes it suitable for small-scale testing setups like the one you're using with the DC motor and INA219.

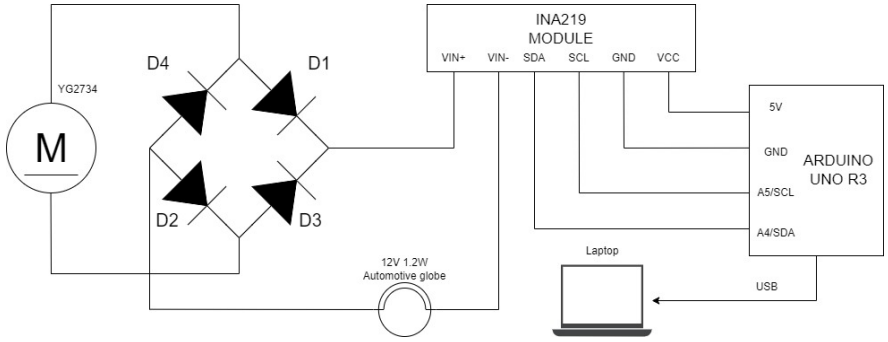

Figure 6.3: *Circuit diagram for the experiment's prototype.*

Circuit for the Integration of the Energy Harvester with Energy Storage: Concept Design

The concept design of a circuit for the integration of the energy harvester with energy storage is shown in Figure 6.4. The battery in this circuit can be substituted with other energy storage devices, such as a supercapacitor.

The circuit is designed to effectively harvest kinetic energy generated by the motion of the wearer using the YG2734 12V DC motor. The harvested energy is then processed through several stages to ensure a stable and usable output suitable for powering devices.

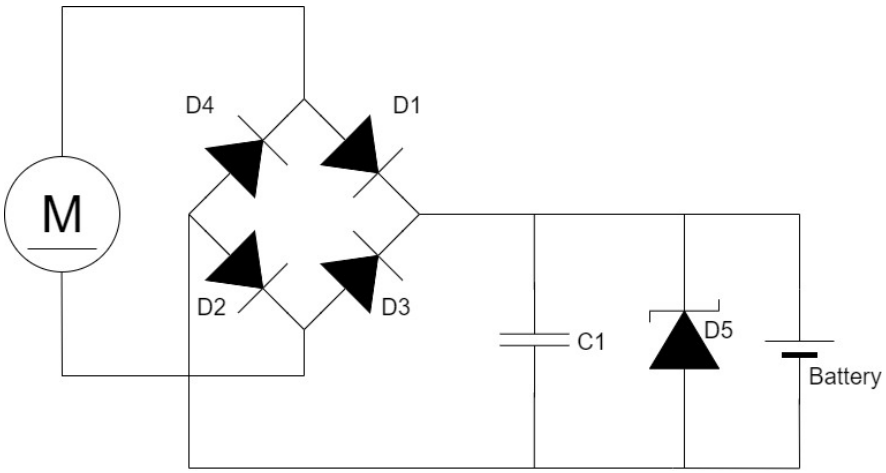

Figure 6.4: *Circuit diagram for DC motor as the energy harvester.*

The circuits consist of the following components

1. **Bridge Rectifier**: it is the same as the one used in the prototype discussed above.

2. **Smoothing Capacitor (C1)**: Capacitor C1 smooths the pulsating DC output from the rectifier by charging during voltage peaks and discharging during troughs, providing a more stable DC output. An 8200μF/25V capacitor is suggested but the actual value should be reconsidered according to the production design. A smoothing capacitor is not included in the prototyping energy harvesting setup to prioritise the analysis of raw, unsmoothed voltage and current outputs, which better reflect the system's dynamic behaviour under varying motions. This omission simplifies the circuit, making it easier to assemble and modify during testing. However, in a production-level design, a smoothing capacitor is essential to stabilise the output voltage, reduce electrical noise, and protect connected electronics, ensuring reliable and robust operation for practical applications.

3. **Voltage Regulation and Safety**: A Zener diode (D5) is incorporated into the circuit to protect it from over-voltage conditions, which may occur if the motor generates excessive voltage during high-speed rotations. The Zener diode clamps the voltage to a safe level, typically around 5V or 12V, depending on the specific Zener diode used. The suggested value for the zenor diode is 15V with a power rate of 2W but the actual value should be reconsidered during the production design stage.

- This ensures that downstream components, such as sensors, are protected from over-voltage damage.
- A voltage regulator can be used after the Zener diode to provide a consistent output voltage, such as 3.3V or 5V, that is suitable for powering low-power devices like sensors or communication modules. The regulator steps down and stabilises the voltage to match the input requirements of these devices.

A Zener diode is not included in the prototyping energy harvesting setup as its primary purpose is to regulate voltage and protect circuits from overvoltage conditions, which is not a critical requirement during testing. The experimental focus is on evaluating the raw performance of the energy harvester without adding components that could influence the voltage output. However, in a production-level design, incorporating a Zener diode would be beneficial to ensure voltage stability and safeguard connected electronics against surges or spikes. This would enhance the reliability and longevity of the system, making it more suitable for real-world applications.

4. **Energy Storage**: The energy harvested by the motor is stored in a supercapacitor or a rechargeable battery, depending on the application's specific needs. The choice between a supercapacitor and a battery depends on the energy storage and delivery requirements:

   - **Supercapacitor**:

     A supercapacitor is an energy storage device that operates by storing electrical energy in an electric double layer at the interface between an electrolyte and electrode material [104] [105]. Unlike conventional capacitors, supercapacitors have significantly higher capacitance, allowing them to store more energy. This is achieved through the use of materials with high surface areas, such as activated carbon, and electrolytes that facilitate efficient charge separation.

     Supercapacitors are well-suited for applications that require rapid charge and discharge cycles. They have a longer operational lifespan and can handle a higher number of charge cycles compared to batteries. Supercapacitors are ideal for short-term energy storage, where quick bursts of energy are needed.

- **Battery**: Batteries provide higher energy density and are more appropriate for storing energy over longer periods. However, they have a more limited number of charge-discharge cycles. In applications where energy needs to be stored for a longer duration, batteries may be the preferred option, although they require more frequent replacement or maintenance.

5. **Load Considerations**: The final stage of the circuit involves powering the load, which may include various sensors or low-power electronic devices. The load is connected across the output of the energy storage component (either a supercapacitor or a battery). The stored energy ensures that the load receives a steady supply of power, even during periods of low or no motion, when the motor is not generating energy.

6.3 Integration with the Lifejacket

To integrate with the lifejacket, the energy harvester should be compact and lightweight enough without compromising the user's mobility or the lifejacket's primary safety function. The positioning of the device must not interfere with the lifejacket's buoyancy and overall performance during emergency scenarios. Before moving into the physical design, it is helpful to create digital models of both the lifejacket and the human body to carefully design the position of the energy harvester. These models will also be used in the energy harvesting calculations in the later stage of the research.

6.3.1 Modelling of the Lifejacket

Before analysing the energy that can be harvested, it is helpful to develop a digital mechanical model of the lifejacket. It will account for key mechanical properties such as elasticity, stiffness, and the deformation characteristics of the material under load. The lifejacket to be modelled is Hutchwilco Easy-Fit Inflatable Lifejacket [3].

The model is developed using advanced computer-aided design (CAD) software, such as Solidworks. The primary purpose of this modelling is to simulate the interaction between the lifejacket, the wearer, and the energy harvesting device during different stages of use, including

deflated and inflated states. Where material properties are not provided by the manufacturer's datasheet, they will need to be measured and input into the modelling software to ensure accuracy.

Two distinct models of the lifejacket are created. The first model represents the lifejacket in its worn but deflated state, where it will be rolled up and lie flat against the wearer's body. The second model simulates the lifejacket in its fully inflated state, which occurs when the lifejacket is activated during an emergency. As shown in Figures 6.5a and 6.5b, the deflated and inflated states exhibit clear asymmetries, especially in terms of volume and distribution. For this research, the inflated state will be focused. Once the lifejacket's chamber is inflated, it becomes fairly firm. However, because it is filled with air, the chamber can still be slightly compressed, which helps absorb impact while providing floatation for the wearer. On the other hand, the straps that secure the lifejacket have minimal stretch. Once tightened, there is minimal motion, even with impact or in water.

In addition, the integration of leg straps (Figure 6.5c) plays a key role in maintaining the lifejacket's position during inflation. These straps provide additional support from the lower body, ensuring that the lifejacket does not ride up or displace, which is vital for both buoyancy to the wear and the effective operation of the energy harvesting mechanism. The volume of the inflated lifejacket is approximately 1.317×10^7 mm^3, a critical parameter for determining the buoyancy force acting on the lifejacket in water.

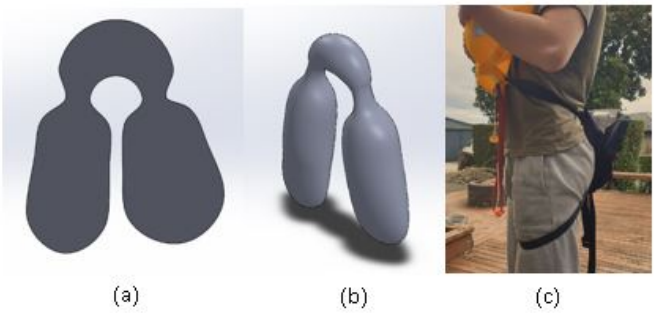

Figure 6.5: *(a) Deflated lifejacket's tube (b) Inflated lifejacket's tube (c) Side view of the leg strap.*

6.3.2 Modelling of the Human Body

The human body model from Chapter 3 is reused for the design purpose in this chapter, below is a brief description of the human body model.

According to the data provided by Drowning Prevention Auckland, an alarming 80.1% of fatal drownings in New Zealand between 2016 and 2020 involved males [106]. This figure highlights the significant gender disparity in drowning fatalities, with males being overwhelmingly more susceptible. In particular, the demographic most at risk comprises male Europeans over the age of 15 who frequently engage in water-based activities, especially in open sea environments.

To gain a deeper understanding of the shape of the human body, researchers have employed advanced 3D scanning technology. Specifically, a 3D scanner known as the EinScan Pro 2X Plus has been utilised to create a highly accurate model of human body geometry [2]. This model is based on an adult male subject, aged 26, who is 1.71 metres tall and weighs 65 kilograms. The data captured from the 3D scan provides a detailed digital representation of the human body. For this research, this data will be used as a reference. Since the energy harvesting device is intended for use by different lifejacket wearers, it is not needed to obtain precise details of the body. A key step in this research is the simplification of the human body geometry to facilitate dynamic modelling. Simplifying the model without losing essential biomechanical properties is needed for the analysis. In this study, a multi-rigid body geometric model is developed, which breaks the human body into 18 rigid segments. These segments include major anatomical parts such as the head, neck, shoulders, upper trunk, mid trunk, lower trunk, thighs, spines, feet, arms, and hands. The segment boundaries and their geometric characteristics are listed in Table 6.1.

To accurately represent the shape of each segment, truncated elliptical cones are used as the geometric basis. This modelling approach simplifies the body parts while maintaining the overall proportions and motion capabilities of the human body. For example, the head is modelled as an ellipsoid, the hands and feet as pyramidal shapes, and the other segments are represented by truncated elliptical cones. An illustration of this simplified human body model is presented in Figure 6.6. Figure 6.7 shows a stick-figure schematic indicating the joints, their types (e.g. ball-and-socket, hinge), and the way the segments are linked. This schematic clarifies how the model captures the kinematic chain and joint constraints relevant to energy harvesting

simulations.

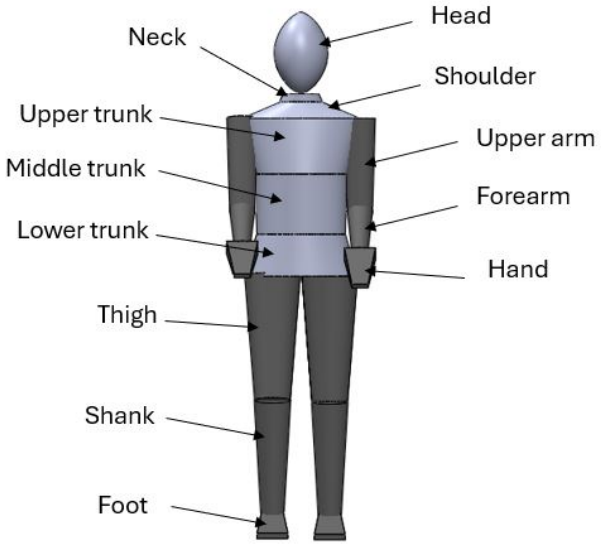

Figure 6.6: *Body segments for motion analysis*

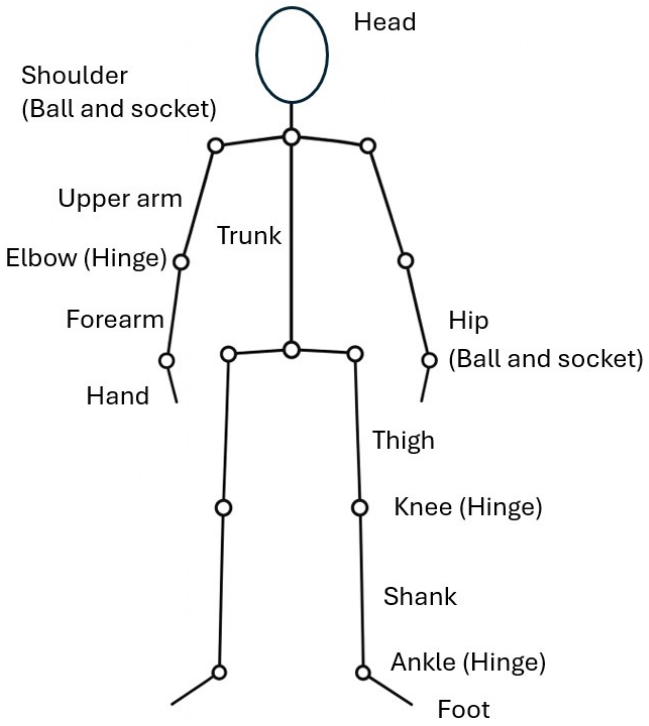

Figure 6.7: *Biomechanical stick-figure model of the human body*

Despite the fact that a real human body is not perfectly symmetrical, the model is designed

with symmetrical geometric parameters to simplify both the modelling and analysis processes. This symmetry ensures that the rigid body model remains computationally manageable while still accurately reflecting the essential characteristics of human motion. The density of each segment is adjusted based on the weight of the participant and data from previous research.

By using a segmented rigid body model, these motions can be simulated and calculate the energy that could be harvested from the wearer's motions in a drowning event.

Segment	Boundary
Head	Top of head to lower margin of mandible
Neck	Inferior border of the mandible to upper margin clavicle
Shoulder	Upper margin clavicle to acromion
Upper trunk	Acromion to chest sword joint
Middle trunk	Chest sword joint to upper umbilicus
Lower trunk	Upper umbilicus to anterior superior spine
Thigh	Anterior superior spine to the knee joint
Shank	Knee joint to lower margin of medial malleolus
Foot	Lower margin of the medial malleolus to sole
Upper arm	Acromion to elbow joint
Forearm	Elbow joint to wrist joint
Hand	Wrist joint to middle fingertip

Table 6.1: *Segment boundaries of the human body*

6.3.3 Positioning of the Energy Harvesting Device

After careful evaluation of multiple factors including the functionality of the lifejacket, energy harvesting efficacy and the safety of the drowning person, the waist strap of the lifejacket has been identified as the most suitable position for integrating the DC motor.The 3D models of a human and a lifejacket provide a detailed visual and spatial representation of the human body and the lifejacket, allowing precise positioning of the energy harvester in relation to key body movements. The models ensure that the integration of the energy harvester does not interfere

with the lifejacket's primary functions, such as buoyancy and wearer comfort. This location is near the hip joint, which plays a pivotal role in generating kinetic energy. The hip joint experiences significant motion, particularly during "ladder climbing" motions as studied in the model capture experiment. By placing the energy harvester close to this source of motion, the design maximises the efficiency of energy conversion. It also avoids interfering with the flotation capabilities of the lifejacket and minimises the risk of damaging the lifejacket's critical flotation components, even during motions such as ladder climbing. Furthermore, both the arms and legs do not come into contact with the waist area during ladder climbing motions, making this location ideal for positioning the motor without compromising the wearer's mobility. Finally, the limbs' motion relative to the waist is more predictable as the trunk's motion is very insignificant.

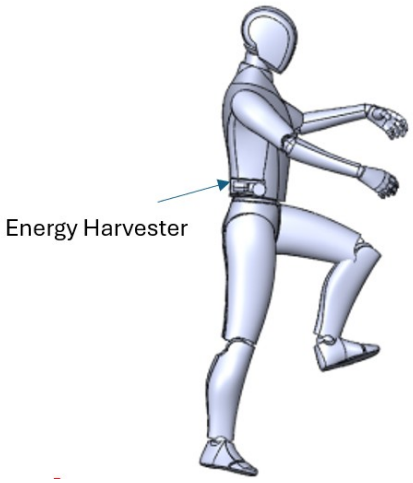

Figure 6.8: *Energy harvester positions at the waist.*

Additionally, the side waist area is less exposed to potential impacts with other objects compared to the front or back of the lifejacket, enhancing the motor's durability in harsh and dynamic conditions. In high-pressure environments such as search and rescue operations, the side waist region remains relatively protected, minimising the risk of damage, preserving the integrity and functionality of the energy harvester over prolonged use. The side waist is also more accessible for maintenance and inspection compared to other parts of the lifejacket, such as the inside of the flotation chamber. Access to the waist area allows for quicker and easier

checks or repairs.

From a design perspective, the side waist area also offers greater scalability. The flexibility of this location allows for the development of energy harvesters in various shapes and sizes, which would otherwise be constrained by the physical dimensions and structural requirements of the flotation chamber. This adaptability is important for future iterations of the energy harvester design, as it enables the development of more powerful or compact designs based on the specific energy demands of the lifejacket or other devices.

6.4 Energy Harvesting Device Mechanism Overview

The design of an energy harvesting mechanism integrated into a lifejacket focuses on motion transmission from the thigh's vertical motion for the YG2734 12V brushed-DC motor for harvesting kinetic energy.

The primary challenge in mechanism design is efficiently transmitting the angular motion of the thigh, specifically at the hip joint into the rotational motion for the DC motor. A telescopic rod has been selected as a link between the thigh and the motor for this purpose as shown in Figure 6.10. It (represented by the red line) maintains a consistent connection as the distance between the motor and thigh changes during the motion cycle, ensuring that the rotational motion transmitted to the motor remains smooth and efficient.

The telescopic design is advantageous in that it accommodates the natural variability in motion distance without slack, ensuring the mechanical connection remains taut throughout the entire motion. The mounting of the energy harvester is another key consideration. In this prototype, the DC motor is securely affixed to a wooden platform, which provides a stable foundation for the motor to operate without introducing additional motion.

As shown in Figure 6.9, the harvester mounting platform is designed in an L-shape. The horizontal section of the platform holds the motor, allowing its shaft to extend outward and connect to the telescopic linkage via a coupling. The vertical section of the platform has two belt loops, allowing it to be securely attached to the lifejacket's waist strap. When worn, the waist strap pulls the platform securely against the wearer's body, holding the motor firmly in

place. This setup ensures that the motor shaft can rotate freely, without causing the platform or motor to move while minimising disruption to the wearer's motions.

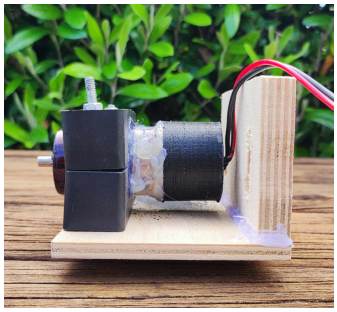

Figure 6.9: *Overview of the energy harvester*

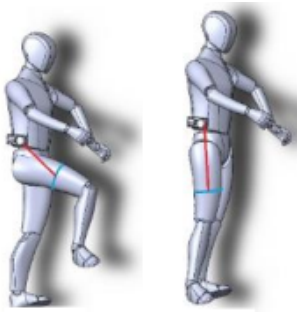

Figure 6.10: *Energy harvester with the telescopic linkage*

To provide further technical detail, the telescopic linkage mechanism is designed with specified materials and dimensions to ensure reliable motion transmission and minimal restriction to the wearer. The outer aluminium tube has an outer diameter of 12 mm, an inner diameter of 10.5 mm, and an approximate length of 400 mm. The inner wooden rod has a diameter of 10 mm and a length of 200 mm. A rigid coupling interface connects the linkage to the energy harvester's 5 mm shaft using a matching 5 mm hole with a key slot for secure engagement. These design parameters are summarised in Table 6.2, and the overall schematic kinematic diagram is shown in Figure 6.11.

Table 6.2: *Telescopic linkage design parameters*

Component	Material	Dimensions
Outer tube	Aluminium	Ø12 mm (OD), Ø10.5 mm (ID), 400 mm length
Inner rod	Wood	Ø10 mm, 200 mm length
Motor shaft	Steel	Ø5 mm with key slot
Coupling	Aluminium	5 mm hole with matching key slot

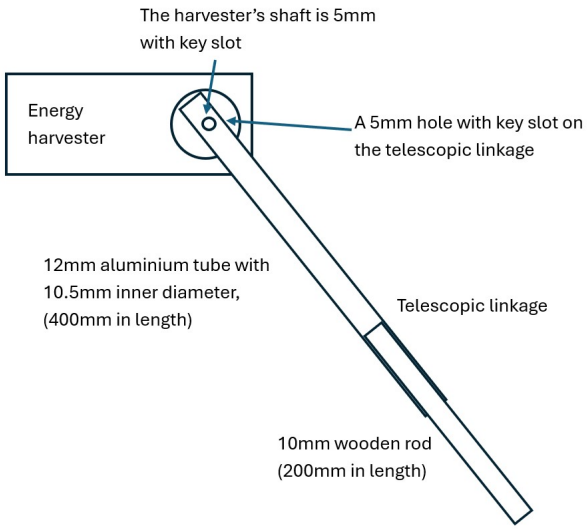

Figure 6.11: *Schematic kinematic diagram of the telescopic linkage and energy harvester mechanism.*

This design also guarantees the robustness of the mechanism. During a rescue, the lifejacket and its integrated components are subjected to significant physical stress. This includes being pulled, bumped, or dragged as the wearer is rescued. As such, the linkage and motor must be securely attached to the lifejacket and constructed from materials capable of withstanding such stresses without failure. Another feature that should be considered but not implemented in this prototype is an emergency release feature. If the mechanism is causing any safety issues during the drowning event, this feature would allow the wearer to detach the harvester easily.

Efficiency is another essential design consideration. The telescopic linkage is designed to be both lightweight and low-friction, allowing it to capture the thigh's vertical motion without placing excessive load or resistance on the wearer's motions which could hinder their ability to move. The high gear ratio of the YG2734 12V DC motor allows the system to generate

sufficient electrical power from relatively slow and low-speed motions of the thigh.

Simplicity in the design is also key to both its functionality and cost-effectiveness. It minimises the number of moving parts, reducing the likelihood of mechanical failure and simplifying assembly and disassembly for maintenance. Especially for this prototype, the readily available components such as the YG2734 DC motor and the telescopic linkage further reduce costs and ensure easy replacements or repairs.

In conclusion, the telescopic linkage and DC motor provide a reliable method for capturing kinetic energy from the thigh's vertical motions while maintaining the lifejacket's core functionality. The simplicity and cost-effectiveness of the design, combined with its robust construction and compatibility with drowning motions, make it an ideal solution, especially during the prototyping stage of a design process.

6.5 Other Design Considerations

6.5.1 Waterproofing of the Energy Harvesting Device

The waterproofing of the energy harvesting device is an important part of its design, particularly since it is intended for use in shallow water due to the buoyant nature of the lifejacket. The International Protection (IP) rating system is widely recognised as the standard for classifying the level of protection provided by a device's enclosure against solids (such as dust) and liquids (such as water). An IP rating consists of two digits: the first represents protection against solid objects, while the second indicates the device's resistance to water ingress.

In the case of this energy harvesting device, it is intended to operate in shallow water due to the buoyant nature of the lifejacket. For this purpose, an IP rating of IP67 is deemed appropriate. An IP67 rating ensures that the device is completely protected against dust ingress and can be submerged in water up to a depth of 1 metre for 30 minutes without sustaining damage. This level of protection is suitable for the conditions that the lifejacket and energy harvesting device will encounter in a typical rescue operation. The rating provides peace of mind that the system will remain operational in the unpredictable and sometimes harsh conditions faced during rescue missions.

For Electronics

Several techniques can be used to waterproof the electronics within the energy harvesting device, each offering varying degrees of protection and complexity. One of the most commonly used methods is conformal coating [107], which involves applying a thin layer of protective material, such as silicone, acrylic, or polyurethane, directly onto the electronic components. Another effective waterproofing technique is "potting" [108], where the entire electronic assembly is encased in a solid or gel-like compound, such as epoxy or silicone.

By using an IP67 electronics enclosure plus the waterproof technique mentioned, the electronics components can be safely waterproofed.

For components such as connectors, switches, or cables, waterproof connectors or sealing with silicone gel can be used to prevent water ingress.

For the YG2732 DC Motor

The YG2732 DC motor, chosen for the energy harvesting device, is not inherently waterproof, making additional protective measures necessary. A practical solution is to encase the motor within a plastic tube-shaped enclosure, which acts as a protective shell to shield the motor from direct contact with water. The challenge, however, lies in waterproofing the motor's rotating shaft, which must remain exposed for the motor to function effectively.

To address this challenge, a waterproof bearing is incorporated into the design. It ensures that the motor shaft can rotate freely while preventing water from entering the motor housing. Silicone is applied around the bearing to further enhance the seal, making the motor assembly both functional and watertight.

6.5.2 Electromagnetic Interference (EMI) Considerations

EMI refers to the unwanted disturbances caused by electromagnetic fields, which can negatively impact the performance of nearby electronics. In the context of an energy harvesting system, the rotating DC motor may generate EMI that can interfere with the operation of sensors, communication devices (such as Bluetooth Low Energy (BLE), LoRa, or GPS modules), and even the motor's own control circuitry. If not properly managed, these disturbances can lead to significant operational issues. This section will focus on identifying the key sources of EMI and

present design strategies to mitigate these effects.

There are several primary sources of EMI within DC motor including the emission of broadband electromagnetic noise from the contact between the brushes and the commutator and magnetic field constantly changes and unwanted electromagnetic waves induced by the changing magnetic fields in the motor.

They can be reduced or eliminated by surrounding the motor and sensitive components with shielded enclosures, such as a Faraday cage [109], electromagnetic emissions can be contained and providing proper grounding is essential for controlling EMI, as it provides a path for unwanted electromagnetic energy to dissipate safely. The Faraday cage blocks external electric fields and electromagnetic waves. It is made of a conductive material, such as metal, which distributes electric charges across its surface when exposed to an external field. This creates a shielding effect, preventing the electric field from penetrating the interior of the cage. The cage stops electromagnetic waves by reflecting and absorbing the electromagnetic energy.

In addition, capacitive or inductive filters can be used to filter high-frequency noise, and snubber circuits consisting of resistor-capacitor (RC) networks, can be used to suppress voltage spikes caused by brush commutation in brushed DC motors.

Another measure to be taken is to keep a safe distance between electronic modules (e.g. wireless transmission electronics) from a DC motor to achieve a safe electric field strength.

It can be decided by following the steps described below:

Determine the Radiated Power (Pr)

The motor selected for energy harvesting has a maximum power output of 4.726 Watts. The radiated power (P_{ERP}) is usually much lower than the motor's power and is assumed to be 1 mW.

Calculate the Electric Field Strength

For a point source radiating power uniformly, the power density S (in watts per square meter) at a distance d is proportional to:

$$S = \frac{P_{ERP}}{4\pi d^2}$$

where

- P_{ERP} is the effective radiated power (in watts, W),
- d is the distance from the source (in meters, m).

The electric field strength E_{field} relates to the power density S by the formula:

$$S = \frac{{E_{field}}^2}{\eta_0}$$

where η_0 is the intrinsic impedance of free space (approximately 377 ohms).

By combing the two equations above, the electric field strength E_{field} at a distance d from a point source can be approximated using the formula:

$$E_{field} = \sqrt{\frac{29.44 \cdot P_{ERP}}{d^2}}$$

Rearrange to solve for d:

$$d = \sqrt{\frac{29.44 \cdot P_{ERP}}{E_{field}}}$$

From the above equations, the safe distance is estimated to be

$$d = 0.099 \text{ m or } 9.9 \text{ cm}$$

It means that the wireless transmission electronics would need to be approximately 10 cm away from the energy harvester to achieve an electric field strength of 3 V/m.

6.6 Conclusion

This chapter discusses the design of an energy harvesting mechanism for lifejackets. The focus is on utilising the vertical motion of the thigh to generate energy, with the electromagnetic energy harvester (YG2734 12V DC motor), emerging as the preferred solution due to its compact size, high energy potential, and robustness.

Key design considerations include ensuring the harvester's small size and lightweight to avoid impacting the lifejacket's functionality and the wearer's mobility. The harvester's ability to generate power from the consistent and substantial motions of the thigh is highlighted as a major advantage. The thigh's vertical motion is identified as the most suitable source of kinetic energy, given its regularity, substantial mass, and higher moment of inertia compared to other body parts.

The electromagnetic energy harvester's compact design allows it to be integrated into a lifejacket without adding significant weight or bulk. This compactness, coupled with the simplicity of construction makes it suitable for applications where space and weight are limited. The harvester's scalability is also emphasised, as the design can be adjusted by increasing the number of coils or using larger magnets if more power is required.

The robustness of the electromagnetic energy harvester is another factor, as it is capable of withstanding the harsh environments typically encountered during search and rescue operations in water. Its design is able to function effectively in conditions involving salt water, varying temperatures, and physical impacts. This robustness ensures the long-term reliability and functionality of the harvester in real-world scenarios.

Minimal maintenance requirements are highlighted as an essential factor for the integration of the harvester into lifejackets, which are often stored for extended periods between uses. The harvester does not require regular servicing or replacement parts, making it a practical solution for lifejackets. The secure wearability of lifejackets ensures that the harvester remains in place during a drowning event, providing a stable fixed point for energy harvesting.

Challenges such as waterproofing, protecting the harvester from saltwater exposure, and maintaining its functionality in extreme conditions are acknowledged. These challenges must be addressed in the design and production phases to ensure the harvester's success in real-world applications.

Electromagnetic interference (EMI) considerations are also important. The rotating DC motor can generate EMI that might interfere with the operation of sensors and communication devices. Mitigation techniques such as physical shielding, proper grounding, filtering, and the use of snubber circuits are discussed to manage and reduce EMI, ensuring the reliability and

efficiency of the system.

Chapter 7

Energy Harvesting Mechanism Design - Modelling, Calculations, and Simulations

This chapter focuses on the modelling of the energy harvesting mechanism, with a focus on the relation between kinetic energy associated with the vertical motion of the thigh joint and the electric energy harvested through a brushed DC motor, followed by the calculations and simulations based on the models established.

7.1 Models for Energy Harvesting

The first step to model the energy harvesting system is to establish the relationship between the motion of the hip joint during ladder climbing and the angular velocity of the energy harvester (a brushed DC motor). Given that the design assumes identical motion for both the left and right hips, the calculations will focus on one side only, which simplifies the process while preserving accuracy. The primary task is to translate the vertical angular velocity of the hip joint into the angular velocity of the DC motor. This requires understanding the mechanical linkage between the hip joint and the motor, specifically how the motion at the hip is converted into rotational energy that can be harnessed by the motor.

In an ideal scenario, the energy harvester would be positioned directly at the hip joint, where the vertical angular velocity of the hip would match the angular velocity of the motor, as illustrated in Figure 7.1. However, as discussed in the previous chapter, the current design of the lifejacket does not allow such positioning. Instead, the energy harvester is situated slightly above the ideal location, at the waist strap of the lifejacket. This offset results in a reduction in both the angular displacement and the angular velocity experienced by the motor compared to the hip joint. Therefore, the first step in the calculations is to quantify this reduction by considering the distances involved specifically, the distance between the hip joint and the thigh strap, as well as the distance between the ideal (hip joint) and actual positions of the energy harvester.

The relationship between the angular velocity at the hip and the angular velocity of the DC motor can be derived by analysing the geometry of the setup. The reduction factor, determined by the relative positioning of the components, will be applied to the angular velocity of the hip to calculate the effective angular velocity of the motor. This angular velocity is the key factor as it directly influences the voltage generated by the motor, which will be further explored in calculations.

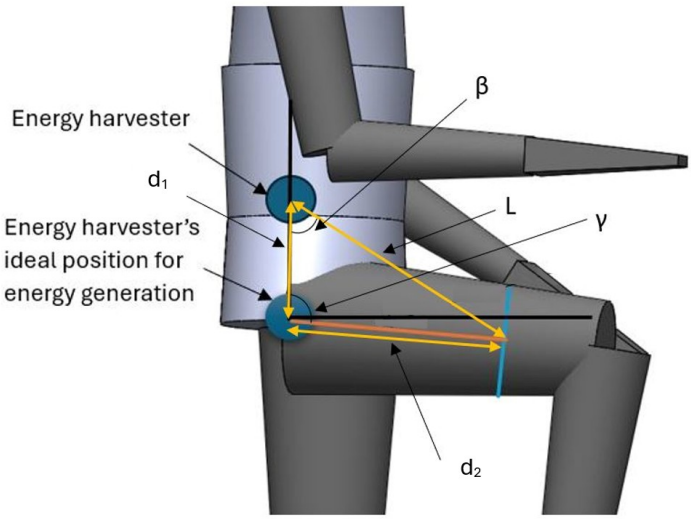

Figure 7.1: *Energy harvester position and angular velocity calculation.*

As illustrated in Figure 7.1, d_1 and Figure 7.2 represents the distance between the hip joint and the energy harvester, while d_2 denotes the distance between the hip joint and the thigh strap.

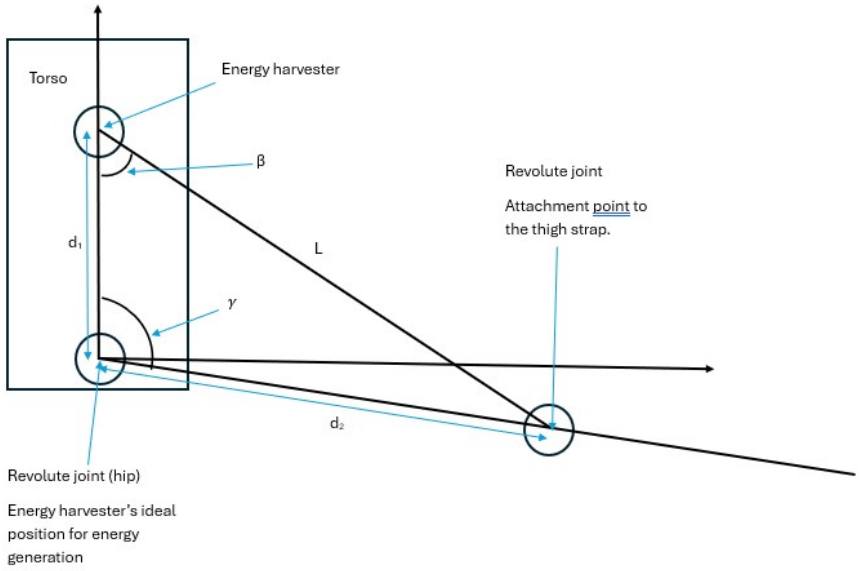

Figure 7.2: *Schematic kinematic diagram of the energy harvesting linkage system*

The length of the telescopic linkage is indicated by L. By considering a triangle with sides d_1, d_2, and L, and the corresponding opposite angles α, β, and γ, we can analyse the relationship between these angles and their angular velocities as the length of side L varies, with d_1 and d_2 remaining constant.

7.1.1 Angular Velocity of the Energy Harvester

The Law of Cosines provides the relationship between the sides and angles of the triangle. Appendix F shows the detailed steps to determine the angular ratio. The summaries are outlined:

Angular velocity of β

Given:

$$\beta = \arccos\left(\frac{d_1^2 + L^2 - d_2^2}{2 \cdot d_1 \cdot L}\right) \tag{7.1}$$

So:

$$\frac{d\beta}{dL} = -\frac{1}{\sqrt{1 - u_\beta^2}} \cdot \frac{d_1^2 + d_2^2 - L^2}{2 \cdot d_1 \cdot L} \tag{7.2}$$

Angular velocity of γ

Given:

$$\gamma = \arccos\left(\frac{d_1^2 + d_2^2 - L^2}{2 \cdot d_1 \cdot d_2}\right) \tag{7.3}$$

So:

$$\frac{d\gamma}{dL} = \frac{L}{d_1 \cdot d_2 \cdot \sqrt{1 - u_\gamma^2}} \tag{7.4}$$

7.1.2 Angular Transmission Ratio between the Hip joint and the Energy Harvester

The ratio of the angular velocities ω_β and ω_γ is:

$$\frac{\omega_\beta}{\omega_\gamma} = \frac{\frac{d\beta}{dL}}{\frac{d\gamma}{dL}} \tag{7.5}$$

Substitute the expressions:

$$\frac{\omega_\beta}{\omega_\gamma} = \frac{-\frac{1}{\sqrt{1-u_\beta^2}} \cdot \frac{d_1^2+d_2^2-L^2}{2 \cdot d_1 \cdot L}}{\frac{L}{d_1 \cdot d_2 \cdot \sqrt{1-u_\gamma^2}}} \tag{7.6}$$

Simplify:

$$\frac{\omega_\beta}{\omega_\gamma} = \frac{d_2 \cdot (d_1^2 + d_2^2 - L^2)}{2 \cdot d_1 \cdot L^2} \cdot \frac{\sqrt{1 - u_\gamma^2}}{\sqrt{1 - u_\beta^2}} \tag{7.7}$$

In this study, the lengths of d_1 and d_2 are held constant, while ω_γ and γ are recorded during the motion capture experiment. Based on these recorded values, ω_β can be derived by rearranging the corresponding equations.

7.1.3 Voltage Measurement using Current Sensing Integrated Circuit

The current sensing integrated circuit can be used to measure voltages and currents in a circuit accurately. When connected correctly, it can measure the bus voltage, shunt voltage, and load voltage. These measurements are essential for analysing the performance of an electrical system, such as the generator circuit used in this study.

Bus Voltage

The bus voltage is the voltage measured at the node where the load and other components

connect. It represents the effective voltage supplied to the load and can be calculated using:

$$V_{\text{bus}} = V_{\text{g}} - I \cdot (R_i + R_{\text{shunt}}) \tag{7.8}$$

where:

- V_{g} is the voltage generated by the generator),
- I is the current flowing through the circuit,
- R_i is the internal resistance of the generator,
- R_{shunt} is the resistance of the shunt resistor.

Shunt Voltage

The shunt voltage is the voltage drop across the shunt resistor. It is directly proportional to the current flowing through the resistor and is given by:

$$V_{\text{shunt}} = I \cdot R_{\text{shunt}} \tag{7.9}$$

This voltage is critical for determining the current in the circuit, as the integrated circuit uses it to calculate the current.

Load Voltage

The load voltage is the voltage across the load in the circuit. It represents the actual voltage available to the load and is calculated using:

$$V_{\text{load}} = I \cdot R_{\text{load}} \tag{7.10}$$

where R_{load} is the resistance of the load. The load voltage depends on the current and the load resistance.

Current Measurement

The current flowing through the circuit is measured using the shunt voltage and the resistance of the shunt resistor. It is calculated as:

$$I = \frac{V_{\text{shunt}}}{R_{\text{shunt}}} \tag{7.11}$$

This value represents the current drawn by the load and other components in the circuit.

Power Measurement

The power consumed by the load can be calculated using the current and the load voltage:

$$P_{\text{load}} = V_{\text{load}} \cdot I \tag{7.12}$$

7.1.4 Power/Energy Generated

With the angular velocity of the energy harvester determined, the next step is to calculate its outputs, which include both the voltage and the power generated by the energy harvester.

As illustrated in Figure 7.1, the hip angle γ is defined as the angle of the thigh from the vertical y-axis at the hip joint. The angular velocity of the hip joint is denoted by ω_γ, the input angular velocity of at the energy harvester before the gearhead is ω_β, and the gearhead has a ratio of μ. If the energy harvester is positioned above the hip joint, the angular displacement of the energy harvester will be reduced compared to the angle at the hip. With the angular velocity of the hip joint calculated previously, the angular velocity of the energy harvester shaft is given by $\omega_{\beta_g} = \mu\omega_\beta$.

During the ladder climbing motion, assuming that the voltage drop across the amateur resistance (7.06Ω) is ignored, the energy harvester produces a voltage V_g according to the following equation:

$$V_g = K_g\omega_{\beta_g} \tag{7.13}$$

where K_g represents the back electromotive-force constant of the motor and ω_{β_g} is the angular velocity of the motor shaft driven by the telescopic linkage as shown in Figure 7.3. The electrical power, denoted by P_g, can be calculated using the formula:

$$P_g = \frac{{V_g}^2}{R_i + R_o} = \frac{{K_g}^2{\omega_{\beta_g}}^2}{R_i + R_o} = C_g{\omega_{\beta_g}}^2 = C_e{\omega_\beta}^2$$

In this equation, R_o represents the external resistive load, R_i is the internal resistance of the energy harvester, C_g is the electromagnetic damping coefficient of the energy harvester, and C_e is the electrical damping coefficient of the entire energy harvesting system. The electrical damping coefficient C_e is derived from the above equations as follows:

$$C_e = C_g\mu^2 = \frac{{K_g}^2\mu^2}{R_i + R_o} \tag{7.14}$$

This expanded calculation provides a more comprehensive understanding of how the energy harvester's output is influenced by both the angular velocity of the hip joint and the gearhead ratio.

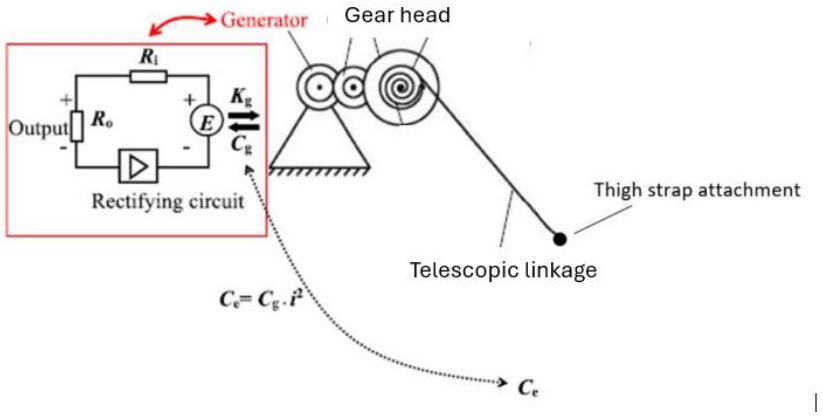

Figure 7.3: *Transmission diagram of the energy harvesting system*

Figure 7.3 presents the transmission diagram of the harvesting system, highlighting the relevant parameters. The output power, denoted by P_{out}, represents the energy dissipation across the external resistive load R_o and is calculated as follows:

$$P_{\text{out}} = \frac{{K_g}^2\mu^2{\omega_\beta}^2 R_o}{(R_i + R_o)^2} \tag{7.15}$$

To obtain a more accurate understanding of the power output, the scenario where the internal resistance (R_i) equals the external load resistance (R_o) is considered. Under this condition, the maximum electrical power output can be calculated using the following equation:

$$P_{max} = \frac{{K_g}^2\mu^2\omega_\beta^2}{4R_i}$$

This equation takes into account the motor's characteristics and the relationship between the angular velocity and the generated voltage.

The output power generated by each half of the energy harvesting system is mainly dependent on both the angular velocity of the hip joint and the external load resistance applied to the system. Consequently, any change in the external load resistance will directly influence the output power and the damping coefficient of the system. The output power reaches its maximum value, given by $\frac{{K_g}^2 \mu^2 \omega_\beta^2}{4R_i}$, when the internal resistance R_i equals the external load resistance R_o. As derived from Equation 7.14, the electrical damping coefficient for the energy harvesting mechanism (C_e) is determined by the external resistive load R_o relative to the energy harvester's characteristics. This underscores the importance of optimising the external load resistance to achieve maximum efficiency within the energy harvesting system. By precisely adjusting the external load resistance, the system can be fine-tuned to operate at its optimal efficiency, thereby maximising the electrical power output generated during the hip joint's motion.

7.2 Calculations

Using the formula presented and based on the angular velocities calculated from the thigh joint data, the spreadsheet allows for the estimation of the voltage generated under different conditions. Assuming the maximum efficiency of the motor (69.7%), only the theoretical maximum voltage is calculated without considering the energy lost in the process.

The motion data used for the above equations are obtained from the motion capture experiments mentioned, where the "ladder climbing" motion is recorded. This data provides the necessary information to calculate the angular velocity of the hip joint, which serves as the initial input for determining the angular velocity of the DC motor. To enhance the accuracy of the calculations related to the energy harvester output, the rolling average method is employed to

By entering the equations into a spreadsheet and setting $d1$ = 0.25 m and $d2$ = 0.3 m, the ratio between the hip joint angular velocity and the energy harvester angular velocity can be determined. The calculated ratio reaches a maximum value of -0.2195501 and a minimum value

of -0.44263, with an average value of -0.32368. These figures indicate that the energy harvester's angular velocity is, at best, 44.26% of the hip joint's angular velocity, with the greatest reduction in velocity occurring when the thigh is nearly fully extended. This reduction is most noticeable at the highest point of the motion. Table B.1 in Appendix B presents an example of the spreadsheet calculations and also shows the calculated length of the telescopic linkage. This length is a key factor for optimising the linkage design to ensure efficient energy harvesting. In Figure 7.4, the two angular velocities are plotted using data collected through computer vision, with the blue line representing the thigh's vertical angular velocity and the orange line depicting the energy harvester's angular velocity. It is evident that the energy harvester's angular velocity remains consistently lower throughout the motion cycle. This spreadsheet can also be used as a calculator for future setups with different $d1$ and $d2$ values, depending on the lifejacket design and the placement of the energy harvester.

The same calculations are repeated using data from the motion capture lab experiment, providing a comparison with the results from the computer vision method. A sample spreadsheet used for the motion capture lab calculations is provided in Table C.1 in Appendix C. Figure 7.5 compares the angular velocities of the thigh and the energy harvester, with the thigh's vertical angular velocity represented by the blue line and the energy harvester's angular velocity shown by the orange line. As expected, the energy harvester's angular velocity is significantly lower than the thigh's angular velocity, reflecting the reduction caused by the mechanical linkage and positioning between the thigh and the harvester. The results from the motion capture lab are more consistent and reliable, clearly displaying the cyclical nature of the motion and making it easier to identify patterns. The ratio between the energy harvester's angular velocity and the thigh's vertical angular velocity in the motion capture data shows a maximum value of -0.18591, a minimum value of -0.48517, and an average value of -0.37707. These values illustrate the substantial reduction in angular velocity from the thigh to the energy harvester.

Although the energy harvester's angular velocity is lower than that of the hip joint, this does not pose a major issue for energy harvesting, as the DC motor's gearhead can compensate for the reduced velocity. The key concern is whether the torque required to drive the DC motor remains within acceptable limits, ensuring that it does not impose excessive load on the participant's

thigh motion. With the angular velocity now established, the next stage involves calculating the energy harvester's power output based on this velocity, which will allow for a more thorough evaluation of the system's performance.

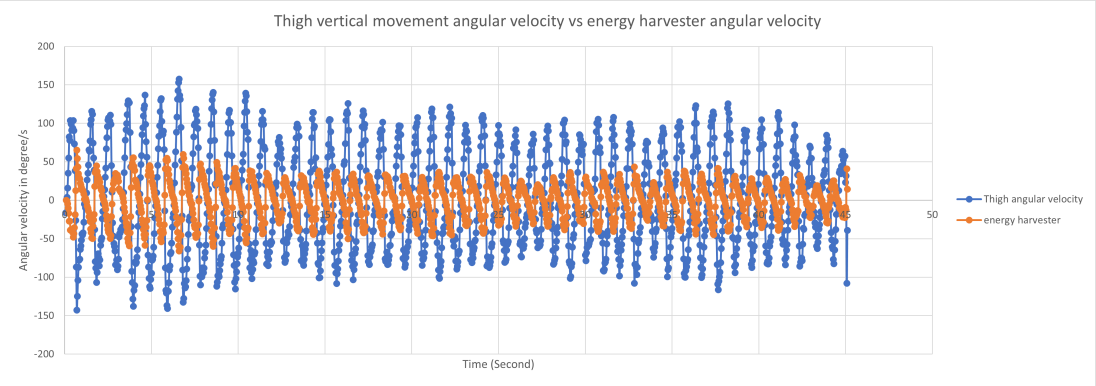

Figure 7.4: *Energy harvester angular velocity vs hip joint angular velocity - computer vision.*

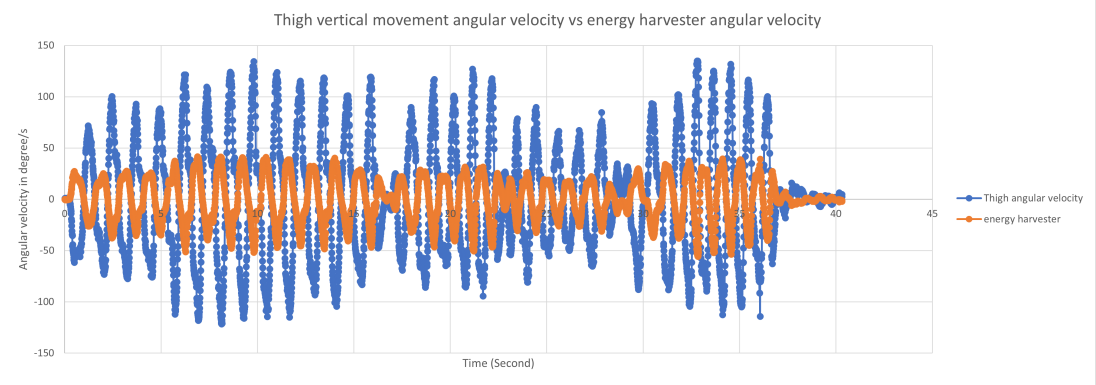

Figure 7.5: *Energy harvester angular velocity vs hip joint angular velocity - motion capture lab.*

The YG2734 brushed DC motor has an electromotive force (E.M.F) constant of 87.921 mV/rad/sec. Additionally, this motor is equipped with a gearhead that provides a reduction ratio of 1:244. Taking this gearhead ratio into account, the angular velocity at the output of the gearhead, ω_{β_g}, can be determined by multiplying the input angular velocity ω_γ by the gear ratio μ, which is 244. With the computed value of ω_{β_g}, the voltage generated by the DC motor, V_g, can be calculated using the equation: Equation 7.13

The results of these calculations, derived from both the computer vision data and the motion capture lab data, are presented in Figures 7.6 and 7.7, respectively. These results are needed for evaluating the efficiency of the energy harvesting mechanism under varying operating

conditions.

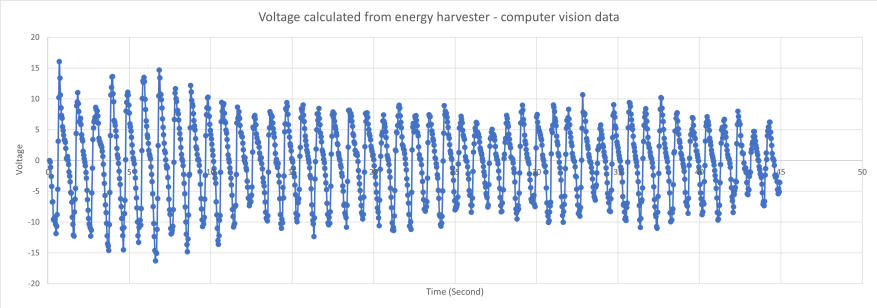

Figure 7.6: *Voltage generated from energy harvester - Computer vision*

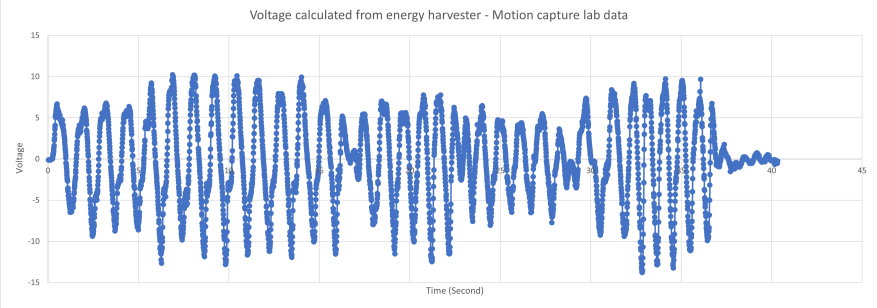

Figure 7.7: *Voltage generated from energy harvester - Motion capture lab*

As expected, the voltage calculated from the computer vision data is higher than the voltage derived from the motion capture lab data. The maximum voltage generated from the computer vision data reaches 16V, with an average peak of approximately 9V. On the other hand, the maximum voltage generated from the motion capture lab data is slightly above 13V, with an average peak of around 8V. This difference can be attributed to the faster angular velocities and the larger range of motion observed in the computer vision data, which directly contribute to the higher potential voltage output. It is important to note that these calculated voltages are theoretical maximum and do not represent the actual power or energy output of the system. This is because the calculations are performed without considering the motor's efficiency and any load in the circuit, these are major factors in real-world applications. Thus, while these voltages indicate the system's potential, they do not offer a comprehensive assessment of its performance under operational conditions.

It is important to clarify that these calculations are based on an idealised scenario, not

accounting for efficiency losses, damping effects, or other real-world factors that can reduce the actual power output. Consequently, the calculated power represents an upper boundary, and the real-world power output is expected to be lower. These calculations are valuable as they establish a benchmark for the system's potential and provide insights for further design refinements. By understanding these theoretical limits, areas for improvement can be identified, and the system's performance under practical conditions can be better predicted.

Figures 7.8 and 7.9 show the maximum power calculated from both motion capture methods. The maximum power derived from the computer vision data reaches 14W, with an average peak of approximately 5W. The maximum power generated from the motion capture lab data is just over 10W, with an average peak of around 3W. As expected, the computer vision data yields a higher potential maximum power output, mainly due to the faster angular velocity captured by this method. The power calculated is using the maximum efficiency value (65.9%) according to the specification sheet; This efficiency will be reduced when the DC motor is used as an energy harvester with different angular velocities. It is also worth noting that the relationship between power generation and angular velocity, as described by the equation, is nonlinear. As angular velocity increases, power generation experiences a significant boost, highlighting the need to optimise the relationship between the hip joint and the DC motor's angular velocity in order to maximise energy harvesting.

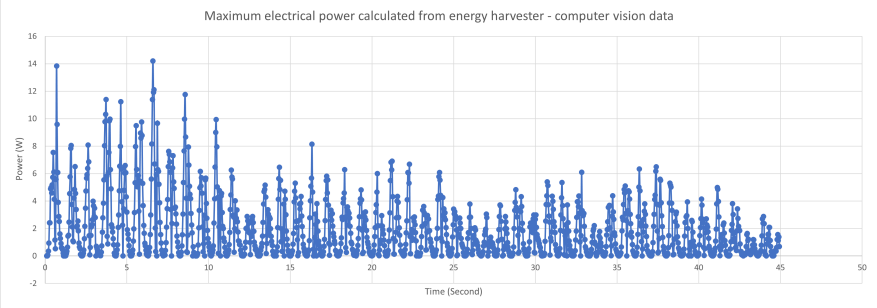

Figure 7.8: *Maximum power calculated from energy harvester - Computer vision*

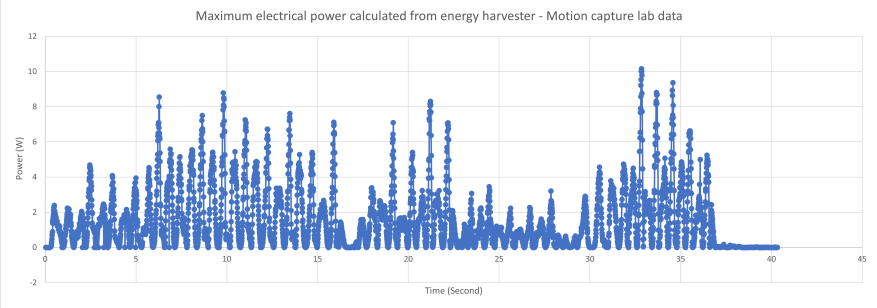

Figure 7.9: *Maximum power calculated from energy harvester - Motion capture*

7.3 Simulations with MATLAB

Following the completion of calculations using Excel spreadsheets, the next step involves leveraging the MATLAB package [110]for comprehensive simulations of the models (including calculations) in different conditions and creating detailed 3D visualisation of the system in operation. This simulation will provide a visual representation of the energy harvester's performance based on the input motion data, offering deeper insights into how the system behaves under various conditions. Such a visualisation is helpful for understanding the dynamics of the system and for validating the model against real-world scenarios. This simulation also calculates the generator's electrical output from measured or assumed thigh angular displacement profiles, allowing evaluation of performance under different movement conditions.

Three methods for inputting motion data into the Simulink model in MATLAB are designed, each suited to different levels of data availability and simulation goals.

The first method imports the x, y, z coordinates of the hip and knee joints, allowing angular displacement and angular velocities to be calculated within Simulink. However, this requires the motion data and the 3D human model to share the same global axis orientation, and misalignment can complicate the process.

The second method inputs the hip joint angular displacement directly, calculated externally and imported into the simulation. This simplifies the setup by avoiding global axis alignment while still providing accurate joint motion data.

The third method directly imports the angular velocity of the energy harvester. This is the simplest approach, as it skips coordinate and joint angle calculations, but does not support 3D

body motion visualisation. It's useful when the focus is on mechanical performance rather than full-body motion.

A human body model, designed in SolidWorks, is recreated in Simulink to simulate body interactions with the energy harvester. Components such as "World Frame," "Mechanism Configuration," and joints like revolute and gimbal joints are used to simulate body part motions. This setup allows for detailed analysis of joint motions, including the hip's vertical angular velocity, which drives the energy harvester simulation.

The energy harvester is modelled as a "DC Machine" converting the body's mechanical motion into electrical energy. The hip's vertical angular velocity feeds into the energy harvester model, processed through Simulink blocks like "Signal Builder" and "Gain" to simulate the motor's behaviour. Mechanical and electrical parameters are set to reflect the real-world performance of the harvester, and output metrics like voltage and power are measured to assess efficiency.

7.3.1 Simulation with the Data from the Motion Capture in the Water

In this section, the data collected from the two different motion capture methods are utilised to run simulations in MATLAB, beginning with the data obtained through the computer vision method. Since the angular velocity is already calculated during the calculation phase of the research, the second data input method is applied. This method involves directly inputting the hip joint angle data into the LHz input of the body module within the Simulink model, bypassing the need for additional coordinate calculations.

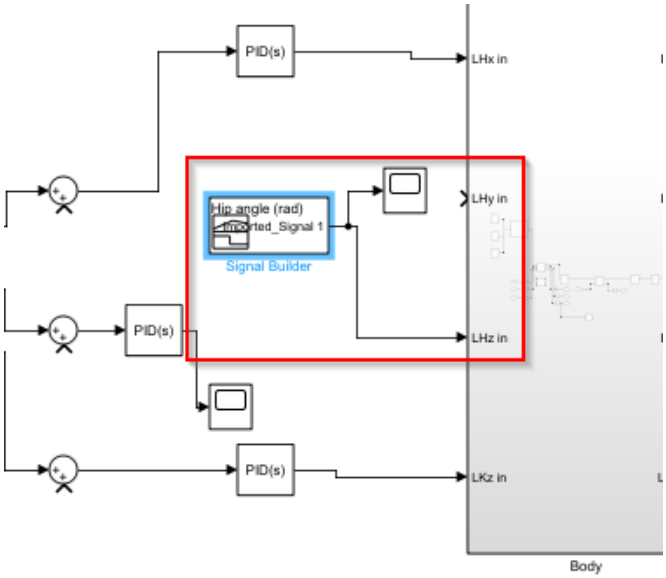

Figure 7.10: *Computer vision hip angle input in MATLAB for calculation and simulation*

To implement this method effectively, the *Signal Builder* block in MATLAB is utilised to import the hip joint angle data over time. This block provides a convenient way to load and manage time-series data. This imported data is then linked directly to the *LHz* input of the body module, as illustrated in Figure 7.10. Once the hip joint angle data is successfully inputted, another *Signal Builder* block is employed to import the angular velocity ratio, which is previously calculated during earlier stages of the research. The complete model is provided in Appendix G.

This angular velocity ratio adjusts the *LHzout* signal from the body module to match the rotation of the energy harvester device. It reflects the relationship between the hip joint's motion and the angular velocity of the energy harvester. As shown in Figure 7.11, the product of the *LHzout* signal and the angular velocity ratio is calculated and passed through a *Product* block. The output of the *Product* block is then routed through a *Gain* block, which is set to a value of 244. This value represents the gear ratio of the DC motor's gearhead. The gear ratio directly influences the torque and speed characteristics of the motor, impacting the overall efficiency of the energy harvesting mechanism. Furthermore, the parameters for the *DC Machine* block which represents the YG2734 motor used in this research have already been configured according to the motor's specific technical specifications. These parameters including armature resistance,

inductance, and back-emf constant ensure the motor's electrical and mechanical characteristics are accurately reflected in the simulation environment.

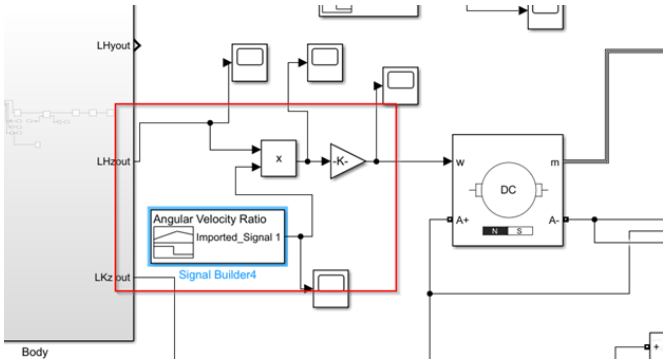

Figure 7.11: *Computer vision angular velocity ratio input in MATLAB for calculation and simulation*

With all the necessary inputs and parameters configured, the final step is to adjust the duration of the simulation so that it corresponds to the time span of the motion data. For this research, the simulation will be set to run for a total of 30 seconds, which mirrors the length of the recorded motion capture data used during the experimental phase. Once the appropriate simulation time is set, the next step involves clicking the *Run* button to initiate the simulation within MATLAB. This action starts the simulation process and applies the previously configured inputs, parameters, and mathematical models.

The time it takes to complete the simulation largely depends on the processing power of the computer being used. Once the simulation has successfully finished running, the results can be accessed and examined using the *Scope* blocks. These blocks are for analysing key outputs such as voltage, current, power, and other performance metrics from the DC machine. The scope tools allow for a detailed analysis of the energy harvesting mechanism's behaviour and efficiency within the simulation environment.

Results using Computer Vision Data

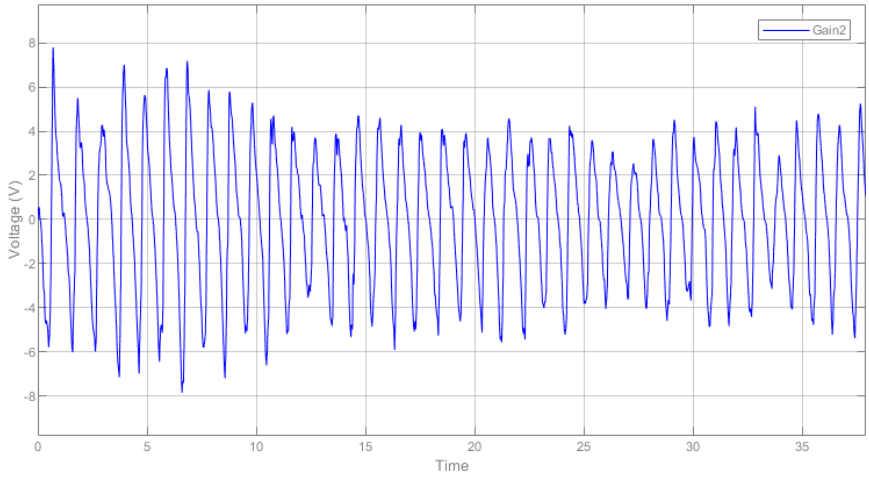

Figure 7.12: *Voltage output from MATLAB calculation using computer vision data.*

Figure 7.12 illustrates the voltage output generated by the energy harvester. The maximum voltage recorded during the simulation reaches approximately 8V, while the average peak voltage fluctuates within the range of 2V to 4V. The cyclical nature of voltage generation is clearly observable, with each cycle spanning roughly 1 second in duration. This cyclical pattern arises due to the alternating motion of the hip joint, which causes changes in the rotational direction of the energy harvester. As a result, negative voltage values are recorded during portions of the cycle when the direction of rotation reverses.

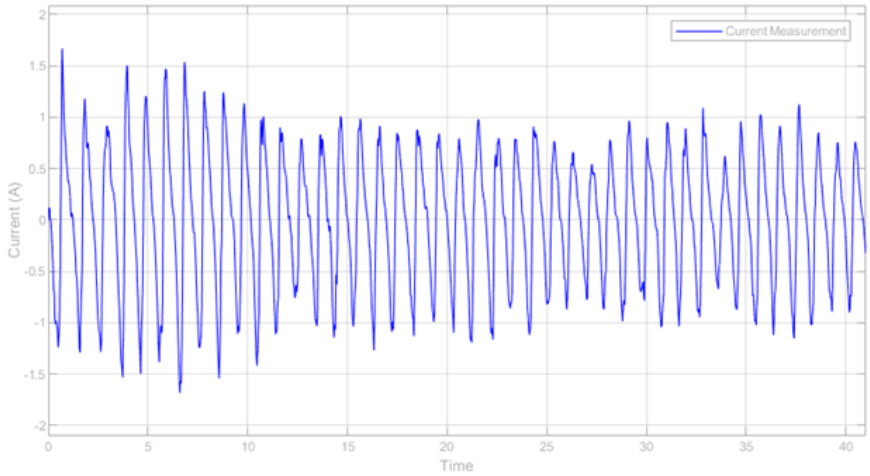

Figure 7.13: *Current output from MATLAB calculation using computer vision data.*

Figure 7.13 displays the current output under load conditions. The maximum current

generated by the energy harvester reaches approximately 1.6A, with the average peak current hovering around 1A. Similar to the voltage output, the current output follows a regular, cyclical pattern, with each cycle lasting around 1 second. Negative current values are observed during the phases of reversed rotational motion, corresponding to the same mechanical motion of the hip joint that causes the negative voltage.

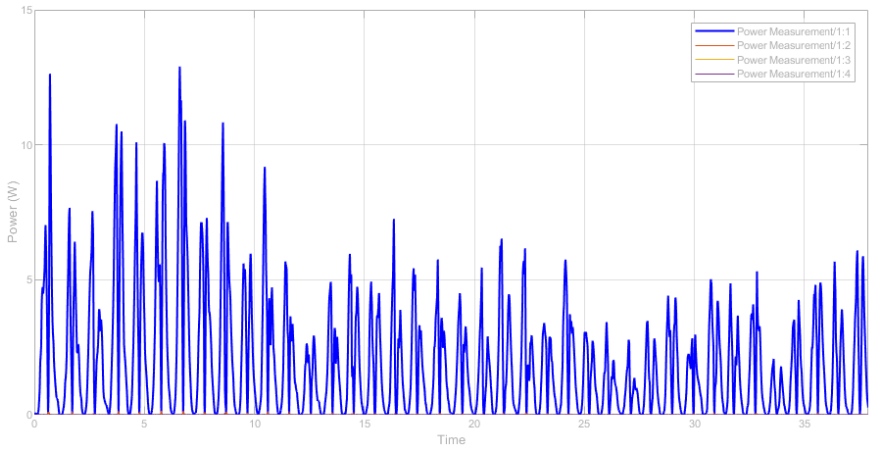

Figure 7.14: *Power output from MATLAB calculation using computer vision data.*

Figure 7.14 demonstrates the power output generated by the energy harvester, with the maximum power output recorded at approximately 13W. The average peak power fluctuates between 4W and 6W throughout the simulation. Like the voltage and current outputs, the power output exhibits a consistent cyclic behaviour, with each cycle lasting roughly 1 second. Notably, the power output remains positive during the entire simulation process, even as the voltage and current oscillate.

These simulation results are produced without accounting for efficiency losses or other real-world factors that can influence the energy harvester's actual performance. Nonetheless, the outcomes provide valuable insights and serve as a meaningful theoretical comparison to the calculations performed earlier in this research. A more realistic simulation approach will be taken in the field experiment chapter. The additional outputs from the DC machine block are captured during the simulation and will be discussed in the next chapter.

7.3.2 Simulation with the Data from the Motion Capture on the Ground

Having completed the calculations using the data obtained from the computer vision method, the same process can now be repeated for the second dataset, with only a few modifications required to accommodate the new data. The first adjustment involves updating the angular velocity of the hip joint by importing the newly recorded data into the Signal Builder block within the Simulink model. In addition, the angular velocity ratio dataset in the Signal Builder also needs to be replaced with the pre-calculated values corresponding to the new motion data. In future work, it may be advantageous to explore the implementation of a function block to further enhance the flexibility of the simulation. Such a block can allow users to easily adjust critical parameters, such as the length and angle of the energy harvester mechanism, without needing to modify the input datasets manually. Incorporating this kind of adaptability can prove especially useful in scenarios where the physical setup of the energy harvester varies or needs to be optimised for specific use cases.

Results using Motion Capture Lab Data

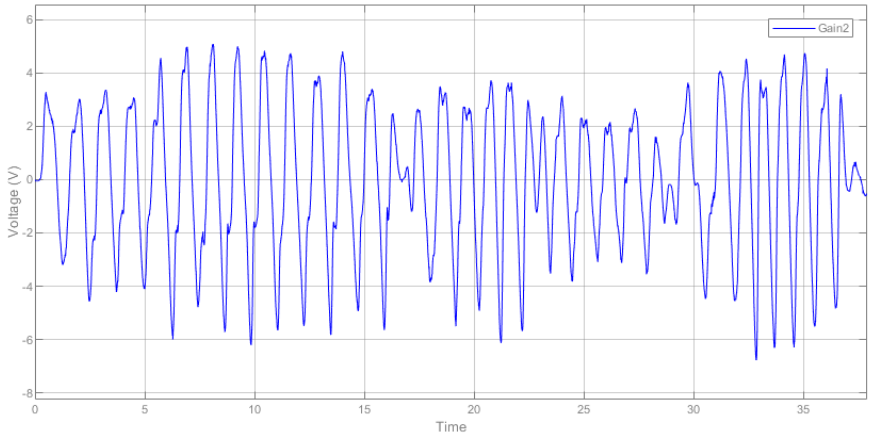

Figure 7.15: *Voltage output from MATLAB calculation using motion capture lab data.*

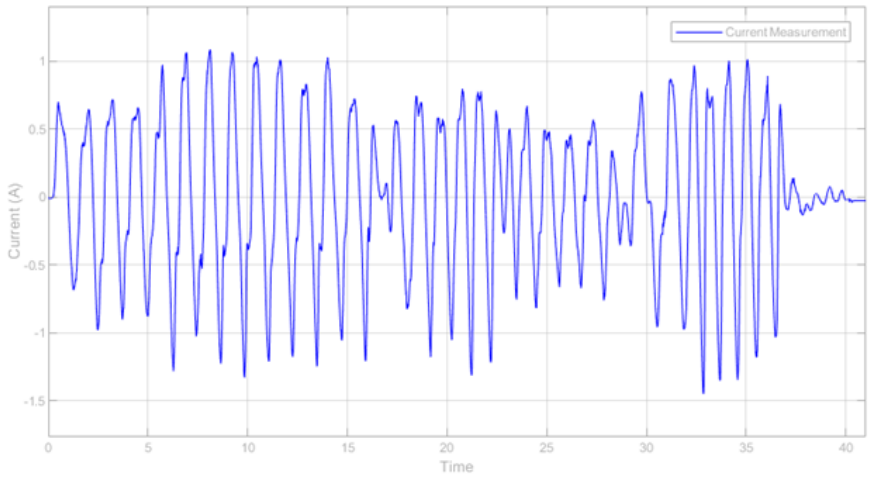

Figure 7.16: *Current output from MATLAB calculation using motion capture lab data.*

After updating the necessary Signal Builder blocks with the new dataset and rerunning the simulation, a new set of outputs is generated, providing insights into the system's behaviour under the new conditions. Figure 7.15 illustrates the voltage output from the DC machine, where the peak voltage reaches nearly -6V. The average peak voltage settles around 3V. The cyclical nature of the voltage generation is also clearly visible, with each cycle lasting approximately 1.5 seconds.

Figure 7.16 presents the current output from the DC machine, which peaks at -1.4A. The average peak current is recorded at approximately 0.7A. Similar to the voltage output, the current follows a well-defined cycle with a duration of about 1.5 seconds. The negative values observed in the current output occur for the same reason as in the voltage output which are from the changes in the rotational direction of the energy harvester mechanism. Lastly, Figure 7.17 displays the power output generated during the simulation. The power output peaks at 10W, while the average peak power ranges from 3W to 5W. The power output cycle mirrors that of both the voltage and current, maintaining the 1.5-second duration. A 3D simulation is also created which helps to visualise the motion as shown in Figure 7.18.

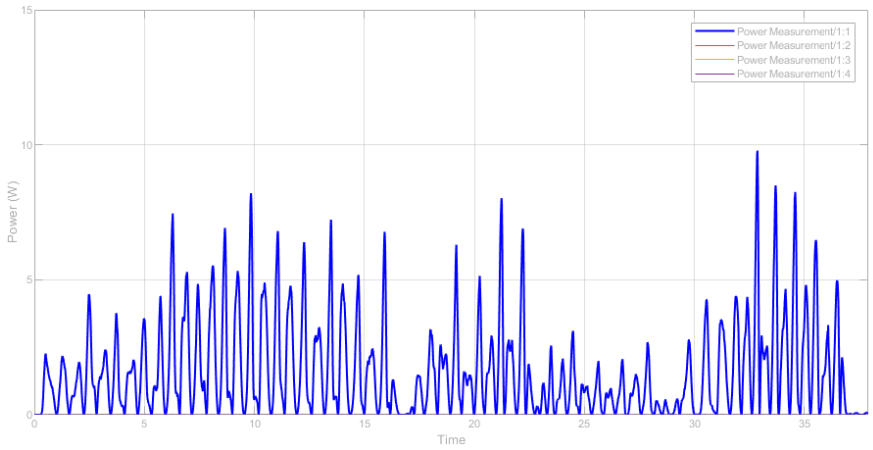

Figure 7.17: *Power output from MATLAB calculation using motion capture lab data.*

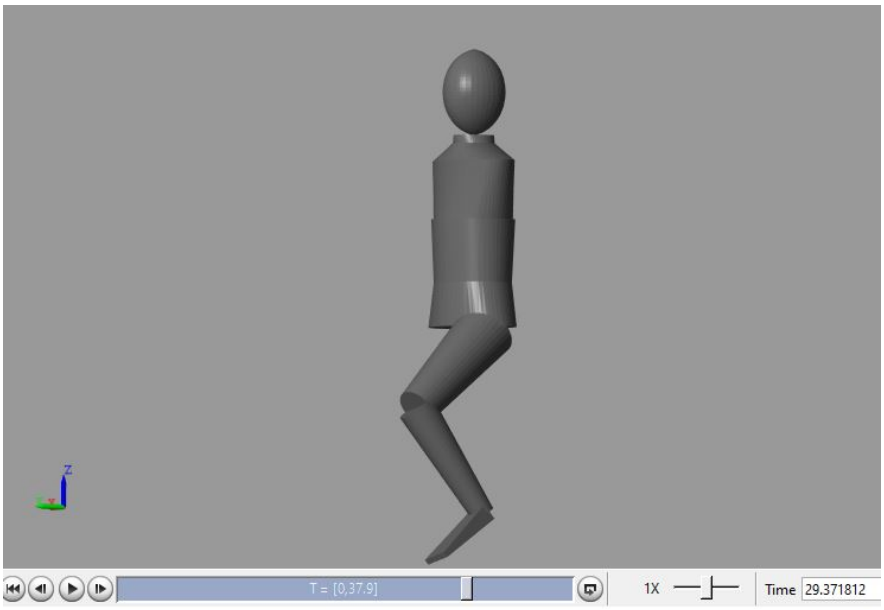

Figure 7.18: *3D simulation from MATLAB calculation using motion capture lab data.*

As in the previous section, it is important to note that these calculations and simulations use the maximum efficiency value of the DC motor and do not account for system efficiency or other coefficients, so the theoretical results will be higher than what would be observed in real-world conditions. A realistic simulation is shown in the next chapter.

7.4 Comparison between the Calculation Results and the Simulation with MATLAB

This section provides a comparison between the calculation method and the MATLAB simulation approach used for evaluating the performance of the energy harvester integrated within the lifejacket system. Both methods offer specific advantages and limitations that are needed for understanding the overall performance of the system under various conditions and scenarios.

Calculation

The manual calculation is conducted using a spreadsheet to establish an initial baseline for understanding the energy harvesting system's behaviour. This method involved calculating the angular velocity of the DC motor, which is driven by the angular velocity generated at the hip joint during ladder-climbing motions. By using motion capture data, the angular velocity at the hip joint is translated into the motor's angular velocity through geometric analysis. This step is essential for understanding how the vertical angular motion of the hip joint drives the motor and produces electrical energy.

The relationship between the hip joint's angular velocity and the angular velocity of the energy harvester is derived by taking into account the mechanical linkage connecting the two. The calculation indicated a significant reduction in angular velocity at the energy harvester compared to the hip joint, with a maximum reduction of approximately 44% (0.44). The calculation yielded maximum voltage outputs of approximately 16V when using the computer vision data, while the motion capture lab data resulted in a slightly lower maximum voltage of around 13V. The maximum power derived from the computer vision data reaches 14W, with an average peak of approximately 5W. The maximum power generated from the motion capture lab data is just over 10W, with an average peak of around 3W. These results provided a baseline for understanding the system's performance and indicated that the energy harvester's angular velocity remained consistently lower due to its offset positioning relative to the hip joint.

Simulation with MATLAB

MATLAB simulations are used to model the energy harvester system in a more detailed and adaptable manner compared to calculations. In this approach, additional motor parameters

such as the dynamic resistance, and torque constant are incorporated, allowing for a more refined analysis of the energy harvester's performance under a variety of operational conditions. MATLAB's advanced computational capabilities enabled dynamic simulations that can accommodate a broader range of variables, providing insights that are not possible with the calculation approach.

For the MATLAB simulations, the angular velocity data that is used in the calculations is directly imported into the model, ensuring consistency between the two methods. The MATLAB results closely mirrored the outcomes of the calculations. For example, the maximum voltage output generated by the motor in MATLAB simulations reached around 8V when using the computer vision data, and approximately 6V when using the motion capture lab data. Beyond voltage, the MATLAB simulations are able to provide additional information on current and power output. The peak power output reached 13W for the computer vision data and 10W for the motion capture data. These additional metrics offered a more comprehensive understanding of the system's performance and efficiency.

7.4.1 Comparison of Results

When comparing the two approaches, the calculation method offers a simple and straightforward way to quickly establish key performance metrics, such as the angular velocity ratio between the hip joint and the energy harvester, and the potential voltage output of the system. However, the calculation method is limited in its ability to handle more complex system dynamics and variations in parameters. Each parameter needs to be manually adjusted, making the process more cumbersome and prone to errors as the complexity of the system increases. The calculations also do not account for the full range of real-world scenarios, reducing their flexibility and applicability to varying conditions.

On the other hand, MATLAB simulations provide a more flexible, accurate, and detailed analysis of the energy harvesting system. MATLAB's ability to automate calculations, adjust motor parameters, and simulate the system under varying load conditions allows for a more in-depth exploration of the system's performance. The use of MATLAB reduces the likelihood of errors and ensures consistency across different simulations, even when dealing with more

complex scenarios. MATLAB simulations also offer insights into power generation and system efficiency that are not feasible with the calculation method, such as the detailed analysis of current and power outputs under varying operating conditions. A comparison of outputs is listed in Table 7.1, which shows that the power outputs calculated from the two methods are similar.

	Computer Vision		Motion Capture	
	Peak value	Average top value	Peak value	Average top value
Calculation (Voltage) (V)	16	9	13	8
Calculation (Max Power) (W)	14	5	10	3
MATLAB (Voltage) (V)	8	4	6	3
MATLAB (Max Power) (W)	13	6	10	5

Table 7.1: *Comparison of calculation and MATLAB simulation results for computer vision and motion capture*

In summary, while calculations are useful for establishing an initial baseline understanding of the system, MATLAB simulations provide a far more comprehensive, adaptable, and precise analysis. MATLAB's ability to model the energy harvester's behaviour in a dynamic environment, account for different system parameters and evaluate performance under diverse conditions made it a much more powerful tool for ongoing research and system optimisation. Therefore, MATLAB simulations offer significant advantages in terms of both accuracy and depth of analysis, making them a more effective approach for the detailed evaluation of the energy harvester. In this calculation, the power outputs from both methods provide a very close result.

Chapter 8

Experimental Validation of the Energy Harvesting System

In earlier chapters, the modelling and design of the energy harvesting system integrated into a lifejacket are discussed in detail. The energy harvester, based on the YG2734 brushed DC motor, is positioned to capture kinetic energy from the vertical rotation of the hip joint during the "ladder climbing" motion. Theoretical calculations and MATLAB simulations demonstrate the potential for the energy harvester to generate power under controlled conditions. These theoretical approaches require validation to ensure the system's efficacy in real-world conditions.

This chapter aims to validate these theoretical results by conducting both ground and field tests. The ground test phase, conducts in a controlled laboratory environment, primarily focuses on the fundamental functionality of the energy harvester. It verifies the system's capability to generate electrical energy and ensures that the energy harvester operates as expected when subjected to the prescribed motion. On the other hand, the field test conducted in a swimming pool offers a more comprehensive understanding of the energy harvester's performance in an environment closer to that of a search and rescue scenario in water. The field tests also provide an opportunity to assess the impact of external factors such as water resistance and real-life motion dynamics on energy generation. The motion data captured from the field test can also be used for simulation in MATLAB with the field test setting including the electrical load for a more realistic comparison.

The motion data used for the initial MATLAB simulation mentioned in Chapter 7 is captured during a motion capture experiment without the energy generator as mentioned in Chapter 4. The purpose of that experiment was solely to record motion data for calculating and simulating the energy harvesting potential in Chapter 4. In this field test, where the energy generator is integrated, motion data is again captured alongside the actual energy harvested. Using this new motion data to refine the MATLAB simulation allows for a more realistic comparison between the simulated energy output and the actual harvested energy. This approach enhances the accuracy of the study by incorporating motion data that reflects the conditions experienced during the energy harvesting test.

The focus of the experimental validation is on the energy harvester's performance, specifically focusing on whether the system can effectively generate power without hindering the wearer's motion. A key aspect of this investigation is understanding the energy harvester's efficiency by comparing the experimental data with the theoretical calculations. This comparison will highlight any difference between the expected and actual power output, enabling a more thorough evaluation of the system's practicality and potential areas for optimisation.

Another focus is the wearability of the system, ensuring that the energy harvester does not impose excessive resistance on the wearer during motion. By calculating the torque generated by the hip joint and the torque output from the MATALAB simulation, the mechanical load on the participant can be quantified. The findings from these calculations provide valuable insights into the system's design, particularly with regard to optimising the gear ratio for future iterations of the energy harvester.

Specifically, the experiments are designed to:

- validate the theoretical approaches discussed in previous chapters by conducting both ground and field tests of the energy harvesting system.
- confirms that the energy harvester, integrated into the lifejacket and using the YG2734 brushed DC motor, can generate electrical energy from the "ladder climbing" motion.
- test the energy harvesting system in a swimming pool to simulate a real-world search and rescue scenario. Assess the impact of water resistance, buoyancy, and other external

factors on the harvester's performance.

- compares the power output generated during the experiments with the values predicted in theoretical simulations to evaluate the harvester's effectiveness.
- examine the wearability and practicality of the energy harvester system in both ground and water environments. Ensure that the system does not impose excessive resistance or discomfort on the participant during motion.
- analyse the efficiency of the energy harvester based on experimental data. Identify areas for improvement, such as optimising the gear ratio or refining the design to enhance energy output and minimise mechanical losses.

The University Ethics Committee reviewed the study proposal and confirmed that formal ethics approval was not required.

8.1 Experiment 1: Ground Test in the Lab

8.1.1 Test Setup

The ground test is conducted in a lab where a prototype of the energy harvester is assembled and securely mounted onto the participant's body, as shown in Figure 8.1. A telescopic linkage is incorporated into the system, connecting the thigh strap and waist strap of the setup, as illustrated in Figure 8.2.

The primary objective of this configuration during ground test is to ensure that the energy harvester mechanism operates as intended under controlled conditions. By assembling and testing the setup in the laboratory, the system's functionality including the motor's ability to generate power from the simulated thigh motion could be validated.

Figure 8.1: *Energy harvester prototype*

8.1.2 Testing and results

In the ground test shown in Figure 8.2, the participant utilised the specified setup for energy harvesting from this leg's motion. The output voltage and current of the YG2732 brushed DC motor are respectively monitored by an oscilloscope and an ammeter. An assistant is present to assist in setting up the apparatus, monitoring the equipment, and recording the oscilloscope and ammeter readings. One of the limitations of the setup is the restriction of leg motion caused by maintaining a straight standing posture. To overcome this, the participant leaned forward, allowing for unrestricted motion of the other leg. This posture is similar to that of a soccer player balancing on one leg while preparing to kick a ball, allowing for greater freedom of motion while reducing any constraints from the floor. A bench is in front of the participant to help him maintain balance throughout the test. The setup is intended to simulate conditions in which the participant's leg had freedom of motion with minimal trunk motion, similar to the motion observed during the motion data capture process.

Figure 8.2: *Ground test in AUT lab. The participant is leaning to one side to ensure the floor does not impede the leg's free motion.*

Following initial checks, the participant performed the leg motions consistent with the motion data collection and simulation phases. The assistant ensured that the range and frequency of the participant's leg motion closely matched the parameters used in the simulation to maintain accuracy and consistency. Throughout the test the maximum voltage recorded during the test is 14V, as shown in Figure 8.4, while the maximum current reached 50mA, as shown in Figure 8.3. These peak readings are observed during the downward motion of the participant's hip, where the rotational velocity reached its maximum. This phase of the motion is responsible for generating the maximum power output, confirming the system's ability to capture kinetic energy from the leg motion effectively.

The data collected from this ground test is important for validating the energy harvester design and will serve as a baseline for the field test. It is essential to note that during the ground test, no electrical load is applied to the system. As a result, the recorded output may not fully represent the system's actual performance in a real-world application, where an electrical load would be present. The ground test excluded an electrical load to focus on measuring the raw voltage output of the generator, providing a clear view of its baseline performance without external influences. This simplified setup minimised complexity and ensured that observed

voltage fluctuations were directly attributable to the generator's behaviour under motion. As a preliminary validation, the test aimed to confirm the generator's functionality and voltage potential, with the inclusion of an electrical load deferred to later tests focused on efficiency and power delivery. Despite this limitation, the ground test results indicate that the design can generate electrical power as expected, with the output values following the predicted pattern outlined in the energy harvesting model.

Figure 8.3: *. Max current reading from ground test is 50.19mA.*

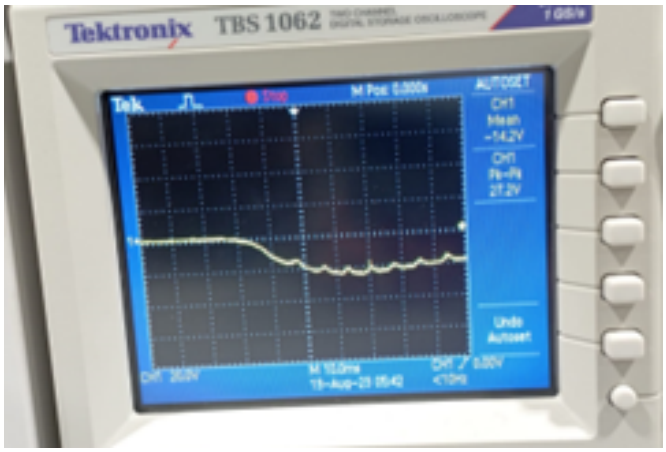

Figure 8.4: *Voltage reading from ground test with a peak value of -14.2V.*

8.2 Experiment 2: Field Test in the Water

Following the completion of the ground test, it has been confirmed that the energy harvester mechanism design and setup function as expected under controlled conditions. The next phase of the research focuses on preparing for field test, which will serve as the ultimate validation of

both the design and the theoretical approaches developed in earlier stages. To ensure the energy harvester performs effectively in real-world conditions, several key modifications and additional preparations are required.

One of the primary adjustments is waterproofing the entire system. This involves sealing critical parts such as the motor and exposed electronic components. Careful attention must be given to the waterproofing process, as even minor leaks could compromise the electrical integrity. The electrical circuit must also be constructed and integrated into the system to facilitate accurate measurement of the energy generated during the test. This includes ensuring that the sensors and electronics used to measure parameters such as voltage, current, and power are fully operational underwater.

The energy harvester must be integrated with a real-life lifejacket to replicate the actual conditions during a rescue operation. This integration is critical to evaluate how the energy harvester interacts with the lifejacket and the wearer, ensuring that the harvester does not impede the lifejacket's function or the participant's motion. This setup will closely resemble the conditions expected during search and rescue missions, where energy harvesting devices must operate seamlessly without disrupting normal rescue procedures.

To accurately capture the data during the field test, several electronic components are installed to measure the output of the energy harvester. These components include sensors that monitor electrical parameters such as voltage, current, and power, as well as software designed to record these data in real-time.

The field test is conducted in the same swimming pool where the motion data is captured using computer vision technology. The participant will wear the modified lifejacket with the integrated energy harvester, ensuring that the setup mimics real-life conditions as closely as possible. An underwater camera will record the participant's motions, which will later be analysed using the same computer vision techniques used in earlier stages of the research. This motion data will be synchronised with the output data from the energy harvester, enabling a direct comparison between the participant's motions and the corresponding energy generated by the harvester.

In the following sections, the steps involved in preparing the system for field test, including

the necessary hardware and software modifications, the setup of the field test, and the analysis of the final results are described.

8.2.1 Preparation

Waterproofing

The selected DC motor, YG2734, is not inherently waterproof and waterproofing is needed before using it in the field test.

It is housed in a transparent plastic film canister holder, chosen for its lightweight and cost-effective properties, as illustrated in Figure 8.5. The holder serves as a casing to protect the motor from water ingress. A waterproof bearing is installed at the shaft end of the motor. The outer surface of the bearing is glued to the casing, and the seal is reinforced using a liquid insulating tape, a rubberised coating that acts as a waterproof sealant. Two small holes are drilled into the canister holder to accommodate the cables. The same liquid insulating tape is used to seal these openings.

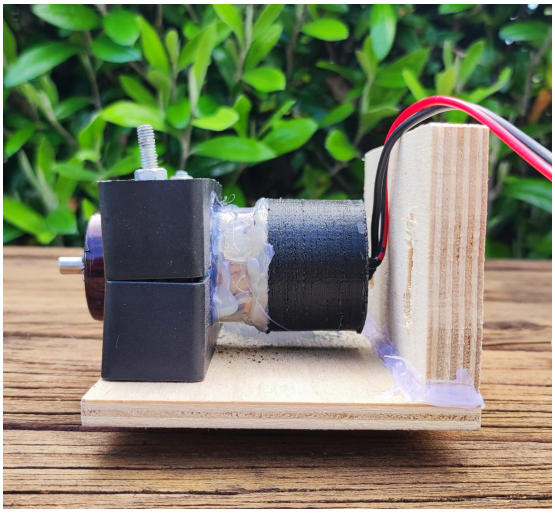

Figure 8.5: *Energy harvester casing.*

For simplicity, the electrical board is not mounted onto the lifejacket as the primary goal of the field test is to assess the effectiveness of the energy harvesting mechanism and the DC motor. In the test, the electrical board remains outside of the water, connected to a computer on the ground, thereby minimising the risk of water damage. In future iterations, the electrical

board could be enclosed in a waterproof casing with an IP67 or IP68 rating.

Once passing the waterproof test, the motor is integrated into the energy harvesting mechanism and attached to the lifejacket.

Electronics setup

The electronics setup used in this study is designed for collecting key data related to the energy harvester's performance, including bus voltage, shunt voltage, load voltage, current, and power as described in Section 7.1.3. The core of the system is the integration of an INA219 current sensor with an Arduino Uno board, as illustrated in Figure 8.6.

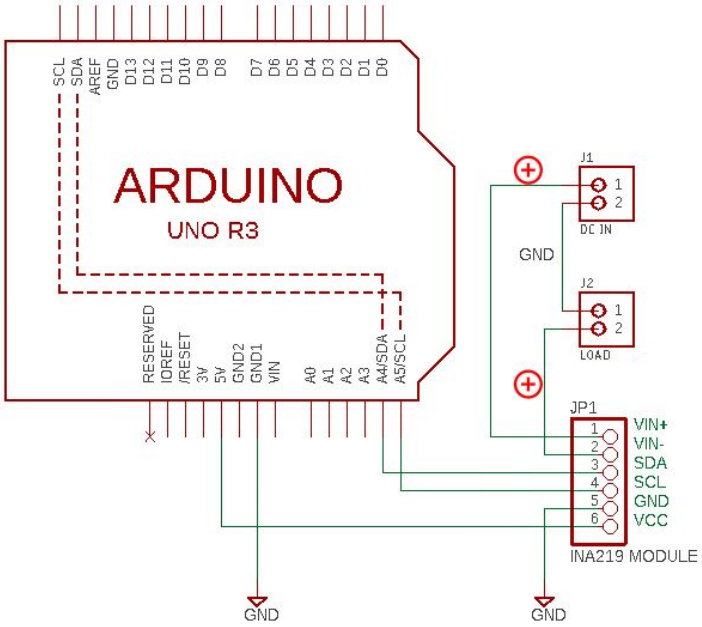

Figure 8.6: *Circuit diagram of the energy harvester.[17] [18]*

The INA219 current sensor, produced by Texas Instruments, operates as a high-side current shunt and power monitor. It is widely employed for monitoring and regulating power consumption across various electronic devices, making it particularly suitable for this study. The sensor is connected to the Arduino Uno board, which serves as the microcontroller in this configuration. The load in this setup is a $12V$, $1.2W$ automotive globe from Enduralight. Power is generated by the YG2734 motor, which is coupled with a rectifier to convert the alternating current (AC) produced by the motor into direct current (DC), ensuring that the system operates with stable

and usable power.

The Arduino Uno board is connected to a computer via USB, allowing the data collected by the INA219 sensor to be directly transferred and recorded on the computer for further analysis. This connection facilitates the real-time recording of critical parameters such as voltage, current, and power. The captured data can be used to make informed decisions regarding the efficiency and performance of the energy harvesting mechanism which will be discussed in the later sections.

The Arduino and INA219 current sensor were programmed using the Arduino IDE, with specific libraries like Wire.h for I2C communication and Adafruit_INA219.h for sensor interaction. The Arduino code enables the real-time measurement of key parameters, such as voltage, current, and power, which are transmitted to the serial monitor for analysis. Data recording was facilitated using CoolTerm [111], a serial port terminal application, configured with the appropriate port and baud rate to capture experimental data continuously. CoolTerm's functionality allows for seamless data export into text files for subsequent analysis. The complete programming and software setup, including the configuration details, are provided in Appendix D to ensure clarity and reproducibility.

8.2.2 Test Setup

The setup for the field test includes:

- **Participant Preparation**: The participant is fitted with an inflatable lifejacket that has the energy harvesting device integrated into it. Prior to entering the water, the lifejacket is fully inflated on the ground, allowing for the secure attachment of the device and all necessary connections. This ensures that everything is in place before testing commences. The assistant checks that the lifejacket is worn securely and verified that both the energy harvesting mechanism and thigh strap are fastened correctly.

- **Motion Capture System**: To capture the participant's motion during the test, an underwater camera is mounted at the side of the pool, replicating the setup used during the earlier

motion data collection phase. The distance between the camera and the participant is pre-measured to ensure the footage can capture the full body. However, since Wi-Fi signals cannot penetrate through water, the underwater camera has to be manually activated by the assistant.

- **Measurement Equipment**: Before proceeding into the water, a final ground test is conducted to confirm that all systems are functioning properly. This final check involved ensuring that the DC motor generated output, the Arduino board is accurately receiving data from the energy harvester, and that the data transmission to the computer through CoolTerm is seamless.

Once the ground test is completed and all components are verified, the participant safely enters the swimming pool. The final position of the participant and components are shown in Figure 8.7.

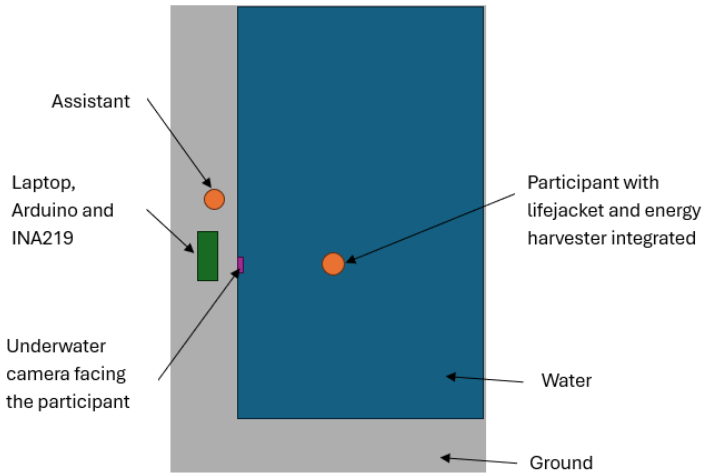

Figure 8.7: *Positions of the participant and components for field test at the swimming pool.*

8.2.3 Testing Procedure

With all preparations complete, the field test experiment is ready to proceed. Each test run lasts for approximately 30 seconds to ensure that a sufficient and reliable dataset can be collected for analysis. The participant takes short breaks between each run to ensure that he can rest and maintain a steady performance during each test. An assistant is present throughout the test to

monitor the participant's well-being, operate the camera to record the experiment, and handle the data collection process using CoolTerm on the computer.

The participant is positioned approximately 4 metres from the camera, similar to the setup used during the motion data collection phase. The camera is set up to capture the participant's motions, ensuring that the participant's limbs remain clearly visible throughout the test. The participant's coronal plane is aligned directly with the camera, replicating the positioning used in previous tests to ensure consistency between the datasets.

Before the start of each run, the participant performs an exaggerated clapping motion. This exaggerated motion acts as a visual cue, serving as a reliable reference point for synchronising the motion data and the energy harvester's output during the post-experiment processing stage. By using such a clear and distinguishable marker, the post-processing alignment of the video footage and output data could be performed more accurately. During each test run, the participant simulates the "ladder-climbing" motion, a motion pattern that closely resembles the instinctive actions of a person in distress during a drowning event.

8.2.4 Results and Observations

From the footage of the experiment, it is clear that the lifejacket does not interface with the accuracy of the computer vision analysis, ensuring that the motion data obtained is reliable. A screenshot from the footage showing the clear visibility of limb motions is presented in Figure 8.8.

During the field test process, the Arduino Uno communicates with the INA219 current sensor to collect data, including voltage, current, and power generation. As illustrated in Figure 8.9, the peak power output reaches $754mW$, while the average peak values hover around $450mW$. The minimum recorded power is $0mW$, which occurs when the participant's motions are too slow to generate sufficient angular velocity for energy production. This variation in power output can be attributed to the presence of a "dead zone," where the angular speed of the participant's motion falls below 2 degrees per second and the power generation is negligible.

As expected, a clear relationship between angular speed and power generation is observed, with higher angular velocities correlating with greater power output. While the motor is rated

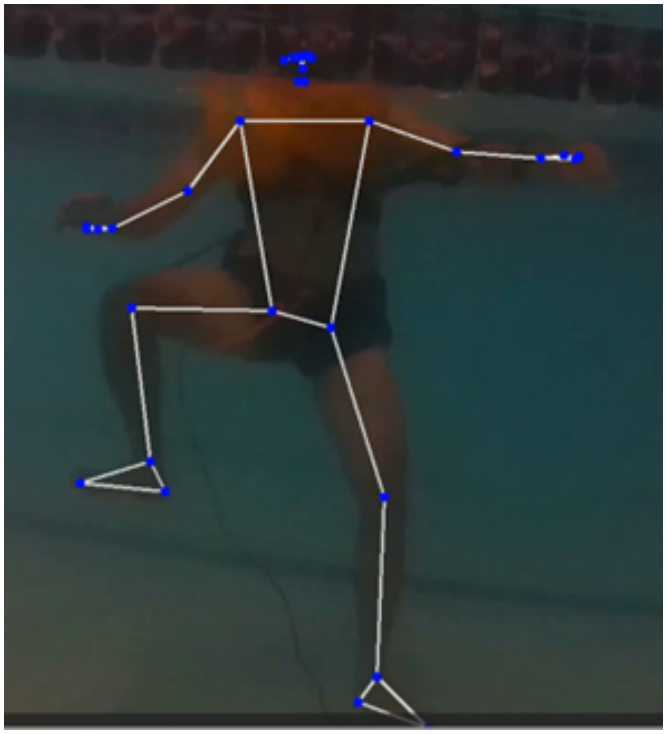

Figure 8.8: *A screenshot of the footage capture from the field test*

at $12V$, the maximum bus voltage recorded during the experiment is $9.08V$, with the shunt voltage and load voltage peaking at $9.95V$ and $9.09V$, respectively. The peak current recorded is $101.1mA$, corresponding to the moment of maximum power generation. Figures 8.10 to 8.13 provide detailed visual representations of the voltage and current fluctuations observed during the experiment, further highlighting the correlation between these electrical parameters and the angular velocity of the energy harvester.

Analysis of the collected data reveals that the highest power generation occurs during the downward phase of the "ladder-climbing" motion when the participant's knee transits from the uppermost to the lowermost position. Although the upward motion of the knee also contributes to power generation, it produces lower power outputs, with a peak of $394mW$. These observations align with the expected behaviour of the energy harvester, as the downward motion generates higher angular speeds, leading to greater power output. This phase of the motion involves more rapid and forceful extension of the leg, which translates into faster rotational motion at the harvester and higher power generation.

The results of the field test demonstrate that the energy harvester mechanism is capable

of generating power effectively during the ladder-climbing motion, confirming the expected relationship between angular velocity and power output. However, the presence of the dead zone highlights a limitation of the system, where power generation drops to zero when the angular velocity falls below the threshold. This finding underscores the importance of optimising the system to minimise the effects of the dead zone and maximise power output across a broader range of motion speeds. One approach to minimise this effect and maximise power output is the addition of a flywheel or mechanical energy storage, as discussed in Section 9.3.1.

In summary, the field test validated the overall design and performance of the energy harvester, demonstrating that the mechanism could generate power under real-world conditions. The relationship between the participant's motions and the power output is confirmed, and areas for potential optimisation, such as addressing the dead zone, are identified.

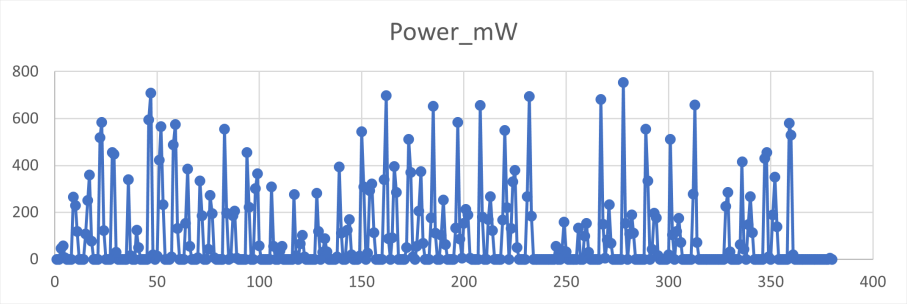

Figure 8.9: *Power(mW) vs time(s)*

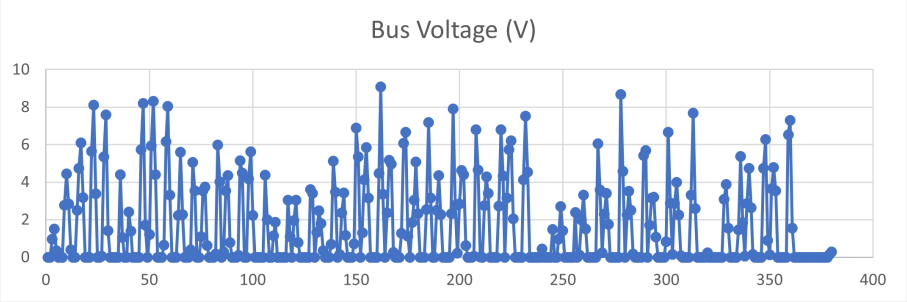

Figure 8.10: *Bus Voltage (V) vs time(s)*

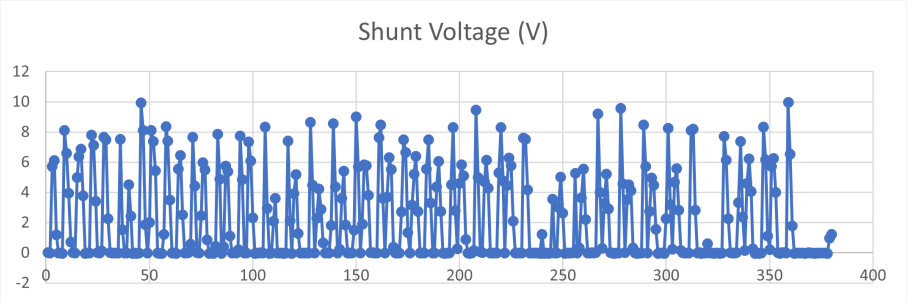

Figure 8.11: *Shunt Voltage (V) vs time(s)*

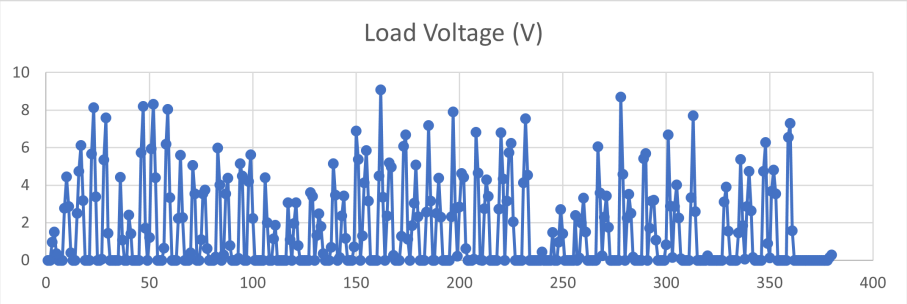

Figure 8.12: *Load Voltage (V) vs time(s)*

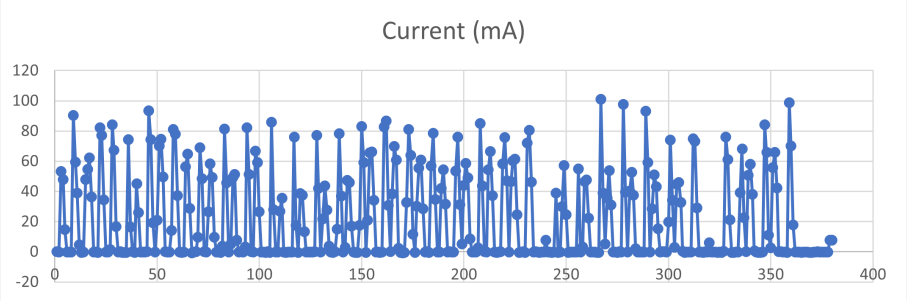

Figure 8.13: *Current (mA) vs time(s)*

8.3 Processing of the Motion Data of Experiment 2

In this section, the data collected from the field test and those obtained during the ground test are further processed.

Based on the collected in Experiment 2, the output power generated by the energy harvester can be calculated using manual methods, followed by simulations in MATLAB. Since all the measurements including the actual output measured by the Arduino board, the manual

calculations, and the MATLAB simulations are derived from the same field test scenario, this comparison will offer a reliable validation of the energy harvester's performance and the theoretical approach.

The calculation process follows several key steps. Firstly, the motion data collected from the field test is used to calculate the maximum power output through manual calculations, which are done in a spreadsheet. This step follows the previous manual calculations outlined in Chapter 7 and it now applies directly to the field test data. Secondly, the angle changes and ratios obtained from the motion data are input into the MATLAB simulation, where the power output is calculated again. During this simulation, the electrical load corresponding to the 12V automotive light bulb used in the field test is included to reflect the actual conditions more accurately. By adjusting the MATLAB simulation for this load, the power output results from the simulation can be compared directly with the actual measurements from the Arduino board.

8.3.1 Calculations from the Motion Capture Results

In the calculations, the primary goal is to determine the maximum potential power output, which occurs when the internal resistance of the system matches the external load resistance. This condition ensures optimal energy transfer between the generator and the load. Based on the data acquired from the field test, the maximum power output is calculated to be 7.5W, as shown in Figure 8.14. The average peak power output is recorded at approximately 2.5W, reflecting the energy harvester's performance under optimistic operating conditions. With the electrical load of 120 Ω added, the maximum power output is calculated to be 1.6W and the average peak power is approximately 0.75W as shown in Figure 8.15.

The voltage calculations using the field test data further validate the power output results, with the maximum voltage observed reaching close to 11.8V. The average peak voltage ranges between 5V and 6V, as illustrated in Figure 8.16. These values are consistent with the expectations based on the harvester's angular velocity during the field test. The relatively high voltage generated is indicative of the system's ability to effectively convert the mechanical motion of the thigh into electrical energy. This is especially significant given that the energy harvesting system must operate under variable conditions, where the angular speed of the

participant's motion directly affects the output.

The time duration for each complete energy harvesting cycle is approximately one second which aligns well with the motion pattern of the participant during the motion capture phase. This consistency in cycle duration suggests that the motion dynamics remained stable and repeatable throughout the experiment, leading to reliable and predictable energy output. It is important to note the maximum efficiency value (65.9%) of the DC motor used in the manual calculations does not account for factors such as frictional losses, variable electrical load conditions, and the energy losses associated with the DC motor's conversion of mechanical to electrical energy. However, the results obtained from this manual calculation serve as a critical reference point for validating the MATLAB simulations and comparing these calculations with the actual data obtained during the field test to be discussed in the next section.

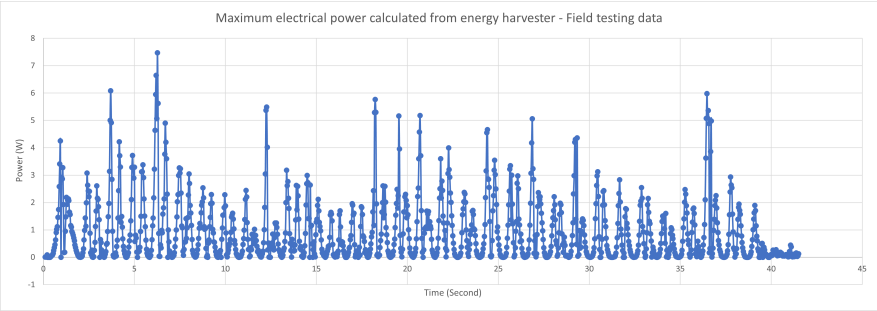

Figure 8.14: *Maximum power calculated by using the data from field test.*

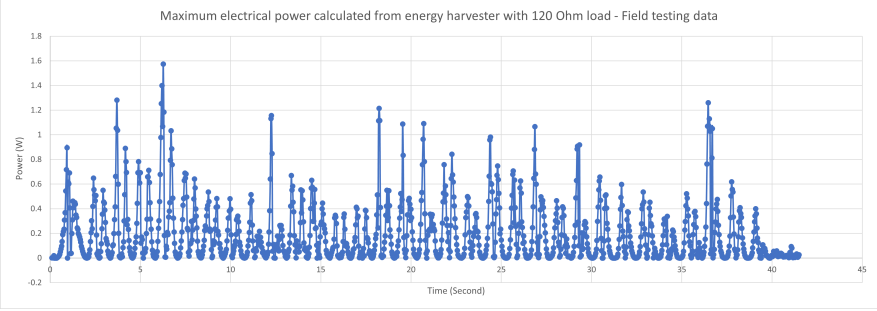

Figure 8.15: *Maximum power calculated by using the data from field test with 120 Ohm electrical load.*

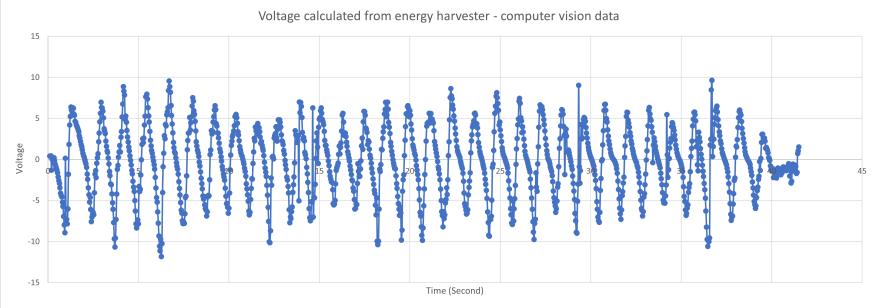

Figure 8.16: *Maximum voltage calculated by using the data from field test.*

8.3.2 Simulation with MATLAB

After the manual calculation, next is using the motion data collected during the field test and inputting it into MATLAB for simulation. The inputting method is explained in Appendix G. The goal of these simulations is: first, to validate the results obtained from the manual calculations, and second, to evaluate the performance of the energy harvester with the electrical load of the automotive light bulb used in the field test to validate the theoretical approach with the field test results.

In order to accurately simulate the conditions of the field test, two separate runs for simulations are performed. The first run will simulate the theoretical maximum power output from the energy harvester, allowing for a direct comparison with the results obtained through manual calculations. The second run will simulate the system with the electrical load of the automotive light bulb, providing a more realistic assessment of the system's performance in practical applications to validate with the test results.

The automotive light bulb, which is rated at 12V and 1.2W, introduces a specific electrical load into the system. The resistance of this load can be calculated using Ohm's Law, which states that:

$$R = \frac{V^2}{P}$$

Substituting the known values for voltage and power, the resistance of the light bulb is:

$$R = \frac{12^2}{1.2} = 120\,\Omega$$

This resistance value will be used in the second MATLAB simulation to assess the system's performance with an actual load.

The input data for the MATLAB simulations consist of the hip joint angle and the angular velocity ratio between the hip joint and the energy harvester. These two values are calculated outside of MATLAB using the motion data from the field test, as detailed in the previous chapter. The hip joint angle is measured using computer vision techniques, while the angular velocity ratio is determined based on the mechanical design of the energy harvester and the linkage between the hip joint and the motor.

In the first simulation, where the goal is to simulate the maximum power output, the results show that the maximum power generated by the energy harvester is 6.8W, with the average peak value ranging between 2W and 3.5W as shown in Figure 8.17. This closely aligns with the results obtained from the manual calculations, where the maximum power output is found to be 7.5W with an average peak of around 2.5W. The small discrepancy between the two results can likely be attributed to extra parameters of the motor that can be entered in MATLAB.

The voltage output in the first simulation reaches a maximum of 5.9V, with an average peak value between 3V and 4V as shown in Figure 8.18. This is lower than the theoretical voltage calculated in the manual calculations, which has a maximum of 12V. It is important to note that the MATLAB simulation accounts for various factors that are not considered in the manual calculations.

The current output from the first simulation also provides valuable insights into the system's behaviour. The maximum current is recorded at 1.2A, with the average peak value ranging between 0.6A and 0.8A as shown in Figure 8.19. These values are consistent with the power and voltage outputs observed in the simulation, confirming the validity of the results.

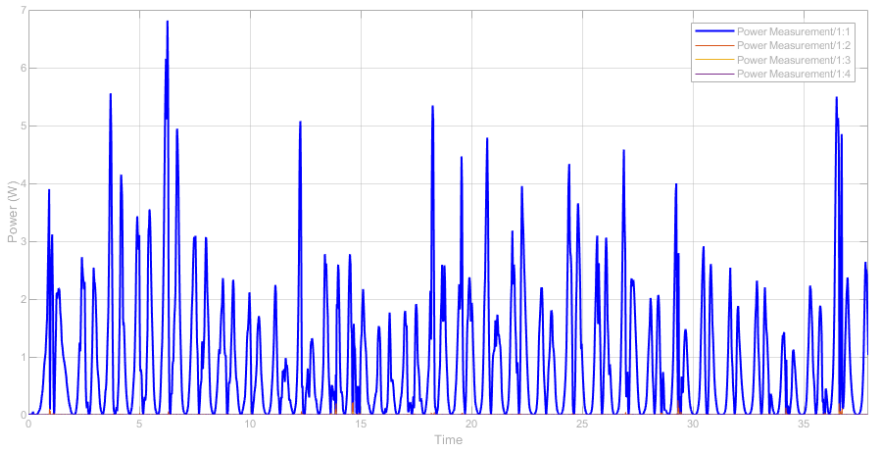

Figure 8.17: *Maximum power calculated in MATLAB by using the data from field test.*

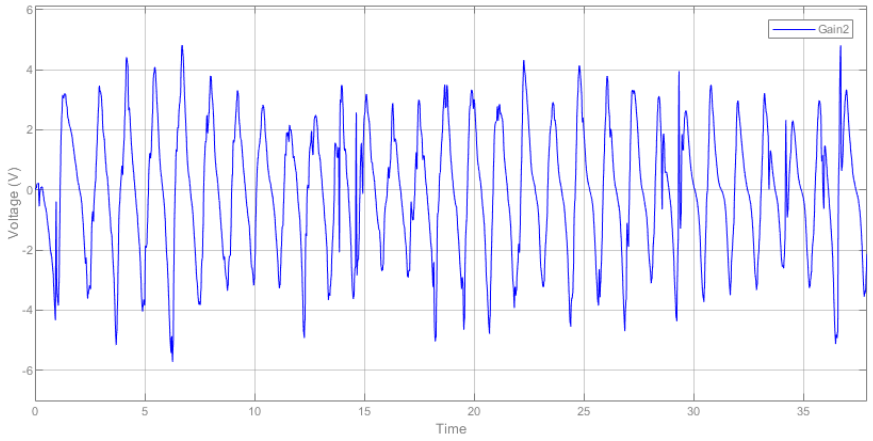

Figure 8.18: *Maximum voltage calculated in MATLAB by using the data from field test.*

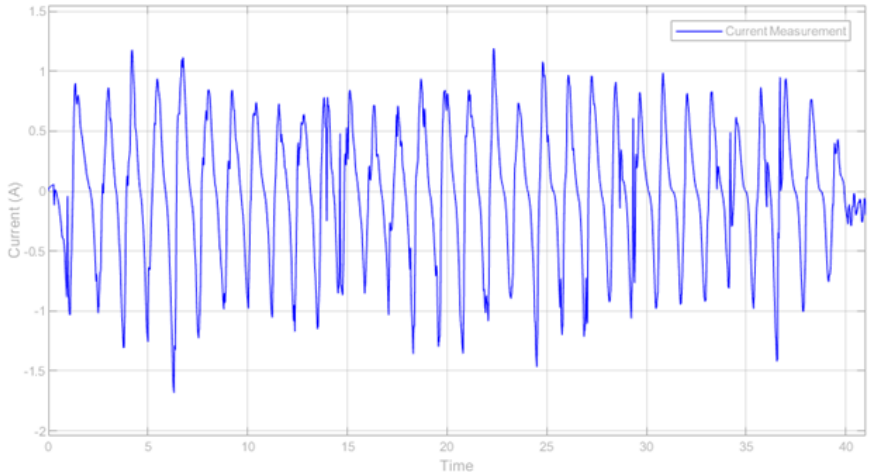

Figure 8.19: *Maximum current calculated in MATLAB by using the data from field test.*

In the second simulation, an electrical load of 120 ohms is added to the design, while the rest of the simulation settings remained unchanged, including the two inputs: the hip joint angle and the angular velocity ratio between the hip joint and the energy harvester. With the introduction of this load, the results showed a reduction in the overall power output when compared to the first simulation. The maximum power output in this case is 1.55W, with the average peak value recorded at approximately 0.55W as shown in Figure 8.20. The voltage output reached a maximum of 11V, with an average peak value of around 8V as shown in Figure 8.21. In terms of current, the maximum output is recorded at 0.14A, while the average peak value is around 0.07A as shown in Figure 8.22.

These results reflect the impact of adding an electrical load to the system, which influences both the power and current outputs. Despite the reduction in power, the voltage output remained significant, which highlights the ability of the system to generate useful electrical energy even when under load. These findings are important for understanding the practical performance of the energy harvester in real-world conditions where it would be powering a device such as an automotive light bulb. Also, the simulated results align closely with the field test results which validate the success of the theoretical approach.

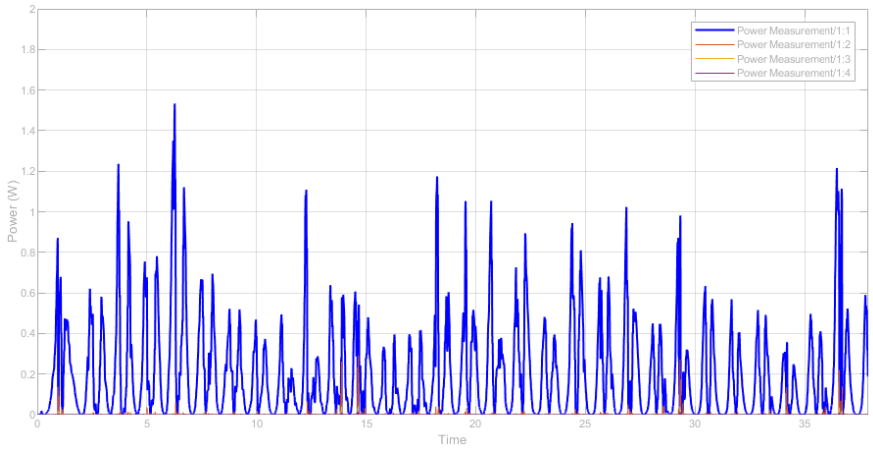

Figure 8.20: *Power calculated in MATLAB with the electrical load by using the data from field test.*

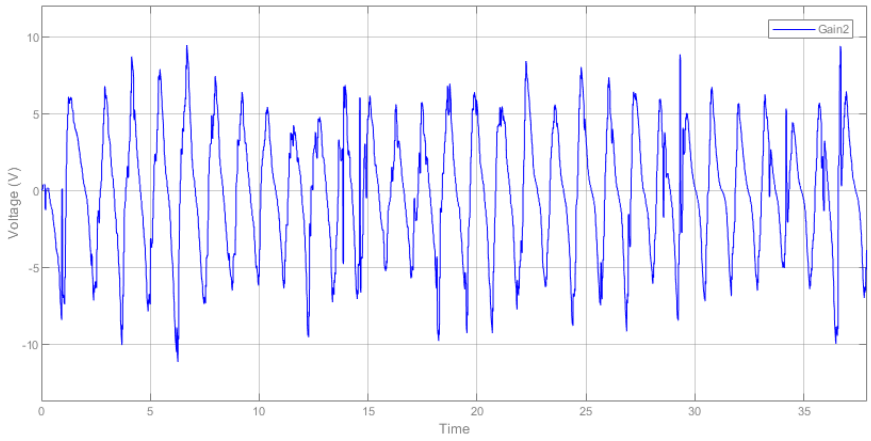

Figure 8.21: *Maximum voltage calculated in MATLAB with the electrical load by using the data from field test.*

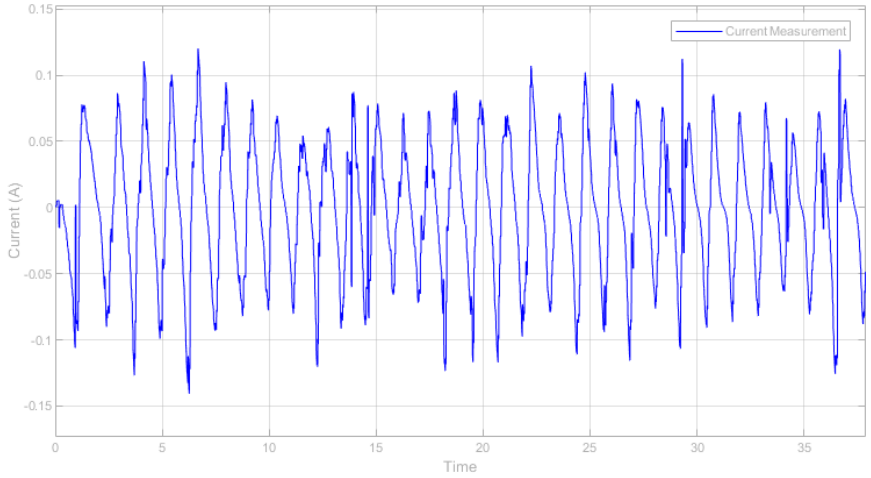

Figure 8.22: *Maximum current calculated in MATLAB with the electrical load by using the data from field test.*

8.4 Comparison between Experiment and MATLAB's Simulation Results

In this section, the comparison between the energy harvested during the experiment and the results from the MATLAB simulation is presented.

To calculate the amount of energy harvested from the experiment, the basic energy equation is used, where energy is equal to power multiplied by time:

$$E = P \cdot t$$

Using this equation and the data obtained from the power output during the experiment, the total energy harvested is calculated. The results of this calculation are shown in Figure 8.23. Over a duration of 37.9 seconds, the total energy harvested amounts to 3.7584 joules.

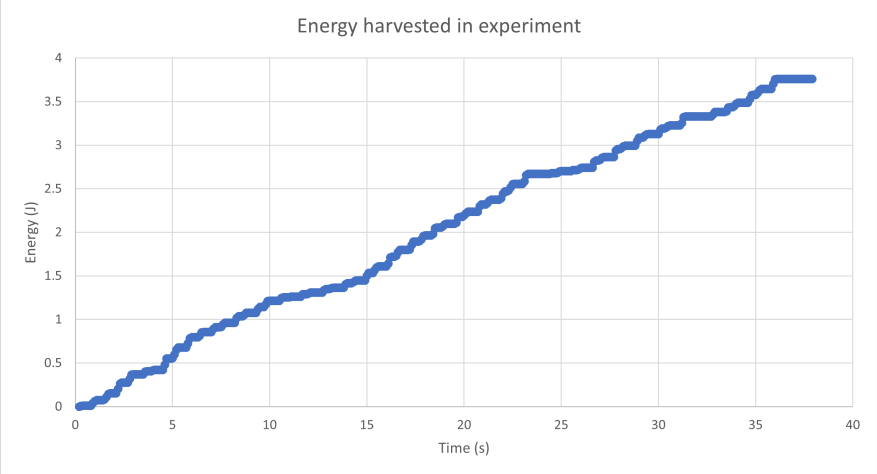

Figure 8.23: *Energy harvested in experiment*

Through the MATLAB simulation, the sum of the energy harvested over the same duration (37.9 seconds) is approximately 7.73 joules as shown in Figure 8.24.

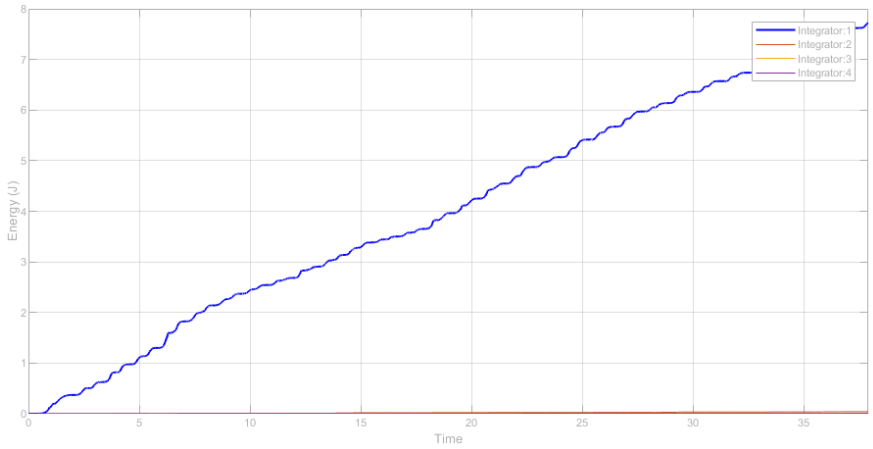

Figure 8.24: *Energy harvested in MATLAB simulation*

The actual energy harvested in the experiment is only about 48.6% of what was obtained

from the MATLAB simulation

This discrepancy highlights a difference between the experimental results and the theoretical values predicted by the simulation. Several factors contribute to this lower-than-expected energy harvesting efficiency in the real-world experiment.

The first factor is the difference between the actual power output and the simulated power output. During the MATLAB simulation, the efficiency of the DC motor, which is used as the energy harvester, is fixed at the maximum value of 65.9%. However, the motor's efficiency as a generator at different rotational speeds is not provided in the specification sheet. Therefore, the simulation results, which assume ideal conditions, are likely overestimated compared to real-world performance, where the motor operates with less than optimal efficiency.

The second factor is the "dead zone" observed during the experiment, which is mentioned in the experiment results section. This dead zone refers to periods during the experiment when there is no power output when the angular speed of the thigh joint fell below 2 degrees per second. In contrast, the MATLAB simulation did not account for this dead zone, and power output is continuously generated throughout the motion cycle. This dead zone effectively reduces the overall energy harvested, as the energy harvester fails to produce any power during slow motions.

By accounting for the dead zone in the MATLAB simulation to be presented in the next section, a more realistic estimate of the energy harvested will be provided, allowing for a more precise comparison with the experimental data.

8.4.1 MATLAB Simulation accounting for the "dead zone"

In order to introduce the "dead zone" in the power measurement during the simulation with MATLAB, several additional blocks need to be implemented into the existing model as shown in Figure 8.25 where number 1 is the "Compare to Constant" block, number 2 is the "Switch" block and number 3 is the "Integrator" block. This modification will allow us to simulate the periods when the angular speed of the thigh joint drops below 2 degrees per second, during which no power is generated by the energy harvester. By introducing this dead zone, the simulation results will more closely align with the real-world observations from the experiment.

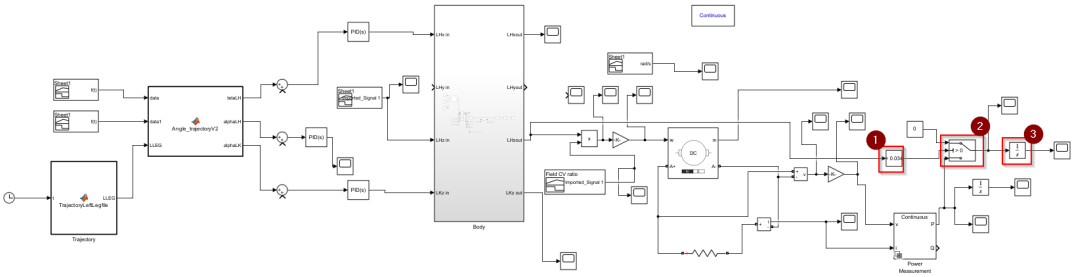

Figure 8.25: *High-level view of new blocks needed in MATLAB simulation*

The first step in implementing this feature is to add a "Compare to Constant" block into the simulation as shown in Figure 8.26. This block will be positioned after the body module but before the input of the angular velocity ratio. The "Compare to Constant" block functions by comparing the angular speed data with a predefined threshold value. In this case, the operator should be set to "smaller or equal to," and the constant value should be set to 0.0349 rad/s, which is equivalent to 2 degrees per second. The output of this block will be a Boolean value (true or false), indicating whether the angular speed has fallen below the specified threshold. If the angular speed is less than or equal to 2 degrees per second, the Boolean value will be true, indicating that the system is in the dead zone and no power should be generated.

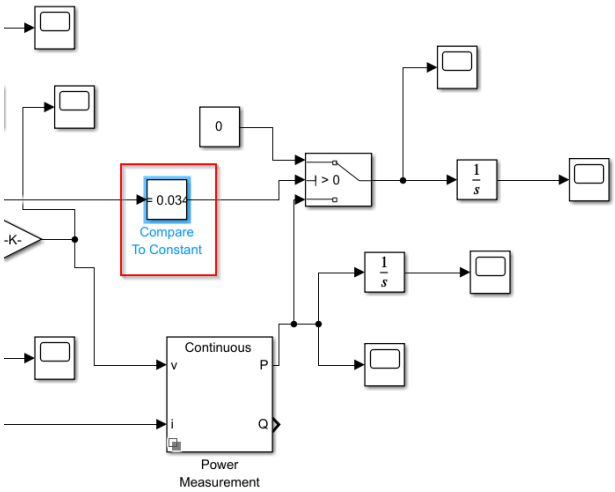

Figure 8.26: *"Compare to Constant" block in MATLAB simulation*

Next, a "Switch" block is introduced into the model as shown in Figure 8.27. This block

has three inputs: Input 1, Input 2, and Input 3. Input 2 will be connected to the output of the "Compare to Constant" block, which will act as the condition for the switch. When the condition is satisfied (i.e., when the angular speed is less than or equal to 2 degrees per second), the value from Input 1 will be passed through. Otherwise, the value from Input 3 will be passed through. In this case, Input 3 will be connected to the original power output calculated by the power measurement block, while Input 1 will be set to zero, ensuring that no power is generated when the system is in the dead zone.

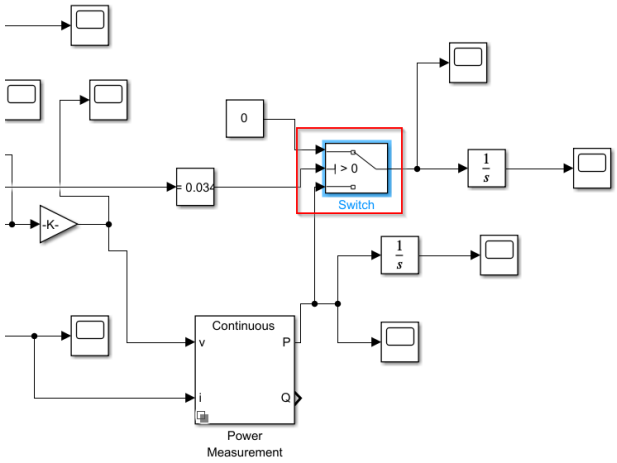

Figure 8.27: *"Switch" block in MATLAB simulation*

Once the switch logic is configured, the next step is to reintroduce the "Integrator" block as shown in Figure 8.28. The integrator is responsible for accumulating the power over time to calculate the total energy harvested during the motion cycle. This is the same approach used in the previous simulations but with the addition of the dead zone condition. By integrating the power values over the entire duration of the simulation, we can obtain an updated estimate of the total energy harvested more accurately.

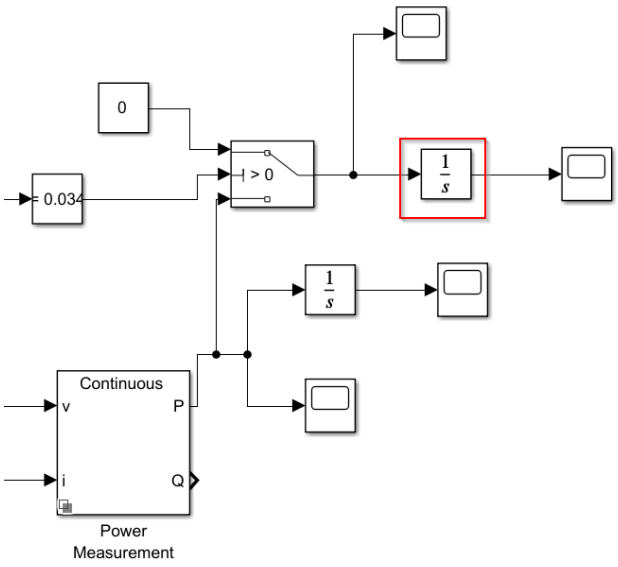

Figure 8.28: *"Integrator" block in MATLAB simulation*

Figure 8.29 illustrates the updated power output with the introduction of the "dead zone." While the maximum power remains unchanged, a clear difference can be observed in the enlarged gaps between each cycle, where the power output drops to zero. These gaps, absent in the previous simulations, align more closely with the real-world data collected during the experiment. This adjustment enhances the realism of the simulation by reflecting the periods of inactivity when the thigh's angular velocity is too low to generate power, as seen in the actual experiment.

The new power output graph with the "dead zone" now has a much closer shape to the measured power output from the field test. This alignment indicates that the modification has effectively captured the system's behaviour under real-world conditions. With these changes, the power output more accurately reflects the limitations observed in practice.

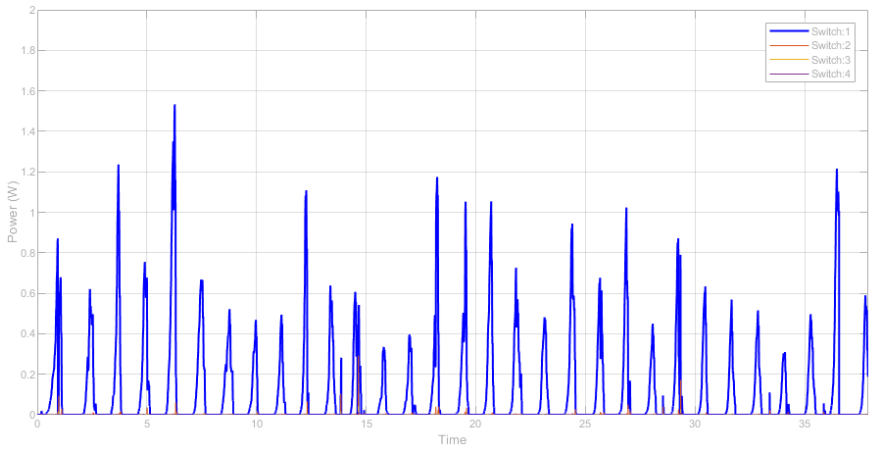

Figure 8.29: *Power generated in MATLAB simulation with "dead zone" introduced.*

Figure 8.30 displays the recalculated energy harvested from the updated MATLAB-Simulink simulation. The new value of the harvested energy is approximately 4.19 Joules for the duration (37.9 seconds) which is close to that from the experiment (3.7584 Joules), This confirms the impact of the "dead zone" on the overall system performance, resulting in a reduction of the theoretical energy output due to the periods of zero power generation.

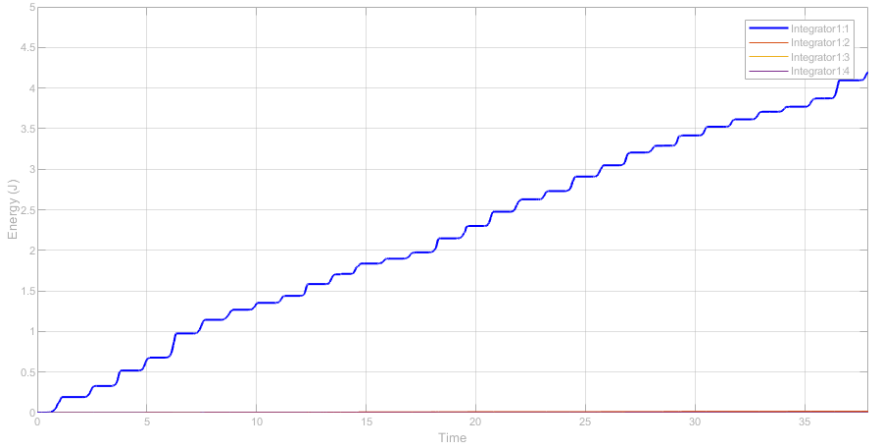

Figure 8.30: *Energy harvested in MATLAB simulation with "dead zone" introduced.*

8.4.2 Energy Converter Conformity

To calculate the conformity of the actual energy harvested in the experiment versus the simulated result, the following equation is used:

$$\frac{3.7584}{4.19} = 0.89.7$$

This calculation yields a conformity of around 89.7%. One challenge in accurately determining the system's efficiency is the variability in the DC motor's performance when used as a generator. The motor's efficiency changes significantly with different rotational speeds, making it difficult to pinpoint an exact value. However, based on the specification sheet, the DC motor has maximum efficiency when operating as a motor at 29 RPM. Considering this, the calculated 89.7% overall conformity during the experiment appears reasonable. It is important to note that the motor did not maintain a constant rotational speed throughout the test, and the motor's efficiency fluctuates considerably depending on the speed.

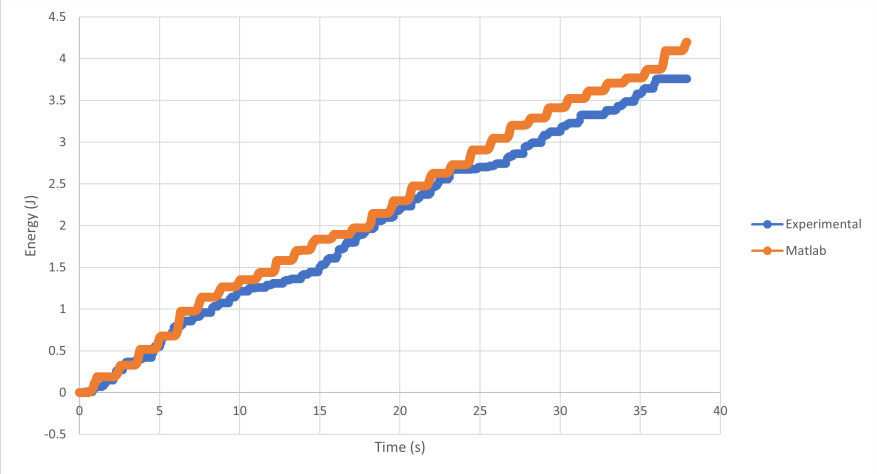

Figure 8.31: *Energy harvested from field test vs energy harvested in MATLAB simulation with "dead zone" introduced.*

Figure 8.31 summarises the comparison between the experimental and simulated results, highlighting the difference between the two methods. While the MATLAB simulation provides an upper bound of the system's potential energy harvesting capability, the experimental data reflect real-world limitations and inefficiencies that can be addressed to improve the system's design.

The comparison between the simulated and actual energy generation has provided valuable insights into the system's performance during the field test. However, energy generation alone does not fully determine the practicality of the energy harvester. To ensure that the system is

suitable for real-world use, it is important to evaluate the torque required from human motion to drive the generator. Excessive torque can create significant resistance, leading to rapid fatigue and limiting the ability to sustain movement. The next section focuses on analysing the torque generated during the field test to assess its impact on user effort.

8.5 Torque for the Energy Harvesting Mechanism Without the Energy Harvester (DC Motor)

To assess the impact of the energy harvester (DC motor) on the torque to move the energy harvesting mechanism by working backward from the available motion data of the thigh, the torque at the hip joint can be determined using the parameters of the human model developed in Chapter 6. From the angular velocity, the acceleration and velocity of the thigh can be computed, taking into account the length of the thigh and the position of the centre of gravity.

A simplified approach to calculating the torque is to use the following equation for rotational motion:

$$\tau = I \cdot \alpha$$

where τ is the torque, I is the moment of inertia, and α is the angular acceleration. However, this simplified method does not account for external forces such as drag, buoyant forces, or gravity, which are necessary in a water environment. While this method provides an initial approximation, it may not fully reflect the resistance experienced by the thigh during motion.

8.5.1 Fluid Forces and Torque Calculation

To achieve a more accurate calculation of the torque, it is necessary to account for the different forces acting on the thigh in water. These include the drag force, added mass force, buoyant force, and gravity force as shown in Figure 3.4 and Figure 3.6. The relevant equations for these forces are discussed Equation 3.3 to Equation 3.8 in Chapter 3. By integrating these equations, the total force acting on the thigh in the vertical direction can be expressed as:

$$F_y = F_{y(\text{drag})} + F_{y(\text{thigh})}$$

where $F_{y(\text{drag})}$ represents the sum of the fluid forces, and $F_{y(\text{thigh})}$ represents the forces required for the motion itself.

As shown in Figure 8.32, the torque can be determined by:

$$\tau = F_y \cdot r$$

where r is the distance from the centre of rotation to the point where the force is applied. Figures 8.33 and 8.34 respectively show the force and the torque evolving with time.

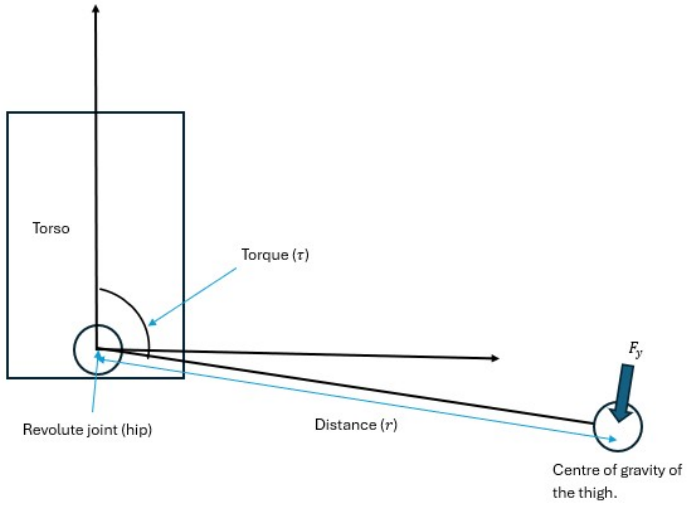

Figure 8.32: *Free body diagram of the thigh segment for force analysis*

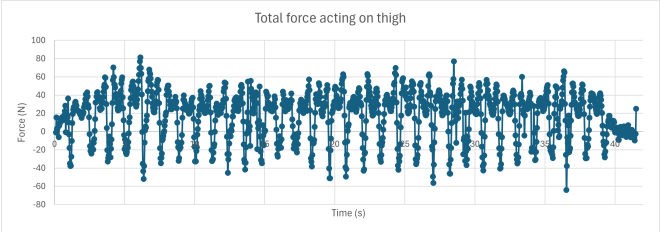

Figure 8.33: *Total force acting on the thigh*

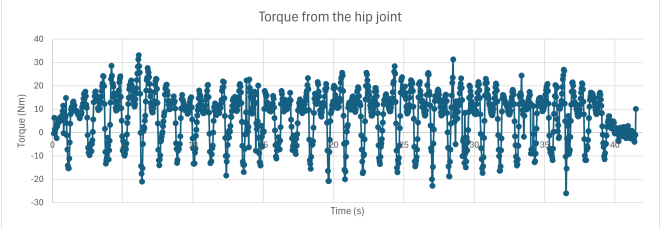

Figure 8.34: *Torque from hip joint*

8.5.2 Torque Required to Drive the Energy Harvester

To determine whether the energy harvester adds significant resistance, the torque required to drive it needs to be calculated. The torque can be calculated using the torque constant of the DC motor, while the preferred method is to extract the torque data from the MATLAB simulation in which, a Scope block is linked to the block of the DC motor (the energy harvester) to monitor its output. Since the Scope block does not have a direct export option, the data must be logged to a file in the MATLAB workspace. The format can be set to "Structure with Time" to ensure that the data is recorded correctly, as shown in Figure 8.35.

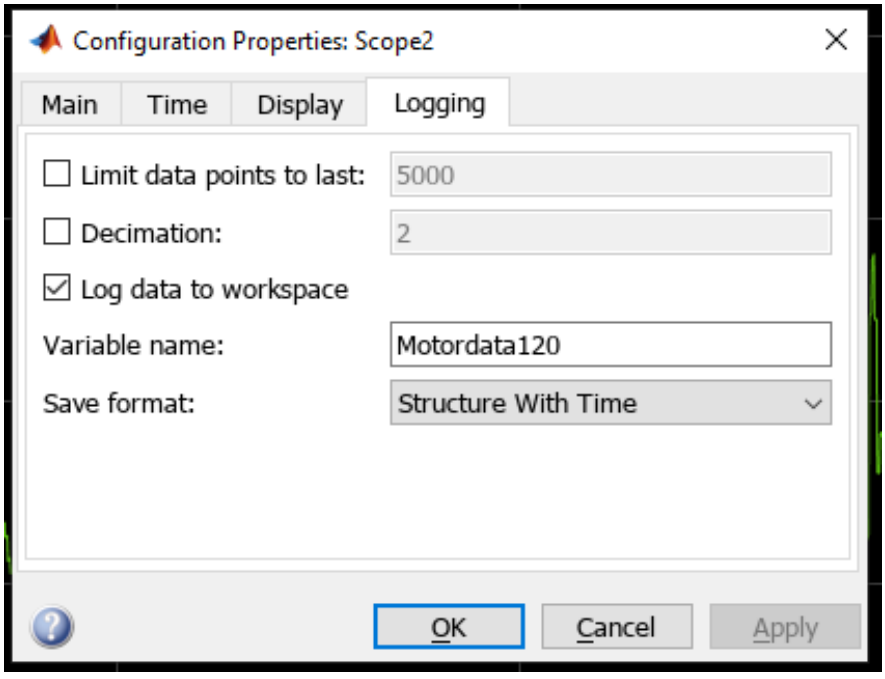

Figure 8.35: *Data exporting configuration in MATLAB*

Once the logging is configured, the simulation can be re-run, and the data will be recorded

in the workspace. The recorded data file, stored in MATLAB's ".mat" format, contains several key columns: armature current (iA), field current (iF), rotor speed (ω), and electromagnetic torque (T_e). The column of interest is the electromagnetic torque (T_e), which represents the torque required by the energy harvester.

Since the energy harvester is fitted with a gearhead, which has a reduction ratio of 244:1, the electromagnetic torque (T_e) is multiplied by this ratio to obtain the actual torque experienced by the wearer:

$$\tau_{\text{harvester}} = T_e \times 244$$

8.5.3 Comparinson of the Torques

Figure 8.36 illustrates the torques required to move the thigh joint and the torque required to rotate the energy harvester respectively. This graph provides insight into whether the energy harvester imposes excessive resistance on the wearer.

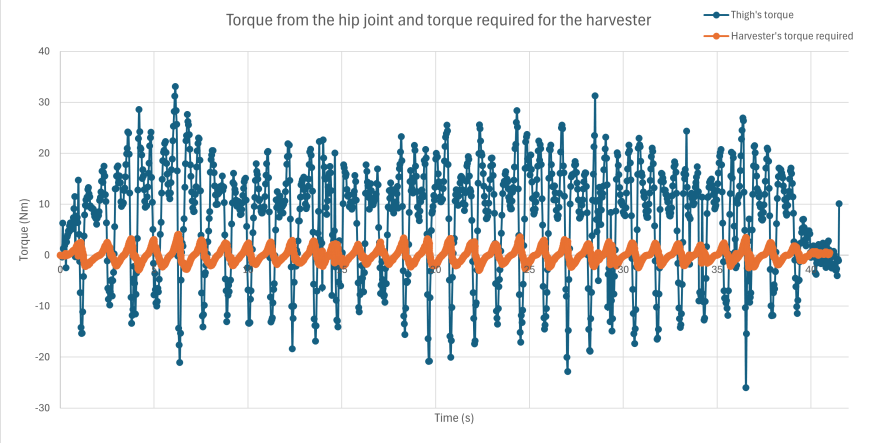

Figure 8.36: *Torque required for the thigh motion (blue) and torque required for the energy harvester (orange)*

Figure 8.36 illustrates the comparison between the torque required for the thigh motion (blue line) and the torque needed to rotate the energy harvester (orange line) during the experiment.

It can be seen that the maximum torque required for the thigh motion reaches a peak of 33.0889 Nm, while the maximum torque necessary to drive the energy harvester is 4.105091 Nm and as shown in the graph, these maximum torque values occur simultaneously, indicating

that both the thigh and energy harvester experience their highest levels of resistance at the same point during the motion.

The torque to drive the DC motor seems like a notable fraction relative to the torque to move the hip joint. It is important to consider that the hip joint can produce significantly higher torques. For example, the hip joint can generate between 100-300 Nm of torque during extension and 80-200 Nm during flexion [112]. Therefore, adding an additional 4.105091 Nm of resistance due to the energy harvester represents a relatively small load for the wearer, particularly when compared to the overall capacity of the hip joint.

Furthermore, this calculation only accounts for the thigh's contribution to the motion and does not include the torque required for other parts of the leg, such as the tibia. In real-world scenarios, where the entire leg's contribution is considered, the percentage of torque consumed by the energy harvester would likely be even lower. This further reduces the impact of the energy harvester on the overall motion of the participant.

During the field test, the participant did not report any noticeable discomfort or difficulty in performing the ladder-climbing motion, which supports the notion that the additional torque resistance posed by the energy harvester is within a tolerable range for normal physical activity. The relatively small additional load imposed by the energy harvester allows the system to function without impacting the natural motion of the participant, which is a major factor in ensuring the practical usability of the energy-harvesting system in real-life situations.

8.6 Ratio between Harvested Energy and Kinetic (Mechanical Energy)

As discussed in Chapter 3, the amount of electrical energy harvested from the motion of the thigh is a fraction of the mechanical energy produced. The ratio (η) between them determines how much of the mechanical energy is converted into electrical energy. It also helps us understand how the energy collected affects the thigh's motion, making sure that the person wearing the device can still move without needing too much extra energy.

$$E_{\text{elec}} = \eta \cdot E_{\text{mech}}$$

where:

- E_{elec} is the electrical energy harvested,
- E_{mech} is the mechanical energy generated by the limbs (thighs and arms).

Figure 8.37 shows the sum of the kinetic energy (grey line) and the sum of the electrical energy harvested (blue line) in the 37.9 seconds period. The sum of kinetic energy is 1,154.99J and the sum of electrical energy harvested is 3.76J which is 0.33% of the sum of kinetic energy.

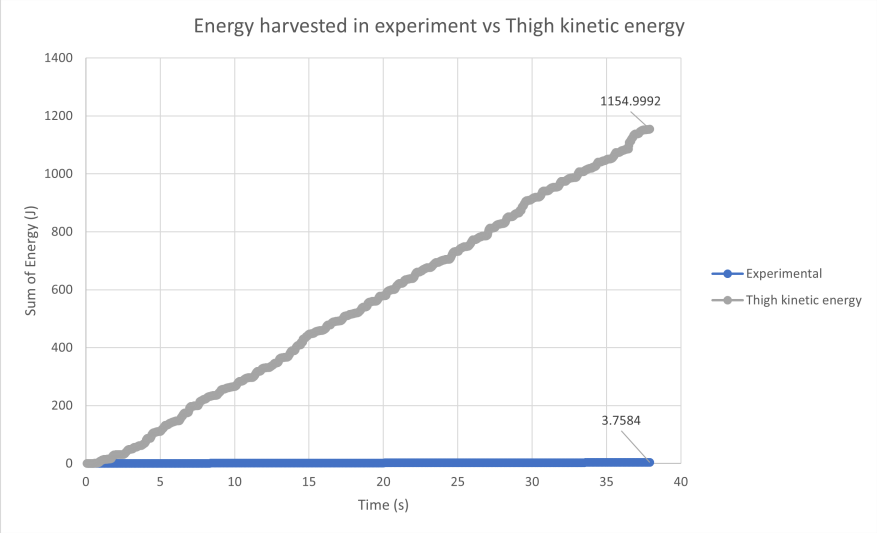

Figure 8.37: *Energy harvested vs thigh kinetic energy*

8.7 Conclusions

The field test and simulation results present a clear picture of the potential of the energy harvesting system integrated within the lifejacket. To validate the theoretical calculations and models developed in the earlier chapters, a series of ground and field tests are conducted. While the ground tests provided a controlled environment to verify basic functionality, the field tests offered a more realistic representation of the system's performance under real-world conditions, simulating a scenario where the device is used in a search and rescue operation. The field

test results and the simulated results with the electrical load align closely which validates the theoretical approach.

The results from both the experimental and simulation phases reveal several key insights. Most notably, the energy harvester's performance in the field tests is lower than that predicted by the MATLAB simulations. The total energy harvested in the field tests added to 3.76 Joules over 37.9 seconds, whereas the MATLAB simulation predicted 4.19 Joules over the same period. This discrepancy between the actual and simulated results shows the difference between theoretical models and real-world applications.

When analysing the power output, the average peak power from the field test is 0.45W, compared to the average peak power of 0.5W from the MATLAB simulation with the electrical load of the automotive light bulb. This comparison indicates that the experimental power output is approximately 90% of the simulated value. Several factors contributed to this reduction in performance.

One of the primary reasons for the lower-than-expected energy output is the presence of a "dead zone" during the field tests. This dead zone refers to periods when the angular velocity of the participant's thigh fell below 2 degrees per second, at which point the energy harvester failed to generate any power. In contrast, the MATLAB simulation did not account for this limitation, as the simulation assumed continuous power generation regardless of the angular velocity. By introducing the dead zone into the MATLAB simulation and re-running the analysis, the simulated energy harvested is reduced to 4.19 Joules, bringing the experimental results and the simulation closer together. This adjustment to the simulation demonstrated that the system's inefficiencies are largely due to the dynamic nature of the thigh motion and the sensitivity of the energy harvester efficiency to lower angular velocities.

Another key factor affecting the power output is the efficiency of the DC motor when operating as a generator. The YG2734 motor has a maximum efficiency of 65.9% when used as a motor, but the exact efficiency when used as a generator varies with the rotational speed and is not provided in the motor's specification sheet. The field test revealed that the motor is not operating at a constant speed, which likely caused fluctuations in the efficiency, further contributing to the reduced power output. Future research should focus on obtaining more

detailed information on the motor's efficiency across a range of speeds, as this would enable more accurate modelling and predictions of the energy harvester's performance.

Despite the lower-than-expected power output, the system demonstrated several positive aspects during the field tests. One important consideration is whether the energy harvester imposed too much resistance on the participant's motion, which would negatively impact the usability of the system. The torque calculations showed that the energy harvester required only 11.58% of the total torque generated by the thigh during the "ladder climbing" motion. This finding is significant because it confirms that the energy harvester does not impose excessive mechanical resistance on the wearer, and the participant did not report any noticeable discomfort during the field tests. Given that the human hip joint can produce between 100-300 Nm of torque during extension and 80-200 Nm during flexion, the additional torque required by the energy harvester is relatively small and did not affect the participant's ability to perform the ladder climbing motion.

The comparison between the experimental results and the simulation provides valuable insights into the energy harvesting potential of the system. While the field tests revealed some inefficiencies that are not accounted for in the initial simulation, the adjustments made to the MATLAB model, such as the introduction of the dead zone, brought the simulated and experimental results closer together. This highlights the importance of iterative testing and simulation in refining the design and improving the accuracy of theoretical models.

Chapter 9

Discussions

The purpose of this chapter is to provide a detailed analysis and interpretation of the experimental results obtained from the ground and field tests and to discuss their implications in the context of the research objectives and existing literature. This chapter also explores the broader significance of the findings, the practical applications of the energy harvesting system, and the limitations of the study. The chapter concludes with recommendations for future research and potential improvements to the energy harvesting system.

9.1 Field Test Observations

The experimental phase focuses on evaluating the performance of the energy harvester integrated into a lifejacket during a simulated drowning scenario in a water-based environment. The field test is conducted in a swimming pool, with the participant performing the "ladder climbing" motion while wearing the lifejacket. This test provided important data on how the system behaved under water-specific conditions such as resistance, buoyancy, and drag. The results obtained during the field test are summarised below.

The field test produces a range of quantitative data, including power output, voltage, current, and total energy harvested. The key results from the test are presented in Table 9.1 and summarised as follows:

- **Peak and Average Power Output:** The maximum power output recorded during the

field test is 754 mW, with the average peak power output stabilising around 450 mW. The power output fluctuated depending on the participant's motion intensity and velocity, showing a strong dependency on the dynamics of the "ladder climbing" motion. The minimum power output of 0 mW is observed during moments of low angular velocity or when the participant temporarily ceased motion.

- **Voltage and Current Measurements:** The highest bus voltage observed is 9.08 V, with the shunt voltage reaching a peak of 9.95 V. The load voltage is measured at 9.09 V during periods of maximum power generation. The peak current recorded is 101.1 mA, corresponding to the highest power output. Periods of lower voltage and current are observed when the participant's motions slowed down, resulting in reduced power generation.

- **Total Energy Harvested:** Over the duration of the test, which lasted 37.9 seconds, a total of 3.76 Joules of energy is harvested. This is slightly lower than the MATLAB simulation's predicted output of 4.19 Joules for the same time period.

- **Dead Zone Effect:** The power output drops to zero during moments when the angular velocity of the participant's thigh fell below 2 degrees per second. This dead zone effect highlights a limitation in the current design, where the system is unable to generate power at very low motion velocities.

- **Electrical Stability:** The electrical measurements remained stable throughout the test, with no signs of voltage spikes, short circuits, or power irregularities. The waterproofing of the system is effective, as indicated by the absence of any electrical faults or performance degradation in the water environment.

Table 9.1: *Summary of key findings from the field testing*

Parameter	Measured Value
Maximum Power Output	754 mW
Average Peak Power Output	450 mW
Minimum Power Output	0 mW
Maximum Bus Voltage	9.08 V
Maximum Shunt Voltage	9.95 V
Maximum Load Voltage	9.09 V
Maximum Current	101.1 mA
Total Energy Harvested	3.76 Joules

The field test demonstrates that the energy harvesting system could generate electrical power under water-based conditions, despite facing challenges such as water resistance and varying motion dynamics. The following observations provide an overall summary of the system's performance:

- The average peak power output achieves during the test (450 mW) is lower than the theoretical prediction as predicted (550 mW), but it is sufficient to power the small IoT devices listed in literature reviews which can be integrated into the lifejacket.
- The variations in voltage and current measurements are consistent with the fluctuations in power output, indicating that the energy harvester's performance is closely linked to the velocity and intensity of limb motions.
- The total energy harvested is slightly lower than the simulated output as predicted, showing the need to refine the theoretical models to better account for real-world inefficiencies and environmental factors. The results from this experiment can help with the refinement directly.
- The system maintains electrical stability and waterproof integrity throughout the test, suggesting that it is well-suited for use in water-based environments.

These findings provide a comprehensive overview of the energy harvester's behaviour in a water-based environment. The results obtain from the field test will serve as a basis for further discussion and analysis in the subsequent sections of this chapter, where they will be compared with theoretical models and used to explore the broader implications of the research.

9.2 Findings from the Experiments

The field test results provide a comprehensive view of the performance and limitations of the energy harvesting system when integrated into a lifejacket and used in a water-based environment. This section interprets the experimental findings by comparing the actual power output, energy conversion efficiency, and mechanical performance with the theoretical predictions from MATLAB simulations. The aim is to identify the factors contributing to the discrepancies between simulated and experimental outcomes, and to evaluate the system's overall efficiency under real-world conditions.

9.2.1 Comparison with Theoretical Calculations

As expected, the experimental power output records during the field test is slightly lower than the theoretical predictions generated through MATLAB simulations. The simulations result in an average peak power output of 550 mW, whereas the actual average peak power output observed during the field test is only 450 mW. This indicates that the theoretical models do not fully capture several real-world inefficiencies present during the experiment which is expected when creating the theoretical models due to the lack of certain data.

One of the primary reasons for this difference is the assumption of maximum efficiency of the DC motor in the theoretical models. This assumption is made intentionally due to the lack of detailed efficiency specifications for the DC motor when used as a generator. Since the motor's efficiency varies significantly with changes in angular velocity and load conditions, it is difficult to input the efficiency line without the data from the supplier or intensive testing. Therefore, the maximum efficiency assumption allows for the calculation of the ideal maximum power output, providing an upper bound for comparison with the experimental results. The

experimental findings can then be used to determine the actual efficiency of the system, serving as a benchmark for refining future models.

During the field test, the efficiency of the motor varied significantly due to fluctuations in angular velocity and load conditions. The observed overall design efficiency is approximately 89.7%, which is lower than the idealised efficiency (100%) assumed in the simulations. This discrepancy is caused by the impact of mechanical and electrical losses, as well as the variability in the motor's performance when operating as a generator. Despite this, the general trend observed in the experimental data—an increase in power output with higher motion velocities—is consistent with theoretical predictions. This suggests that, although the absolute values differed, the behaviour of the energy harvesting system is accurately represented by the models, highlighting their usefulness for predicting system performance under different conditions.

The efficiency of the energy harvesting system is calculated by comparing the ideal maximum electrical energy output from the simulation with the electrical energy output recorded during the test. The overall efficiency of the system is determined to be around 89.7%. This value is lower than the idealised efficiency assumed in the simulations, primarily due to mechanical losses in the telescopic linkage, electrical losses during energy conversion, and the non-linear behaviour of the DC motor when operating as a generator.

Key observations regarding system efficiency include:

- **Motor Efficiency Variability** The efficiency of the brushed DC motor used in the system varied considerably with changes in angular velocity. As a motor, its maximum efficiency is 65.9% at a constant angular velocity of 29 RPM. However, when operating as a generator, the efficiency fluctuates depending on the load and angular velocity. During the field test, the angular velocity of the motor varied due to the changing dynamics of limb motions in water, resulting in an overall efficiency of 89.7% of the maximum efficiency.

- **Mechancial Losses in the Telescopic Linkage** The telescopic linkage connecting the motor to the participant's thigh introduced frictional and inertial losses that reduced the amount of mechanical energy transferred to the motor. These mechanical losses are not accounted for in the simulations, which assumed ideal mechanical efficiency. This factor

contributed to the lower overall system efficiency observed during the field test.

- **Electrical Conversion Losses** Electrical losses occurred during the conversion of mechanical energy into electrical energy, particularly due to resistive heating in the motor windings. These losses are not included in the simulations, which assumed a perfect energy conversion process. The observed fluctuations in voltage and current during the test further indicate that the energy conversion efficiency is affected by the dynamic nature of the participant's motions.

The overall system efficiency of 89.7% observed during the field test is considered reasonable, given the variability in motor efficiency and the presence of real-world mechanical and electrical losses. This result highlights the limitations of the theoretical models, which did not account for these factors. The experimental findings provide valuable data that can be used to refine the efficiency estimates in future modelling efforts. Without the efficiency curve from the manufacturer, the actual efficiency of the motor working as a generator can only be found through experiments.

The field test results confirm that the energy harvesting system can generate electrical power in a water-based environment, but its performance is influenced by several factors not fully captured in the theoretical models. The slightly lower-than-expected power output and overall system efficiency highlight the need for further refinement of the design and modelling approach. The observed efficiency of 89.7% is reasonable given the variability in motor performance and the presence of mechanical and electrical losses. These findings suggest that, while the system is functional, there is significant room for optimisation to improve its performance and expand its range of applications.

The experimental results provide valuable insights into the limitations of the theoretical models and the challenges of developing wearable energy harvesting systems for water-based environments. The knowledge gained from these findings will inform future research efforts to enhance the system's design and improve its performance under real-world conditions.

The findings from the field test provide valuable insights into the practical application and effectiveness of the energy harvesting system integrated into a lifejacket. This section discusses

the broader significance of the experimental results, evaluates the system's ability to power IoT devices, and compares the output power with typical IoT sensor requirements. The results confirm the feasibility of using the energy harvester as a sustainable power source for basic IoT functionalities in lifejackets, validating the research objectives and contributing to the ongoing development of wearable technology for water safety applications.

9.2.2 Validation of the System Design

The close correlation between the theoretical predictions and the experimental outcomes validates the system design in terms of accuracy and robustness. The MATLAB model is important in predicting the power output of the energy harvester under various motion conditions, and the experimental results confirmed the reliability of these predictions with only a limited margin of error. This demonstrates the accuracy of the theoretical approach taken to simulate the complex dynamics of human motion and energy conversion.

A key achievement of this research is the system's ability to consistently generate sufficient power to meet the demands of IoT devices, as outlined in the literature review. The harvester produced an average power of **450 mW**, which is significantly higher than the power requirements for small IoT sensors typically used in life-saving applications, such as GPS, health monitoring, and emergency communication systems. The IoT devices reviewed generally require about **210.6915 mW** (Table 2.2), meaning that the harvester can provide more than double the required energy, ensuring a robust margin for reliable operation even under less-than-ideal conditions.

The simulation process is particularly successful in predicting the performance of the system under varying electrical loads. By incorporating the automotive light bulb with a **120 ohm** resistance into the simulation, the MATLAB model demonstrates that the energy harvester can generate approximately **0.55 W** with a steady output voltage of **8 V**. This simulated result closely matches the experimental findings, where the system performs within similar ranges. Such validation of the simulation model through real-world data solidifies the credibility of the modelling approach.

Furthermore, the integration of a "dead zone" in the simulations, which accounts for the system's inability to generate power when the thigh's angular velocity falls below **2 degrees per**

second, enhances the realism of the model.

9.2.3 Quatification of the Impact on Human Motion

One of the important aspects of the energy harvesting system design is ensuring that it does not hinder the wearer's motion by creating excessive mechanical resistance. To assess this, torque calculations are carried out to compare the forces required for normal motion with and without the energy harvester attached. The results of these calculations demonstrate that the energy harvester operates without placing a significant load on the wearer, allowing for normal motion with minimal additional resistance.

The torque generated by the hip joint during motion is calculated based on the motion data collected from the field experiments. The total torque needed to move the leg without the energy harvester is estimated to be around **33.1 Nm** at its peak. This value represents the force exerted by the thigh during the "ladder-climbing" motion, which simulates the motions of a person in distress during a drowning event. This type of motion is critical to the energy harvesting process as it allows the system to capture kinetic energy from the wearer's natural motions.

When the energy harvester is attached, the maximum additional torque required to rotate the device is calculated to be **4.1 Nm**. This value is obtained by considering the torque required to overcome the resistance of the brushed DC motor. Importantly, the torque generated by the energy harvester represents only about **11%** of the total torque produced by the hip joint. This shows that the system introduces only a small amount of additional resistance. In reality, the percentage will be lower as the torque calculated at the hip joint does not include the tibia. With the weight and distance of the tibia from the hip joint, the percentage of driving energy harvester will be lowered significantly.

To further confirm that this additional torque does not significantly impact the wearer's motion, the energy harvested from the system is compared to the total kinetic energy generated by the thigh (not including the tibia) during motion. The energy harvested from the system during the field tests amounted to about 3.76 Joules. In contrast, the total kinetic energy produced by the thigh during motion is far greater, indicating that only a small portion of the wearer's thigh kinetic energy is being converted into electrical power. This suggests that the energy

harvester is efficient without creating noticeable drag or resistance.

By keeping the torque generated by the energy harvester low, the design ensures that the wearer can perform natural motions without feeling hindered. The **4.1 Nm** of additional torque is small enough that it does not cause significant strain on the wearer's muscles or joints, allowing them to continue moving freely. This is essential in ensuring that the lifejacket with the energy harvesting system remains comfortable to wear, even during active situations like a search and rescue scenario.

In summary, the torque and energy calculations clearly show that the energy harvesting system does not create excessive resistance for the wearer. The additional **4.1 Nm** of torque is well within acceptable limits and does not disrupt normal motion, making the system practical for use in real-life scenarios. By maintaining low resistance, the design ensures that the energy harvester can generate sufficient power without compromising the wearer's mobility or comfort.

9.2.4 Sustainability and Reliability of the Energy Harvesting System

The ability of the energy harvesting system to generate power from the wearer's motions in a water-based environment has important implications for the sustainability and reliability of IoT-enabled lifejackets. Traditional battery-powered systems are prone to degradation over time, require regular maintenance, and may fail in critical situations due to power depletion. In contrast, the energy harvesting system developed in this thesis provides a continuous power source that is sustained by the wearer's natural motions. This eliminates the need for frequent battery replacements and reduces the overall maintenance burden, making the system more reliable in emergency situations.

The experimental results confirm that the energy harvester can support basic IoT functionalities without relying on external power sources. This capability enhances the overall safety and effectiveness of the lifejacket, as it ensures that emergency devices remain operational. By providing a self-sustaining power source, the energy harvesting system improves the reliability and longevity of IoT lifejackets, making them a more viable option for widespread use in water safety applications.

The experimental findings validate the proposed energy harvesting design and demonstrate

its capability to meet the power requirements of basic IoT functionalities in lifejackets. The results contribute to the ongoing development of wearable technology for water safety and support the feasibility of integrating energy harvesting systems into life-saving equipment for search and rescue operations.

One of the main design objectives for this energy harvesting system is to ensure that the device did not interfere with the wearer's natural motions or cause discomfort, particularly during the "ladder climbing" motion. This focus on wearability is critical because the system must be integrated into a lifejacket, which is intended for emergency situations. Any added discomfort or restriction could impair the wearer's ability to move freely, and in turn, affect the safety and effectiveness of the lifejacket.

To evaluate wearability, several factors are taken into account during the design process. First, the energy harvester is positioned on the waist and thigh strap to minimise interference with the wearer's legs and hips. This placement ensures that the harvester can capture kinetic energy from the vertical rotation of the thigh without restricting motion. The telescopic linkage connecting the motor to the thigh strap is designed to be flexible, allowing it to extend and contract naturally with the wearer's motion, reducing the risk of discomfort or mechanical interference.

The torque calculations carries out in this study provides a deeper understanding of the mechanical load the harvester places on the wearer. The results show that the additional torque required to rotate the energy harvester is **4.1 Nm**, which is less than **12%** of the total torque generated by the hip joint during normal motion. This small increase in mechanical load is unlikely to be noticeable by the wearer, meaning the device does not impose excessive strain on the thigh or hip joint.

Field testing further confirmes that the harvester's design does not negatively affect the wearer's comfort. The participant reports no significant discomfort while wearing the lifejacket during the simulated "ladder climbing" motion. The energy harvester operated smoothly without introducing excessive drag or resistance. The fact that the device could harvest energy effectively without any noticeable impact on comfort is a major success of the design.

In addition to these mechanical factors, the overall weight and size of the energy harvester

are carefully considered to avoid burdening the wearer. The DC motor and telescopic linkage are compact and lightweight, ensuring that the system integrates seamlessly into the lifejacket without adding significant bulk. This attention to the physical dimensions of the system is important for maintaining the wearer's mobility, particularly when transitioning between different motions such as swimming or climbing.

The flexibility of the mechanical components also plays a role in maintaining comfort. The telescopic linkage is designed to move with the wearer's body, adjusting as the thigh moves through its range of motion. This prevents the system from pulling or tugging on the wearer's body, reducing the risk of discomfort over time. The smooth operation of the telescopic linkage ensures that the system works in harmony with the wearer's natural motions, rather than obstructing them.

In conclusion, the energy harvester is designed with wearability and comfort as a primary focus. The torque generated by the system is minimal, and the flexibility and lightweight nature of the components ensure that the wearer can move freely and comfortably, even during strenuous motions like "ladder climbing". The system's design ensures that the wearer can perform essential motions in an emergency without any significant restriction or discomfort, making the energy harvester suitable for real-world use in lifejackets.

9.3 Future Work and Research Recommendations

The findings from this research have demonstrated the feasibility of integrating energy harvesting systems into wearable lifejackets to support basic IoT functionalities. However, the study has also identified several limitations and opportunities for further refinement and optimisation. This section outlines the potential future research directions that could be pursued to enhance the performance, reliability, and applicability of the energy harvesting system for real-world applications.

9.3.1 Prototype Design and Component

The energy harvesting system tested in this study is a prototype specifically built for experimental purposes. As a result, several aspects of the design and component selection are constrained by the availability of materials and equipment. The following limitations are identified:

- **Motor Selection and Efficiency:** The prototype utilises a brushed DC motor (YG2734) as the energy harvester. While this motor is selected due to its specification matching the design requirement, availability and ease of integration into the prototype, it may not necessarily be the optimal choice for a production-level design. If the system is to go into production, a different type of motor, such as a brushless DC motor, could be used. Brushless motors typically offer higher efficiency, longer lifespan, and lower maintenance requirements compared to brushed motors, making them more suitable for long-term use in wearable devices.

- **Housing and Mounting of the Motor:** The housing and mounting of the motor in the prototype are not fully optimised for real-world applications. The current design is primarily focused on ease of assembly and functionality for experimental testing. In a production model, the motor housing and mounting could be customised to improve the system's waterproofing, durability, and integration into the lifejacket. This would ensure better protection against saltwater exposure and other environmental factors, reducing the risk of mechanical failure during extended use.

- **Telescopic Linkage Design** The telescopic linkage connecting the motor to the participant's thigh is fabricated using standard components such as 12mm aluminium tube and 10mm wooden rod, and its design is not optimised for efficiency or wearability. The linkage introduced additional mechanical losses due to friction and inertial effects, which contributed to the lower overall system efficiency. If the system is to be further developed, the telescopic linkage could be replaced with a more efficient design that minimises mechanical losses and improves energy transfer to the motor. Alternative materials or configurations could also be explored to reduce the impact of water resistance and improve user comfort.

- **Designing a Mechanical Rectifier and Flywheel System:** The experimental findings highlight the presence of a "dead zone" where no power is generated when the motor's angular velocity falls below a certain threshold. One potential solution to eliminate this issue is to design a mechanical rectifier that ensures the motor rotates in only one direction, regardless of the direction of the wearer's limb motions. Incorporating a flywheel-type design could also help maintain the angular velocity of the motor, providing a more consistent energy output. The flywheel would store kinetic energy during periods of high motion intensity and release it during low-velocity motions, ensuring continuous power generation and reducing the impact of the "dead zone."

- **Optimisation of Mechanical Linkage Design:** The telescopic linkage used in the prototype introduced mechanical losses due to friction and inertial effects. Future research could focus on redesigning the linkage to minimise these losses, either by using alternative materials or by refining the geometric configuration of the linkage components. Lightweight and corrosion-resistant materials could be explored to enhance durability and reduce the impact of water resistance on the wearer's motions.

- **Integration of Advanced Control Systems:** The efficiency of the energy conversion process could be enhanced by incorporating advanced control systems that monitor the angular velocity of the motor and adjust the load conditions in real-time. Such systems could optimise the energy transfer process, ensuring that the motor operates at its maximum efficiency under varying motion dynamics.

- **Energy Storage Capacity and Backup Duration:** In cases where the wearer is unconscious or too fatigued to move, stored energy must sustain IoT functions. To operate at approximately 210 mW for 1 hour would require storing at least 756 J. This could be achieved with a supercapacitor of around 420 F at 2 V. Typical sizes for such components range from approximately 40–60 mm in diameter and 60–100 mm in height. Future designs should consider this for reliable emergency operation.

These design and component limitations are inherent to the prototype nature of the system and can be addressed in future iterations of the energy harvester. Optimising the motor, housing,

and linkage would significantly enhance the system's performance, making it more suitable for practical deployment in water-based safety equipment.

9.3.2 Future Experimental Setup and Testing

The experimental setup and testing conditions impose certain constraints that influence the results and may limit the generalisability of the findings. Key constraints include:

- **Controlled Environment:** The field test is conducted in a swimming pool under controlled conditions. While this provides a safe and consistent environment for evaluating the performance of the energy harvesting system, it does not fully replicate the dynamic and unpredictable conditions that may be encountered in open-water scenarios. Factors such as varying water currents, wave motion, and fluctuating temperatures are not considered in this study, which may affect the system's performance in real-world applications.

- **Simplified Motion Patterns:** The participant's motions are limited to a predefined "ladder climbing" motion during the field test. Although this motion is chosen to simulate the typical behaviour of a person during a drowning event, it does not encompass the full range of motions that may occur in an actual emergency situation. motions such as sudden changes in direction, involuntary spasms, or attempts to reach for objects are not simulated, which may influence the energy harvesting system's performance and efficiency.

- **Lack of Long-Term Durability Testing:** The prototype is only tested over a short duration in a controlled environment. Long-term testing to evaluate the durability and reliability of the system under prolonged use is not conducted. Factors such as wear and tear, corrosion, and the impact of continuous exposure to water on the mechanical and electrical components are not assessed. This limits the ability to predict the long-term performance of the energy harvesting system and its suitability for extended use in real-world applications.

- **Evaluation of Wearability and User Comfort** Testing the system under different motion patterns would provide insights into its impact on the wearer's comfort and mobility.

Future research could explore design modifications that reduce resistance and improve wearability, ensuring that the energy harvester does not hinder the wearer's ability to perform survival actions.

These experimental constraints suggest that further testing under more varied and realistic conditions is necessary to fully understand the capabilities and limitations of the energy harvesting system.

9.3.3 Modelling and Theoretical Assumptions

The theoretical models developed in this study assumes ideal conditions for the energy harvesting system, which contributes to discrepancies between the simulated and experimental results. The theoretical calculations assume that the energy harvesting system operated at maximum efficiency, not including all of the real-world mechanical and electrical losses. This assumption is made intentionally due to the lack of detailed efficiency specifications for the motor when used as a generator. While this provided an upper bound for power output, it led to an overestimation of the energy generation capabilities. The experimental findings, which show an overall system efficiency of 89.7%, provide a more realistic estimate of the harvester's performance and can be used to refine future models.

The limitations identified in this study are primarily due to the prototype nature of the energy harvesting system and the constraints imposed by the experimental setup. These limitations do not detract from the overall validity of the findings but rather provide a foundation for future research and development efforts aim at optimising the system for practical use.

9.3.4 Integration with Advanced IoT Functionalities

The successful generation of power from the energy harvesting system opens up new opportunities for integrating advanced IoT functionalities into lifejackets. Future research could focus on incorporating additional sensors and communication modules to enhance the safety and functionality of the lifejacket. Potential areas of development include:

- **Real-Time Health Monitoring:** Integrating physiological sensors to monitor the wearer's

heart rate, body temperature, and oxygen saturation could provide critical data to rescue teams during an emergency. This information could be transmitted in real-time to improve situational awareness and support more effective rescue efforts.

- **Environmental Sensing and Monitoring:** Adding sensors to monitor water quality, temperature, salinity, and other environmental parameters could provide valuable data for assessing the safety of the water environment. These sensors could be powered by the energy harvesting system, enabling continuous monitoring without the need for external power sources.

- **Automated Distress Signalling and Communication:** Implementing automated distress signals that activate when certain conditions are met (e.g., prolonged submersion or abnormal physiological readings) could enhance the wearer's safety. The energy harvesting system could support these functionalities, ensuring that the communication modules remain active throughout the duration of a search and rescue mission.

The integration of advanced IoT functionalities would significantly expand the capabilities of IoT-enabled lifejackets, making them a more powerful tool for enhancing safety and communication in water-based environments.

9.3.5 Design Optimisation

Given that the energy harvesting system developed in this research is a prototype, future research could focus on refining the design for potential commercialisation. This would involve optimising the system for mass production, improving its wearability and durability, and reducing production costs. Potential areas of development include:

- **Customising the Motor and Linkage Design:** The motor and telescopic linkage could be redesigned to achieve higher efficiency and better integration into the lifejacket. This would involve collaborating with manufacturers to develop customised components that meet the specific requirements of the energy harvesting system.

- **Enhancing Waterproofing and Mechanical Stability:** The housing and mounting of the motor could be further optimised to improve waterproofing and mechanical stability. This would ensure that the system can withstand prolonged exposure to water and operate reliably in harsh conditions.

- **Exploring New Materials and Manufacturing Techniques:** Using advanced materials, such as lightweight composites or corrosion-resistant alloys, could improve the system's durability and reduce its weight. Future research could also explore new manufacturing techniques, such as 3D printing, to create more complex and efficient designs.

- **Investigating Maximum Torque:** Future research could explore the maximum torque resistance that the energy harvester can impose on the participant's thigh motion under various conditions. It is crucial to ensure that the energy harvester does not generate excessive resistance, which could cause discomfort during movement. The findings could provide insights into system limitations, assist in refining the gear ratio, and optimise the rotational speed of the DC motor, enhancing power generation efficiency while maintaining user comfort.

Design optimisation for commercialisation would bridge the gap between the prototype developed in this research and a market-ready product, making the energy harvesting system a viable solution for enhancing water safety equipment.

Overall, the future research directions outline in this section provide a roadmap for further developing the energy harvesting system and enhancing its performance, efficiency, and applicability in water-based environments.

9.4 Conclusion

The energy harvesting system integrated into the lifejacket is successfully tested in a simulated drowning scenario, demonstrating its capability to generate electrical power from the wearer's motions in a water-based environment. Despite facing challenges such as the presence of a "dead zone" at low angular velocities and lower-than-expected power output, the system is able

to produce sufficient energy to power basic IoT devices, validating its potential for practical applications.

The field test results show a maximum power output of 754 mW and an average power output of 450 mW, which is higher than the typical power consumption of IoT sensors (210.6915 mW) as discussed in the Literature Review chapter. This confirms that the energy harvesting system is capable of supporting basic IoT functionalities in lifejackets, such as GPS tracking, communication modules, and environmental sensors, without relying on external batteries. The experimental findings provide a realistic benchmark for assessing the performance of wearable energy harvesters and highlight the need for further optimisation of the system's design to achieve higher efficiency and reliability.

The study identifies several limitations of the current prototype, including variability in motor efficiency, and mechanical losses in the telescopic linkage. These limitations contribute to the lower harvesting system efficiency of 89.7%, compared to the idealised maximum efficiency assumed in the theoretical models. Addressing these limitations through the use of alternative motor types, such as brushless DC motors, and redesigning the mechanical linkage could significantly enhance the system's performance.

The chapter also discusses the potential for future research to develop improved theoretical models that incorporate the variable efficiency of the motor and other motion patterns. Such models would provide a more accurate representation of the energy harvesting system's performance under diverse conditions and guide future design optimisations. Testing the system under varied environmental conditions, such as open water scenarios and long-term durability assessments, is also recommended to gain a deeper understanding of its capabilities and limitations.

Furthermore, the inclusion of a mechanical rectifier and flywheel system is suggested as a possible solution to eliminate the "dead zone" issue observed during the experiment. This would ensure that the motor rotates in a single direction and maintains a consistent angular velocity, thereby improving energy generation at low motion velocities.

Overall, the findings from this chapter validate the feasibility of the proposed energy harvesting system for integration into IoT-enabled lifejackets. The system's ability to generate power from the wearer's natural motions supports its use as a sustainable and reliable power

source for basic IoT devices in water safety equipment. Future research and development efforts should focus on optimising the system's efficiency, refining its design, and exploring new applications to fully realise its potential for enhancing water safety and supporting search and rescue operations.

This thesis has explored the development and experimental validation of an energy harvesting system integrated into IoT lifejackets, with the goal of providing a sustainable power source for advanced functionalities such as real-time location tracking, health monitoring, and emergency communication. The research addresses the key challenge of limited energy storage in IoT devices by proposing a novel solution that generates power from the wearer's natural motions during a simulated drowning event. Through detailed modelling, experimental testing, and analysis, the study has demonstrated the feasibility and potential of the proposed system to enhance water safety and support search and rescue operations.

List of Symbols

α	Angular acceleration (rad/s^2)
η	Energy harvester balance ratio
η_0	Intrinsic impedance of free space (Ohms)
μ	Gearhead ratio
ω	Angular velocity (rad/s)
ω_{β_g}	Angular velocity of the generator shaft (rad/s)
ω_β	Angular velocity of the energy harvester before gearhead (rad/s)
ω_γ	Angular velocity of the hip joint (rad/s)
ρ	Density (kg/m^3)
τ	Torque (Nm)
θ	Angular displacement (degrees or radians)
A	Cross-sectional area (m^2)
a	Acceleration (m/s^2)
B	Magnetic flux density (T)
C	Capacitance (F)
C_a	Added mass coefficient

C_{pd}	Passive drag coefficient
d	Distance (m)
E	Energy (J)
e	Ellipse eccentricity
E_{elec}	Electrical energy harvested (J)
E_{field}	Electric field strength (V/m)
E_{mech}	Mechanical energy (J)
F	Force (N)
f	Frequency (Hz)
F_a	Added mass force (N)
F_b	Buoyancy (N)
F_n	Normal drag force (N)
f_r	Resonant frequency (Hz)
F_t	Tangential drag force (N)
F_{ad}	Active drag force (N)
F_{pd}	Passive drag force (N)
g	Gravitational acceleration (9.81 m/s^2)
I	Moment of inertia (kg·m^2)
J	Rotational inertia (kg·m^2)
k	Spring constant (N/m)
Kg	Electromotive-force constant (V·s/rad)

L Length (m)

m Mass (kg)

P_g Electrical power (W)

P_{ERP} Effective radiated power (W)

P_{in} Input power (W)

P_{load} Power consumed by the load (W)

P_{max} Maximum electrical power (W)

P_{out} Power output (W)

Q Charge (C)

R Resistance (Ohms)

r Radius or distance from center of rotation (m)

R_i Internal resistance (Ohms)

R_o External resistance (Ohms)

R_{load} Resistance of the load resistor (V)

R_{shunt} Resistance of the shunt resistor (V)

S Power density (W/m^2)

t Time (s)

v Velocity (m/s)

V_g Voltage generated (V)

V_{bus} Bus voltage (V)

V_{load} Load voltage (V)

V_{shunt} Shunt voltage (V)

Z Impedance (Ohms)

Appendix A

Data Collected by Computer Vision

Landmark	x	y	z	Confidence
0	0.484963059	0.333721846	-0.217802867	0.999979496
1	0.488899052	0.321554661	-0.21238032	0.999950051
2	0.492736697	0.321667999	-0.212400466	0.999936938
3	0.495788723	0.321850657	-0.21248354	0.999922395
4	0.479836673	0.322546661	-0.204936296	0.99995482
5	0.477822483	0.323011816	-0.204967842	0.999940634
6	0.476036906	0.323996425	-0.205019102	0.999950409
7	0.500341237	0.325608492	-0.145651981	0.999941349
8	0.473731101	0.330042303	-0.111377828	0.999985099
9	0.49235943	0.345472425	-0.19023104	0.999993801
10	0.483088523	0.345552117	-0.180463657	0.999996543
11	0.528059006	0.389805317	-0.088473909	0.999925613
12	0.452477872	0.38676703	-0.056246422	0.999996424
13	0.560082555	0.450066537	-0.195516557	0.966762543
14	0.415857017	0.441281646	-0.083209597	0.991085231
15	0.544317007	0.422199845	-0.361873895	0.842974365

Table A.1: *Sample table of the data collected by computer vision*

Table A.2: *Landmark codes and anatomical definitions used in Mediapipe Pose model.*

Code	Anatomical Landmark	Code	Anatomical Landmark
X0	Nose	X17	Left pinky
X1	Left eye inner	X18	Right pinky
X2	Left eye	X19	Left index finger
X3	Left eye outer	X20	Right index finger
X4	Right eye inner	X21	Left thumb
X5	Right eye	X22	Right thumb
X6	Right eye outer	X23	Left hip
X7	Left ear	X24	Right hip
X8	Right ear	X25	Left knee
X9	Mouth left corner	X26	Right knee
X10	Mouth right corner	X27	Left ankle
X11	Left shoulder	X28	Right ankle
X12	Right shoulder	X29	Left heel
X13	Left elbow	X30	Right heel
X14	Right elbow	X31	Left foot index
X15	Left wrist	X32	Right foot index
X16	Right wrist		

Appendix B

Data on Energy Harvester's Angular Velocity from the Motion Capture in the Water

d1	d2	L	$u\beta$	$u\gamma$	Ratio	$\omega\beta$ deg/s
0.25	0.3	0.477556041	0.839942353	-0.503731818	-0.316443584	
0.25	0.3	0.482078442	0.850067567	-0.532664162	-0.331479765	-19.27656773
0.25	0.3	0.486755388	0.860517675	-0.562872049	-0.346912677	-21.53302119
0.25	0.3	0.491700634	0.871544589	-0.595130089	-0.363105138	-24.69755293
0.25	0.3	0.496911803	0.88313998	-0.629475599	-0.380032591	-28.38317074
0.25	0.3	0.501941534	0.894308554	-0.662968692	-0.396242578	-29.89928637
0.25	0.3	0.507014509	0.90555086	-0.697091416	-0.412468324	-33.0069743
0.25	0.3	0.510753295	0.913822507	-0.722459522	-0.424349405	-26.27326869
0.25	0.3	0.514297551	0.921653119	-0.746679808	-0.435553196	-26.7299137
0.25	0.3	0.516386539	0.926263719	-0.761033721	-0.442130262	-16.60413796
0.25	0.3	0.516545322	0.926614023	-0.762127128	-0.442629386	-1.283643688
0.25	0.3	0.515294469	0.923853851	-0.7535226	-0.438694365	9.944809603
0.25	0.3	0.512750336	0.918235993	-0.736086046	-0.430669272	19.34626547
0.25	0.3	0.510884606	0.914112808	-0.723353872	-0.424765513	13.59654814
0.25	0.3	0.509921022	0.911982205	-0.716796327	-0.421710204	6.85033494
0.25	0.3	0.509139765	0.910254182	-0.711488666	-0.419229875	5.463934082

Table B.1: *Example of energy harvester angular velocity data from computer vision*

Appendix C

Data on Energy Harvester's Angular Velocities from the Motion Capture on the Ground

d_1	d_2	L	$u\beta$	$u\gamma$	Ratio	$\omega\beta$ deg/s
0.25	0.3	0.527238009	0.950158804	-0.836532786	-0.475989651	0
0.25	0.3	0.527247714	0.950180135	-0.836601013	-0.47601971	-0.339646681
0.25	0.3	0.527260458	0.950208144	-0.836690605	-0.47605918	-0.446145311
0.25	0.3	0.527274937	0.950239967	-0.836792395	-0.476104023	-0.507069672
0.25	0.3	0.52728716	0.95026683	-0.836878325	-0.476141876	-0.428208277
0.25	0.3	0.527301447	0.950298231	-0.836978775	-0.476186124	-0.500742378
0.25	0.3	0.527313246	0.950324162	-0.837061728	-0.476222663	-0.413657382
0.25	0.3	0.527323622	0.950346967	-0.837134683	-0.476254798	-0.363905266
0.25	0.3	0.527336974	0.950376312	-0.837228562	-0.476296146	-0.468424108
0.25	0.3	0.52735018	0.950405335	-0.837321414	-0.476337041	-0.463462106
0.25	0.3	0.527363818	0.95043531	-0.837417314	-0.476379276	-0.478844636
0.25	0.3	0.527377678	0.950465769	-0.837514766	-0.476422193	-0.486770982
0.25	0.3	0.527386766	0.950485743	-0.837578674	-0.476450336	-0.319308236
0.25	0.3	0.527400658	0.950516274	-0.837676361	-0.476493354	-0.488241474
0.25	0.3	0.52741137	0.950539815	-0.837751685	-0.476526522	-0.376584587
0.25	0.3	0.527419128	0.950556865	-0.837806241	-0.476550544	-0.272816465

Table C.1: *Example of angular velocities and ratios from motion capture lab*

Appendix D

Arduino programming & software setup for field test

Arduino Programming

Arduino programming is relatively straightforward. Figure E.1 in Appendix E displays the full programming codes for the serial communication between the Arduino and the computer and sensor reading. The libraries "Wire.h" and "Adafruit_INA219.h" are respectively used for I2C communication and the interaction with the INA219 current sensor.

This electronics setup and the accompanying Arduino codes provide an efficient and straightforward method for gathering real-time data, enabling analysis and interpretation of the energy harvester's performance.

Software setup

The Arduino IDE is utilised as the programming platform to configure the Arduino Uno board, specifically with the INA219 current sensor. The Adafruit INA219 library is employed to simplify the measurement process for current, voltage, and power. This library offers an accessible template that can be easily modified to adjust voltage and current ranges, enhancing the measurement accuracy. The real-time data from the Arduino board can be viewed through the serial monitor in the Arduino IDE. To capture and store the data for later analysis, CoolTerm

[111] is selected to enable seamless data recording as a serial port terminal applicaiton. CoolTerm, developed by Roger Meier, is widely used by professionals who need to communicate and exchange data with devices such as microcontrollers, GPS receivers, servo controllers, and robotic kits. It allows for continuous data capture over a serial connection, with the added capability to export data into a text file for subsequent analysis.

Before data recording could begin, several configurations within CoolTerm have to be set up to ensure proper communication with the Arduino board. One of the initial steps involved establishing the correct port and baud rate settings, both essential for synchronising data exchange between CoolTerm and the Arduino. Figure D.1 displays the options selection page in CoolTerm, where these settings are adjusted.

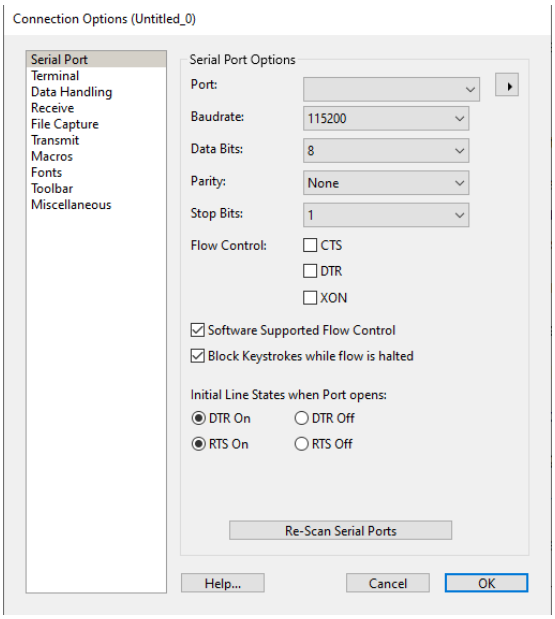

Figure D.1: *Coolterm configuration settings*

Since the baud rate is configured to 115200 in the Arduino code, it is necessary to match this baud rate within CoolTerm. The port setting is determined by the specific USB port to which the Arduino board is connected. This port can be identified from the list of available COM ports in the CoolTerm settings. Once both the port and baud rate are correctly configured, the connection between CoolTerm and the Arduino board is established by simply clicking the *"Connect"* button in the software.

To begin recording data, the option *"Capture to Text/Binary File"* is selected from the CoolTerm interface, as shown in Figure D.2. This option enables data streaming from the Arduino to be saved in a text format for later analysis. Once recording is initiated, clicking the *"Start"* button begins capturing the incoming data. During the experiment, data collection intervals are set at 0.1 seconds, ensuring that the dataset remains precise and detailed, thus providing information for further analysis and comparison.

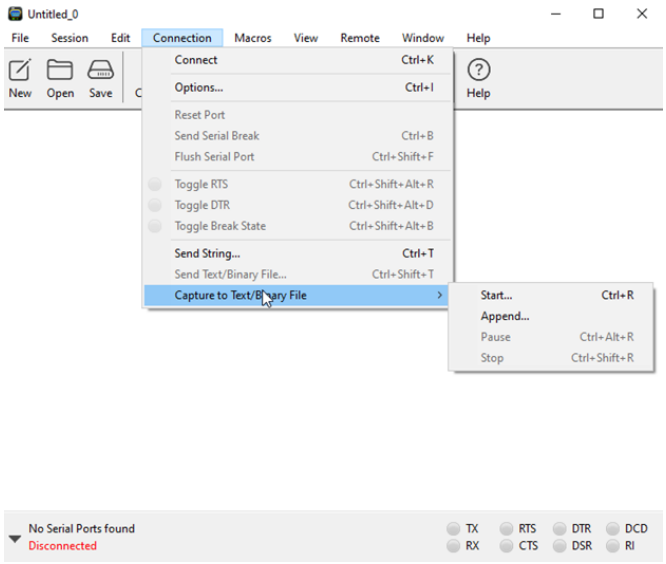

Figure D.2: *Coolterm recording steps.*

After completing the data collection, the recording process can be stopped by clicking the "Stop" button in CoolTerm. At this point, the software prompts the user to save the captured data file. The file can then be stored in a designated location on the computer, ready for further analysis using spreadsheet software or other tools suitable for examining the experimental results.

Appendix E

Programming Codes for Voltage and Current Measurement

```
#include <Wire.h>
#include <Adafruit_INA219.h>

Adafruit_INA219 ina219;

void setup(void)
{
  Serial.begin(115200);
  while (!Serial) {
      // will pause Zero, Leonardo, etc until serial console opens
      delay(1);
  }

  Serial.println("Hello!");

  // Initialize the INA219.
  // By default the initialization will use the largest range (32V,
     2A).  However

  if (! ina219.begin()) {
    Serial.println("Failed to find INA219 chip");
    while (1) { delay(10); }
  }

  Serial.println("Measuring voltage and current with INA219 ...");
}

void loop(void)
{
  float shuntvoltage = 0;
  float busvoltage = 0;
  float current_mA = 0;
  float loadvoltage = 0;
  float power_mW = 0;

  shuntvoltage = ina219.getShuntVoltage_mV();
  busvoltage = ina219.getBusVoltage_V();
  current_mA = ina219.getCurrent_mA();
  power_mW = ina219.getPower_mW();
  loadvoltage = busvoltage + (shuntvoltage / 1000);

  Serial.print(busvoltage);
  Serial.print(" ");
  Serial.print(shuntvoltage);
  Serial.print(" ");
  Serial.print(loadvoltage);
  Serial.print(" ");
```

Appendix F

Angular Velocity of the Energy Harvester

The Law of Cosines provides the relationship between the sides and angles of the triangle. To determine the angular velocity ratio, the following steps are outlined:

Angular velocity of β

Given:

$$\beta = \arccos\left(\frac{d_1^2 + L^2 - d_2^2}{2 \cdot d_1 \cdot L}\right) \tag{F.1}$$

Let:

$$u_\beta = \frac{d_1^2 + L^2 - d_2^2}{2 \cdot d_1 \cdot L} \tag{F.2}$$

Then:

$$\beta = \arccos(u_\beta) \tag{F.3}$$

The derivative of β with respect to L is:

$$\frac{d\beta}{dL} = -\frac{1}{\sqrt{1 - u_\beta^2}} \cdot \frac{du_\beta}{dL} \tag{F.4}$$

Differentiate u_β with respect to L:

$$\frac{du_\beta}{dL} = \frac{2L \cdot 2 \cdot d_1 - (d_1^2 + L^2 - d_2^2) \cdot 2 \cdot d_1}{(2 \cdot d_1 \cdot L)^2} \tag{F.5}$$

Simplify:

$$\frac{du_\beta}{dL} = \frac{L \cdot (d_1^2 + d_2^2 - L^2)}{d_1^2 \cdot L^2} \tag{F.6}$$

So:

$$\frac{d\beta}{dL} = -\frac{1}{\sqrt{1 - u_\beta^2}} \cdot \frac{d_1^2 + d_2^2 - L^2}{2 \cdot d_1 \cdot L} \tag{F.7}$$

Angular velocity of γ

Given:

$$\gamma = \arccos\left(\frac{d_1^2 + d_2^2 - L^2}{2 \cdot d_1 \cdot d_2}\right) \tag{F.8}$$

Let:

$$u_\gamma = \frac{d_1^2 + d_2^2 - L^2}{2 \cdot d_1 \cdot d_2} \tag{F.9}$$

Then:

$$\gamma = \arccos(u_\gamma) \tag{F.10}$$

The derivative of γ with respect to L is:

$$\frac{d\gamma}{dL} = -\frac{1}{\sqrt{1 - u_\gamma^2}} \cdot \frac{du_\gamma}{dL} \tag{F.11}$$

Differentiate u_γ with respect to L:

$$\frac{du_\gamma}{dL} = -\frac{L}{d_1 \cdot d_2} \tag{F.12}$$

So:

$$\frac{d\gamma}{dL} = \frac{L}{d_1 \cdot d_2 \cdot \sqrt{1 - u_\gamma^2}} \tag{F.13}$$

Appendix G

Methods for Motion Data Input in MATLAB

When utilising Simulink in MATLAB for modelling and simulations, it is essential to understand both the advantages and limitations of the various methods available for inputting motion data. In this research, three primary parameters can serve as inputs: the x, y, z coordinates of the hip and knee joints, the hip joint angle, and the angular velocity of the hip joint. Each of these methods has distinct benefits and drawbacks that impact their suitability for different types of simulations.

The first input method involves using the x, y, z coordinates of the hip and knee joints. This approach necessitates that the input data and the 3D human models share the same global axis orientation, which can pose a significant challenge. The orientation of the global axis is typically determined by the motion capture method used, and different methods can result in varying orientations. For instance, the orientations may differ between the computer vision method and the motion capture lab method used in this research. This variability can complicate the process, particularly when considering future motion capture methods that might adopt different global axis orientations. Therefore an axis orientation transformation may be necessary to properly align the data before inputting the data into Simulink. However, this method offers a notable advantage: the calculation of the joint angles and angular velocities can be performed within Simulink using the MATLAB Function tool. This standardised approach ensures that as long

as the motion capture method provides the joint coordinates, consistent calculations can be achieved across different datasets. Conversely, if the motion capture method does not provide the necessary coordinates for the hip and knee joints, this input method becomes unusable.

The second input method involves calculating the hip joint angle over time outside of Simulink and then directly importing this angle into the simulation. Similar to the first method, it requires alignment of the global axis orientation with the 3D human models. However, transforming the angle to match the global axis orientation is generally more straightforward compared to adjusting the coordinates. This method is more versatile, as it does not rely on the x, y, z coordinates of both joints, making it applicable to a broader range of motion data capture methods. As long as the hip joint angle can be calculated externally, this input method can be utilised. Also, considering the location of the energy harvester outside of Simulink simplifies the process and avoids the complexity of inputting additional parameters into the simulation environment.

The third input method involves directly importing the angular velocity of the hip joint into the model, with the angular velocity calculated externally. One key limitation of this method is that Simulink will not generate a 3D human model simulation, focusing instead on the calculations and modelling of the DC motor. This approach eliminates the need for aligning any global axis, which simplifies the input process. However, the angular velocity must be specifically calculated and selected before importation. For instance, in this research, the angular velocity of the energy harvester is derived from the vertical angular velocity of the hip joint.

Figure G.1 provides an overview of the Simulink design for this research, while Figure G.2 offers a detailed view of the Number 1 area. The design accommodates all three methods of data input discussed earlier. The Number 1 area specifically highlights the first method, where the coordinates of the hip and knee joints are imported as the initial step in the calculation and modelling process. These coordinates can be integrated into the simulation environment using the Signal Builder in Simulink, allowing for a seamless incorporation of motion data. Alternatively, for cyclical movements like ladder climbing, a function can be written to represent the coordinates along each axis, which can then be imported into the MATLAB Function block named "$Angletrajectory V2$" as shown in Figure G.2. This block calculates the angular

velocity, which is then processed through a Proportional-Integral-Derivative (PID) controller before being inputted into the human model for further analysis.

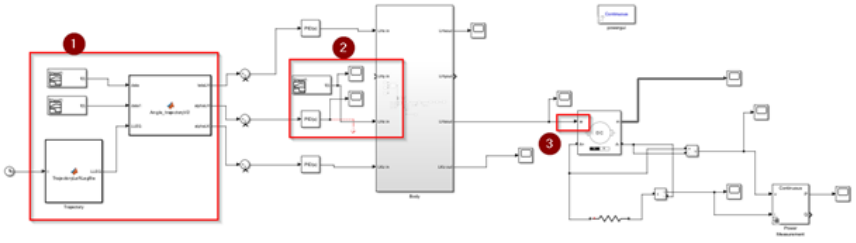

Figure G.1: *Overview of the Simulink design*

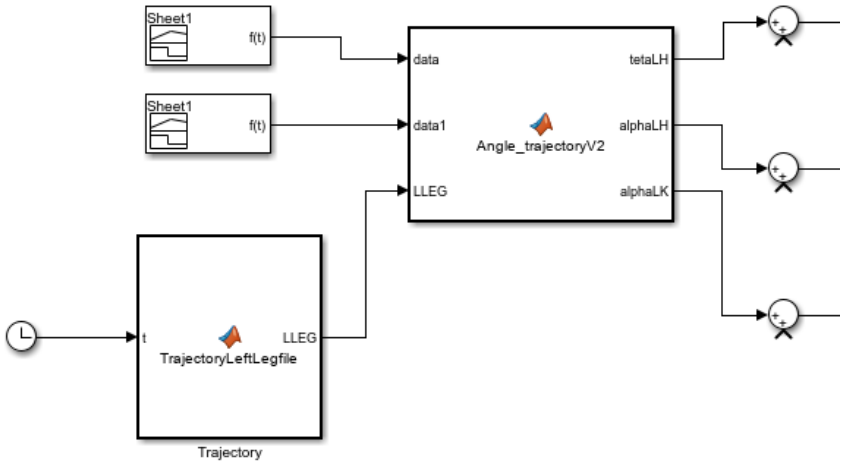

Figure G.2: *Area 1 of the Simulink design*

In addition to the first method, the design also incorporates the Number 2 area, which highlights the second method of data input. In this section, the Signal Builder tool is used to directly import the hip joint angle into the human model within Simulink. A scope is added to this area to verify the accuracy of the data being imported, ensuring that the input angle aligns precisely with the simulation's requirements. The inclusion of the scope serves as an important validation tool, as it allows real-time monitoring of the data and ensures that any misalignments between the imported angle and the actual movement patterns are quickly identified and corrected.

The Number 3 area is dedicated to the third input method, which focuses on directly

importing the angular velocity of the hip joint into the model. This method provides a more direct approach to inputting data, as it bypasses the need for calculating joint angles or handling coordinate data. Despite its simplicity and potential advantages, this method was not utilised in the current research due to the availability of sufficient data from the first two methods. Additionally, the use of the third method does not support the generation of a 3D human model simulation, which is a key aspect of this research. Since the 3D visualisation of the energy harvester's performance plays a important role in understanding the system's behaviour under varying conditions, the third method was deemed less suitable for the objectives of this study. Nevertheless, the third method remains a valuable option for future research or applications where the focus is primarily on the mechanical aspects of the energy harvesting system, such as the dynamics of the DC motor, rather than the full-body motion analysis. Its simplicity can be advantageous in scenarios where detailed 3D simulations are not required, or where external computational resources may be limited.

This Simulink design offers a highly flexible and comprehensive framework for modelling and analysing the energy harvesting mechanism. The integration of all three methods ensures that various types of motion data can be accurately incorporated into the simulation, depending on the specific needs and constraints of the research. By supporting multiple input methods, this design enables researchers to adapt the simulation to different data sources and motion capture techniques, making it highly adaptable to future developments in motion capture technology. Furthermore, the design ensures that all critical aspects of the energy harvesting process are simulated with precision, from the input of motion data to the real-time calculation of angular velocity and power output.

G.1 Human Model Input

In Simulink, which is part of the MATLAB software suite, users can create detailed 3D models for running simulations, making it a highly effective tool for simulating mechanical systems and analysing their dynamic behaviour. This capability is particularly valuable in research involving human body mechanics and wearable systems, as it allows researchers to model the physical

interactions between the body and external devices. In the context of this research, the body model, as illustrated in Figure G.3, serves as a fundamental component of the overall design. The ability to visualise the body in three dimensions, combined with a high-level perspective on the system's functionality, provides insights into how the simulated movements correlate with the actual design intent. This not only aids in validating the accuracy of the simulations but also ensures that the mechanical dynamics of the system are correctly represented.

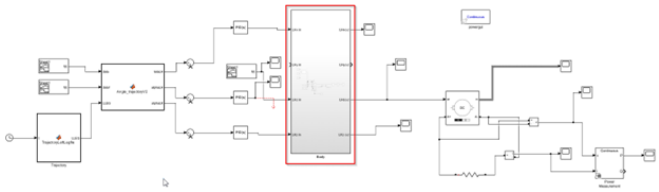

Figure G.3: *Area 2 of the Simulink design - human body modelling*

The process of constructing this 3D model within Simulink is relatively straightforward; however, it requires attention to detail to ensure that each component is accurately defined and functions as intended. Every part of the body model must be treated as an individual element within the overall simulation framework. For this research, the model initially created during the design phase is reused, offering continuity and consistency in the simulation process. The components of this body model are originally designed using SolidWorks, a CAD software frequently employed for creating detailed mechanical parts and assemblies. While MATLAB-Simulink offers a feature that enables the direct import of SolidWorks assemblies, this functionality is often accompanied by errors and misinterpretations of certain parameters, leading to unreliable simulations. These issues are primarily due to differences in how SolidWorks and Simulink handle constraints, joints, and other mechanical relationships.

To mitigate these potential errors and ensure the highest level of accuracy, the model was manually constructed within Simulink, using the SolidWorks parts primarily as visual guides. Figure G.4, a detailed view of the module shown in Figure G.3, illustrates the thigh section of the body model within Simulink. Constructing the model directly within Simulink allows for seamless integration with other simulation elements, such as the energy harvester and the DC motor, ensuring that all parts of the system work together harmoniously. This approach provides

a more reliable and cohesive framework for evaluating the system's performance, particularly when investigating the effects of different motion data inputs or varying operating conditions.

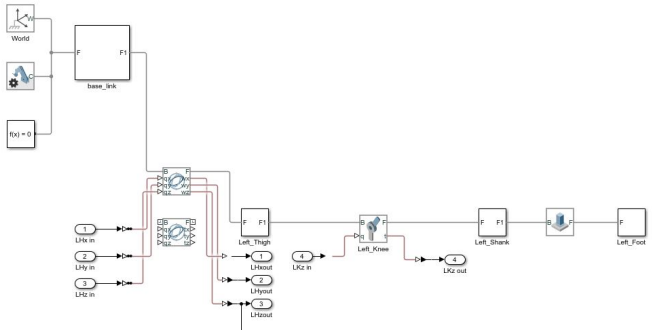

Figure G.4: *Detailed view of the body module*

Within the body model, certain fundamental blocks are needed. The "World Frame" block acts as the foundation for all frame networks in the mechanical model, essentially functioning as the ground or base reference for the entire system. This block defines the global coordinate system against which all other components are positioned and oriented. Similarly, the "Mechanism Configuration" block is essential for establishing mechanical and simulation parameters that are applied uniformly across the entire system. These parameters include settings such as gravity, which must be consistently applied to every part of the model. In this research, gravity was set to a uniform value based on the standard acceleration. Finally, the "Solver Configuration" block is critical for specifying the simulation settings, such as the type of solver used and the numerical accuracy required.

To show the motion and interaction between different parts of the model, "Joint" blocks are placed at every point where two parts are connected. These joints must be defined to replicate the specific type of motion they are intended to model. For instance, the knee joint connecting the thigh and shank is represented as a "Revolute Joint" block, which allows for rotation around a single axis, mimicking the natural motion of the human knee. Within each "Joint" block, a variety of parameters must be set to ensure accurate simulation. These include state targets, which define the joint's initial position or velocity, and internal mechanics settings, which account for factors such as the joint's equilibrium position, spring stiffness, and damping coefficient. Motion range limits must also be specified to prevent unrealistic movements, ensuring that the

joint operates within the anatomical limits of the human body. The actuation method of whether the joint is driven by torque or a predefined motion and sensing options, which include position, velocity, acceleration, and torque, is also configured within these blocks to capture the necessary data during the simulation.

In this research, particular focus is given to the "Gimbal Joint" between the hip and thigh, as shown in Figure G.4. This joint is important in measuring the vertical angular velocity of the hip, which is the primary motion of interest in the context of energy harvesting. The joint outputs, labelled as LHxout, LHyout, and LHzout, represent the velocity of the hip joint in different directions. Of these, LHzout is especially important, as it corresponds to the vertical angular velocity of the hip joint, which is directly linked to the energy harvester mechanism. This output is connected to the energy harvester device within the simulation to measure and analyse its performance, with more details on the integration of the energy device in Simulink provided in later sections.

Before the parts of the body model designed in SolidWorks can be integrated into Simulink, they must be exported as "STEP" files. This file format is compatible with Simulink. Importing these STEP files into Simulink allows for the physical geometry of the parts to be incorporated into the simulation, while maintaining the mechanical properties and dimensions from SolidWorks. Once imported, the design structure within Simulink needs to be defined to ensure proper connectivity between the parts. For example, Figure G.5 illustrates the thigh model within Simulink. Each part requires a "Reference Frame" block, which establishes the local coordinate system for that specific part. Several "Rigid Transform" blocks are also used to connect different components of the model, such as linking the knee joint to the hip joint. The "Visual" block is then connected to the "Reference Frame" via a "VisualOriginTransform", allowing the imported SolidWorks model to be visually represented within Simulink. An "InertiaOriginTransform" is also used to incorporate the inertia properties of each part, ensuring that the dynamic effects of mass distribution and rotational inertia are properly accounted for in the simulation.

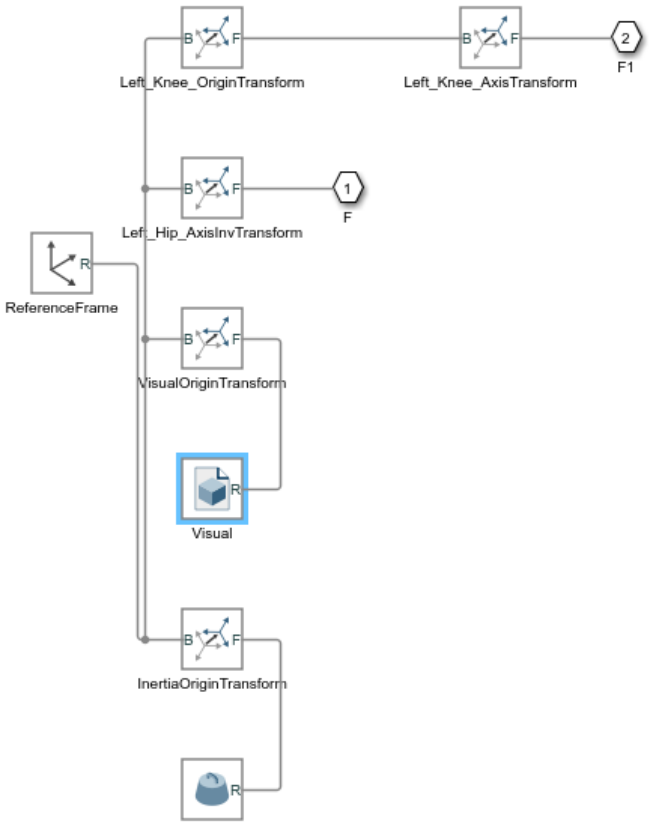

Figure G.5: *Detailed view of the Thigh module*

For simplicity, this research only incorporates one leg into the Simulink model. However, the same methodology can be extended to include additional parts and limbs within the body module. As long as there are actuation signals provided to the joints, the model can simulate the movement of multiple limbs, allowing for a more comprehensive analysis of the mechanical system.

In summary, the integration of SolidWorks parts into a Simulink model requires careful consideration of both the mechanical design and the simulation parameters. By accurately defining each component and joint, and by properly configuring the simulation settings, the model can effectively simulate the desired movements, providing valuable insights into the system's dynamics.

G.2 Energy Harvester Design Input

The final component of the Simulink MATLAB design is the energy harvester section. This part is a focal point of the research. Itis highlighted in Figure G.6. The primary purpose of this section is to model the energy harvester system, which is accomplished by simulating a DC motor functioning as a generator within the Simulink environment. To properly simulate a DC motor as a generator, the "DC Machine" block is utilised, which has been specifically designed for this type of operation. Unlike other generic DC motor blocks available in Simulink, the "DC Machine" block is uniquely suited for handling both mechanical and electrical configurations required for the generation process. This ensures that the model reflects real-world behaviours as a generator and interactions as closely as possible.

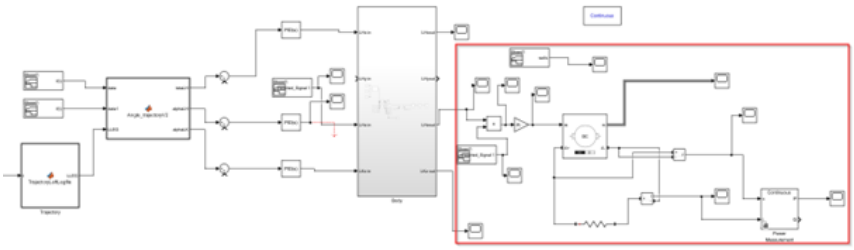

Figure G.6: *Overview of the energy harvester part in MATLAB*

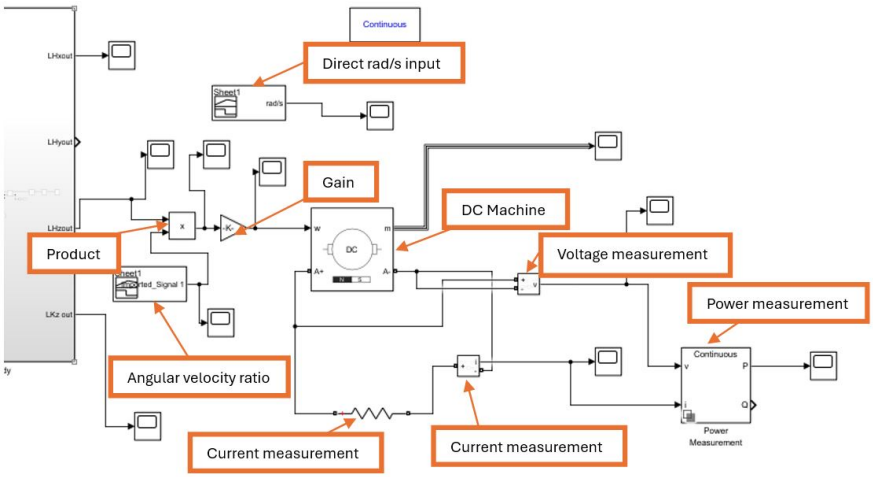

Figure G.7: *Details of the energy harvester part in MATLAB*

As shown in Figure G.7, the simulation begins by taking the signal representing the hip

joint's vertical angular velocity, denoted as "LHzout", which is an output from the gimbal joint block discussed earlier. This signal is then processed through a "Signal Builder" block coupled with a "Product" block. This step is required for adjusting the "LHzout" signal according to the ratio calculated earlier between the angular velocity of the hip joint and that of the energy harvester. This ratio represents the scaling factor needed to transform the input signal into one that accurately reflects the rotation speed of the energy harvester. Since the energy harvester is physically positioned on the body, any changes in its position or configuration would require this ratio to be recalculated and subsequently updated within the simulation model. A "Gain" block is also introduced into the model to simulate the effect of the gearhead in the DC motor. The gearhead is for increasing the mechanical advantage by adjusting the angular velocity input based on the gear ratio. By incorporating this aspect into the simulation, the model becomes more representative of the actual system performance, making the simulation results more reliable and applicable to real-world scenarios.

Within the DC Machine block, the user has the flexibility to choose different mechanical inputs, such as speed, torque, or mechanical rotation, depending on the nature of the simulation and the specific system being modelled. This feature provides control over the motor's input conditions, tailoring the simulation to reflect real-world behaviours. The block also provides the option to select between two field types: permanent magnet or wound. These field types are essential characteristics that influence the motor's operation, and the choice between them depends on the type of DC motor being simulated. In this research, a permanent magnet motor is selected in the block, as it closely aligns with the physical DC motor chosen during the design and experimental phase. The DC Machine block further enables the input of various key motor parameters, including the armature resistance, armature inductance, and the back-electromotive-force (back-emf) constant. These parameters are usually provided in the technical specifications of the DC motor. However, in some cases, particularly with inductance, these values may not be readily available and may need to be estimated or measured separately.

Once the mechanical input and motor parameters are fully configured, the focus shifts to measuring and analysing the electrical output generated by the DC motor. This is accomplished by connecting a Series RLC Branch block across the positive and negative terminals of the

DC Machine block, effectively simulating a resistive load. This resistor acts as the electrical load that the motor would drive in a real-world scenario, representing the energy consumer connected to the energy harvester. To monitor the electrical output, Voltage Measurement and Current Measurement blocks are introduced into the system. These blocks are connected to scopes, which display the real-time voltage and current generated by the DC motor during the simulation.

In addition to measuring voltage and current, these outputs are also routed to a Power Measurement block. This block calculates the electrical power generated by the DC motor, offering a direct measure of the energy harvested from the hip joint's motion. This setup enables researchers to observe how changes in the input motion, such as variations in angular velocity, impact the power generated by the DC motor. This is particularly useful for evaluating the efficiency of the energy harvester under different conditions.

An additional scope is connected directly to the DC Machine block to monitor several important outputs, such as the armature current, field current, angular velocity of the rotor, and the electromechanical torque produced by the DC motor. These parameters provide valuable insights into the internal workings of the motor as it operates in generator mode. By analysing the armature current and electromechanical torque, for instance, researchers can better understand the relationship between the mechanical input (the hip joint's motion) and the electrical output (the power generated), leading to a more refined and efficient design. With this Simulink design, the electrical power output generated by the DC motor can be observed, analysed, and optimised using the Power Measurement block. The design serves as the foundation for the next section where motion capture data from the two different methods discussed earlier will be inputted into the simulation. These datasets will be used to calculate and compare the power output of the energy harvester under different conditions.

References

[1] Digitech, "Digitech waterproof floating marine handheld vhf radio 3w," October 24 2022, retrieved from MarineDeals: https://www.marine-deals.co.nz/vhf-radios-handheld/digitech-waterproof-floating-marine-handheld-vhf-radio-3w.

[2] Y. Bao and H. Fu, "Effects of currents on human freestyle and breaststroke swimming analysed by a rigid-body dynamic model," *Machines - MDPI*, vol. 10, p. 17, 2022.

[3] "Hutchwilco easy-fit inflatable life jacket 170n with ets," August 9 2022, retrieved from Marine Deals: https://www.marine-deals.co.nz/inflatable-life-jackets/hutchwilco-easy-fit-inflatable-life-jacket-170n-with-ets?gclid=CjwKCAjwi8iXBhBeEiwAKbUofZiJDg792Bctx_UPO9LE6pWXiy1_Rnzv8PTZKGwpmruc5rYAjuFjABoCoBEQAvD_BwE.

[4] J. Xiong, P. Cui, X. Chen, J. Wang, K. Parida, M.-F. Lin, and P. S. Lee, "Skin-touch-actuated textile-based triboelectric nanogenerator with black phosphorus for durable biomechanical energy harvesting," *Nature communications*, vol. 9, no. 1, p. 4280, 2018.

[5] Y. Zou, P. Tan, B. Shi, H. Ouyang, D. Jiang, Z. Liu, H. Li, M. Yu, C. Wang, X. Qu *et al.*, "A bionic stretchable nanogenerator for underwater sensing and energy harvesting," *Nature Communications*, vol. 10, no. 1, p. 2695, 2019.

[6] Y. Xi, J. Hua, and Y. Shi, "Noncontact triboelectric nanogenerator for human motion monitoring and energy harvesting," *Nano Energy*, vol. 69, p. 104390, 2020.

[7] D. Yan, D. Tao, D. Xu, Y. Sun, B. Deng, G. Cao, J. Fang, and W. Xu, "Flexible arc-shaped triboelectric nanogenerator for all directions and highly efficient biomechanical energy harvesting and human motion monitoring," *Nano Energy*, p. 110000, 2024.

[8] Y.-H. Shin, I. Jung, M.-S. Noh, J. H. Kim, J.-Y. Choi, S. Kim, and C.-Y. Kang, "Piezoelectric polymer-based roadway energy harvesting via displacement amplification module," *Applied Energy*, vol. 216, pp. 741–750, 2018.

[9] D. Yun and K.-S. Yun, "Woven piezoelectric structure for stretchable energy harvester," *Electronics letters*, vol. 49, no. 1, pp. 65–66, 2013.

[10] Y. Zhu, G. Chen, J. Zhang, Z. Li, and S. Zhou, "A flexible piezoelectric energy harvester featuring an eccentric pendulum via frequency up-conversion for human motion," *Smart Materials and Structures*, vol. 33, no. 8, p. 085032, 2024.

[11] G. Sui, X. Shan, C. Hou, H. Tian, J. Hu, and T. Xie, "An underwater piezoelectric energy harvester based on magnetic coupling adaptable to low-speed water flow," *Mechanical Systems and Signal Processing*, vol. 184, p. 109729, 2023.

[12] P. Maharjan, T. Bhatta, M. S. Rasel, M. Salauddin, M. T. Rahman, and J. Y. Park, "High-performance cycloid inspired wearable electromagnetic energy harvester for scavenging human motion energy," *Applied Energy*, vol. 256, p. 113987, 2019.

[13] X. Zhao, J. Cai, Y. Guo, C. Li, J. Wang, and H. Zheng, "Modeling and experimental investigation of an aa-sized electromagnetic generator for harvesting energy from human motion," *Smart Materials and Structures*, vol. 27, no. 8, p. 085008, 2018.

[14] T. Wang and Y. Zhang, "Design, analysis, and evaluation of a compact electromagnetic energy harvester from water flow for remote sensors," *Energies*, vol. 11, no. 6, p. 1424, 2018.

[15] X. Pan, G. Zhang, N. Yu, C. Cai, H. Ma, and B. Yan, "Low-frequency human motion energy scavenging with wearable tumbler-inspired electromagnetic energy harvesters," *International Journal of Mechanical Sciences*, vol. 268, p. 109029, 2024.

[16] Jaycar, "YG2734-dataSheetMain," Datasheet, 2017. [Online]. Available: https://www.jaycar.com.au/medias/sys_master/images/images/10221499809822/YG2734-dataSheetMain.pdf

[17] M. El-Hajj, H. Mousawi, and A. Fadlallah, "Analysis of lightweight cryptographic algorithms on iot hardware platform," *Future Internet*, vol. 15, no. 2, p. 54, 2023.

[18] T.K. Hareedran, "INA219 Current Sensor Module Primer," 2021. [Online]. Available: https://www.electroschematics.com/ina219-current-sensor-module-primer/

[19] W. S. N. Zealand, "New zealand water safety sector strategy 2020," Wellington, Tech. Rep., 2020.

[20] W. N. Zealand, "Drowning report 2020," Available at https://drowningreport2020.watersafety.org.nz/ (2021/01/28).

[21] C. Thirkell, K. MacIver, G. Mitchell, and E. Asbury, "Nzsar fatality study."

[22] E. F. van Beeck, C. M. Branche, D. Szpilman, J. H. Modell, and J. J. Bierens, "A new definition of drowning: towards documentation and prevention of a global public health problem," *Bulletin of the World Health Organization*, vol. 83, pp. 853–856, 2005.

[23] W. S. N. Zealand, "Drowning prevention report 2023," 2024, water Safety New Zealand.

[24] D. P. Auckland, "Preventative drowning 2011 - 2020 (excludes homicide, suicide, road transport)," Drowning Prevention Auckland, Auckland, Tech. Rep., 2021.

[25] E. F. van Beeck and C. B., "A new definition of drowning: Toward documentation and prevention of a global public health problem," World Health Organization, Tech. Rep. 83, 2005.

[26] C. N. Zealand, "Lifejackets," https://www.coastguard.nz/boating-safely/lifejackets/, 2022, accessed: 2022-05-14.

[27] M. N. Zealand, "Lifejacket and pfd standards identified," https://www.maritimenz.govt.nz/magazines/safe-seas-clean-seas/issue-41/issue-41-12.asp, 2022, accessed: 2022-02-21.

[28] K. Renusha, S. Sindhumathy, S. Sujitha, and B. Udhayasuriya, "Intelligent safety life jacket using lora technology," *i-Manager's Journal on Future Engineering and Technology*, vol. 19, no. 3, p. 10, 2024.

[29] T. Aderinto and F. H.-F. Hua, "Design and potential application of small scale wave energy converter," in *ASME 2017 International Mechanical Engineering Congress and Exposition*. Florida: ASME, 2017, p. 3.

[30] D. B. Nguyen, T. Le Minh, N. Van Truc, and H. V. Tran, "Building a smart life jacket based on the iot platform," in *2023 International Conference on Advanced Technologies for Communications (ATC)*. IEEE, 2023, pp. 527–533.

[31] K. Wang, K. Zhao, M. Su, J. Qi, Y. Hou, and S. Tang, "An intelligent life jacket system based on onenet," in *2021 6th International Conference on Intelligent Computing and Signal Processing (ICSP)*. IEEE, 2021, pp. 1071–1074.

[32] A. K. Singh, R. Raj, and S. Chattopadhyay, "An overview of factors influencing solar power efficiency and strategies for enhancing," in *Innovations in Power and Advanced Computing Technologies (i-PACT)*, 2021.

[33] A. Carballo-Fazanes, J. J. Bierens, and I. E. G. to Study Drowning Behaviour, "The visible behaviour of drowning persons: A pilot observational study using analytic software and a nominal group technique," *International journal of environmental research and public health*, vol. 17, no. 18, p. 6930, 2020.

[34] "Beacons," February 23 2022, retrieved from Maritime New Zealand: https://www.maritimenz.govt.nz/recreational/safety/communications/beacons/default.asp.

[35] "What is an emergency position indicating radio beacon," May 27 2024, retrieved from Marine Insight: https://www.marineinsight.com/marine-safety/what-is-epirb-emergency-position-indicating-radio-beacon/.

[36] J. Mulheron, "Plb's: When to push the button and what to do next," June 18 2017, retrieved from Wilderlife New Zealand: https://wilderlife.nz/2017/06/when-to-push-the-button-and-what-to-do-next/.

[37] CoastGuard, "In an emergency," February 24 2022, retrieved from Coastguard New Zealand: https://www.coastguard.nz/boating-safely/in-an-emergency/.

[38] M. Gao, P. Wang, L. Jiang, B. Wang, Y. Yao, S. Liu, D. Chu, W. Cheng, and Y. Lu, "Power generation for wearable systems," *Energy & Environmental Science*, vol. 14, no. 4, pp. 2114–2157, 2021.

[39] J.-Y. Wu, Y. Wang, C. T. S. Ching, H.-M. D. Wang, and L.-D. Liao, "Iot-based wearable health monitoring device and its validation for potential critical and emergency applications," *Frontiers in Public Health*, vol. 11, p. 1188304, 2023.

[40] N. S. Khaanghah, S. Krik, H. de Souza Oliveira, A. Carrasco-Pena, M. Ciocca, L. Petti, M. Haller, G. Cantarella, and N. Münzenrieder, "Thin-film thermistor temperature sensors on animal-based substrates," in *2024 IEEE International Conference on Flexible and Printable Sensors and Systems (FLEPS)*. IEEE, 2024, pp. 1–4.

[41] P. S. Malvade, A. K. Joshi, and S. P. Madhe, "Iot based monitoring of foot pressure using fsr sensor," in *2017 International Conference on Communication and Signal Processing (ICCSP)*. IEEE, 2017, pp. 0635–0639.

[42] A. Maier, A. Sharp, and Y. Vagapov, "Comparative analysis and practical implementation of the esp32 microcontroller module for the internet of things," in *2017 Internet Technologies and Applications (ITA)*. IEEE, 2017, pp. 143–148.

[43] M. Shahidul Islam, M. T. Islam, A. F. Almutairi, G. K. Beng, N. Misran, and N. Amin, "Monitoring of the human body signal through the internet of things (iot) based lora wireless network system," *Applied Sciences*, vol. 9, no. 9, p. 1884, 2019.

[44] R. Wittmann, F. Henkel, A. Ripp, A. Meyer, R. Wunderlich, S. Heinen, and M. Dietrich, "Innovative design methodology for analog-to-digital and digital-to-analog converters," in *ANALOG 2020; 17th ITG/GMM-Symposium*. VDE, 2020, pp. 1–6.

[45] M. Ahmed, S. Kuriry, M. Shafiullah, and M. Abido, "Dc microgrid energy management with hybrid energy storage systems," in *2019 23rd International Conference on Mechatronics Technology (ICMT)*. IEEE, 2019, pp. 1–6.

[46] M. Bhargava, *IoT projects with bluetooth low energy*. Packt Publishing Ltd, 2017.

[47] M. U. bin Aftab, *Building bluetooth low energy systems*. Packt Publishing Ltd, 2017.

[48] P. Seneviratne, *Beginning LoRa Radio Networks with Arduino: Build Long Range, Low Power Wireless IoT Networks*. Apress, 2019.

[49] A. Lavric, "Lora (long-range) high-density sensors for internet of things," *Journal of Sensors*, vol. 2019, no. 1, p. 3502987, 2019.

[50] S. M. Adam, L. Goossens, F. Panafidin, B. J. Mackenzie, Y. Li, S. Michiels, D. Hughes, and K. L. Man, "Resource: Energy-efficient gps-based localization for resource-constrained iot devices." *International Journal of Design, Analysis & Tools for Integrated Circuits & Systems*, vol. 13, no. 1, 2024.

[51] W.-Y. Lin, C.-H. Chen, and M.-Y. Lee, "Design and implementation of a wearable accelerometer-based motion/tilt sensing internet of things module and its application to bed fall prevention," *Biosensors*, vol. 11, no. 11, p. 428, 2021.

[52] S. Abdulmalek, A. Nasir, W. A. Jabbar, M. A. Almuhaya, A. K. Bairagi, M. A.-M. Khan, and S.-H. Kee, "Iot-based healthcare-monitoring system towards improving quality of life: A review," in *Healthcare*, vol. 10, no. 10. MDPI, 2022, p. 1993.

[53] D. Salar, "Miniature wave energy converter," Uppsala Universitet, Uppsala, Tech. Rep., 2018.

[54] T. Starner, "Human-powered wearable computing," *IBM systems Journal*, vol. 35, no. 3.4, pp. 618–629, 1996.

[55] R. Riemer and A. Shapiro, "Biomechanical energy harvesting from human motion: theory, state of the art, design guidelines, and future directions," *Journal of neuroengineering and rehabilitation*, vol. 8, pp. 1–13, 2011.

[56] J. Mi, L. Xu, Y. Yang, and L. Zuo, "Design and characterization of an ocean wave powered lifejacket using 2dof floating boards," in *Active and passive smart structures and integrated systems XII*, vol. 10595. SPIE, 2018, pp. 490–497.

[57] L. Xie, G. Huang, L. Huang, S. Cai, and X. Li, "An unpowered flexible lower limb exoskeleton: Walking assisting and energy harvesting," *IEEE/ASME Transactions on Mechatronics*, vol. 24, no. 5, pp. 2236–2247, 2019.

[58] F. Invernizzi, S. Dulio, M. Patrini, G. Guizzetti, and P. Mustarelli, "Energy harvesting from human motion: materials and techniques," *Chemical Society Reviews*, vol. 45, no. 20, pp. 5455–5473, 2016.

[59] S. Zareei and J. D. Deng, "Energy harvesting modelling for self-powered fitness gadgets: a feasibility study," *International Journal of Parallel, Emergent and Distributed Systems*, vol. 34, no. 4, pp. 412–429, 2019.

[60] T. Von Buren, P. D. Mitcheson, T. C. Green, E. M. Yeatman, A. S. Holmes, and G. Troster, "Optimization of inertial micropower generators for human walking motion," *IEEE Sensors journal*, vol. 6, no. 1, pp. 28–38, 2006.

[61] L. Ren, M. Cong, W. Zhang, and Y. Tan, "Harvesting the negative work of an active exoskeleton robot to extend its operating duration," *Energy Conversion and Management*, vol. 245, p. 114640, 2021.

[62] A. S. Khan and F. U. Khan, "A survey of wearable energy harvesting systems," *International Journal of Energy Research*, vol. 46, no. 3, pp. 2277–2329, 2022.

[63] Y.-W. Chong, W. Ismail, K. Ko, and C.-Y. Lee, "Energy harvesting for wearable devices: A review," *IEEE Sensors Journal*, vol. 19, no. 20, pp. 9047–9062, 2019.

[64] F.-R. Fan, Z.-Q. Tian, and Z. L. Wang, "Flexible triboelectric generator," *Nano energy*, vol. 1, no. 2, pp. 328–334, 2012.

[65] Z. L. Wang, J. Chen, and L. Lin, "Progress in triboelectric nanogenerators as a new energy technology and self-powered sensors," *Energy & Environmental Science*, vol. 8, no. 8, pp. 2250–2282, 2015.

[66] T. Q. Trung and N.-E. Lee, "Flexible and stretchable physical sensor integrated platforms for wearable human-activity monitoringand personal healthcare," *Advanced materials*, vol. 28, no. 22, pp. 4338–4372, 2016.

[67] S. Wang, M. Bi, Z. Cao, and X. Ye, "Linear freestanding electret generator for harvesting swinging motion energy: Optimization and experiment," *Nano Energy*, vol. 65, p. 104013, 2019.

[68] Q. Shi, T. He, and C. Lee, "More than energy harvesting–combining triboelectric nanogenerator and flexible electronics technology for enabling novel micro-/nano-systems," *Nano Energy*, vol. 57, pp. 851–871, 2019.

[69] K. G. Motora, C.-M. Wu, C. R. M. Jose, and G. M. Rani, "Waste-to-energy: Development of a highly efficient keratin enhanced chitosan bio-waste-derived triboelectric nanogenerator for energy harvesting and real applications," *Advanced Functional Materials*, p. 2315069, 2024.

[70] Q. Zhang, K. Barri, S. R. Kari, Z. L. Wang, and A. H. Alavi, "Multifunctional triboelectric nanogenerator-enabled structural elements for next generation civil infrastructure monitoring systems," *Advanced functional materials*, vol. 31, no. 47, p. 2105825, 2021.

[71] K. Shi, B. Chai, H. Zou, Z. Wen, Y. Liu, M. He, J. Chen, P. Jiang, and X. Huang, "Direct-current triboelectric nanogenerators based on contact–separation mode and conductive–adhesive interface," *Advanced Functional Materials*, p. 2400204, 2024.

[72] X. Zhao, H. Xiang, and Z. Shi, "Piezoelectric energy harvesting from vehicles induced bending deformation in pavements considering the arrangement of harvesters," *Applied Mathematical Modelling*, vol. 77, pp. 327–340, 2020.

[73] W. S. Hwang, J. H. Ahn, S. Y. Jeong, H. J. Jung, S. K. Hong, J. Y. Choi, J. Y. Cho, J. H. Kim, and T. H. Sung, "Design of piezoelectric ocean-wave energy harvester using sway movement," *Sensors and Actuators A: Physical*, vol. 260, pp. 191–197, 2017.

[74] Z. Ji and M. Zhang, "Highly sensitive and stretchable piezoelectric strain sensor enabled wearable devices for real-time monitoring of respiratory and heartbeat simultaneously," *Nanotechnology and Precision Engineering (NPE)*, vol. 5, no. 1, 2022.

[75] A. Proto, M. Penhaker, D. Bibbo, D. Vala, S. Conforto, and M. Schmid, "Measurements of generated energy/electrical quantities from locomotion activities using piezoelectric wearable sensors for body motion energy harvesting," *Sensors*, vol. 16, no. 4, p. 524, 2016.

[76] G. Giuliani, "Electromagnetic induction: How the "flux rule" has superseded maxwell's general law," *American Journal of Physics*, vol. 91, no. 4, pp. 278–287, 2023.

[77] M. T. Rahman, S. S. Rana, M. Salauddin, P. Maharjan, T. Bhatta, and J. Y. Park, "Biomechanical energy-driven hybridized generator as a universal portable power source for smart/wearable electronics," *Advanced Energy Materials*, vol. 10, no. 12, p. 1903663, 2020.

[78] X. Yuan, X. Gao, J. Yang, X. Shen, Z. Li, S. You, Z. Wang, and S. Dong, "The large piezoelectricity and high power density of a 3d-printed multilayer copolymer in a rugby ball-structured mechanical energy harvester," *Energy & Environmental Science*, vol. 13, no. 1, pp. 152–161, 2020.

[79] C. Chen, H. Guo, L. Chen, Y.-C. Wang, X. Pu, W. Yu, F. Wang, Z. Du, and Z. L. Wang, "Direct current fabric triboelectric nanogenerator for biomotion energy harvesting," *ACS nano*, vol. 14, no. 4, pp. 4585–4594, 2020.

[80] G. Bovi, M. Rabuffetti, P. Mazzoleni, and M. Ferrarin, "A multiple-task gait analysis approach: Kinematic, kinetic and emg reference data for healthy young and adult subjects," *Gait & Posture*, vol. 33, no. 1, pp. 6–13, 2011.

[81] P. M. Nakashima, "What is swum?" August 2014, retrieved from SWUM. [Online]. Available: http://www.swum.org/

[82] A. B. H., "Adams student edition," 2022, retrieved from Hexagon. [Online]. Available: https://hexagon.com/products/adams-student-edition

[83] AUT Motion Capture Lab, "About the facility," https://mocap.aut.ac.nz/facility, n.d., accessed: 2024-09-30.

[84] J. Zhang, H. Liu, Q. Chang, L. Wang, and R. X. Gao, "Recurrent neural network for motion trajectory prediction in human-robot collaborative assembly," *CIRP annals*, vol. 69, no. 1, pp. 9–12, 2020.

[85] Z. Zhao and I. Patras, "Prompting visual-language models for dynamic facial expression recognition," *arXiv preprint arXiv:2308.13382*, 2023.

[86] C. Zheng, W. Wu, C. Chen, T. Yang, S. Zhu, J. Shen, N. Kehtarnavaz, and M. Shah, "Deep learning-based human pose estimation: A survey," *ACM Computing Surveys*, vol. 56, no. 1, pp. 1–37, 2023.

[87] A. Cappozzo, A. Cappello, U. Della Croce, and F. Pensalfini, "Surface-marker cluster design criteria for 3-d bone movement reconstruction," *IEEE Transactions on Biomedical Engineering*, vol. 48, no. 3, pp. 289–299, 2005.

[88] D. Robertson, G. Caldwell, J. Hamill, G. Kamen, and S. Whittlesey, *Research Methods in Biomechanics*. Human Kinetics, 2013.

[89] U. Della Croce, A. Cappozzo, and D. C. Kerrigan, "Pelvis and lower limb anatomical landmark calibration precision and its propagation to bone geometry and joint angles," *Medical & Biological Engineering & Computing*, vol. 43, no. 3, pp. 310–318, 2005.

[90] D. A. Winter, *Biomechanics and Motor Control of Human Movement*. John Wiley & Sons, 2009.

[91] C. J. De Luca, "Surface electromyography: Detection and recording," *DelSys Incorporated*, vol. 10, pp. 1–10, 2002.

[92] L. Chiari, U. D. Croce, A. Leardini, and A. Cappozzo, "Human movement analysis using stereophotogrammetry: Part 2: Instrumental errors," *Gait & Posture*, vol. 21, no. 2, pp. 197–211, 2005.

[93] R. Baker, J. McGinley, and R. Wolfe, "Motion analysis: Clinical applications," *Gait & Posture*, vol. 36, no. 1, pp. 86–92, 2012.

[94] M. Menolotto, D.-S. Komaris, S. Tedesco, B. O'Flynn, and M. Walsh, "Motion capture technology in industrial applications: A systematic review," *Sensors*, vol. 20, no. 19, p. 5687, 2020.

[95] W. Supanich, S. Kulkarineetham, P. Sukphokha, and P. Wisarnsart, "Machine learning-based exercise posture recognition system using mediapipe pose estimation framework," in *2023 9th International Conference on Advanced Computing and Communication Systems (ICACCS)*, vol. 1. IEEE, 2023, pp. 2003–2007.

[96] G. Bradski, "The opencv library," *Dr. Dobb's Journal of Software Tools*, 2000.

[97] A. P. Ismail, F. A. Abd Aziz, N. M. Kasim, and K. Daud, "Hand gesture recognition on python and opencv," in *IOP Conference Series: Materials Science and Engineering*, vol. 1045, no. 1. IOP Publishing, 2021, p. 012043.

[98] V. Koltun and R. Girshick, "Pystruct and opencv: Integrating structured prediction with computer vision," in *Proceedings of the IEEE International Conference on Computer Vision*, 2015, pp. 5319–5327.

[99] Z. Zhang and M. Cose, "Efficient estimation of body pose in 3d space using mediapipe," in *Proceedings of the 2021 IEEE International Conference on Robotics and Automation (ICRA 2021)*, 2021.

[100] Z. Cao, T. Simon, S. Wei, and Y. Sheikh, "Realtime multi-person 2d pose estimation using part affinity fields," in *Proceedings of the IEEE Conference on Computer Vision and Pattern Recognition*, 2017, pp. 7291–7299.

[101] V. S. P. Bhamidipati, I. Saxena, D. Saisanthiya, and M. Retnadhas, "Robust intelligent posture estimation for an ai gym trainer using mediapipe and opencv," in *2023 International Conference on Networking and Communications (ICNWC)*. IEEE, 2023, pp. 1–7.

[102] C. Lugaresi, M. Tang, H. Nash, H. McMahan, J. Shlens, and K. Murphy, "Mediapipe: A framework for building perception pipelines," *arXiv preprint arXiv:1906.08172*, 2019.

[103] P. Brinckmann, W. Frobin, G. Leivseth, and B. Dreup, *11 Dimensions, Mass, Location of the Center of Mass, and Moment of Inertia of the Segments of the Human Body*. Springer, 2015.

[104] P. Simon and Y. Gogotsi, "Materials for electrochemical capacitors nature materials," 2008.

[105] B. E. Conway, *Electrochemical supercapacitors: scientific fundamentals and technological applications*. Springer Science & Business Media, 2013.

[106] D. P. Auckland, "Statistics," https://www.dpanz.org.nz/research/statistics/, 2022, retrieved February 21, 2022, from Drowning Prevention Auckland.

[107] Z.-T. Gong, D.-X. Sun, and Y.-N. Liu, "Effects of a conformal coating on the signal integrity of space electronics systems," *IEEE Transactions on Components, Packaging and Manufacturing Technology*, vol. 12, no. 11, pp. 1882–1889, 2022.

[108] S. Meguid, C. Zhuo, and F. Yang, "Effective mitigation of shock loads in embedded electronic packaging using bilayered potting materials," *Journal of Electronic Packaging*, vol. 136, no. 4, p. 041010, 2014.

[109] S. Kumar, R. Bhooshan, S. Varshney, C. Verma, and L. Gideon, "Faraday cage for emc improvement of electronic devices," in *2015 IEEE 17th Electronics Packaging and Technology Conference (EPTC)*. IEEE, 2015, pp. 1–3.

[110] The MathWorks, Inc., *MATLAB version 9.15.0 (R2024b)*, The MathWorks, Inc., Natick, Massachusetts, United States, 2024. [Online]. Available: https://www.mathworks.com/products/matlab.html

[111] R. Meier, *CoolTerm version 1.9.2*, Freeware, 2024, terminal software for serial communication. [Online]. Available: https://freeware.the-meiers.org/

[112] M. Nordin, "Basic biomechanics of the musculoskeletal system," *Lippincott Williams & Wilkins google schola*, vol. 2, pp. 267–275, 2001.

Notes